UNIVERSITÀ DEGLI STUDI DI FIRENZE

DIPARTIMENTO DI FISICA

Tesi di Dottorato di Ricerca in Fisica (FIS/04)
di
Matteo Sani

Search for the Standard Model Higgs Boson in the decay channel into four muons with the CMS detector

Relatore:
Dott. Vitaliano Ciulli

Coordinatore:
Prof. Alessandro Cuccoli

XVIII CICLO DI DOTTORATO IN FISICA

Lo scienziato o l'uomo che cercano la veritá
possono scegliere davanti a se la via
dell'amore o quella della ragione, ma anche,
dentro di se, quella di un piccolo universo da scoprire.
Cosí qualche senese puó cercare la veritá e
trovarla nel piccolo mondo del Palio anziché nelle
vaste dimensioni filosofiche, politiche o religiose
dei movimenti di pensiero dell'umanitá.

Contents

Introduction

One of the open issues in High Energy Physics is the origin of the masses of elementary particles or, in terms of Quantum Field theory, the mechanism of spontaneous breaking of the electroweak symmetry. The most probable scenario is the Higgs mechanism which solves the problem of the generation of the gauge boson and fermion masses. This mechanism furthermore predicts the existence of a new particle, the Higgs boson.

Experimental observations have confirmed the validity of the Standard Model, but the Higgs boson itself has never been detected. It is an extremely elusive particle, because the production cross section is extremely low and, since its mass is a free parameter of the theory, it must be searched over a wide range of values. Direct searches for the Higgs boson through its decay channels, made at the LEP and Tevatron accelerators gave no evidence of its existence, fixing an exclusion limit $M_H > 115$ GeV/c^2. Theoretical arguments based upon self-consistence of the Standard Model, however fix an upper limit on the Higgs boson mass at ~ 1 TeV/c^2.

The resulting mass range will be explored by a new accelerator, the Large Hadron Collider (LHC), under construction at the European Laboratory for Particle Physics (CERN) in Geneva. This collider, which will start its operation in summer 2007, will have two proton beams with an energy of 7 TeV/c^2 each and a total center of mass energy of 14 TeV/c^2.

The Compact Muon Solenoid (CMS) detector is one of the two general purpouse detectors which will operate at LHC and it is designed not only to search for the Higgs particle but to detect also other possible sources of new physics (supersymmetry, extra dimensions, ...). The main feature of the CMS detector is the 4 Tesla superconducting solenoid magnet that permits a compact design of the detector with a strong magnetic field. Furthermore the high bending power of the magnet allows a precise measurement of particle momentum, which will be provided by the inner silicon microstrip tracking detector.

My contribution to the CMS activities has been the study of the discovery potential of Standard Model Higgs boson in its decay channel $H \rightarrow ZZ^{(*)} \rightarrow 4\mu$. This is the *golden channel* for Higgs boson discovery at LHC. The four muons in the final state make it particularly promising despite the very small cross section, barely few fb. The fully muonic decay of the Higgs boson has indeed the cleanest

experimental signature and would allow a very good estimate of the Higgs boson mass thanks to the excellent muon momentum resolution of the CMS detector. A clear signal in this channel is expected in the mass range $130 \lesssim M_H \lesssim 600$ GeV/c^2.

The kinematical characteristics of signal and background events have been studied in detailed. The attention has been focused in the analysis of those variables which mainly allow a selection of the signal events against background. Selection cuts were designed to maximize the expected signal statistical significance with an integrated luminosity of 20 fb^{-1}, one year of LHC operation at designed low luminosity ($\mathcal{L} = 2 \cdot 10^{33}$ cm^{-2} s^{-1}). To account for the presence of one or two on shell Z bosons in the final state, two different mass regions were considered: below and above the ZZ threshold. Furthermore a mass dependent threshold optimization has been performed.

Among the various source of background, special attention has been dedicated to the Z boson production in association with two b quarks. The cross section for this process is related to the b quark parton density function and it is therefore not precisely known. Moreover Zb$\bar{\text{b}}$ events are an important background to many other interesting physics channel at LHC, for example the SM channel pp$\rightarrow$ HZ with H $\rightarrow$ b$\bar{\text{b}}$, and a measurement of the production cross section is useful for b-quark parton density function evaluation.

Thus a technique to measure the Zb$\bar{\text{b}}$ cross section has been developed and few pb^{-1} of luminosity will be enough to cross-check Monte Carlo predictions for this channel.

The results of this work show that a Higgs boson with a mass of about 200 GeV/c^2 would be discovered after few months of data taking at the nominal low luminoisity. A discovery in the mass range below 130 or above 500 GeV/c^2, and in the region $160 \div 180$ GeV/c^2, will instead require to combine different channels in order to be obtained in the first year of data taking.

Chapter 1

The Electroweak Interactions and the Higgs Boson

Interactions between elementary particles are nowadays best described by the Standard Model [1]. In this Chapter the basic concepts of this model are introduced starting with the description of the gauge symmetry $SU(2) \otimes U(1)$, and how spontaneous breaking of the symmetry yields the massive bosons $W^{\pm}$ and Z and a yet undiscovered particle, the Higgs boson. In the last Section is described how fermions, through their interaction with this new particle, acquire mass. Finally the Higgs boson field and its properties are reviewed.

In the following natural units are used, unless clearly specified, and both in formulae and in experimental results is $\hbar = c = 1$.

1.1 The elementary particles

The elementary particles can be divided into fermions and bosons. The latter are responsible of the interactions and are described in the following paragraphs. Fermions are classified into three lepton families and three quark families:

$$\begin{pmatrix} \nu_e \\ e \end{pmatrix} \quad \begin{pmatrix} \nu_\mu \\ \mu \end{pmatrix} \quad \begin{pmatrix} \nu_\tau \\ \tau \end{pmatrix}$$

$$\begin{pmatrix} u \\ d \end{pmatrix} \quad \begin{pmatrix} c \\ s \end{pmatrix} \quad \begin{pmatrix} t \\ b \end{pmatrix}$$

Known matter is made of leptons and quark combinations (hadrons).

All the elements belonging to the three generations have been directly observed and up to now there are no experimental evidences of a fourth generation of elementary particles.

1.2 A gauge theory of weak interactions

From a historical point of view, the starting point of electroweak interactions is Fermi's theory of β and muon decay [2]. This theory was based on an effective four-fermion Lagrangian which is usually written as follows:

$$\mathcal{L} = -\frac{G_\beta}{\sqrt{2}}\bar{p}\gamma^\alpha(1 - a\gamma_5)n\bar{e}\gamma_\alpha(1-\gamma_5)\nu_e - \frac{G_\mu}{\sqrt{2}}\bar{\nu}_\mu\gamma^\alpha(1-\gamma_5)\mu\bar{e}\gamma_\alpha(1-\gamma_5)\nu_e\,, \quad (1.1)$$

with

$$G_\mu \approx 1.16639 \times 10^{-5}\ \mathrm{GeV}^{-2}\,, \qquad G_\beta \approx G_\mu\,, \qquad a \approx 1.24 \pm 0.09\,. \quad (1.2)$$

This point like interaction is usually referred to as V-A interaction, being formed by a vectorial and an axial component. The operator $(1-\gamma_5)/2$ is the negative helicity projector whose results are helicity eigenstates if the particle energy is much greater than its mass. So right-handed neutrinos and left-handed antineutrinos [3] do not participate to this interaction.

The Lagrangian in eq. 1.1 is not renormalizable and it results in a non-unitary $\mathcal{S}$ matrix. This problem can be overcome if electroweak interactions possesses local invariance under the action of some group, i.e. it can be described by a *gauge* theory like *quantum electrodynamics* (QED) [4]. This theory must reduce to eq. 1.1 in the low energy limit, in the sense that the local four-fermion interaction of the Fermi Lagrangian will be interpreted as the exchange of a massive vector boson (force carrier) with a momentum much smaller than its mass.

In order to obtain this result, a group of local invariance must be chosen and then the particle fields have to be assigned to a representation of this group. Both these steps are made with the help of the information contained in the Fermi Lagrangian. Let us first consider the electron and the electron neutrino. They participate in the weak interaction via the current

$$J_\mu = \bar{\nu}_e \gamma_\mu \frac{1}{2}(1-\gamma_5) e \,. \tag{1.3}$$

The current J_μ should be rewritten in the form of a Noether current

$$\bar{\psi}_i \gamma_\mu T^A_{ij} \psi_j \,, \tag{1.4}$$

where ψ_i are the components of some multiplet of the gauge group and T^A_{ij} are the corresponding group generators. In the case of J_μ, this can be done in the following way. The current J^+_μ can be expressed as

$$J^+_\mu = \bar{L} \gamma_\mu \tau^+ L \,, \tag{1.5}$$

where

$$L = \frac{1}{2}(1-\gamma_5) \begin{pmatrix} \nu_e \\ e \end{pmatrix} \equiv \begin{pmatrix} \nu_{eL} \\ e_L \end{pmatrix} , \tag{1.6}$$

$$\tau^+ = \frac{1}{2}(\tau_1 + i\tau_2) \tag{1.7}$$

and τ_i are the usual Pauli matrices.

In the context of gauge theories, currents are in one to one correspondence with generators of the symmetry group. The group generators, in turn, form a closed set with respect to the commutation operation, therefore the current

$$J^-_\mu = \bar{L} \gamma_\mu \tau^- L \,, \tag{1.8}$$

where $\tau^- = (\tau_1 - i\tau_2)/2$ and

$$J^3_\mu = \bar{L} \gamma_\mu \tau_3 L \tag{1.9}$$

will also participate in the interaction.

No other current must be introduced since $[\tau_3, \tau^\pm] = \pm 2\tau^\pm$; the current J_μ has been interpreted as being one of the three conserved currents of a theory with $SU(2)$ gauge invariance and left-handed neutrino and electron fields have been assigned to an $SU(2)$ doublet.

The right-handed neutrino and electron components, ν_{eR} and e_R, do not take part in the weak interaction phenomena described by the Fermi Lagrangian, so they must be assigned to the singlet (or scalar) representation. Of course, this is not the only possible choice, but it's the simplest one since it does not require the introduction of fermion fields other than the observed ones.

The current J_3^μ is a *neutral* current: it contains operators of particles with the same charge. This neutral current cannot be identified with the electromagnetic one. First, the electromagnetic current involves both left-handed and right-handed fermion fields with the same weight; second, the electromagnetic current does not contain a neutrino term, the neutrino being chargeless.

As customary in gauge theories the covariant derivative is

$$D^\mu = \partial^\mu - igW_i^\mu \frac{\tau_i}{2}\,, \tag{1.10}$$

where a vector field W_i^μ and a coupling constant g have been introduced. Now the gauge-invariant Lagrangian for fermion fields is

$$\mathcal{L} = i\bar{L}\gamma_\mu D^\mu L + i\bar{\nu}_{eR}\gamma_\mu D^\mu \nu_{eR} + i\bar{e}_R\gamma_\mu D^\mu e_R\,. \tag{1.11}$$

This Lagrangian $\mathcal{L}$ contains the usual kinetic term for fermions and a term $\mathcal{L}_W$ that describes the interaction of fermions with the gauge bosons W_i^μ. The interaction term can be split into two parts, corresponding to neutral-current and charged-current interaction:

$$\mathcal{L}_W^n = \frac{g}{2}W_3^\mu(\bar{\nu}_{eL}\gamma_\mu\nu_{eL} - \bar{e}_L\gamma_\mu e_L) \tag{1.12}$$

and

$$\mathcal{L}_W^c = \frac{g}{\sqrt{2}}\bar{L}\gamma^\mu\tau^+ L W_\mu^+ + \frac{g}{\sqrt{2}}\bar{L}\gamma^\mu\tau^- L W_\mu^-\,, \tag{1.13}$$

where the charged part is expressed in terms of the fields

$$W_\mu^\pm = \frac{1}{\sqrt{2}}(W_\mu^1 \mp iW_\mu^2) \tag{1.14}$$

as usual.

The interaction foresees the existence of intermediate vector bosons as weak force mediators, in contrast with the Fermi theory which describes a point like interaction as stated above.

1.2.1 Electroweak unification

It has been already observed that neutral current J_3^μ cannot be identified with the electromagnetic current. The simplest way of extending the gauge group $SU(2)$ to include another neutral generator is to include an abelian factor $U(1)$:

$$SU(2) \to SU(2) \otimes U(1)\,. \tag{1.15}$$

The Lagrangian is required to be invariant also under the $U(1)$ gauge transformations

$$\psi \rightarrow \psi' = \exp\left[ig' a \frac{Y}{2}\right]\psi\,, \tag{1.16}$$

where ψ is a generic field of the theory, g' is the coupling constant associated with the $U(1)$ factor of the gauge group and Y is a quantum number, usually called the *weak hypercharge*, to be specified for each field ψ. Since the $SU(2)$ factor of the gauge group acts in a different way on the left-handed and right-handed fermions, it is natural to allow for the possibility of assigning different hypercharge quantum numbers to the left and right components of the same fermion field. A new gauge vector field must be introduced together with a new covariant derivative

$$D^\mu = \partial^\mu - igW_i^\mu \frac{\tau_i}{2} - ig'\frac{Y}{2}B_i^\mu\,, \tag{1.17}$$

where Y is a diagonal matrix with the hypercharge values in its diagonal entries. Since Y is diagonal, only the term $\mathcal{L}_W^n$ is modified. If we form a column vector Ψ with all the fermionic fields present in the theory (with left and right-handed components of the same particle counted separately), the neutral current electroweak interaction Lagrangian can be written in the following form

$$\mathcal{L}_W^n = g\bar{\Psi}\gamma_\mu T_3 \Psi W_3^\mu + g'\bar{\Psi}\gamma_\mu \frac{Y}{2}\Psi B^\mu \tag{1.18}$$

($T_3 = \pm 1/2$ for ν_{eL} and e_L respectively, and $T = 0$ for ν_{eR} and e_R). Now the quantum numbers Y are assigned in such a way that the electromagnetic interaction term appears in Eq. 1.18. To do this, we first perform a rotation by an angle θ_W (*weak mixing angle*) [5] so that

$$B^\mu = A^\mu \cos\theta_W - Z^\mu \sin\theta_W\,, \tag{1.19}$$

$$W_3^\mu = A^\mu \sin\theta_W + Z^\mu \cos\theta_W\,. \tag{1.20}$$

In terms of the new vector fields A_μ, Z_μ Eq. 1.18 takes the form

$$\begin{aligned}\mathcal{L}_W^n = {} & \bar{\Psi}\gamma_\mu \left(g\sin\theta_W T_3 + g'\cos\theta_W \frac{Y}{2}\right)\Psi A^\mu \\ & + \bar{\Psi}\gamma_\mu \left(g\cos\theta_W T_3 - g'\sin\theta_W \frac{Y}{2}\right)\Psi Z^\mu\,.\end{aligned} \tag{1.21}$$

To identify one of the two neutral vector fields, say A_μ, with the photon fields, $Y(L)$, $Y(\nu_{eR})$ and $Y(e_R)$ must be chosen so that A^μ couples to the electromagnetic current. In other words, it must be

$$g \sin\theta_W T_3 + g' \cos\theta_W \frac{Y}{2} = eQ\,, \tag{1.22}$$

where Q is the electromagnetic charge matrix in units of the positron charge e. Equation 1.22 restricted to the doublet of the left-handed leptons gives immediately

$$g \sin\theta_W = e\,. \tag{1.23}$$

Choosing

$$g' \cos\theta_W = e \tag{1.24}$$

we finally get

$$T_3 + \frac{Y}{2} = Q \qquad \text{or} \qquad Y = 2(Q - T_3)\,. \tag{1.25}$$

For the electron and its neutrino we find

$$Y(L) = -1\,, \qquad Y(\nu_{eR}) = 0 \qquad \text{and} \qquad Y(e_R) = -2\,. \tag{1.26}$$

Notice that the right-handed neutrino has zero charge and zero hypercharge, and it is an $SU(2)$ singlet: it does not take part in electroweak interactions. The extension of the theory to other lepton doublets is straightforward.

1.2.2 Quark sector

The introduction of the hadrons in the theory can be performed in term of quark fields taking as a starting point the hadronic current responsible for β decay.

The left-handed components of the quarks are arranged into $Y = +1/3$ isospin doublets

$$\mathrm{Q}_L = \begin{pmatrix} U_L \\ D_L \end{pmatrix} \in \left(2, \frac{1}{3}\right) \tag{1.27}$$

and the right-handed into singlets

$$\begin{aligned} U_R &\in (1, \tfrac{4}{3})\,, \\ D_R &\in (1, -\tfrac{2}{3})\,, \end{aligned} \tag{1.28}$$

where U and D are combinations of the mass eigenstates $u_i = \mathrm{u, c, t}$ and $d_i = \mathrm{d, s, b}$:

$$\mathrm{U}^i_{L,R} = \sum_{j=1}^{3} X(\mathrm{U}^{ij}_{L,R}) u^j_{L,R}\,, \qquad \mathrm{D}^i_{L,R} = \sum_{j=1}^{3} X(\mathrm{D}^{ij}_{L,R}) d^j_{L,R}\,. \tag{1.29}$$

The $X(\mathrm{U,D})_{L,R}$ are 3×3 unitary matrices related to the Cabibbo-Kobayashi-Maskawa quark mixing matrix [6]. In analogy with the leptonic case, the quark electroweak Lagrangian is

$$\mathcal{L}^{quark}_{EW} = i \sum_{i=1}^{3} \left(\mathrm{Q}^{+i}_L \bar{\sigma^\mu} D_\mu \mathrm{Q}^i_L + \mathrm{U}^{+i}_R \sigma^\mu D_\mu \mathrm{U}^i_R + \mathrm{D}^{+i}_R \sigma^\mu D_\mu \mathrm{D}^i_R \right)\,, \tag{1.30}$$

with D_μ from Eq. 1.17.

The Glashow[7], Weinberg [8], Salam [9] model (Standard Model) can be then extended to a gauge field theory $SU(3)_c \otimes SU(2)_L \otimes U(1)_Y$ which includes the strong interaction between hadrons, called *quantum chromodynamics* (QCD). The QCD charge is represented by the colour (red, green or blue) that any quark carries and exchanges through eight different bi-coloured massless *gluons* g [10]. The colour interaction is represented by

$$\mathcal{L}_{QCD} = -g_s \sum_{i,j,k} (\bar{q^k_i} \gamma^\mu T^{ij}_a q^k_j) G^a_\mu - \frac{1}{4} G^a_{\mu\nu} G^{\mu\nu}_a\,, \tag{1.31}$$

which is composed with the gluon kinetic term

$$G^a_{\mu\nu} = \partial_\mu A^a_\mu - \partial_\nu A^a_\nu + g_s f_{abc} A^b_\mu A^c_\nu \tag{1.32}$$

and the interaction between the gluon fields and quarks where g_s is the QCD coupling constant, γ^μ are the Dirac matrices, $T^a_{ij} (a = 1, \ldots, 8)$ are the $SU(3)_c$ colour matrices and f_{abc} the colour structure constant; q^k_i are the Dirac spinors associated with the i-coloured k-type quark fields and $A^a_\mu(x)$ are the eight Yang-Mills gluon fields.

The extension is quite straightforward except for the fact that the symmetry group $SU(3)$ is not an abelian group. As a consequence force carriers of a such theory result charged particle, unlike photons in QED, so in QCD it is possible to have interactions between two or more gluons.

1.2.3 Mass terms

To conclude the construction of the gauge-invariant part of the Standard Model Lagrangian, the pure Yang-Mills term has to be considered

$$\mathcal{L}_{YM} = -\frac{1}{4}B_{\mu\nu}B^{\mu\nu} - \frac{1}{4}W^i_{\mu\nu}W^{\mu\nu}_i \,, \tag{1.33}$$

where

$$\begin{aligned} B^{\mu\nu} &= \partial^\mu B^\nu - \partial^\nu B^\mu \,, \\ W^{\mu\nu}_i &= \partial^\mu W^\nu_i - \partial^\nu W^\mu_i + g\epsilon_{ijk}W^\mu_j W^\nu_k \,. \end{aligned} \tag{1.34}$$

The Lagrangian now describes massless gauge bosons and fermions. A mass term for fermion fields f

$$-m_f\bar{f}f = -m_f(\bar{f_R}f_L + \bar{f_L}f_R) \tag{1.35}$$

manifestly violates gauge invariance because f_L and f_R are members of $SU(2)$ doublet and singlet respectively, therefore it cannot be added by hand.

In order to be consistent with the Fermi theory, which is known to correctly describe low-energy weak interactions, the gauge vector bosons of weak interactions have to acquire a mass. The order of magnitude of the W mass for example can be estimated by requiring the electroweak amplitude to be equal to the Fermi amplitude in the limit of low transfered momentum ($q^2 \to 0$). The comparison between the two amplitude leads to the following equation

$$\frac{G_\beta}{\sqrt{2}} = \left(\frac{g}{2\sqrt{2}}\right)^2 \frac{1}{\mathrm{M_W^2}} \,. \tag{1.36}$$

Recalling that $g = e/\sin\theta_W$, Eq. 1.36 gives the lower bound

$$\mathrm{M_W} \geq 37.3 \text{ GeV/c}^2 \,, \tag{1.37}$$

quite a large value, if compared with the present upper bound on the photon mass [5]

$$\mathrm{m}_\gamma \leq 6 \cdot 10^{-17}\mathrm{eV/c^2} \,. \tag{1.38}$$

So if the weak interactions are to be mediated by vector bosons these must be very heavy. On the other hand, gauge theories are incompatible with mass terms for the vector bosons so one possibility is to break gauge invariance explicitly and insert a mass term for the W boson by hand, but this leads to a non renormalizable theory.

1.3 The Higgs boson

The Higgs mechanism of spontaneous symmetry breaking (the Higgs mechanism for short) solves the problem of generating the gauge boson and the fermion masses without violating $SU(2) \otimes U(1)$ gauge invariance [11]. This mechanism will be briefly sketched in the following subsection and applied to the Standard Model case.

1.3.1 Spontaneous breaking of the symmetry

A simple example is considered to see how a mass term for gauge vector bosons could be introduced without spoiling renormalizability and unitarity, and then generalized to the Standard Model. The simple theory considered is scalar electrodynamics, that is a gauge theory based on $U(1)$ invariance, coupled to one complex scalar field ϕ with charge $-e$. The Lagrangian is given by

$$\mathcal{L} = -\frac{1}{4}F^{\mu\nu}F_{\mu\nu} + (D^{\mu}\phi)^{+}D_{\mu}\phi - V(\phi)\,, \tag{1.39}$$

where $D^{\mu} = \partial^{\mu} + ieA^{\mu}$ and $V(\phi)$ is the so-called scalar potential, which is

$$V(\phi) = \mu^2\phi^*\phi + \lambda(\phi^*\phi)^2\,. \tag{1.40}$$

The Lagrangian is invariant under the usual local $U(1)$ transformation

$$\phi(x) \rightarrow \exp\left[i\alpha(x)\right]\phi(x)\,, \qquad A_{\mu}(x) \rightarrow A_{\mu} - \partial_{\mu}\alpha(x)\,. \tag{1.41}$$

For $\mu^2 > 0$, $\mathcal{L}$ is simply the QED Lagrangian for a charged scalar particle of mass μ and with ϕ^4 self interactions. For $\mu^2 < 0$, the field $\phi(x)$ acquires a vacuum expectation value (vev) and the potential V has no more a unique minimum state which can be chosen at

$$\langle\phi\rangle_0 \equiv \langle 0\,|\phi|\,0\rangle = \left(-\frac{\mu^2}{2\lambda}\right)^{1/2} \equiv \frac{v}{\sqrt{2}}\,. \tag{1.42}$$

The potential V in the case $\mu^2 < 0$ is shown in Fig. 1.1. If the Lagrangian is expanded around the vacuum state $\langle\phi\rangle$

$$\phi(x) = \frac{1}{\sqrt{2}}[v + \phi_1(x) + i\phi_2(x)] \tag{1.43}$$

it then becomes, up to some interaction terms that are omitted for simplicity,

$$\begin{aligned}\mathcal{L} &= -\frac{1}{4}F_{\mu\nu}F^{\mu\nu} + (\partial_\mu + ieA_\mu)\phi^*(\partial^\mu - ieA^\mu) - \mu^2\phi^*\phi - \lambda(\phi^*\phi)^2 = \\ &= -\frac{1}{4}F_{\mu\nu}F^{\mu\nu} + \frac{1}{2}(\partial_\mu\phi_1)^2 + \frac{1}{2}(\partial_\mu\phi_2)^2 - v^2\lambda\phi_1^2 + \frac{1}{2}e^2v^2A_\mu A^\mu - evA_\mu\partial^\mu\phi_2\,.\end{aligned} \tag{1.44}$$

Three remarks can then be made at this stage: there is a photon mass term in the Lagrangian $\frac{1}{2}\mathrm{M}_\mathrm{A}^2 A_\mu A^\mu$ with $\mathrm{M}_\mathrm{A} = ev = -e\mu^2/\lambda$, a scalar particle ϕ_1 is still present with a mass $\mathrm{M}_{\phi_1}^2 = -2\mu^2$, and apparently a massless particle ϕ_2, the so called Goldstone boson, has appeared.

However, there is still a problem to be addressed. In the beginning, the theory had four degrees of freedom, two for the complex scalar field ϕ and two for the massless electromagnetic field A_μ, and now it apparently has five degrees of freedom, one for ϕ_1, one for ϕ_2 and three for the massive photon A_μ. Therefore, there must be a field which is not physical and indeed, in $\mathcal{L}$ there is a bilinear term $evA^\mu\partial_\mu\phi_2$ which has to be eliminated. To do so,it can be noticed that at first

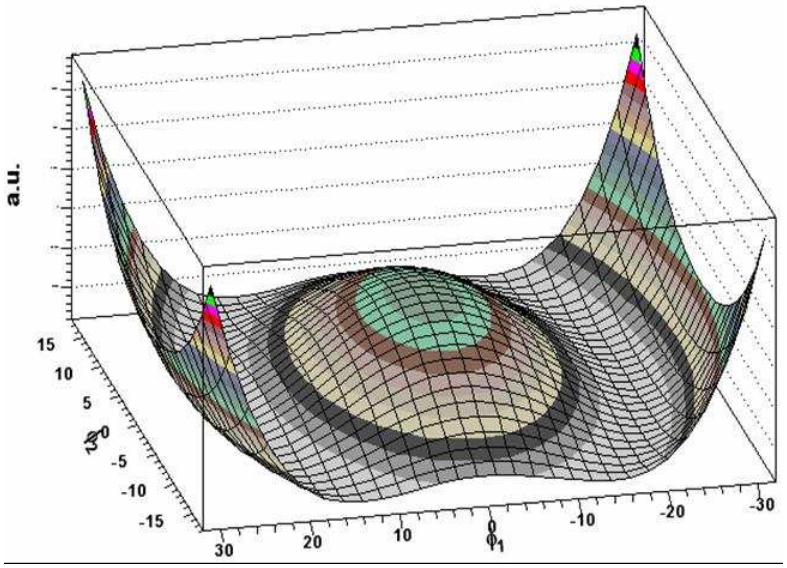

Figure 1.1: The potential V of the scalar field ϕ in the case $\mu^2 < 0$.

order, the original field ϕ becomes

$$\phi = \frac{1}{\sqrt{2}}(v + \phi_1 + i\phi_2) \equiv \frac{1}{\sqrt{2}}[v + \eta(x)] \exp\left[i\zeta(x)/v\right]. \tag{1.45}$$

By using the freedom of gauge transformations and by performing also the substitution

$$A_\mu \to A_\mu - \frac{1}{ev}\partial_\mu \zeta(x) \tag{1.46}$$

the $A_\mu \partial_\mu \zeta$ term, and in fact all ζ terms, disappear from the Lagrangian. This choice of gauge, for which only the physical particles are left in the Lagrangian, is called the unitary gauge. Thus, the photon (with two degrees of freedom) has absorbed the would be Goldstone boson (with one degree of freedom) and has become massive (i.e. with three degrees of freedom): the longitudinal polarization is the Goldstone boson. The $U(1)$ gauge symmetry is no more apparent and we say that it is spontaneously broken. This is the Higgs mechanism which allows to generate masses for the gauge bosons.

1.3.2 The Higgs mechanism

In the slightly more complicated non abelian case of the Standard Model, masses need to be generated for the three gauge bosons $\mathrm{W}^\pm$ and Z but the photon should remain massless and QED must stay an exact symmetry. Therefore, at least three degrees of freedom for the scalar fields are needed. The simplest choice is a complex $SU(2)$ doublet of scalar fields ϕ

$$\Phi = \begin{pmatrix} \phi^+ \\ \phi^0 \end{pmatrix}, \qquad Y_\phi = +1\,. \tag{1.47}$$

The invariant terms of the scalar field part $\mathcal{L}_\mathcal{S}$ has to be added to the Standard Model Lagrangian $\mathcal{L}_{\mathcal{SM}}$ where the strong interaction part has been ignored

$$\mathcal{L}_\mathcal{S} = (D^\mu \Phi)^+ (D_\mu \Phi) - \mu^2 \Phi^+ \Phi - \lambda (\Phi^+ \Phi)^2\,. \tag{1.48}$$

For $\mu^2 < 0$, the neutral component of the doublet field Φ will develop a vacuum expectation value (the vev should not be in the charged direction to preserve $U(1)_\mathrm{Q}$)

$$\langle \Phi \rangle_0 \equiv \langle 0 \left| \Phi \right| 0 \rangle = \begin{pmatrix} 0 \\ \frac{v}{\sqrt{2}} \end{pmatrix} \qquad \text{with} \qquad v = (-\mu^2/\lambda)^{1/2}\,. \tag{1.49}$$

The schema previously sketched can be followed: write the field Φ in terms of four fields $\theta_{1,2,3}(x)$ and $H(x)$ at first order

$$\Phi(x) = \begin{pmatrix} \theta_2 + i\theta_1 \\ \frac{1}{\sqrt{2}}(v+H) - i\theta_3 \end{pmatrix} = \exp\left[i\theta_a(x)\tau^a(x)/v\right] \begin{pmatrix} 0 \\ \frac{1}{\sqrt{2}}(v+H) \end{pmatrix}, \quad (1.50)$$

make a gauge transformation on this field to move to the unitary gauge

$$\Phi(x) \to \exp\left[-i\theta_a(x)\tau^a(x)\right]\Phi(x) = \frac{1}{\sqrt{2}} \begin{pmatrix} 0 \\ v + H(x) \end{pmatrix}, \quad (1.51)$$

then fully expand the term $|D_\mu \Phi|^2$ of the Lagrangian $\mathcal{L}_S$ and pick up the terms which are bilinear in the new fields 1.20 and 1.14 ($\mathrm{W}^\pm$, Z, A)

$$\mathrm{M}_\mathrm{W}^2 \mathrm{W}_\mu^+ \mathrm{W}^{-\mu} + \frac{1}{2}\mathrm{M}_\mathrm{Z}^2 \mathrm{Z}_\mu \mathrm{Z}^\mu + \frac{1}{2}\mathrm{M}_\mathrm{A}^2 \mathrm{A}_\mu \mathrm{A}^\mu \,. \quad (1.52)$$

The W and Z bosons have acquired masses, while the photon is still massless

$$\mathrm{M}_\mathrm{W} = \frac{1}{2} v g_2 \,, \qquad \mathrm{M}_\mathrm{Z} = \frac{1}{2} v \sqrt{g_2^2 + g_1^2} \,, \qquad \mathrm{M}_\mathrm{A} = 0 \,. \quad (1.53)$$

By spontaneously breaking the symmetry $SU(2)_L \otimes U(1)_Y$, three Goldstone bosons have been absorbed by the $\mathrm{W}^\pm$ and Z bosons to form their longitudinal components and to get their masses. Since the $U(1)_Q$ symmetry is still unbroken, the photon which is its generator, remains massless as it should be.

Using the same scalar field Φ, with hypercharge $Y = 1$, and the isodoublet $\tilde{\Phi} = i\tau_2 \Phi^*$, which has hypercharge $Y = -1$ the fermion masses can also be generated. For any fermion generation, an $SU(2)_L \otimes U(1)_Y$ invariant Yukawa term must be introduced in the Lagrangian

$$\mathcal{L}_F = -\lambda_e \bar{L} \Phi e_R - \lambda_d \bar{Q} \Phi d_R - \lambda_u \bar{Q} \tilde{\Phi} u_R + h.c. \,. \quad (1.54)$$

Taking for instance the case of the electron

$$\begin{aligned} \mathcal{L}_F &= -\frac{1}{\sqrt{2}} \lambda_e (\bar{\nu_e}, \bar{e_L}) \begin{pmatrix} 0 \\ (v+H) \end{pmatrix} e_R + \cdots \\ &= -\frac{1}{\sqrt{2}} \lambda_e (v+H) \bar{e_L} e_R + \cdots \end{aligned} \quad (1.55)$$

The constant term in front of $\bar{f}_L f_R$ (and h.c.) is identified with the fermion mass

$$\mathrm{m}_e = \frac{\lambda_e v}{\sqrt{2}}\,, \qquad \mathrm{m}_u = \frac{\lambda_u v}{\sqrt{2}}\,, \qquad \mathrm{m}_d = \frac{\lambda_d v}{\sqrt{2}}\,. \tag{1.56}$$

Again being the λ_f free parameters, the mass of the fermions could not be predicted by the theory.

Very often the Standard Model refers even to $SU(3) \otimes SU(2) \otimes U(1)$ gauge theory when combined with the electroweak symmetry breaking mechanism. In this work we will use this name for both options.

1.3.3 Higgs boson sector

The kinetic part of the Higgs field, $\frac{1}{2}(\partial_\mu H)^2$, comes from the term involving the covariant derivative $|\partial_\mu \Phi|^2$, while the mass and self interaction parts come from the scalar potential

$$V = \frac{\mu^2}{2}(0, v+H)\begin{pmatrix} 0 \\ v+H \end{pmatrix} + \frac{\lambda}{4}\left|(0, v+H)\begin{pmatrix} 0 \\ v+H \end{pmatrix}\right|^2 . \tag{1.57}$$

Using the relation $v^2 = -\mu^2/\lambda$

$$V = -\frac{1}{2}\lambda v^2 (v+H)^2 + \frac{1}{4}(v+H)^4\,, \tag{1.58}$$

so the Lagrangian containing the Higgs field H is given by

$$\mathcal{L}_H = \frac{1}{2}(\partial_\mu H)(\partial^\mu H) - V = \frac{1}{2}(\partial_\mu H)^2 - \lambda v^2 H^2 - \lambda v H^3 - \frac{\lambda}{4}H^4\,. \tag{1.59}$$

From this Lagrangian, the Higgs boson mass simply reads

$$\mathrm{M}_\mathrm{H}^2 = 2\lambda v^2 = -2\mu^2\,, \tag{1.60}$$

where the dependence from the free parameter λ make it an unpredictable parameter of the theory.

From the Lagrangian describing the gauge boson and fermion masses also the Higgs boson couplings to gauge bosons and fermions could be obtained

$$g_{Hff} = i\frac{\mathrm{m_f}}{v}\,, \qquad g_{HVV} = -2i\frac{\mathrm{M_V^2}}{v}\,, \qquad g_{HHVV} = -2i\frac{\mathrm{M_V^2}}{v^2}\,. \tag{1.61}$$

The proportionality of the interaction strength to the fermion mass is a prediction of the theory; interaction with lighter quarks is disfavored, since the vertex couplings depend on the ratio m_f/M_W. Indeed the vacuum expectation value v is fixed in terms of the W boson mass M_W or the Fermi constant G_μ determined from muon decay

$$M_W = \frac{1}{2} g_2 v = \left(\frac{\sqrt{2} g^2}{8 G_\mu} \right)^{1/2} \Rightarrow v = \frac{1}{(\sqrt{2} G_\mu)^{1/2}} \simeq 246 \text{ GeV/c}^2 . \quad (1.62)$$

1.3.4 Higgs boson mass

The Higgs boson mass is the only yet unknown free parameter of the Standard Model.

Both theoretical and experimental constraints however exist, including those from direct search at colliders and in particular at LEP [12, 13, 14].

Theoretical constraints

Theoretical constraints can be derived by imposing the energy range in which the Standard Model shall be valid before perturbation theory breaks down and new phenomena emerge. These include constraints from unitarity in scattering amplitude, perturbativity of the Higgs self coupling, stability of the electroweak vacuum and fine tuning [15].

The tighter theoretical constraints come from one loop matching conditions relating the particle couplings to their masses [16, 17]. The allowed upper and lower limits as a function of the cutoff parameter Λ at which the Standard Model is replaced by a higher energy theory are shown in Fig. 1.2. The upper limit is obtained requiring that the quartic coupling of Higgs potential remain finite (*triviality*). The lower line limits the region in which the quartic coupling becomes negative and the potential is unbounded from below (*vacuum stability*). The allowed region lies between the two bands which illustrate the theoretical uncertainties. If the validity of the Standard Model is assumed up to the Plank scale ($\Lambda \sim 10^{19}$ GeV), the allowed Higgs mass range is between 130 and 190 GeV/c^2. Conversely, a possible discovery of the Standard Model Higgs boson outside this mass range would be a hint of the presence of a new theory above a certain energy scale.

Experimental constraints

Since the Higgs particle contributes to radiative corrections, many electroweak observables can be used to constraint its mass. All the precision electroweak results obtained by the four LEP experiments (ALEPH [19], DELPHI [20], L3 [21] and OPAL [22]) and by SLD [23], CDF [24] and D0 [25], such as cross sections, masses and various couplings of the heavy electroweak gauge bosons, have been combined together assuming the Standard Model to be the correct theory of nature. The results are reported in Fig. 1.3 and the $\Delta\chi^2$ of the fit to all measurements as a function of M_H, with the uncertainties on $\Delta\alpha^{had}$, $\alpha(M_Z)$, $\alpha_s(M_Z)$, m_t as well as on M_Z is shown in Fig. 1.4.

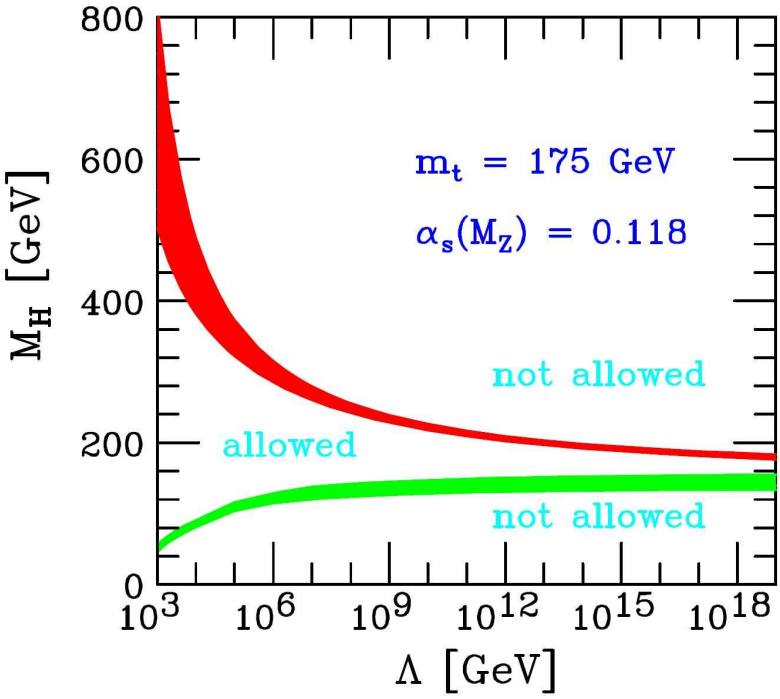

Figure 1.2: The triviality (upper) bound and the vacuum stability (lower) bound on the Higgs boson mass as a function of the new physics or cut-off scale Λ for a top quark mass $m_t = 175 \pm 6$ GeV and $\alpha_s(M_Z) = 0.118 \pm 0.002$; the allowed region lies between the bands and the coloured/shaded bands illustrate the impact of various uncertainties [18].

The one loop corrections to electroweak parameters have at most logarithmic dependence on M_H, as stated by the screening theorem, which explains why the $\Delta\chi^2$ is quadratic with respect to $\log(M_H)$.

The indirectly measured value of the Higgs boson mass, corresponding to the minimum of the curve, is

$$M_H = 129^{+74}_{-49}\ \mathrm{GeV/c^2} \tag{1.63}$$

at 68 percent confidence [26]. The shaded bands represent the uncertainty in the calculation due to neglected higher-order corrections.

The precision electroweak measurements also tell us that the mass of the Standard Model Higgs boson is about 285 $\mathrm{GeV/c^2}$ one-sided 95 percent confidence level upper limit. Instead the area to the left of the vertical band, which is very close to the minimum of the fit, shows the exclusion limit $M_H > 114.4\ \mathrm{GeV/c^2}$ from direct searches at LEP2.

The result 1.63 is obviously model-dependent, being calculated from loop corrections, that could be circumvented by some new physics contributions. This result is well-grounded only within the Standard Model theory and has always to be confirmed by the direct observation of the Higgs boson.

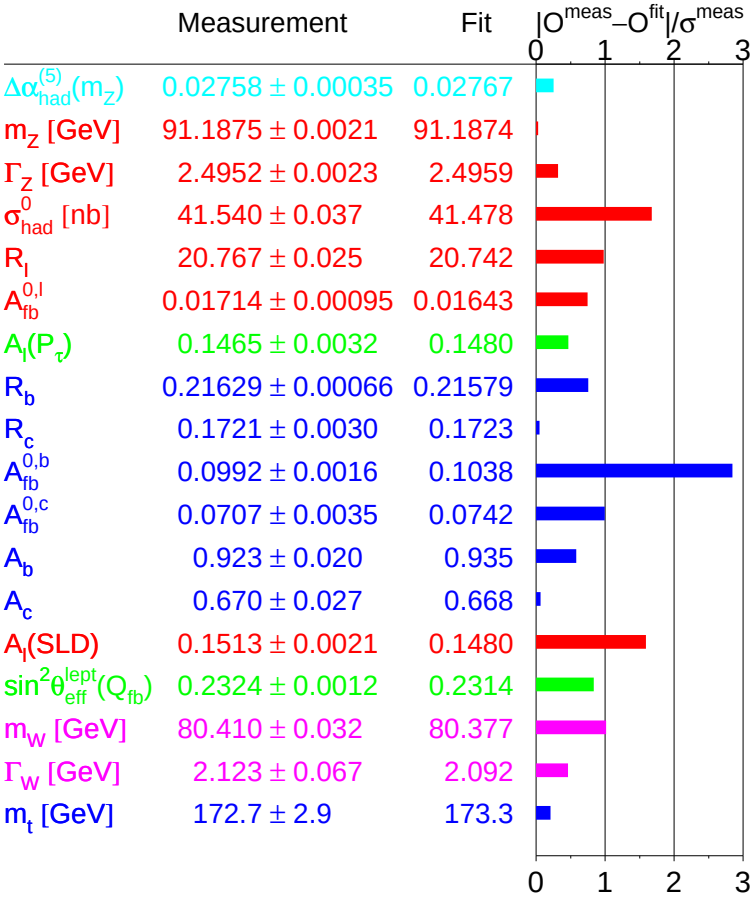

Figure 1.3: Summary of electroweak precision measurements at LEP, SLC and the Tevatron [26]. The Standard Model fit results and the residuals are also shown.

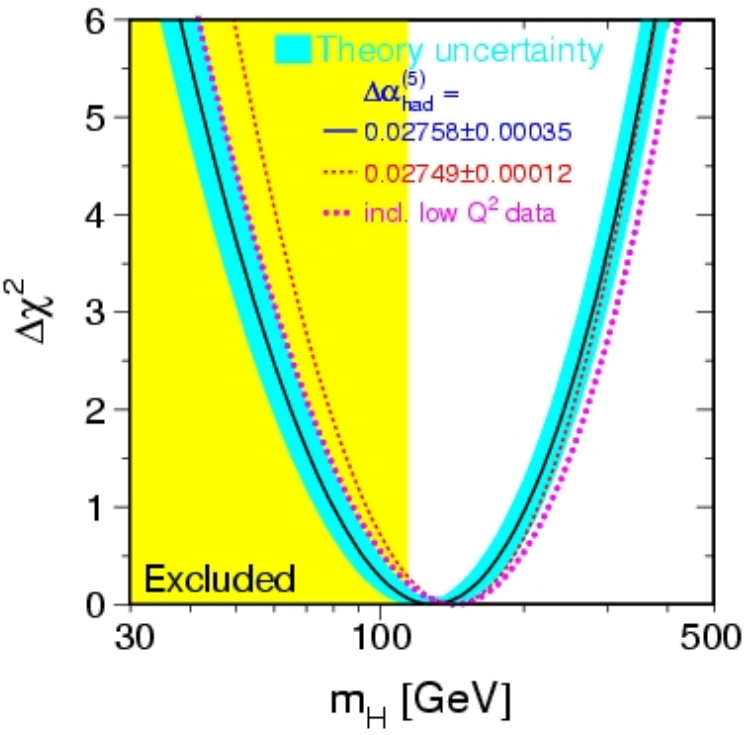

Figure 1.4: The $\Delta\chi^2$ of the fit to the electroweak precision data as a function of M_H. The solid line represents the result when all data are included and the blue/shaded band is the estimated theoretical error from unknown higher-order corrections [26]. The effect of including the low Q^2 data and the use of a different value for $\Delta\alpha_{had}$ are also shown.

Chapter 2

The CMS Experiment at LHC

2.1 The Large Hadron Collider

The Large Hadron Collider (LHC) [27] will be the most powerful hadron collider running in the next two decades. It is under construction in the 27 km tunnel where the LEP [12, 13, 14] collider was situated at CERN laboratories in Geneve, Switzerland. The LHC area is shown in Fig. 2.1.

The new collider, sited about 100 m depth underground across the French-Swiss border, will have two counter-rotating proton beams each with an energy of 7 TeV giving a total collision energy ($\sqrt{s}$) of 14 TeV and it is composed by eight curvilinear sections and eight rectilinear sections, where the beams may collide. Four detectors will be installed in the caverns around the collision points, which are shown in Fig. 2.2. Two of them are multipurpose experiments, ATLAS [28] and CMS [29], the other two are dedicated experiments, one to heavy ion physics, ALICE [30], and the other to B-physics and precision measurements of CP violation, LHCb [31].

The LHC will take advantage of the existing accelerator complex at CERN to create the proton beams and accelerate them. To achieve $\sqrt{s} = 14$ TeV, beams are filled with protons delivered from the SPS and its pre-accelerators at 0.45 TeV. Proton-proton collisions are planned to start in July 2007. Heavy ions will be also accelerated up to total energy of 2.76 TeV/nucleon in Pb-Pb collisions.

The Large Hadron Collider is the natural choice as the next step laboratory for particle physics. The latest discoveries of new particles have since many years happened at hadron colliders extending the accessible energy range upwards. LHC

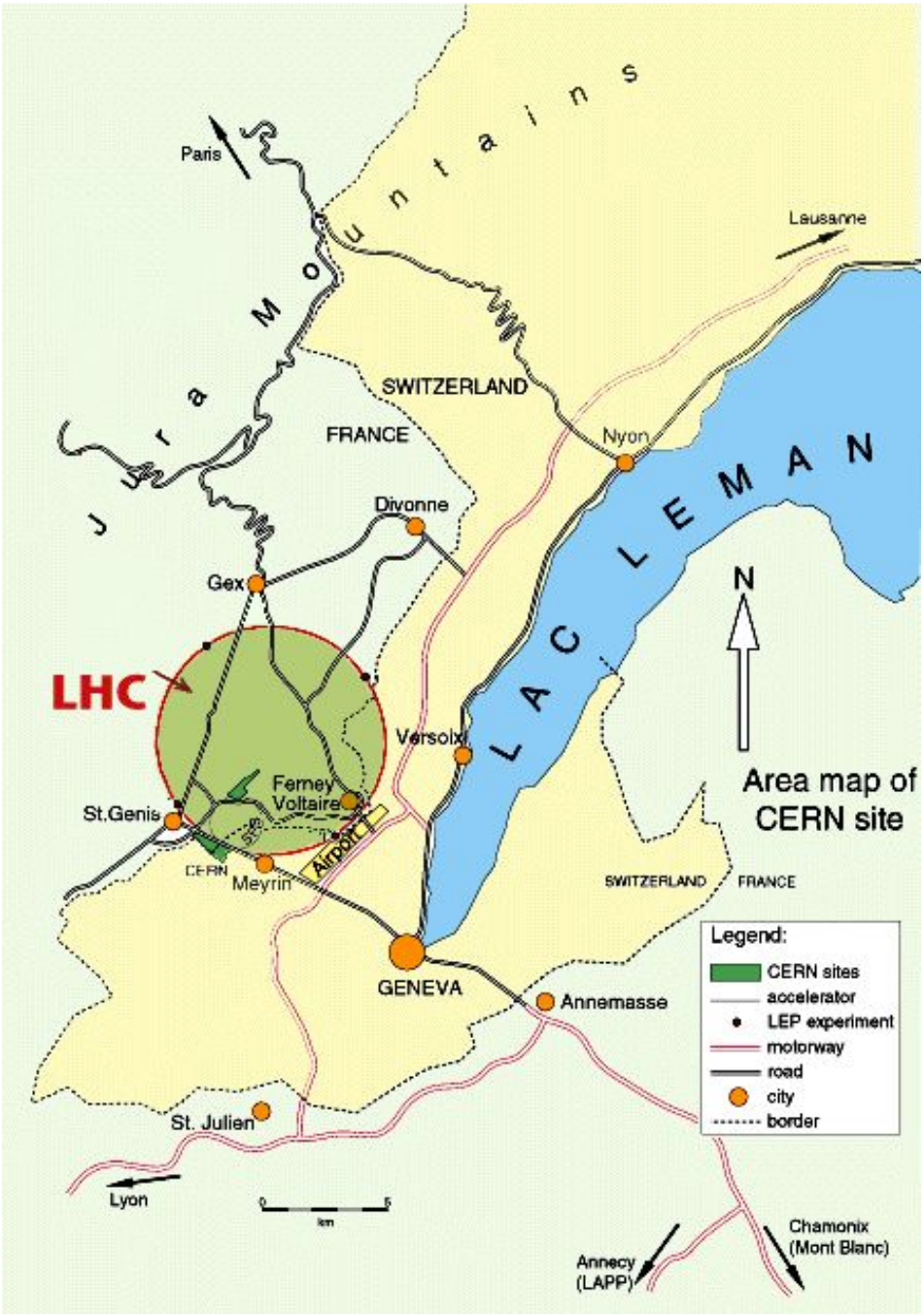

Figure 2.1: The LHC area.

can be seen as a discovery machine with a dynamic range of discovery from energy scales from 5 GeV/c^2, as in the case of B-physics, to a few TeV/c^2, for the discovery of new vector bosons or quark compositeness.

To extend the reach of new physics to as high mass scales as possible and to increase the production cross section of the processes of interest it is important to increase the centre of mass energy as much as possible. However high energy beams need high magnetic bending fields.

The maximum achievable energy at LHC is constrained by the magnetic field needed to keep beams circulating

$$B = \frac{p}{0.3 \cdot \rho}\,, \tag{2.1}$$

where p is the particle momentum and ρ is the radius orbit.

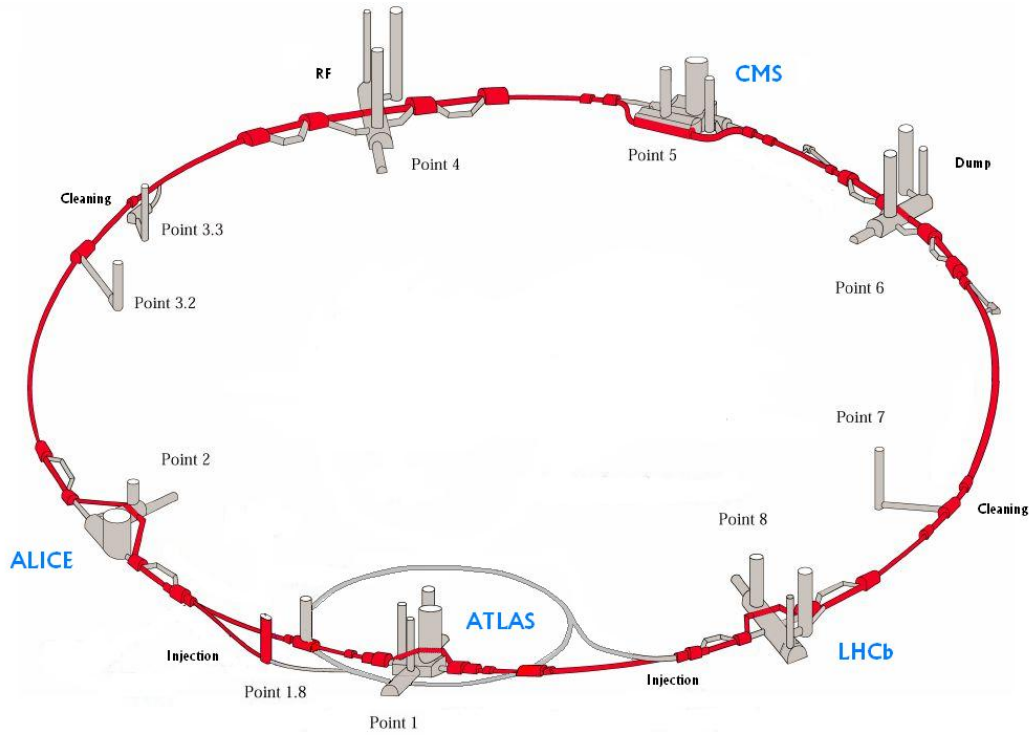

Figure 2.2: The LHC tunnel. The interaction points where the four experiments will be installed are also shown.

The requirement that LHC has to fit inside the existing LEP tunnel fixes $\rho =$ 4.3 Km, therefore, if p is chosen equal to 7 TeV, from Eq. 2.1 $B = 5.4$ T is obtained. However in the LHC tunnel protons are not bended continuously but the 1 232 superconducting magnets act only in the eight curvilinear segments so they are forced to work at 8.3 T, the highest operational magnetic field for affordable superconducting magnets.

LHC magnet coils are 14 metres long and narrow, the inner diameter being 56 mm, so two superconducting magnetic channels will be housed in the same yoke and cryostat (a unique configuration which saves space). LHC magnet coils are made of copper-clad niobium-titanium cables and will be operated at 1.9 K above absolute zero. This unusually low limit puts new demands on cable quality and coil assembly. A picture of an LHC magnet is shown in Fig. 2.3

Magnets are kept cold with superfluid helium, which has extremely efficient heat transfer properties, allowing kilowatts of refrigeration to be transported over more than a kilometre with a temperature increase of less than 0.1 K. Friction can create normally-conducting "hot-spots" which "quench" the magnet out of its cold, superconducting state. A quench in any of the 1 232 LHC superconducting magnets will disrupt machine operation for several hours.

With the beam energy limited, another way to increase the rate of events with

Figure 2.3: Picture of a superconducting magnet being installed in the LHC tunnel, the two channels for the proton beams are clearly visible. LHC will use about 1 200 dipole magnets 14.2 m long which will reach a field strength of 8.3 Tesla.

interesting physics is to raise the *luminosity*. The event rate of a specific process x is given as

$$n_x = \sigma_x \cdot \mathcal{L}\,, \tag{2.2}$$

where $\mathcal{L}$ is the luminosity and σ_x the cross section of the process. The luminosity for a collider is

$$\mathcal{L} = \frac{1}{4\pi}\frac{N^2 f}{t A_T}\,, \tag{2.3}$$

where N is the number of protons in each bunch, t the time interval between individual bunches, A_T the transverse dimension of the bunches at the interaction points and f the fraction of bunch positions actually containing protons [32].

The time between the bunches is limited by the requirement that there should be no additional interactions on each side of the interaction region. For the LHC the bunch crossing time will be 25 ns corresponding to a bunch separation of 7.5 m. The transverse dimensions of the beam at the interaction point can be squeezed down to 15 μm. To be able to fill new bunches into the LHC and operate the beam dump it is necessary to order the proton bunches in trains followed by some empty bunches. In total 2 808 of the 3 557 available spaces with 25 ns separation will contain protons, corresponding to $f = 0.80$. The only remaining way to increase the luminosity is to increase the number of protons in each bunch, which is however limited by electromagnetic forces between the colliding bunches. The maximal luminosity achievable will be close to $2 \cdot 10^{34}$ cm^{-2} s^{-1} but to be in a stable region the nominal luminosity is fixed at 10^{34} cm^{-2} s^{-1}. A summary of the main technical characteristics of the LHC collider are summarized in Tab. 2.1.

The number of observed events for a specific process x is given as

$$n_x = L \cdot \sigma_x \cdot \epsilon\,, \tag{2.4}$$

with σ_x the cross section of the process, ϵ the detection efficiency and L the integrated luminosity

$$L = \int \mathcal{L}\, dt \tag{2.5}$$

or the integral of the luminosity during the effective time the machine is running. A standard year at the LHC is supposed to give a total running time of $t = 10^7$ s.

In the start-up period (the first six months of LHC operation) the instantaneous luminosity should be increased starting from the value of $2 \cdot 10^{26}$ cm^{-2} s^{-1}. In the very first period only 43 equidistant bunches will circulate to perform a deep

Table 2.1: Main technical parameters of LHC.

Circumference	26 658.90 m
Collision energy	2×7.0 TeV
Injection energy	0.45 TeV
Dipole peak field	8.3 T
Luminosity	$10^{34}\text{cm}^{-2}\text{s}^{-1}$
Number of bunches	2 808
Bunch separation	24.95 ns
Particles per bunch	$1.15 \cdot 10^{11}$
Stored beam energy per beam	350 MJ
Radiated power per beam	3.7 kW
Energy loss per turn	7 keV
Circulating current per beam	0.56 A
Beam size at IP	15.9 μm
Beta values at IP	0.55 m
Normalised emittance	3.75 μm
Crossing angle	300 μrad
Beam lifetime	22 h
Luminosity lifetime	10 h

test of the accelerator. Then the number of bunches and the luminosity will be gradually increased up to $0.5 \cdot 10^{33}$ cm^{-2} s^{-1}. In this first six months an integrated luminosity of 0.4 fb^{-1} of data should be collected to calibrate the detectors with physics samples ($Z \to \ell^+\ell^-$, $t\bar{t}$,...).

After a shut-down of six months due to hardware improvement, LHC should work, in the next three years, at $\mathcal{L} = 2 \cdot 10^{33}$ cm^{-2} s^{-1}, the so called *low luminosity* regime. Then luminosity will be finally increased to 10^{34} cm^{-2} s^{-1} for the *high luminosity* data taking period. If LHC is assumed fully efficient, 20 fb^{-1} per year during the three years at low luminosity for a total of 60 fb^{-1} should be collected. Nominally the period of high luminosity data taking will last at least five years for a total of 500 fb^{-1}.

The high requirement on luminosity is the reason for the choice of a proton-proton collider. While a proton-antiproton collider has the advantage that both counter-rotating beams can be kept in the same beam pipe, producing the enormous amounts of antiprotons required for the high luminosity is not realistic and would be more expensive than the proton-proton solution with separate beam pipes. The charge asymmetry introduced with a proton-proton collider is not a serious problem for the physics analysis.

In the collisions at high transferred momentum, the real interaction center of mass energy ($\sqrt{\hat{s}}$) is smaller than the center of mass energy of the machine ($\sqrt{s}$)

$$\sqrt{\hat{s}} = \sqrt{x_a x_b s}\,, \tag{2.6}$$

where x_a and x_b are the fractions of the proton momentum carried by the colliding partons inside the protons. If $x_a \approx x_b \approx x$, then

$$\sqrt{\hat{s}} = x\sqrt{s}\,. \tag{2.7}$$

So the production of a 100 GeV/c^2 mass particle needs two partons carrying 1% of the proton momentum, while a particle with a mass of 5 TeV/c^2 can be produced only with an interaction between partons with $x \approx 36\%$.

The dynamics described above does not have a motionless centre of mass in the LHC reference frame, but on average there is a boost along the direction of the two beams. For this reason, boost invariant quantities have to be defined to characterize the event. The more important are the transverse momentum p_{T}, defined as the magnitude of the projection of the momentum p on a plane

perpendicular to the beam axis, and the rapidity

$$y = \frac{1}{2} \ln \frac{E + p_z}{E - p_z} = \tanh^{-1} \left(\frac{p_z}{E} \right) , \tag{2.8}$$

with E energy and p_z projection of the momentum of the particle along the beam axis [33]. Under a boost in the z direction with velocity β, $y \rightarrow y - \tanh^{-1} \beta$ and hence the rapidity distribution dN/dy is invariant. In the ultrarelativistic approximation $m/|\vec{p}| << 1$, the rapidity may be expanded to obtain

$$y = -\ln \left[\tan \left(\frac{\theta}{2} \right) \right] \equiv \eta \, , \tag{2.9}$$

with $\cos\theta = p_z/|\vec{p}|$. Eq. 2.9 defines the pseudorapidity η, approximately equal to y if $m/|\vec{p}| << 1$ and $\theta >> 1/\gamma$ and in any case measurable when either the mass or the momentum of a particle are unknown.

The number of simultaneous proton-proton inelastic interactions which take place in each bunch crossing is given by a Poisson distribution with an average of [34]

$$\langle n \rangle = \frac{L \cdot \sigma_{tot}^{pp} \cdot t}{f} \, . \tag{2.10}$$

The total proton-proton cross section as a function of the centre of mass energy is shown in Fig. 2.4. The upper and lower estimates are also shown. This gives an average of 25 simultaneous interactions (~ 5 at low luminosity) in each event with an expected value of the total proton-proton cross section $\sigma_{tot}^{pp} \sim 80$ mb (diffractive events are also included).

Out of all these interactions, those with production of high mass objects such as vector bosons or Higgs particles are often called physics events. The term is misleading since all interactions of course contain physics but the dominating QCD-jet processes with low energy transfer are believed to contain little unknown physics and are thus regarded as background without new physics information.

The difference between the total cross section and the cross section of the interesting physics processes is in many cases greater than ten orders of magnitude. The absolute majority of interactions, called *minimum bias* events, are fusion processes of gluons or quarks with a small energy transfer resulting in events with many hadrons of low momentum and nothing else. The distributions of the minimum bias events as a function of η and p_{T} is shown in Fig. 2.5. It is important

to notice that the particle distribution is flat in the region $|\eta| < 6$ and that the average p_{T} of the particle is about 0.5 GeV/c.

Every time a high p_{T} collision occurs, it is then shadowed on average by 25 low p_{T} events which are called *pile-up*. Pile-up is one the serious difficulties at LHC and has a big impact in the detector design. Requirements for a detector to be operated at LHC are a fast response, in order to avoid superpositions between collisions belonging to different bunches (typical response times are between $20 \div 50$ns), and a high granularity to cope with the 20 events and 1 000 tracks produced on average per bunch crossing.

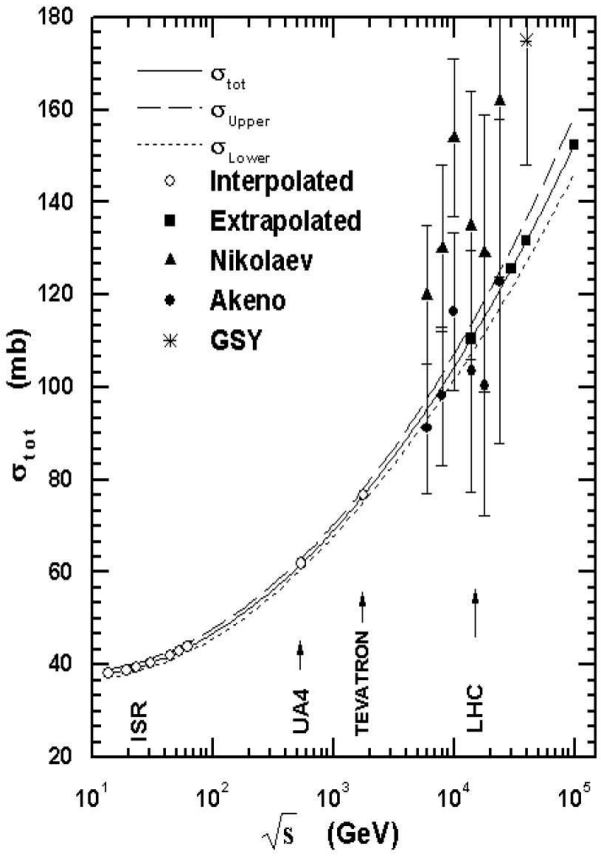

Figure 2.4: Total inelastic proton-proton cross section as a function of the center of mass energy $\sqrt{s}$ [35]. The upper and lower estimations are also shown.

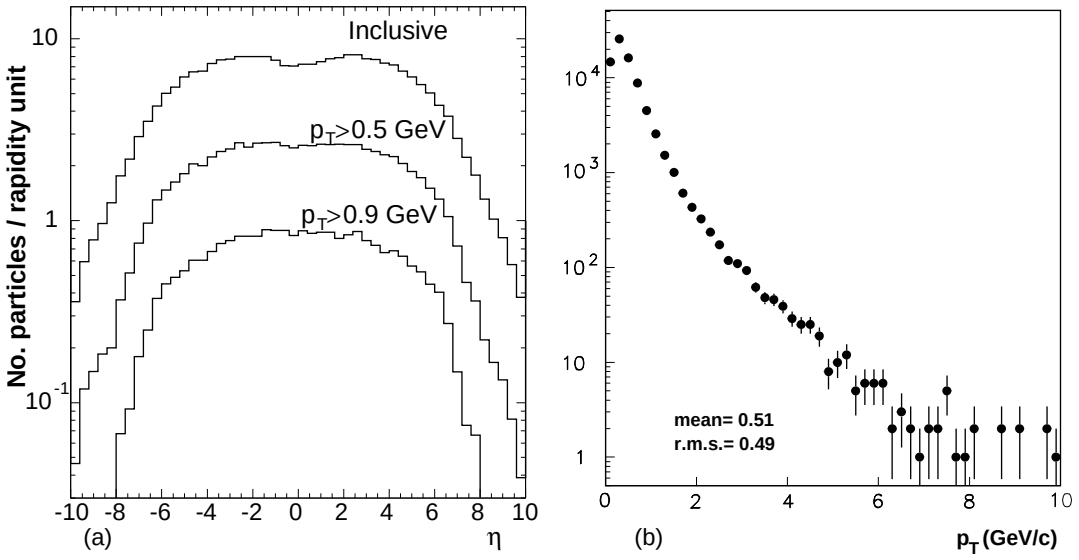

Figure 2.5: Pseudorapidity η (a) and transverse momentum p_{T} (b) distributions of charged particles per minimum bias event [36].

In addition to this a detector installed at LHC must be radiation hard, to operate in such high particle fluence. The fluence near the interaction point, integrated over ten years of data taking, is about 10^{17}neutrons/cm^2 or about 10^7 Gy. This flux can damage detector components and lead to a signal reduction or in the worst case to the detector breaking. Every single component of the detector must pass stringent quality controls, as described in the next Chapter.

2.2 The CMS experiment

The Compact Muon Solenoid experiment, CMS, is a general purpose detector which will operate at LHC [37]. The main feature of CMS is the 4 T superconducting solenoid that permits a compact design of the detector with a strong magnetic field. The design priorities fulfilled by the CMS project are a redundant muon system, a good electromagnetic calorimeter and a high quality tracking system.

The structure of CMS is typical of a general purpose experiment designed for a collider: several cylindrical layers coaxial to the beam direction, referred as barrel

layers, closed at both ends by detector disks orthogonal to the beam pipe, the endcaps, to ensure detector hermeticity. In Fig. 2.6 and Fig. 2.7 schematic views of CMS are drawn pointing out the cylindrical symmetry of the experiment, which has a full length of 21.6 m, a diameter of 15 m and reaches a total weight of 14 500 t.

The natural coordinate frame used to describe the detector geometry is a right handed cartesian system with the x axis pointing to the center of the LHC ring, the z axis coincident with the CMS cylinder axis and the y axis directed upwards along the vertical. The cylindrical symmetry of the CMS design and the invariant description of proton-proton physics suggest to use a pseudo-angular reference frame, given by the triplet (r, ϕ, η) with r distance from the z axis, ϕ azimuthal coordinate with respect to the x axis and pseudorapidity η defined by Eq. 2.9.

As stated before, CMS is built around a superconducting solenoid which contains from inside out:

- Tracker: made of a Silicon Pixel vertex detector surrounded by Silicon Microstrip detectors, with a total active area of 215 m^2, to reconstruct charged particle tracks and primary and secondary interaction vertices;
- ECAL: an electromagnetic calorimeter to precisely measure electrons and photons, composed by $PbWO_4$ scintillating crystals and a forward preshower detector;
- HCAL: a hadron calorimeter system for jet direction and transverse energy measurements, extended in the forward region with the very forward calorimeter.

Outside the magnet coil, the magnet yoke is instrumented with the Muon Chambers to detect and reconstruct muon tracks: Drift Tubes in the barrel and Cathode Strip Chambers in the endcaps, complemented overall by Resistive Plate Chambers.

2.2.1 Magnet

The CMS magnet is the hugest superconducting solenoid ever built in the world and shall be able to generate a uniform magnetic field of 4 Tesla in the inner region storing about 2.5 GJ of energy [38].

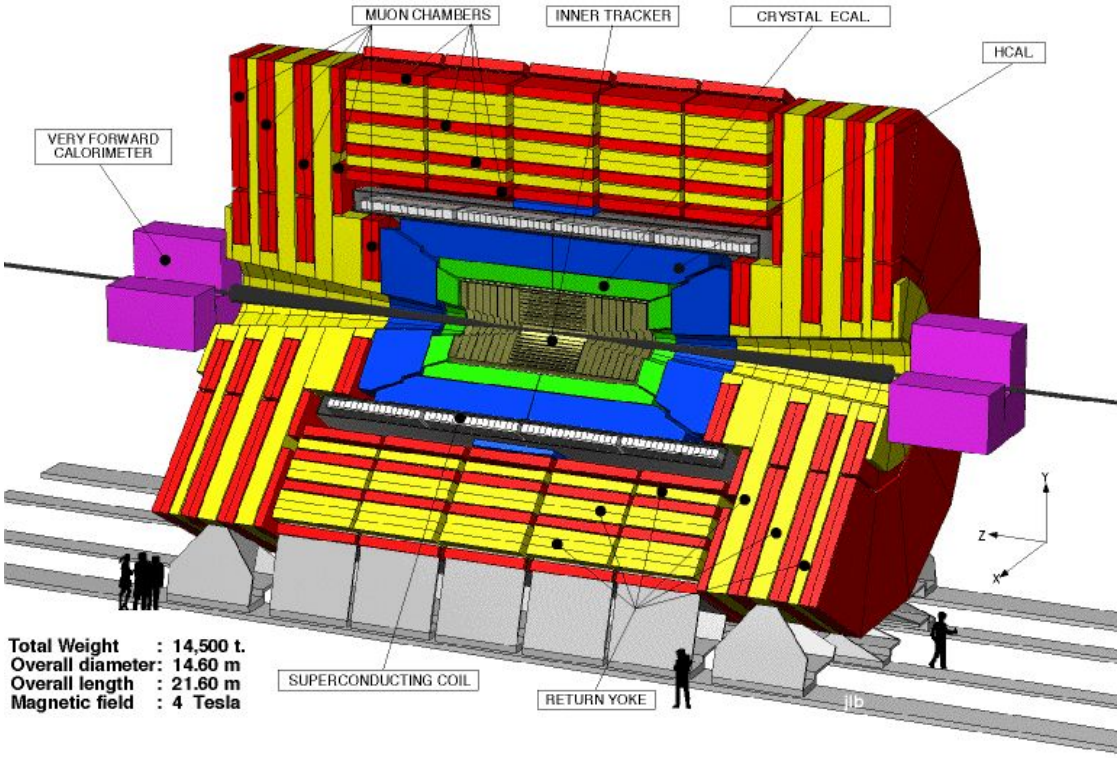

Figure 2.6: View of the CMS detector. In picture all the subdetectors are shown. From inside out: Tracker, Electromagnetic and Hadronic calorimeter, Magnet coil and Muon Chambers.

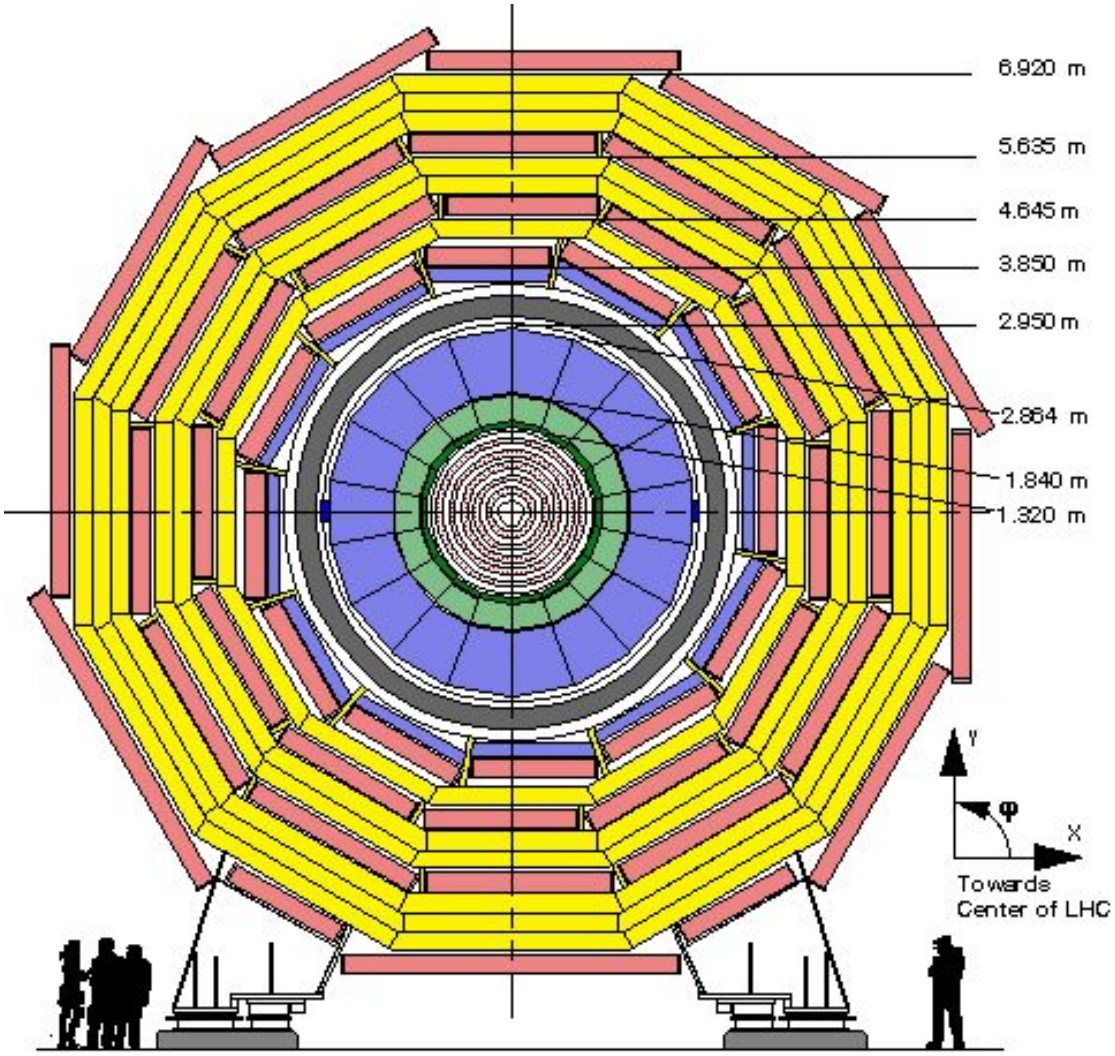

Figure 2.7: A transverse section of the CMS detector. The cylindrical symmetry of the detector is pointed out in this picture.

The magnet is formed by five modules. Every module is 6 metres diameter, 2.5 metres length and 50 tonnes weight. Thanks to a sophisticated helium cooling system, modules will be kept to the low temperature of 4 K, so that the flat NiTb cable will become superconducting allowing the 20 kA current to flow without appreciable loss. The whole magnet is then contained in an enormous vacuum cylinder that will isolate it from the external environment.

Finally a structure composed by 12 000 t of iron (iron yoke) will bridle the lines of the magnetic field that otherwise would get lost causing disturbances. The iron yoke consists of two endcaps, each of which will have three disks, and a barrel yoke that is made up of five rings. The total induction of the magnetic field generated by the CMS solenoid is shown in Fig. 2.8.

The coil is a supporting structure for the inner part of the apparatus, i.e. the tracking system and most of the calorimeters as shown in Fig. 2.11.

Thanks to its large bending power it permits a precise measurement of charged particle transverse momentum. The iron yoke elements surround the muon chambers, thus providing an independent measurement of muon momentum.

2.2.2 Tracker

The Silicon Tracker is the inner subdetector of CMS [36]. It is the closest to the interaction point and represents an essential detector to address the multiplicity

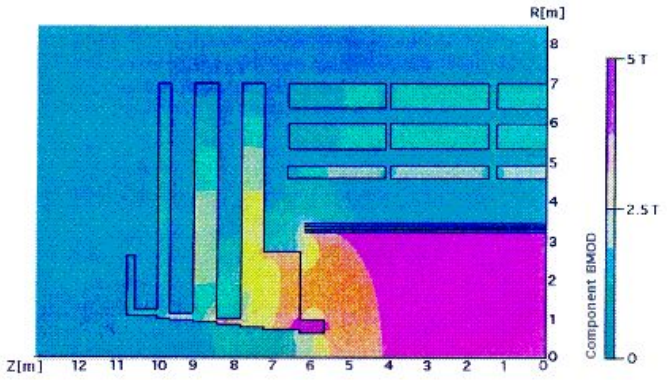

Figure 2.8: Total induction of the magnetic field generated by the superconducting solenoid [38].

of LHC physics goals. It extends in the region $|\eta| < 2.5$, $r < 120$ cm, $|z| < 270$ cm and it is completely based on semiconductor detectors made of Silicon covering the largest ever-designed Si detector surface of 210 m^2. Using the Tracker, vertices and charged particle tracks have to be reconstructed in the highly congested LHC environment.

To better solve the pattern recognition problem, the Tracker is designed to fulfill two basic properties: low cell occupancy and large hit redundancy. For these reasons it is structured in an inner Silicon pixel detector surrounded by several layers of Silicon microstrip detectors of different size and pitch between the strips. The low occupancy is obtained by working with high granularity detectors, mainly the ones closer to the interaction point because they have to cope with higher particle fluxes, and fast primary charge collection, obtained with thin detectors and overdepleting the Silicon bulks. The redundancy is guaranteed by the design (10 layers of Silicon detectors), which allows many measured points per track within an acceptable material budget not to degrade too much the electromagnetic calorimeter performance. In Fig. 2.9 the third Tracker layer, assembled in Florence, is shown.

In this way an average of 12-14 points (hits) per track are guaranteed to permit a high tracking efficiency and a low rate (10^{-3} or less) of fake tracks (reconstructed tracks not corresponding to any real track). A consequence of high particle density is the radiation damage of the Silicon sensors, mainly around the collision area of the proton beams. Another source of radiation is the high flux in the tracking volume due to backscattering of neutrons evaporated from nuclear interactions in the material of the electromagnetic calorimeter. To contrast the malfunctioning caused by the radiation damage, both pixel and microstrips detectors have to be kept cold at a working temperature of -10° C for the whole Tracker volume, except during limited maintenance periods, when they can be *warmed* up to 0° C.

The physics requirements the CMS Tracker has to satisfy are:

- isolated lepton track reconstruction: the efficiency is expected to be close to 100% in $|\eta| < 2.0$ from simulation of single muons within Tracker;
- good lepton momentum resolution: $\sigma(p_T)/p_T < 4\%$ within $|\eta| < 2.0$ for single muons with different transverse momenta, crucial for channels with many muons in the final state;
- tagging and reconstruction of b jets, fundamental requirement for new

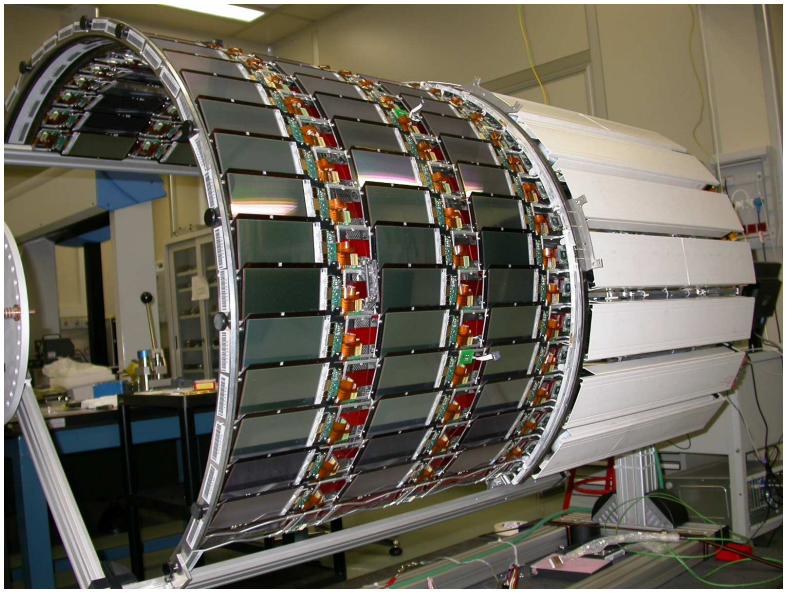

Figure 2.9: The Tracker "layer three" is shown during its assembly in Florence [39].

physics studies and for top quark physics or CP violation;

- several material budget constraints are required for cables and active layers to minimize electron bremsstrahlung and hadronic interactions not to affect tracking performance and at the same time to fully exploit the electromagnetic calorimeter. In Fig. 2.10 both the total radiation length X_0 and nuclear interaction length λ_I for the Tracker material as a function of pseudorapidity are reported. The material budget is higher in the transition region between barrel and endcap ($1 < |\eta| < 2$) due to cables and services that connect the Tracker modules to the outside system.

In the next Chapter the Silicon Tracker is described more in detail and some results on the quality control test of the microstrip sensors are summarized.

2.2.3 Electromagnetic Calorimeter

The Electromagnetic Calorimeter is made out of 74 848 lead tungstate ($PbWO_4$) crystals. Such crystals were chosen because of their excellent energy resolution [41]. For Trigger purposes they are grouped together into 68 Trigger towers whose

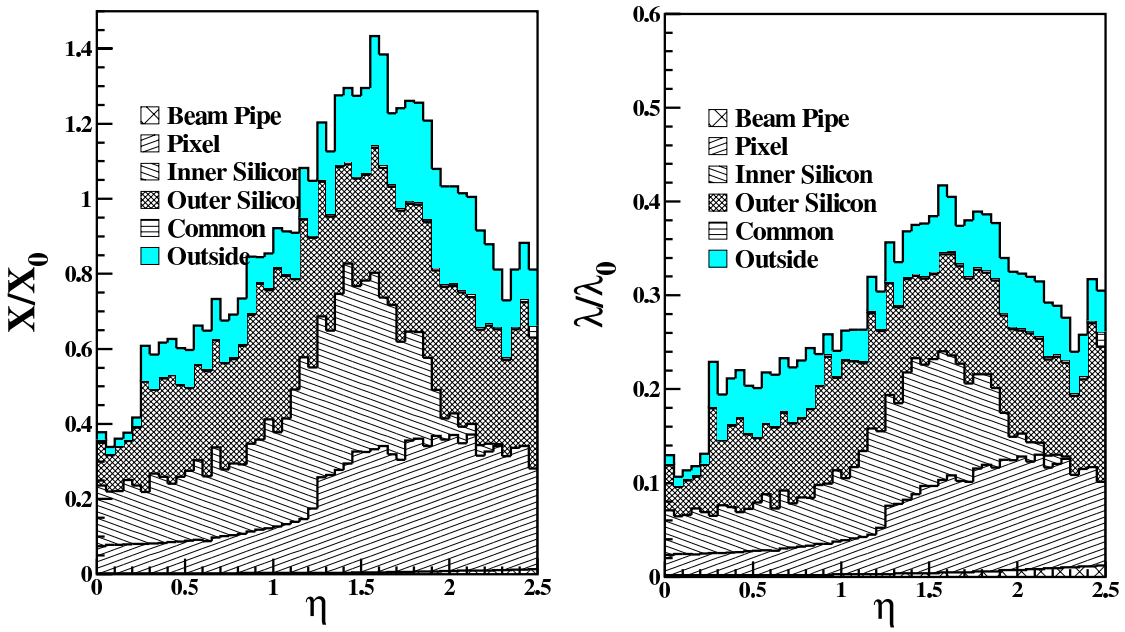

Figure 2.10: Material budget as a function of η for different Tracker subunits: material thickness in units of radiation length X_0 (left) and in units of interaction length λ_0 (right) [40].

boundaries line up with the subdivisions of the HCAL. They are arranged into a barrel, covering the central rapidity region ($|\eta| < 1.48$) and two endcaps, which extend the coverage up to $|\eta| = 3$. A schematic view of the CMS calorimetric system is shown in Fig. 2.11.

Thanks to the high density (8.28 g/cm^3) and the small radiation length (0.89 cm) of $PbWO_4$, the calorimeter is very compact and can be placed inside the magnetic coil. The small value of the Molière radius of 2.2 cm (the Moliere radius measures the transversal dimension length scale of an electromagnetic shower evolving within the calorimeter) well matches the very fine granularity needed because of the high particle density at LHC. In the barrel, crystals with a tapered shape, 2.2×2.2 cm^2 front face and 23 cm length are positioned at a radius of 1.29 m. Hence the total depth is 26 X_0 and the transverse granularity in η and ϕ is given by 0.0175×0.0175. In the endcaps, crystals with 2.47×2.47 cm^2 front face and 22 cm length are positioned at a distance from the interaction point of 3.17 m along the beam line. Tilts of 3° both in η and ϕ gives the structure a

geometry slightly off-pointing from the interaction region, in order to improve the hermeticity of the detector. Moreover the fast scintillation mechanism (80% of the light is emitted within 25 ns) allows the crystals to be used at the crossing rate of 40 MHz. The drawbacks of $PbWO_4$ are the low light yield (100 photons/MeV, 0.2% with respect to NaI or NaTl), which imposes a multiplication mechanism in the photodetector, and the strong temperature dependence of the crystal response

$$\frac{1}{l}\frac{dl}{dT} \sim -1.9\%/^{\circ}\mathrm{C}\,, \tag{2.11}$$

where l represents the light yield.

The collection of light is performed with Silicon avalanche photodiodes (APD), which are able to operate inside a high magnetic field and can address the low light-yield of the crystals. Each crystal is coupled to two APDs, for a total area of 50 mm^2 and consequently 4000 photoelectrons are produced per GeV of deposited energy. In the endcaps the higher irradiation levels would also induce too high leakage currents in APDs, therefore the forward crystals are read by vacuum phototriodes (VPT) [42].

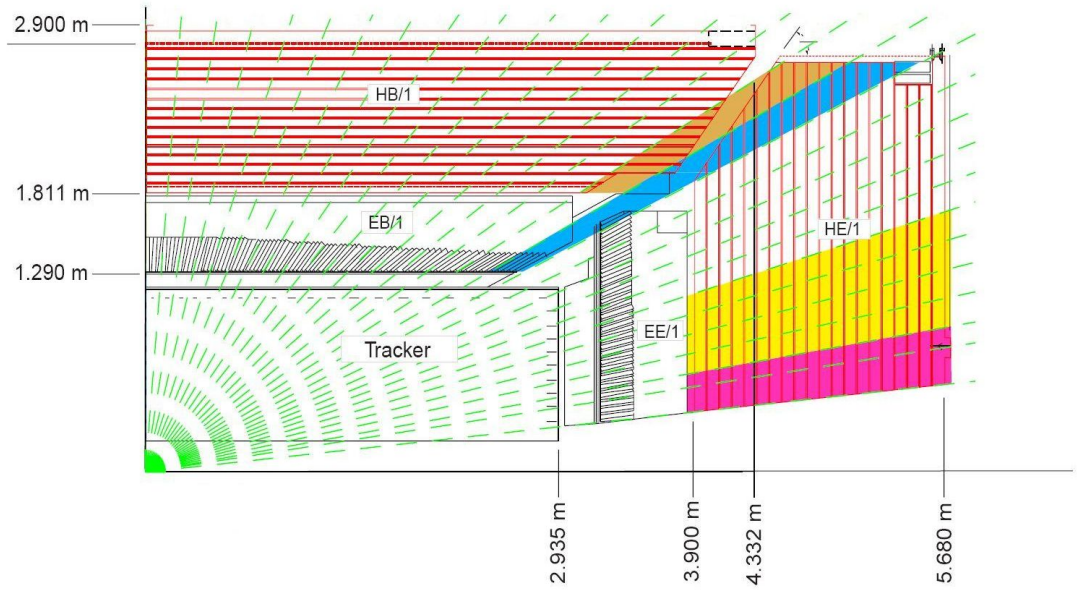

Figure 2.11: Longitudinal view of a quadrant of the CMS calorimetric system.

The energy resolution of the CMS electromagnetic calorimeter is parametrized as

$$\frac{\sigma_E}{E} = \frac{a}{\sqrt{E}} + \frac{b}{E} + c\,. \tag{2.12}$$

The target values for the ECAL are

- 2.7% $\mathrm{GeV}^{1/2}$ for the stochastic term a, limited by the photoelectron statistics;
- 200 MeV for the noise term b corresponding to a reconstructed cluster, which depends on the photodetector dark current, the electronics noise and, at high luminosity, the event pile-up;
- 0.5% for the constant term c, which is related to the longitudinal shower containment, the uniformity of the light collection in the crystals and the precision of the intercalibration.

The three contributions to the energy resolution of ECAL are shown in Fig. 2.12 as a function of the cluster energy. At high energies the most relevant one comes from the constant term. The challenging goal of keeping it very small can be

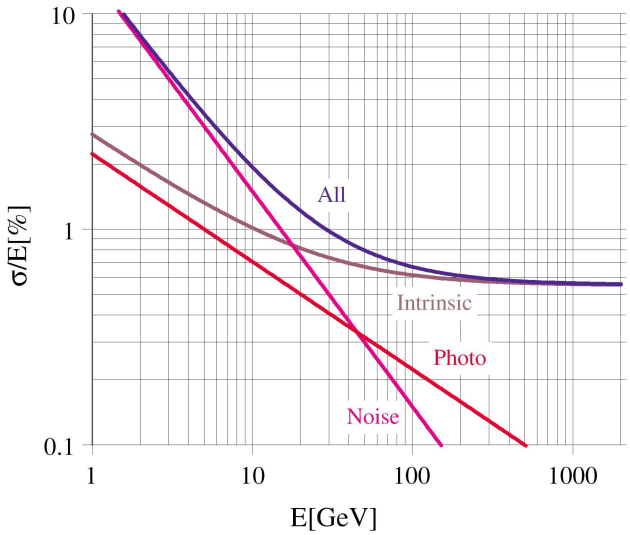

Figure 2.12: Electromagnetic calorimeter energy resolution as a function of the particle energy. The stochastic, noise and constant terms are shown.

reached only provided that the intercalibration between crystals is very precise and there is a very tight control, at the level of few per mille, on instabilities and non-uniformities in the detector response. This puts severe requirements on the control of the temperature stability (cooling system) and on the following of the radiation damage (monitoring system).

Crystal growth methods and doping techniques were carefully optimized in order to improve the radiation hardness of the $PbWO_4$ crystals. The radiation dose at the calorimeter front face foreseen for the LHC running at high luminosity varies from 0.15 Gy/h in the centre of the barrel up to 15 Gy/h in the endcaps. The effect of the ionizing radiation is the creation of colour centers, due to oxygen vacancies or other defects in the crystals. This reduces the crystal transparency without affecting the scintillation mechanism.

At the beginning of data taking it is foreseen to instrument a staged ECAL without endcaps in the forward regions. This scenario is caused by the longer time scale for construction and crystal calibration, but it seems not to affect too much the resolution on di-jet invariant mass and transverse energy measurements [43].

2.2.4 Hadronic Calorimeter

CMS has four kinds of hadronic calorimeters which provide good segmentation, moderate energy resolution and full angular coverage up to $|\eta| = 5$ [44]. The Barrel Hadronic Calorimeter (HB) surrounds the electromagnetic calorimeter, and covers the central pseudorapidity region up to $|\eta| = 1.3$. The end regions are covered up to $|\eta| = 3$ by the two Endcap Hadron Calorimeters (HE). Pseudorapidity coverage is extended up to $|\eta| = 5$ with the two forward calorimeters (HF) which surround the beam pipe 11 m from the interaction point. The HB and HE are located inside the solenoid magnet. Central shower containment is improved with an array of scintillators located outside the magnet which we refer to as the Outer Hadronic Calorimeter (HO).

The HB is divided into two cylindrical sections. These half barrels consist of eighteen identical wedges made of flat absorber plates parallel to the beam axis. The body of the wedges is made of brass, but the innermost and outermost layers are made of stainless steel for structural strength. The active readout scintillator tiles in each of the seventeen layers are divided into $\Delta\eta \times \Delta\phi = 0.087 \times 0.087$ segments. The HB has a minimum depth of $5.8\lambda_I$, and the energy resolution

for single pions is approximately $120\%/\sqrt{E}$. One of the half barrels is shown in Fig. 2.13a. Since the barrel part of the calorimeter is not sufficiently thick to contain all the energy of highly energetic showers, an additional tail-catcher of scintillators tiles is located outside the magnet. It consists of one or two layers of scintillator with the same tower granularity as the HB. Two layers are available in the very central pseudorapidity region.The total depth of the calorimeter system is thus extended to $11.8\lambda_I$, with an improvement in both linearity and energy resolution [45].

The HE is a sampling calorimeter consisting of eighteen 20° modules, each made of nineteen layers of brass and scintillator. The HE extends the η coverage to 3, and has a minimum depth of $10\lambda_I$. Its transverse segmentation is the same as for the HB and provides similar hadron energy resolution. The endcaps have been already assembled and one of them is installed on the endcap iron in the surface hall, as shown in Fig. 2.13b.

The HF calorimeters are located along the beam pipe, 11 m from the interaction point. They are made of steel absorbers and embedded radiation-hard quartz fibers, which provide a fast collection of Cherenkov radiation. The HF extends the η coverage to 5, with a depth of $9\lambda_I$. It is divided into thirteen η towers and the azimuthal segmentation is 10°.

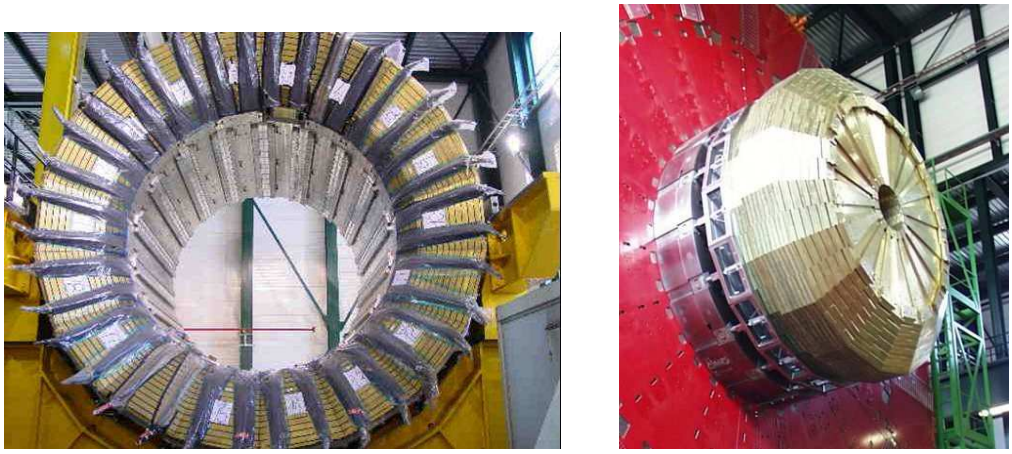

(a) (b)

Figure 2.13: A half barrel hadronic calorimeter (HB) (a) and an endcap (HE) (b) already assembled and installed in the CMS surface hall.

The HF is a crucial tool for tagging forward jets, most of which are very energetic, therefore the HF provides a reasonable energy resolution: 20% for 1 TeV jets.

2.2.5 Muon system

The muon system is placed outside the magnet, embedded in the iron return yoke to make full use of the 1.8 T magnetic return flux [46], a schematic view of this subdetector is shown in Fig. 2.14. It plays an essential role in the CMS Trigger system, because high p_T muons are clear signatures of many physics processes. The main goal of this system is to identify muons and measure, when combined with the Tracker, their transverse momentum p_T. Three different and complementary detection technologies have been used: Drift Tube Chambers (DT) in the barrel region ($0 < \eta < 1.1$), Cathode Strip Chambers (CSC) in the endcap region ($0.9 < \eta < 2.4$) and Resistive Plate Chambers (RPC) in both barrel and endcap regions.

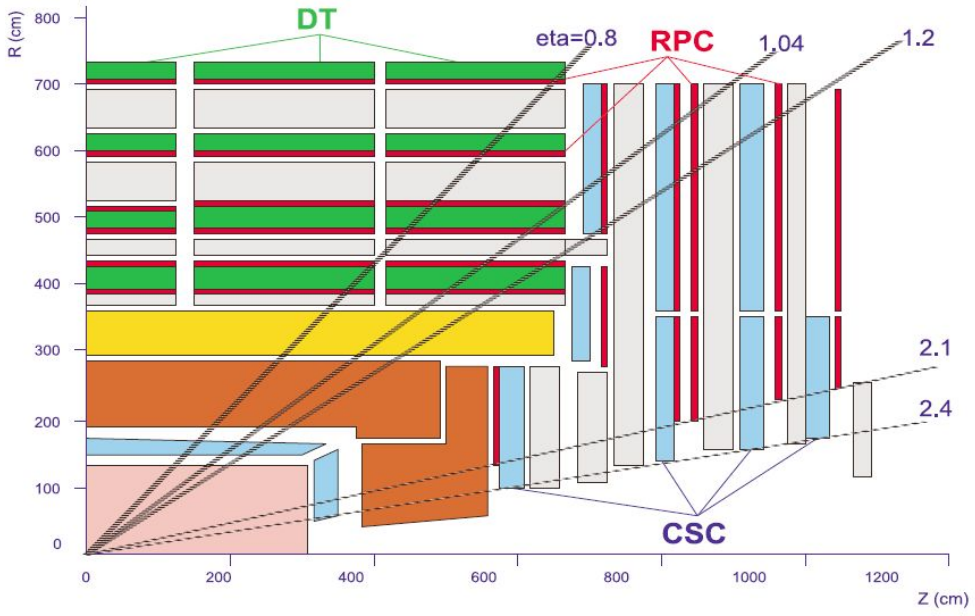

Figure 2.14: Longitudinal view of a quarter of the muon system, subdivided into barrel with Drift Tubes (DT) and Resistive Plate Chambers (RPC) and endcap with Cathode Strip Chambers (CSC) and RPCs.

In the barrel region, the expected occupancy is low (< 10 Hz/cm^2), allowing for the use of drift tubes as detection element. In Fig. 2.15(a) a schematic view of a Drift Tube Chamber is shown.

The chamber design is very redundant: each chamber is made up of twelve layers of drift tubes, packed in three independent subunits called superlayers (SL), two of them with the anode wires parallel to the beam axis for measuring the transverse coordinate ($r\phi$) and the remaining SL orthogonal to the other two for determining the longitudinal coordinate (z). The Drift Tubes are parallel aluminum plates insulated from perpendicular "I" shaped aluminum cathodes by polycarbonate plastic profiles. The anodes are 50 μm diameter stainless steel wires placed between the cathodes. The internal volume is filled with a gas mixture of Ar(85%) + CO_2(15%) at atmospheric pressure, because this gas is non-flammable and can be safely used in underground operations in large volumes, as required in CMS. The single hit position resolution is better than 200 μm at nominal voltage values. The position and angular resolution of the full chamber are 98 μm ($r\phi$) and 570 μrad respectively.

Due to the larger occupancy of the endcap regions, from few Hz/cm^2 to more that 100 Hz/cm^2, and the intense and non uniform magnetic field, Cathode Strip Chambers (CSC) have been chosen in this region. The CSCs are multiwire proportional chambers with one cathode plane segmented in strips running orthogonal to the wires. The chosen gas mixture is Ar(40%) + CO_2(50%) + CF_4(10%). In the CMS endcap muon system each chamber is formed by six trapezoidal layers, with strips in the radial direction for a precise measurement of the azimuthal direction. A picture of a CSC detector is shown in Fig. 2.15(b). The single plane spatial resolution is between 150 and 350 μm depending on the location of the hit on the strip position. The estimated overall chamber resolution is calculated to be 80-85 μm independently of the hit position.

Resistive Plate Chambers are installed both in the barrel and endcap regions. They have a limited spatial resolution but thanks to their fast response (~ 3 ns) they are used as a dedicated Trigger subsystem, mainly for unambiguous bunch crossing identification. The RPCs used in CMS are double gap RPCs filled with a $C_2H_2F_4$ and C_4H_{10} gas mixture, with common pickup strips in the middle and work in avalanche mode to sustain the high event rate.

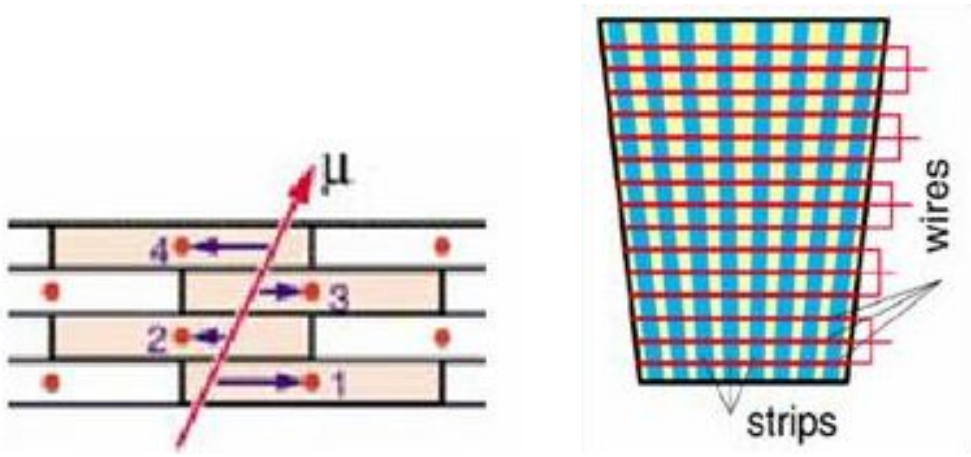

(a) (b)

Figure 2.15: Schematic view of (a) Drift Tube Chamber and (b) Cathode Strip detector.

2.2.6 Trigger system

For the nominal LHC design luminosity of 10^{34} cm^{-2} s^{-1}, an average of 25 events occurs at the beam crossing frequency of 25 ns. This input rate of 10^9 interactions every second must be reduced to 100 Hz, the maximum rate that can be archived by the on-line computer farm. CMS has chosen to reduce this rate in two steps: a Level-1 Trigger [47] and a High-Level Trigger (HLT) [40].

The Level-1 Trigger runs on custom synchronous processors and has access to a coarse granularity information from calorimeters and muon detectors. It receives data at the full LHC bunch crossing rate of 40 MHz and takes the Trigger decision for each bunch crossing within a latency time of 3.2 μs. During this latency time, the full detector data are stored in front-end pipeline memories. The output rate is limited by the capabilities of the CMS data acquisition system to 100 kHz.

The High-Level Trigger is the second step of the Trigger chain. It is designed to reduce the Level-1 output rate of 100 kHz to a final output rate of 100 Hz. The HLT code runs on a farm of commercial processors and performs the reconstruction and selection of physics objects using the full event data with fine granularity and matching information from different sub-detectors. The complete data flow in the CMS Trigger system is shown in Fig. 2.16.

The Trigger is the start of the physics event selection process. The decision to

retain an event is based on the event's suitability for inclusion in one of the various data sets to be used for analysis. The data sets to be taken are determined by CMS physics priorities as a whole. These data sets include di-lepton and multi-lepton data sets for top and higgs searches, lepton plus jet data sets for top physics, and inclusive electron data sets for calorimeter calibrations. In addition, other samples are necessary for measuring efficiencies in event selection and studying backgrounds. The Trigger has to select these samples in real time along with the main data samples.

2.2.7 Level-1 Trigger system

The CMS Level-1 Trigger is based on the identification of muons, electrons, photons, jets, and missing transverse energy. The Trigger must have a sufficiently

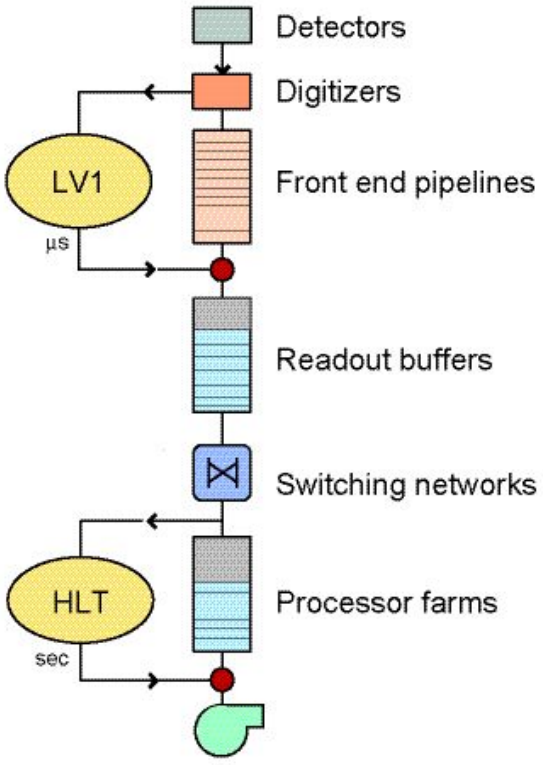

Figure 2.16: Data flow in the CMS Trigger/DAQ system.

high and understood efficiency at a relatively low threshold to ensure a high yield of events.

The CMS L1 Trigger rate is limited by the speed of the detector electronics readout and the rate at which the data can be harvested by the data acquisition system. The L1 Trigger electronics itself is pipelined and deadtimeless, and as such can render a decision on every beam crossing. The design capability of the readout, event builder and event filter are each at 100 kHz.

The L1 Trigger System is organized into three major subsystems: the L1 Calorimeter Trigger, the L1 Muon Trigger, and the L1 Global Trigger. The L1 Muon Trigger also has a Global Muon Trigger that combines the Trigger information from the three DT, CSC and RPC Trigger subsystems and sends this to the L1 Global Trigger. A diagram of the L1 Trigger system is shown in Fig. 2.17.

Calorimeter Trigger

The input to the Calorimeter Trigger are energy sums in towers of (0.035 η) $\times$ (0.035 ϕ) provided from the ECAL, HCAL and HF by the upper level readout

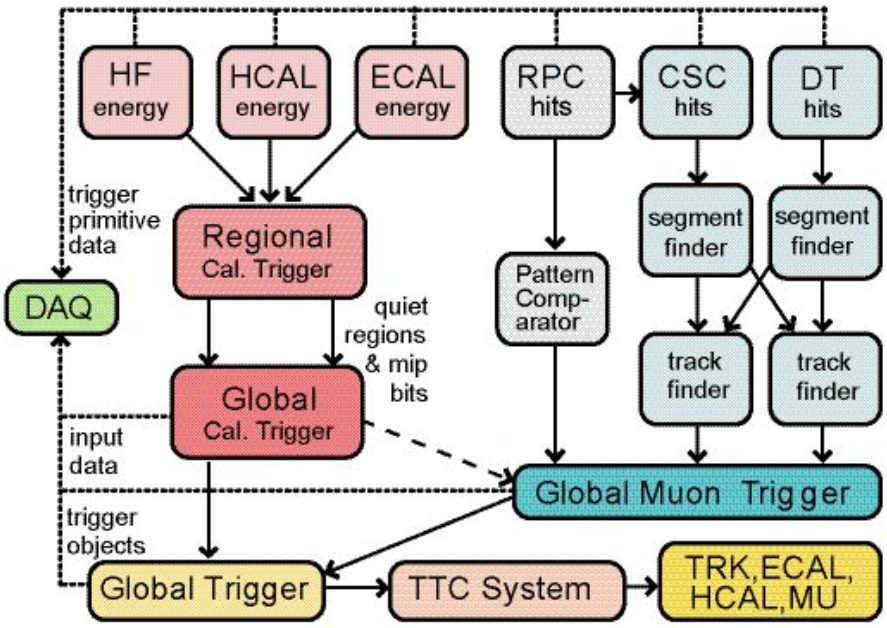

Figure 2.17: Overview of CMS Level-1 Trigger.

Trigger Primitive Generator (TPG) circuits. The Regional Calorimeter Trigger (RCT) finds candidate e/γ, taus and jets from the data received by the TPG and transmits the candidates along with sums of transverse energy to the Global Calorimeter Trigger (GCT). Then it sorts the candidates and forwards the top four of each type to the Global Trigger. The GCT also calculates the total transverse energy and total missing energy vector.

Muon Trigger

Each of the L1 Muon Trigger systems has its own Trigger logic. The RPC strips form Trigger segments to find the tracks and calculate the p_{T}. The RPC logic also provides some hit data to the CSC Trigger system to improve resolution of ambiguities caused by two muons in the same CSC.

The Cathode Strip Chambers form Local Charged Tracks (LCT) from the cathode strips, which are combined with the anode wire information for bunch crossing identification. The system assigns a p_{T} and a quality flag, which are used to sort the candidates. The top three tracks in a sector (up to nine CSC chambers) are transmitted to the CSC Track Finder, which combines the data into full muon tracks and assigns p_{T} values to them.

The Barrel Muon Drift Tubes are equipped with Bunch and Track Identifier electronics that finds track segments from coincidences of aligned hits in four layers of one drift tube superlayer. The track segments positions and angles are sent to the Track Correlator, which attempts to combine the segments from the two superlayers measuring the ϕ coordinate. The best combinations of a single chamber together with the superlayer η segments are collected. The overall best two segments are sent to the Track Finder, which combines the segments from different stations into full muon tracks and assigns p_{T} values to them.

The Global Muon Trigger sorts the RPC, DT and CSC muon tracks, converts these tracks into the same η, ϕ and p_{T} scale, and validates the muon sign. It then attempts to correlate the CSC and DT tracks with RPC tracks. The final ensemble of muons are sorted based on their initial quality, correlation and p_{T} and then the four top muons are sent to the Global Trigger.

Global Trigger

The Global Trigger accepts muon and Calorimeter Trigger information, synchronizes data arriving at different times and communicates the Level-1 decision to the timing, Trigger and control system for distribution to the sub-systems to start the event readout. The Global Trigger decision is made using logical combinations of the Trigger data from the Calorimeter and Muon Global Triggers.

The CMS L1 system sorts ranked Trigger objects. This allows all Trigger criteria to be applied and varied at the Global Trigger level rather than earlier in the Trigger processing. All Trigger objects are accompanied by their coordinates in (η, ϕ) space. This allows the Global Trigger to vary thresholds based on the location of the Trigger objects. It also allows the Global Trigger to require Trigger objects to be close or opposite from each other. In addition, the presence of the Trigger object coordinate data in the Trigger data permits a quick determination of the regions of interest where the more detailed HLT analysis should focus. Finally the Global L1 Trigger transmits a decision to either accept or reject each bunch crossing.

The uncertainties in estimates of cross sections at high energies and limited knowledge of branching ratios impose a large error on the estimated Trigger rates. In addition we cannot assume that the CMS DAQ system will always run at its maximum design capacity. Therefore, we provide for a safety margin of a factor of three from the planned initial 50 kHz maximum L1 output rate to 16 kHz, in designing algorithms for L1 Triggers. The L1 thresholds of the various Trigger channels are reported in Tab. 2.2.

2.2.8 High-Level Trigger

The High-Level Trigger is designed to reduce the Level 1 output rate of 100 kHz to a final output rate of 100 events/second written data on mass storage. The HLT code runs on a farm of commercial processors and performs the reconstruction and selection of physics objects using the full event data with fine granularity and matching information from different subdetectors. Data from the front-end electronic modules are assembled by an event builder switching network that dispatches complete events to the processing nodes of the HLT farm by means of asynchronous protocols. The switching network has a bandwidth of 1 Tbit/s.

The choice of executing the HLT on a single processor farm provides the max-

Table 2.2: Level-1 Trigger table at low (high) luminosity. Thresholds correspond to values with 95% efficiency [40].

Trigger	**Threshold** (GeV/c^2 **or** GeV/c)	**Rate** **(kHz)**	**Cumulative Rate** **(kHz)**
Inclusive isolated e/γ	29 (34)	3.3 (6.5)	3.3 (6.5)
Di-e/di-γ	17 (19)	1.3 (3.3)	4.3 (9.4)
Inclusive isolated μ	14 (20)	2.7 (6.2)	7.0 (15.6)
Di-μ	3 (5)	0.9 (1.7)	7.9 (17.3)
Single τ-jet	86 (101)	2.2 (5.3)	10.1 (22.6)
Two τ-jet	59 (67)	1.0 (3.6)	10.9 (25.0)
1-jet, 3-jets, 4-jets	177,86,70 (250,110,95)	3.0 (3.0)	12.5 (26.7)
Jet $\otimes$ E_T^{miss}	86 $\otimes$ 46 (113 $\otimes$ 70)	2.3 (4.5)	14.3 (30.4)
e $\otimes$ jet	21 $\otimes$ 45 (25 $\otimes$ 52)	0.8 (1.3)	15.1 (31.7)
μ $\otimes$ jet	- (15 $\otimes$ 40)	- (0.8)	15.1 (32.5)
Minimum bias		0.9 (1.0)	16.0 (33.5)
Total			**16.0 (33.5)**

imum flexibility and modularity to the Trigger system, because it has neither architectural nor design limitations other than the total bandwidth and CPU that the experiment can acquire. In a fully programmable environment, the physics algorithms have the maximum freedom in what data to access and in the complexity of the reconstruction tools. Algorithmic changes can be easily introduced to improve the selection of various physics channels as well as to deal with unforeseen experimental conditions. Moreover, the system can benefit from the evolution of network, processor and memory technologies and it is sufficiently modular to deal with the evolution of both the accelerator and detector performance ensuring, at any time, the minimal requirements adequate to fulfill the CMS physics program.

The HLT code runs on a single processor for a given event, and has to select/reject the event after a total processing time of about 300 ms. The real-time nature of the selection imposes significant constraints on the resources that the algorithms can use. The reliability of these algorithms is a key issue, since the events rejected by the HLT are lost forever.

To minimize the CPU time required to process each event it is useful to discard backgrounds events as soon as possible. Therefore, the HLT reconstruction and selection is arranged in a chain of virtual Trigger levels, which consist of algorithms of increasing complexity and CPU time consumption. Virtual Trigger levels are usually:

- the Level 2, which uses calorimeter and muon detector information;
- the Level 2.5, which additionally uses the Tracker pixel information;
- the Level 3, which accesses the full event information, including all tracking detectors.

At the end of each level a set of selection criteria reject a significant fraction of the events selected by the previous step. Other selection strategies used in implementing the software are the reconstruction on demand and the regional reconstruction. Physics objects are reconstructed only if they are requested, and the track reconstruction is performed only in a region of interest of the detector. The region of interest is chosen by objects reconstructed in the previous Trigger levels. Additionally, conditional reconstruction allows more CPU time to be saved during track reconstruction. Because the ultimate resolution is not needed at HLT,

the reconstruction is performed with a reduced number of hits, and is stopped as soon as the desired resolution is achieved.

Table 2.3 shows the HLT requirements (threshold, allocated bandwidth...) at low luminosity for the selection of various simulated streams, in order to have a cumulative storage rate of 100 Hz. The selection is highly efficient for the benchmark physics channels, as can be seen from the efficiency listed in Tab. 2.4. Nevertheless, it remains inclusive by avoiding specific topological requirements.

Due to the real-time nature of the HLT selection, a key issue is the CPU power required for the execution of the algorithms. The third column in Tab. 2.3 reports the CPU time needed to process events on a Pentium-III 1 GHz CPU [48]. The current requirements vary from 50 ms for jet reconstruction to 700 ms for muon reconstruction. Weighting the CPU needs of the algorithms by the frequency of their application (the Level-1 Trigger rate), a mean CPU time of 271 ms is found per event that passes the Level-1 Trigger. This mean time implies that the CMS HLT farm must consist of 15,000 CPUs, in order to run the HLT with 50 kHz input rate. Extrapolating these figures to the LHC start-up (2007), on the basis of *Moore's Law*, the CPU units are expected to be a factor eight more powerful than at the time of these studies. Therefore, at the LHC start up, the HLT system will need about 2,000 CPUs.

During the time interval needed by HLT, the data are stored in random-access memories and if an event passes the High-Level Trigger selection it is stored and is available for offline analysis. Assuming a total time of 20 hours data taking per day and an event size of 1 MB, a total disk space of 10 TB per day will be filled at full luminosity.

Table 2.3: High-Level Trigger thresholds at low luminosity for various channels [40]. The CPU figures refer to a 1 GHz Intel Pentium III CPU.

Trigger	**HLT Threshold** (GeV/c^2 **or** GeV/c)	**HLT Rate (Hz)**	**CPU time (ms)**
1e ,2e	29, 17	33, 1	160
1μ, 2μ	19, 7	25, 4	710
1τ, 2τ	86, 59	3, 1	130
Jet $\otimes$ E_T^{miss}	180 $\otimes$ 123	5	50
e $\otimes$ jet	19 $\otimes$ 45	2	165
Inclusive b jets	237	5	300

Table 2.4: Performance of HLT selection at low luminosity after applying the cuts listed in Tab. 2.3.

Channel	**Efficiency**
H(115 GeV/c^2)$\rightarrow \gamma\gamma$	77%
H(160 GeV/c^2)$\rightarrow$WW*	99%
H$\rightarrow$ZZ$\rightarrow$4μ	99%
A/H(200 GeV/c^2)$\rightarrow$ 2τ	45%
SUSY (0.5 TeV/c^2 s-particles)	60%
W$\rightarrow$eν_e	67%
W$\rightarrow \mu\nu_\mu$	69%
$t\bar{t} \rightarrow \mu$+X	72%

Chapter 3

The CMS Tracker

In this Chapter the CMS Silicon Tracker [36] is described in detail. The construction and the use of such a detector in the LHC environment represents an important effort both from the experimental physics and engineering points of view. The huge amount of detector units (modules) to produce, test and assemble is astonishing and involves hundreds of people from several worldwide institutes. A large number of tests were done to study the performance of different silicon detectors and minimize the effect due to the exploitation of this detector in the hard radiation environment present in an LHC experiment. In the first part of this Chapter the Pixel detector and the Silicon Strip Tracker are described while in the last Section some results in the quality control of the sensors in which the candidate has been involved are reported.

3.1 The Pixel Vertex detector

The inner part ($r < 15$ cm) of the CMS Tracker is covered by the Pixel Vertex detector. This subdetector, shown in Fig. 3.1, is a fundamental device for b-tagging studies and impact parameter measurements. It also has paramount importance as a starting point in reconstructing charged particle tracks.

The Pixel detector layout consists of three barrel layers with two endcap disks on each side. The three barrel layers are located at mean radii 4.4, 7.3 and 10.2 cm and are 53 cm long. The two disks are placed at 34.5 and 46.5 cm from the interaction point. At high luminosity conditions, the inner barrel layer will be substituted by an outer layer placed at r =13 cm to improve resolution and limit

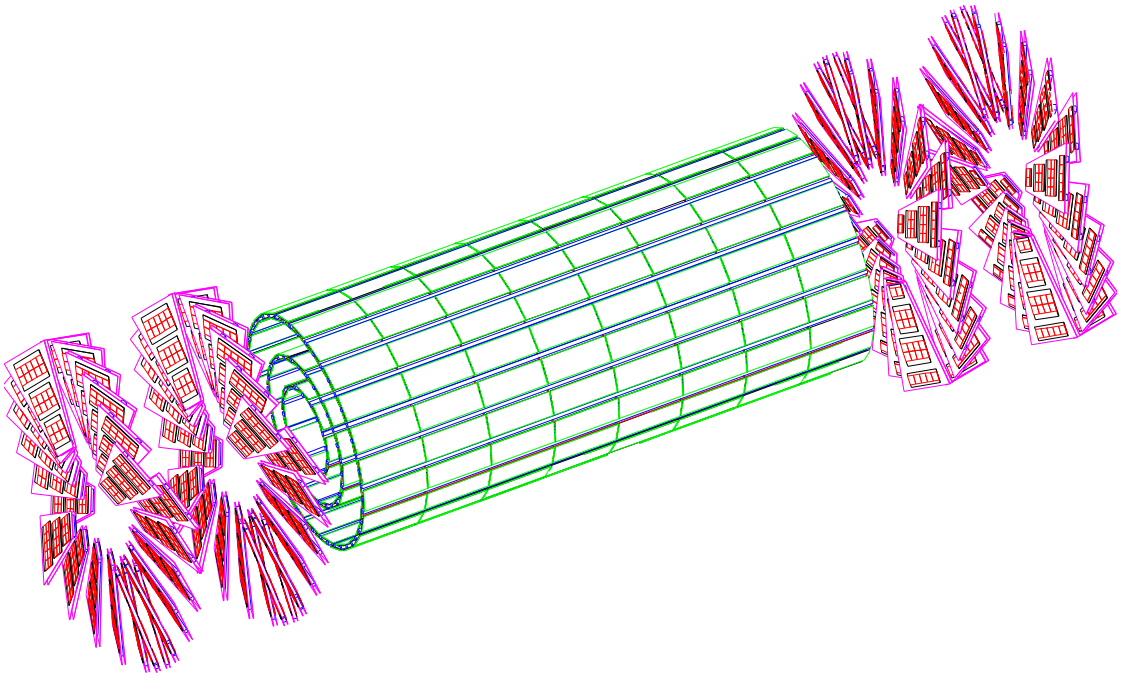

Figure 3.1: Perspective view of the CMS Pixel system in the high luminosity configuration.

radiation damages. Therefore initial n-type substrate sensors are chosen to collect electron signals on n^+ implants, which are more radiation hard. However it can not be avoided that in the barrel layers with $r < 10$ cm the pixel and readout chip lifetime is reduced by hostile radiation environment below CMS lifetime. Hence the layer at $r = 7.3$ cm should be replaced after six or seven years of operations.

A good resolution in the vertex position both in the transverse and the longitudinal planes is achieved using rectangular pixels of dimensions 150×100 μm^2 (with 100 μm in the $r\phi$ direction in the barrel and in the rz direction in the endcaps) and thickness 250 μm. A scheme of a pixel detector unit is shown in Fig. 3.2.

To enhance the spatial resolution by analog signal interpolation the effect of charge sharing induced by the large Lorentz drift in the 4 T magnetic field is used. Hence the detectors are deliberately not tilted in the barrel layers but are tilted in the end disks resulting in a turbine like geometry. The charge sharing between pixels is due to the Lorentz drift of charge carriers, which is about 28° for electrons

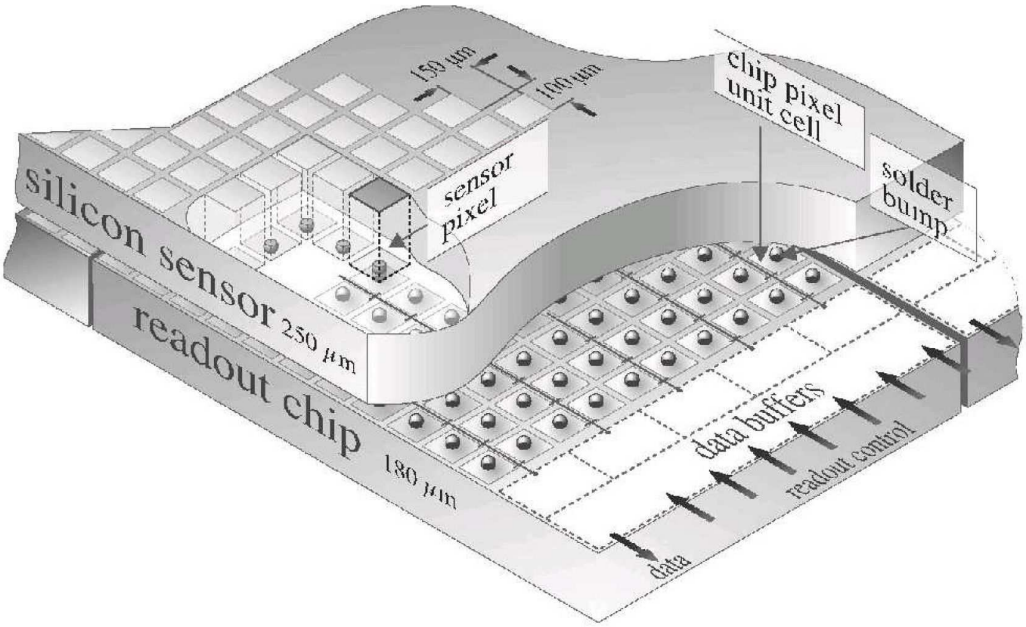

Figure 3.2: Schematic view of a Pixel detector unit.

in the CMS magnetic field, three times wider than for the holes. In the barrel the significant charge sharing between neighboring implants in the $r\phi$ plane improves the intrinsic hit resolution down to 10-15 μm, far below the 150 μm width of each n^+ implant, with the mechanism drawn in Fig. 3.3. Charge sharing is present also along z direction for inclined tracks leading to a similar resolution. The detectors placed on the disks are rotated with an angle of 20° around the central radial axis to benefit of charge sharing improved both in r and $r\phi$ directions by induced Lorentz effects. Despite a Lorentz angle reduced with respect to the barrel case, the resolution in r and $r\phi$ is expected to be 15 μm at CMS start and degrading to 20 μm when radiation damages arise.

The whole Pixel system consists of about 1 400 detector modules arranged into half-ladders of four identical modules each in the barrel, and blades with seven different modules each in the endcaps. The Pixel detector has been designed to provide two-hit coverage up to a rapidity of about $|\eta| = 2.2$.

Each pixel signal is read by a Pixel Unit Cell (PUC) bump-bonded directly to the pixel module. The PUC is integrated on the readout chip, which attends to 52

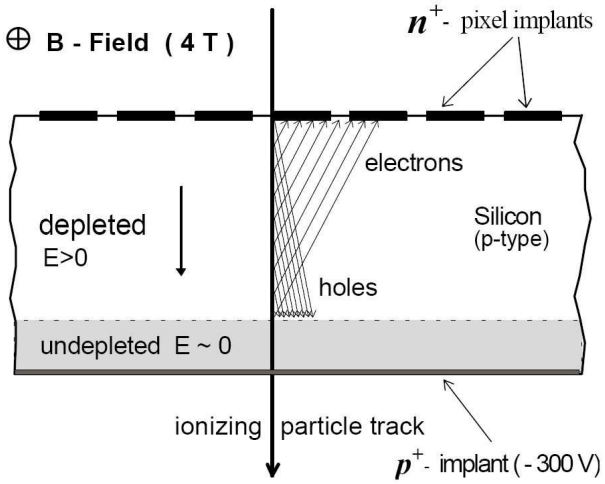

Figure 3.3: Charge sharing induced by Lorentz drift. After bulk type inversion the detector depletes from the n-pixel side. With increasing radiation dose the detector cannot be fully depleted and the collected charge is reduced.

columns and 80 rows for a total of 4 160 pixels. Since the number of channels is very high (44 millions), zero-suppression is mandatory to reduce the huge data volume down to a reasonable size. Each PUC is equipped with an analog circuit, which provides a logical positive output if the collected signal exceeds a tunable threshold. To reduce the number of channels to readout, two nearby PUC columns are read by one circuit placed in the periphery. The analog signals are temporarily stored into dedicated pipelines and on positive Level-1 Trigger decision are transmitted through optical fibers to the front-end driver in the counting room.

3.2 The Silicon Strip Tracker

3.2.1 Silicon Microstrip detector

The outer part of the Tracker is made with layers of Silicon Microstrip detectors. Each detector unit (*module*) is made with one or two sensors glued on a carbon fiber mechanical support together with the readout electronics. In Fig. 3.4 a module assembled in Florence is shown.

Figure 3.4: Picture of a single side module assembled in Florence.

The sensor is a n-type phosphorus doped substrate with p^+ implant strips, as shown in Fig. 3.5. The p^+ implants are only at one side of substrate and are coupled to aluminum strips which form the contact for the readout electronic. The dielectrics used in the couplings are SiO_2 and Si_3N_4. The resulting capacitance (C_{AC}) is $\sim$ 25 pF/cm, which is much higher than the total capacitance coupled to the strip ($C_{tot} \sim$ 1.2 pF/cm), in order not to lose a significant fraction of the signal.

The active surface of the detector is rounded by a p^+ ring (*bias ring*) used to polarize the strips. Poly-silicon resistors, with a value (R_{poly}) between 1 and 2 MΩ, connect every strip to the bias ring. The sensor is reversely biased applying a positive voltage (hundreds of Volts) on the backplane of the sensor, heavily n^+ doped and covered by a aluminum layer, and keeping the strips grounded. The region between the junction and the backplane is therefore completely depleted of free charge carriers, with exception of the thermally created ones.

When an ionizing particle passes through the depleted region, it interacts in the bulk creating electron-hole pairs (e/h) which drift in the electric field toward the backplane and the p^+ implants respectively. The mean energy required to create a e/h pair in silicon is 3.6 eV, therefore a minimum ionizing particle (*mip*), which has an average energy loss per path length of 390 eV/μm, should create 32 500 e/h pairs passing through a 300 μm thick sensor. Since the energy loss distribution

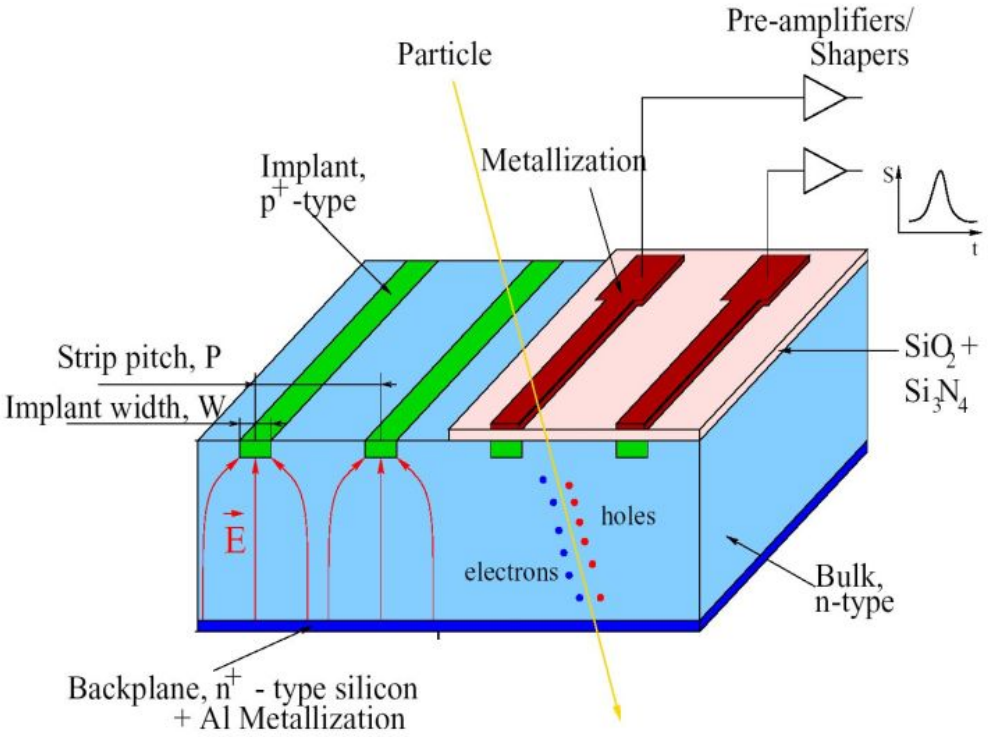

Figure 3.5: Principle of operation of a Silicon Microstrip detector.

is Landau shaped, the most probable value, being about 288 eV/μm, differs from the average. For this reason the most probable value of e/h pairs produced by a mip is usually quoted, which is 24 000 in a 300 μm sensor and represents a rough estimate of the charge to collect.

Some arrangements are made to improve the device. The n^+ implant backplane forms an ohmic contact and avoid charge injection into the bulk from the connected aluminum layer. On the opposite side the active area is surrounded by a p^+ implant, the *guard ring*, which limits the dark current contribution from sensor bounds. At the detector edges, uniform n^+ implants are placed to limit charge injection from the regions damaged by the cut on the wafer.

A passivation layer of SiO_2 covers the sensor surface, with the exception of the ohmic contacts, to protect from scratches and to reduce influences from external environment (humidity and chemical pollution).

At the end of the strips AC pads allow the bonding to an array of readout chips APV25 [49] housed on a thin hybrid circuit. The analog signal of each strip is transmitted to ADCs located in the counting room via optical links.

With these microstrip sensors it is possible to measure one coordinate, interpolating the crossing position by means of charge sharing between adjacent strips. A configuration to allow the bidimensional measurement of coordinates is realized gluing two detectors back-to-back with 100 mrad tilted strip directions. This configuration is referred to as stereo or double-sided and is preferred to the pixel segmentation, although the resolution is worse, because the number of readout channels is lower.

The Silicon Strip Tracker covers a tracking volume up to $r = 1.1$ m with a length of 5.4 m and is divided in three parts:

- inner Tracker
  - 4 barrel layers (Tracker Inner Barrel = TIB)
  - 3 disks per endcap (Tracker Inner Disks = TID)
- outer Tracker
  - 6 barrel layers (Tracker Outer Barrel = TOB)
- Tracker endcaps
  - 9 disks per endcap (Tracker End-Cap = TEC)

The TIB has four layers assembled in shells; the two innermost layers host double sided detectors, pointed out in blue in Fig. 3.6. The two TIDs, each one made of three small disks, complement the TIB region. The outer barrel structure (TOB) consists of six concentric layers, also in this case the two inner layers are double-sided. The TEC modules are mounted on nine disks on both side of the barrel. The detectors of ring 1, 2 and 5 are made of double-sided modules. All of them have a trapezoidal shape to follow the ring geometry.

The detector geometry is optimized following these criteria:

- The *pitch*, i.e. the distance between two consecutive electronic channels, changes between 80 μm in the inner TIB layers to 180 μm in the outer of the TOB, reducing the number of channels without degrading significantly performances.

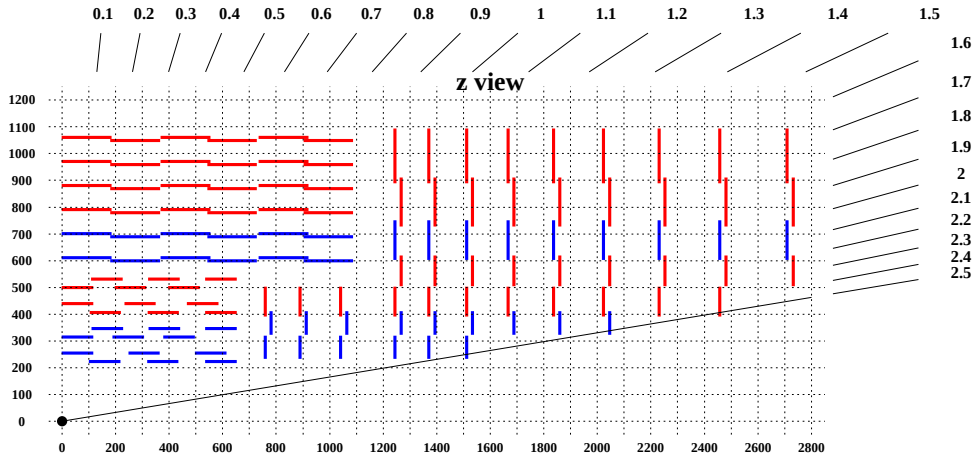

Figure 3.6: Schematic view of the Silicon Tracker layout. Single and double sided detectors are pointed out in red and blue respectively.

- The width of the strips (w) depends on the pitch (p): the choice of the ratio (w/p) is 0.25. This value ensures a low value of the total capacitance without endangering the functional stability at high voltage (with small w/p values in fact high electric fields can be generated near the strip ends limiting the breakdown performance of the detector).

- The strip length is 11 cm in inner barrel and 20 cm in the outer barrel. Longer modules in the outer layer allow the reduction of the total number of channels keeping a limited occupancy.

- The thickness of the substrate in the TIB sensors is 320 μm, while in the outer barrel is 500 μm in order to counterbalance the higher noise due to the longer strips. The collected charge therefore is higher keeping constant the signal to noise ratio.

The total number of modules is 15 148, 6 052 thin and 9 096 thick for a total

of 9 648 128 strips to be readout in groups of 128 by 73 736 APV chips [40]. Some geometrical parameters of the sensors used in the CMS Tracker are reported in Tab. 3.1.

3.2.2 Readout electronics

The scheme of the readout system for the CMS Silicon Tracker is sketched in Fig. 3.7.

The signal is collected through the metalized strip in one of the 128 input channels of the APV chips placed on the front-end hybrid. Since the strip pitch is different from module to module and only one type of readout chip is foreseen, a pitch adapter is designed to connect groups of 128 strips to the input pads of the APV.

The APV25 circuit has been developed for the readout of the analog signal of the CMS Microstrip detectors. Every APV channel is equipped with a preamplifier, a shaper, 192 memory cells and a deconvolution circuit. The chip is radiation hard, low noisy and has been designed to have low power consumption.

The charge, collected by a strip of the silicon sensor, is read through a charge sensitive amplifier followed by a CR-RC shaper with a *peaking time* of 50 ns. The

subdetector	**layer**	**pitch (μm)**	**length (mm)**	**thickness (μm)**	**n° strips**
TIB	layer 1-2	80	119.2	320	768
TIB	layer 3-4	120	119.2	320	512
TOB	layer 5-6	122	2×94.5	500	768
TOB	layer 7-10	183	2×94.5	500	512
TID	layer 1	81 - 112	89.5	320	768
TID	layer 2	113 - 143	90.3	320	768
TID	layer 3	124 - 158	112.8	320	512
TID	layer 4	113 - 139	117.1	320	512
TEC	layer 5-7	126 - 156	84.0 + 66.1	500	768
TEC	layer 8-10	163 - 205	99.0 + 87.8	500	512
TEC	layer 11-13	140 - 172	109.8 + 98.8	500	512

Table 3.1: Geometrical parameters of the sensors used in the CMS Tracker.

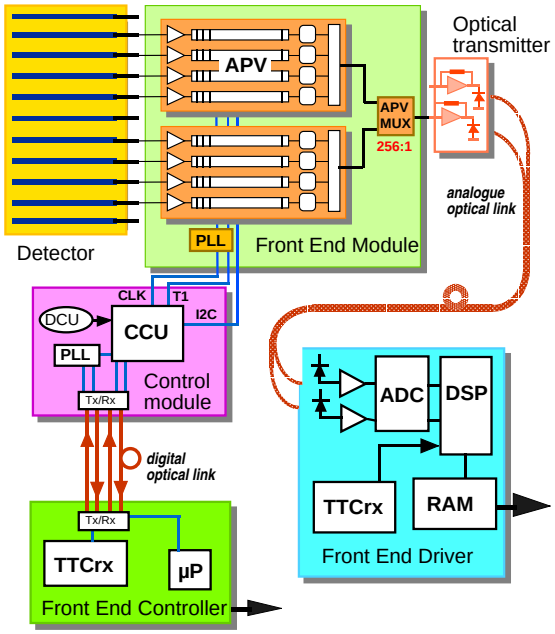

Figure 3.7: Scheme of the readout system for the CMS Silicon Microstrip Tracker.

time constant has to be very small to avoid the overposition of the events.

The output of the shaper is sampled at 40 MHz synchronously with the LHC bunch-crossing frequency, and the final analog signal is stored into a pipeline. The pipeline is a 128×192 matrix of capacitor cells (0.25 pF each) that can contain the output of all the 128 strips for a maximum of 192 locations which correspond to the number of bunch crossings, waiting for a response of the Level 1 Trigger. The pipeline length allows to store data for an amount of 4.8 μs, well above the latency time of the Level 1 Trigger (3.2 μs).

In case Level 1 accepts the event, the signal is further processed by the APV circuit which can operate in two different modes: *peak* and *deconvolution*. Only the maximum value reached by the signal is stored in the pipeline in peak mode, while in the deconvolution mode the Analog Pulse Signal Processor circuit (APSP) processes the signal using the triggered and the two preceding samples. The three measurements are weighted and combined together, with a rise time constant of 25 ns, to effectively reduce the signal duration to one bunch crossing, at expense of increasing noise [50]. This mode of operation is the most suitable at LHC rates,

especially at high luminosity, because it reduces the signal tails of adjacent bunch crossings and the contribution of the pile-up. Peak mode instead can be used during the low luminosity or in the start up period for calibration purposes.

The APV output is formed by a 12 bits *frame* (the digital header formed by: 3 bits for the frame identification, 8 bits for the pipeline address, and one error bit) followed by 128 analog signals, the output of the APSP serialized by a 20 MHZ *multiplexer*. The total readout time is $(12 + 128) \times 50$ ns $= 7$ μs, hence if two Trigger signals were closer than 7 μs, the information from the APV would be lost. To avoid this potentially long APV dead time, an internal FIFO is able to temporarily store up to a maximum of 31 (10) Trigger frames when working in peak (deconvolution) mode, thus allowing to absorb the Level 1 Trigger time fluctuations.

The pulse height data coming from two APVs are multiplexed onto a differential line over the short distance to a laser driver transmitting at 1 300 nm wavelength. The optical transmitter conveys the analog signals through a 100 m optical link fiber to the counting room, located outside the CMS cavern. Then detector data are digitized by a 9 bits ADC of the Front-End Driver (FED), which then processes digital signals, reducing them via zero suppression.

All the readout system is controlled by the Front-End Controller (FEC), which distributes the clock and Trigger signals to the APVs. The global Timing Trigger Command (TTC) sends the LHC machine clock and CMS Level 1 Trigger through the FEC interface. The two signals are transmitted by the FEC to the front-end hybrids through a digital optical link and distributed to series of modules by some Communication and Control Units (CCU). The clock signals are locally recovered and eventually time-tuned by Phase Locked Loop chips (PLL) to reduce at minimum the phase jitter and ensure high reliability.

3.2.3 Radiation damage of Silicon Microstrip detectors

The Tracker is the CMS subdetector closest to the interaction point, hence it has to sustain the highest radiation flux, which deteriorates the modules. The radiation damage is caused not only by particles produced in primary proton-proton collisions, but also by albedo neutrons emitted from the calorimeters surrounding the Tracker. Two different effects have been observed in Silicon detectors: surface damages and bulk damages.

When an incident particle crosses the detector it produces e/h pairs. The surface damages [51] are caused by the missing recombination of the e/h pairs created into the oxide layers of the detector surface by the crossing particles. Bulk damages originate from the removal of some atoms from their regular sites on the silicon lattice [52]. A point-like defect in the lattice (vacancy) is created and can be considered an acceptor impurity, while the displaced atom behaves as a donor; this couple of defects is referred to as Frenkel pair. Various combinations and even clusters of these defects are also observed. The principal effects caused by the radiation damage are classified as follows.

Inversion point and depletion voltage

One of the major effects of bulk damage due to radiation is the change in the effective doping concentration of the silicon crystal. An empirical model, called *Hamburg model* [53, 54], which is in agreement with experimental data, describes the behavior of the effective doping concentration as a function of the fluence, the annealing time and the storage temperature. When the fluence, normalized to a 1 MeV neutron equivalent, has reached a certain value, the effective bulk donor density approaches zero. At that point, continuing the irradiation, the bulk behaves as p-type and the effective acceptor density starts to grow up. This phenomenon is called *bulk type inversion* [55] and leads to an increase of the depletion voltages for highly irradiated silicon sensors. The polarity of reverse biasing of the device does not change after inversion, while the junction moves from the p^+ strip side to the n^+ backplane side.

Leakage current

The current passing through the junction (*leakage current*) increases proportionally to the fluence, i.e. $\Delta J = \alpha\Phi$. The proportional constant α is the damage constant, which depends on temperature and it is 3×10^{-17} A/cm at -5° C. As a result, the electronic noise contribution coming from the leakage current is enhanced.

Interstrip capacitance

With irradiation, the positive charge density in the oxide increases until it reaches a saturation point, as a consequence negative charges accumulate at the inter-

face between Silicon and oxide increasing the capacitance (C_{int}) between adjacent strips and leading to a worsening of the signal to noise ratio of the device. A significant increase in the interstrip capacitance after radiation has been found on detectors with $< 111 >$ crystal orientation, but not on sensors with $< 100 >$ crystal orientation, which have been chosen for the Tracker [56].

Charge collection efficiency

The signal collected by the electrodes is reduced by charge trapping into the damaged bulk since the defects produced by the irradiation can increase the fraction of the trapped charge carriers (the charge is not necessarily lost, but can be released after a latency time of the order of μs). Experimentally the loss of efficiency of charge collection is around 10% for dose greater than 10^{14} neutrons/cm^2.

Sensor characteristics

Selected sensors must have a breakdown voltage (V_{break}) greater than 500 V so that they can be biased with voltage V_{bias} greater than depletion voltage ($V_{bias} \sim 1.5\ V_{depl}$). Typical values for V_{bias} are 300 V for TIB modules and 120 for TEC and TOB modules. When the detectors work in the overdepletion regime the charge collection is faster due to the higher electric field, thus reducing the influence of the bulk damages in charge trapping. Test results performed on irradiated sensors agree with the expectations. The signal to noise ratio as a function of V_{bias}/V_{depl} after an irradiation corresponding to ten years of LHC operation is shown in Fig. 3.8a.

Furthermore the sensor bulk is made of low resistivity silicon for TIB modules. The low resistivity in fact, delays the inversion point and keeps the depletion voltage low even after a fluence of 10^{14} neutrons/cm^2. This behavior is shown in Fig. 3.8b, which reports the depletion voltage as a function of the irradiation time for low and high resistivity detectors. It is clear that a low resistivity detector does not need voltages greater than 300 V.

Finally detectors will work at low temperature (-10° C or less) both to minimize the dark current and the *reverse annealing* effect that increases the depletion voltage when the irradiated material is kept at room temperature for a long time.

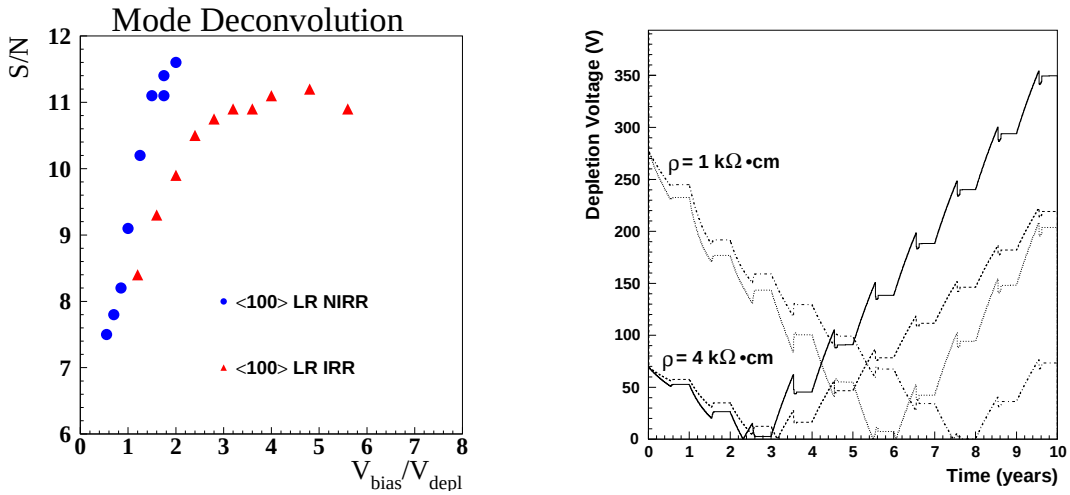

(a) (b)

Figure 3.8: (a) The signal to noise ratio as a function of V_{bias}/V_{depl} before (dot) and after (triangle) an irradiation corresponding to ten years of LHC operation. (b) Depletion voltage for high ($\rho > 4$ kΩ·cm) and low ($\rho \sim 1$ kΩ·cm) resistivity detector as a function of the irradiation time (years of LHC operation). The irradiation is calculated according to the dose foreseen in the inner layer of the TIB.

3.3 Process Quality Control

The number of Silicon sensors needed for the CMS Tracker will be close to 25 000. This huge number of sensors has forced the Collaboration to develop a complex scheme for the sensor quality control [57]. One of the step involved in this procedure is the Process Quality Control (PQC), carried out in Florence, Strasbourg and Wien. The aim of the PQC is to monitor the stability of the sensor fabrication process throughout the production and to identify any problem as soon as possible, in order to give a fast feedback to the producers (ST Microelectronics [58] and Hamamatsu Photonics K.K. [59]).

The PQC is performed on a dedicated set of nine test-structures (*standard half moon*) hosted in all the wafers used for the production of the CMS sensor, with a design common to the two manufacturer companies. The percentage of wafers tested is 5% of the total number and at least one wafer per sensor batch is analysed.

In this Section the test structures used in the Process Quality Control and the

main parameters controlled with them are described. In the last part the main results obtained with the measurements carried out in Florence and in the other PQC centers are reviewed.

3.3.1 PQC measurements

The PQC setup is based on a probe card contacting the test structure, interfaced through a switching system, to a DC voltage source and to an LCR meter. The test structure is hosted inside a probe station during the measurements to shield it from the light. The device is located on a chuck (the only mechanical movable part in $x-y$ plane) which supplies the high voltage to the back of the silicon wafer. The probe card is mounted on the *platen* that can move along the z axis (vertical direction).

First an alignment step is needed in our procedure in which the structure under test is rotated to be aligned with the probe card. Then measurements are carried out with a software which runs in `Labview` [60] and which is made of three parts: acquisition, analysis and database interface. The acquisition part controls the instruments and stores the results, the analysis software is used to extract the relevant physical parameters from data, whereas the last component transfers all the acquired information to the central CMS Tracker database [61].

The standard half moon is shown in Fig. 3.9 and from left to right is composed by nine structures which are described in the following.

Test Structure for Capacitance

The first structure is formed by an array of 26 AC coupled strips (TS-CAP) characterized by the same dielectric composition of the main sensor (submicron layers of SiO_2 and Si_3N_4) but with a direct connection to the bias ring, without poly-silicon resistors. Each strip can be read out by its AC pad that is placed alternatively on the two opposite ends of the strips. This device is used to analyse the quality of the dielectric by the measurements of the capacitance (C_{ac}) and the dielectric breakdown voltage (V_{diel}).

The thickness of the oxide layer is derived from the common parallel plate capacitor equation. However, the oxide layer is composed of two oxides, which can be described by two capacitors connected in series, therefore the only way to calculate the oxide thickness is to assume a value for the thickness of the Si_3N_4

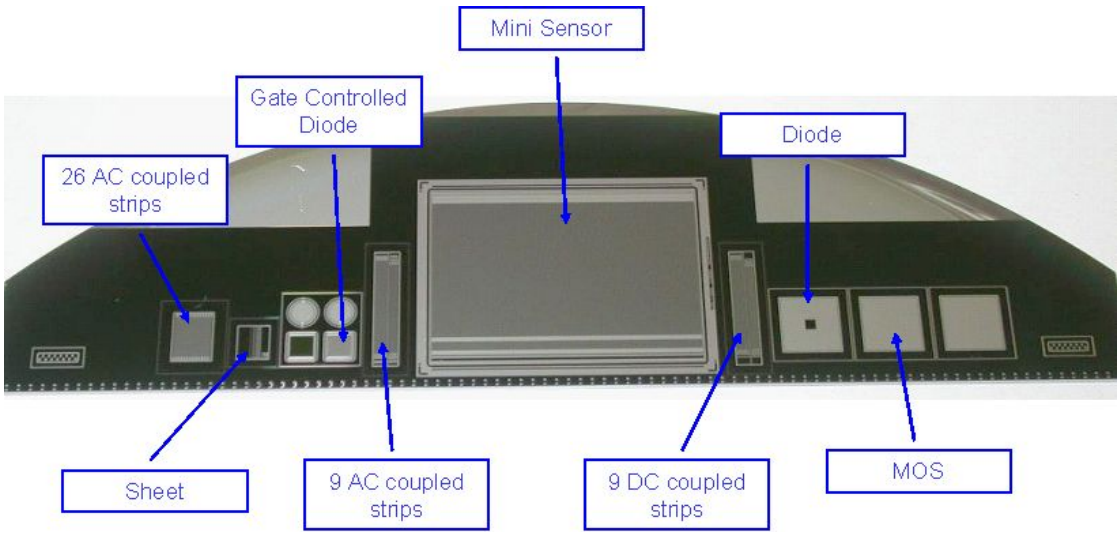

Figure 3.9: The nine test structures of the *standard half moon* analysed in the PQC.

and calculate the thickness of the SiO_2 from the following formula

$$d_1 = \epsilon_0 \epsilon_{SiO_2} \left(\frac{A}{C_{tot}} - \frac{d_2}{\epsilon_0 \epsilon_{Si_3N_4}} \right) . \tag{3.1}$$

The CMS specifications of the coupling capacitance are $C_{ac} > 1.2$ pF cm^{-1} μm^{-1} per implanted strip width. For this structure, the capacitance of one strip is

$$1.2 \text{ pF cm}^{-1}\mu\text{m}^{-1} \times \underbrace{4.413 \text{ mm}}_{\text{strip length}} \times \underbrace{30\ \mu\text{m}}_{\text{strip width}} = 15.89 \text{ pF} . \tag{3.2}$$

Due to the expected small value, in order to extract the 6 values of C_{ac} it is important to subtract the stray capacitance of the system.

The other parameter which can be studied in the TS-CAP structure is the breakdown voltage of the dielectric, corresponding to the maximum voltage that can be applied across the dielectric before a substantial current flows from the p^+ implant to the metal pad. Contrary to the breakdown of the silicon bulk, which is caused by avalanche effects of the charge carriers, the effect of the breakdown of the dielectric is caused by stripping electrons from their atoms. Every impurity of the oxide can serve as the nucleation point for this breakdown effect. The

measurement is performed by applying GND to the bias ring and a negative HV to the metal pads (up to -200 V in -10 V steps). When the current limit (and thus the dielectric breakdown) is reached, the measurement is stopped for that strip. The breakdown causes irreversible damage to the crystal structure and therefore this destructive test cannot be done on the real sensor.

Sheet

Measurements on a structure called sheet (see Fig. 3.9) are foreseen to determine some important resistance values. It consists of nine sheet structures used to measure the resistivity of the aluminum layer, of the p^+ implant and of the poly-silicon resistors. All nine structures have individual contacts at the bottom of the device, whereas the other side is connected to the common bias ring.

Gate Controlled Diode

The surface current is measured to determine the interface recombination velocity and the interface state density [62]. This measurement is done on a structure hosting four *gate controlled diodes* (GCD), two circular and two square ones, see Fig. 3.9.

The standard measurement is carried out on the right square GCD which is built of comb-shaped p^+ implanted strips intertwined with comb-shaped strips made of MOS (*metal oxide semiconductor*) material. The SiO_2 layer in the MOS region corresponds to the oxide in the interstrip region of the real sensor with a thickness of 1.4 μm (for STM).

A constant reverse bias voltage V_{bias} is applied to the diode between the backplane and the p^+ strips, while the current through this diode is measured as a function of the gate voltage V_{gate}. In our case, the backplane is grounded, the bias voltage is -5 V and the gate voltage varies between +5 and -20 V with respect to the the backplane potential.

The measured current through the diode is a superposition of two components:

$$I_{measured} = I_{surf} + I_{jd}\,. \tag{3.3}$$

While the bulk current remains constant during the measurement, the surface current, caused by a depletion zone which is developed underneath the gate, varies. The observed effects are:

- **Accumulation**: if V_{gate} is less then *flatband voltage*, V_{fb}, the voltage at which there is no electrical charge in the semiconductor and, therefore, no voltage drop across it, only the volume current I_{jd} arising from the p-n junction is observed. The electrons which are induced by the static oxide charge beneath the gate are preventing the reverse voltage to completely deplete the volume.

- **Depletion**: when $V_{gate} \lesssim V_{fb}$, a depletion region under the gate strips is formed which connects to the depletion region of the diode. This effect is caused by the repulsion of the free electrons underneath the gate by the negative gate potential. Now the generation-recombination-centers at the Si - SiO_2 interface contribute to the total current, visible as a sharp increase.

- **Inversion**: if $V_{gate} > V_{fb}+V_{bias}$, an inversion layer under the oxide consisting of electrons is formed, which crushes out the depletion region. This is seen in a sharp decrease of the total current. Higher negative gate voltages do not change this state anymore.

The analysis software extracts the surface current from the measured curve as the difference of the current level at inversion to the current during depletion and calculates the interface recombination velocity S_O using

$$S_O = \frac{I_{surf}}{n_i \times e \times A_{gate}}\,, \tag{3.4}$$

where e is the elementary charge, $n_i = 1.45 \cdot 10^{10}$ cm^{-3} the intrinsic carrier density and $A_{gate} = 2.3 \cdot 10^{-2}$ cm^2.

A high value of the surface current indicates oxide contamination problems during the manufacturing of the sensors and thus can induce problems during operation when further charges are introduced by irradiation into the oxide layer.

Interstrip Capacitance in AC

The interstrip capacitance is an important parameter related to the readout electronics. A higher value leads to higher detector noise and thus lower signal to noise ratio. The measurement of the interstrip capacitance is done by connecting to the connectors of an LCR meter a central strip and the two neighboring strips of the IS-TS-AC structure. The half moon is operated now at a reverse bias voltage of $V_{bias} = 400$ V. The common acquisition software subtracts the stray capacitance value from the result to figure out the true value.

Mini sensor

It is a small size replica of the main sensor. The structure is composed by 192 strips with a pitch of 120 μm which is an average value among the pitches of the different sensor geometries characterizing the CMS Tracker sensors. The mini sensor has an active area of 2.3×1.6 cm^2. The test on this device consists of an IV curve from 0 to 700 V in 5 V steps, from which the breakdown voltage and the current value at 450 V are extracted.

Interstrip Capacitance in DC

The Interstrip Capacitance in DC (IS-TS-DC) structure is used to measure the interstrip resistance. It has the same geometry as IS-TS-AC with two exceptions: the lack of poly-silicon resistors avoids their contribution to the measurement, which means that the strips are isolated from the bias ring. Moreover the p^+ implant is directly connected to the metal layer all along the length of the strips through vias. Thus the implant layer can be contacted using either DC or AC pads. The interstrip resistance is measured between the central strip and its two neighbors (which are tied to ground). The central strip is set to a potential of a few volts and the current between them is measured.

The device is inversely polarized with $V_{bias} = 100$ V. This voltage is enough to deplete the interesting region underneath the implants on the p-side. The voltage drop between the central strip and its two neighbors must be kept small with respect to the bias voltage to avoid a perturbation of the depletion field. Since the interstrip resistance should be high, a very low current across the strips of a few pA is expected. Therefore an instrument with a high current sensitivity is needed.

The resistance value is extracted with a linear fit of the IV curve obtained by a voltage scan between ± 2 V. This procedure is more precise than a single measurement because the contribution of a constant leakage current is removed.

Diode

Using a simple diode, the wafer thickness or the Silicon resistivity can be determined through a CV curve. The Silicon bulk is biased by a voltage varied between 0 and 300 V, and the capacitance is measured at steps of 5 V. Two linear fits are applied to the $1/C^2$ curve as a function of the applied voltage. The shape of this curve is linear until full depletion is reached. Then the capacitance reaches a

plateau and the curve becomes a horizontal line. The depletion voltage corresponds to the intersection of the two linear regions. In order to extract the parameters we are interested in, the diode surface is needed. This can be better defined if the diode guard ring is set to ground. Taking into account the fact that the field lines extend into the intermediate region between the central implanted square and the guard ring, the area entering into the calculation has been chosen as the average between the one inside the central square and the one inside the guard ring.

The depletion depth, which should be near to the wafer thickness (320 or 500 μm) is calculated by using an equation derived from the well know parallel plate capacitor

$$d = \frac{\epsilon_{Si} \times A_{diode}}{C_{depl}}\,, \tag{3.5}$$

where $\epsilon_{Si} = 106.25 \cdot 10^{-12}$ F m^{-1}, $A_{diode} = 0.246$ cm^2. The bulk resistivity is calculated assuming the nominal wafer thickness as

$$\rho = \frac{d^2}{2 \times \epsilon_{Si} \times \mu \times V_{depl}}\,, \tag{3.6}$$

where $\mu = 1350$ cm^2/(V·s) is the electron mobility for the lightly doped Silicon, as the one in the bulk.

Metal Oxide Semiconductor

One MOS structure is used to extract the value of the flatband voltage (V_{fb}) through a CV plot. MOS structure consists of the same SiO_2 oxide layer as the thick interstrip layer. This measurement shows how the interface mobility charge underneath the gate reacts to an applied bias voltage. This voltage is applied to the back while keeping the gate to ground, hence the sign convention is reverted with respect to what is normally found in literature, referring to V_{gate}.

Starting from a negative bias voltage of -10 V, we can identify three regions:

- **accumulation** ($V_{gate} > 0$): free electrons are accumulated beneath the gate. The measured capacitance is the oxide capacitance only $C_{ox} = \epsilon_{ox} A_{gate}/d_{ox}$. Therefore, the oxide thickness can easily be extracted from this value.

- **depletion** ($V_{gate} \leq V_{fb}$): rising the voltage, the Si region underneath the gate depletes of free electrons. The capacitance decreases until the complete

absence of charges on the armature of the capacitor, the flat band condition. In a theoretical situation, this happens when $V_{fb} \approx 0$ V, but humidity, chemical pollution, migration through the surface or light particle irradiation may cause an increase of the induced charge. The shift of the flatband voltage measures the trapped positive charge in the oxide. This is the main parameter we are interested in.

- **inversion** ($V_{gate} << V_{fb}$): holes accumulate beneath the metal gate.

V_{fb} is identified looking at the behavior of the CV curve and picking up the voltage corresponding to the intermediate capacitance between the two values that we fit in the accumulation and inversion regions.

As soon as we have the V_{fb} value, the oxide charge can be calculated as

$$V_{fb} = \phi_{ms} - \frac{Q_{ox}}{C_{ox}}\,, \tag{3.7}$$

where ϕ_{ms} is the work function between metal and semiconductor. For an aluminum gate and n-type silicon with a doping in the range $10^{11} \div 10^{12}$ $\phi_{ms} \approx -0.5$ V. The oxide charge concentration (N_{ox}) can be then extracted using the fact that $Q_{ox} = qN_{ox}A_{gate}$, leading to

$$N_{ox} = \frac{C_{ox}}{qA_{gate}}(\phi_{ms} - V_{fb})\,. \tag{3.8}$$

In order to apply correctly this formula we have to remember that we have an opposite sign convention for the measured V_{fb} with respect to what is usually quoted in literature.

3.3.2 PQC results

In this Section a selection of the results obtained with sensor batches delivered so far is presented. At the moment the number of wafers that have been tested in the PQC is around 4 200.

The strength of the dielectric layer to a voltage difference as measured in TS-CAP is shown in Fig. 3.10. This is an important feature since it is foreseen that some beam loss events in the CMS Tracker could cause a voltage drop across the coupling capacitance, estimated to be in the order of 100 V. The lower acceptance

limit on the breakdown voltage is set to 120 V and almost all the structures received so far survived beyond this value.

Other fundamental parameters monitored are related to the quality of the interstrip insulator. Typical values of the density of the oxide charge at the interface, both in HPK and STM test structures, are in the range $(5 \div 10) \cdot 10^{10}$ cm^{-2}. Chemical pollution may cause an increase of the induced charge at the interface and a shift of the V_{fb} value would measure the trapped charge.

This effect is enhanced by the sensor irradiation. This can be seen in Fig. 3.11 where the interstrip capacitance is shown for different values of the V_{fb} after a proton irradiation at the cyclotron of the Karlsruhe Forschungzentrum, at a fluence corresponding to 10 years of operation at LHC.

At the beginning of 2003 some STM batches were rejected due to a high V_{fb} value. This problem was traced back in the manufacturer company to the contamination introduced by a particular machine that has been then excluded from the production line.

In the same period some other STM batches had problems with the too low interstrip resistance. The R_{int} values for those batches were below the 1 GΩ which ensures a good electrical separation of adjacent strips. This failure was traced back

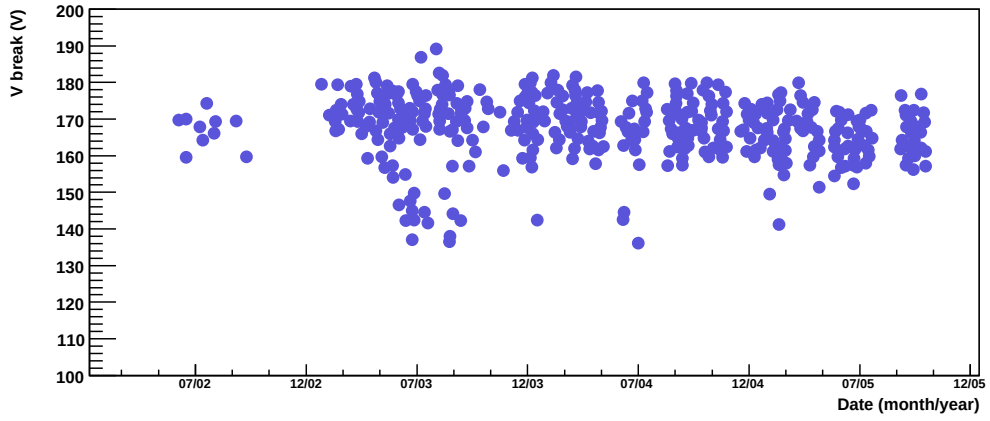

Figure 3.10: Dielectric breakdown voltage as function of the delivery date of the test structures. The high quality of the sensors (all well above the 120 V limit) and the good stability in time of this parameter are clearly shown.

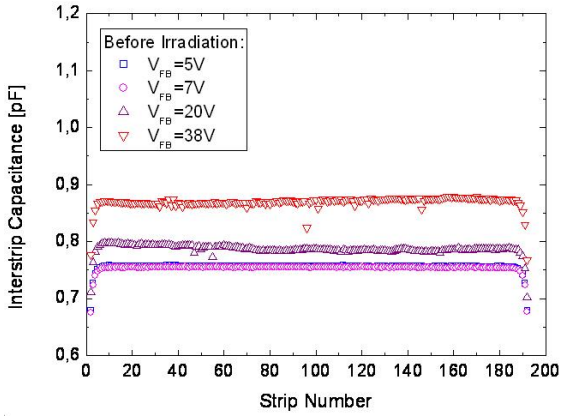

(a)

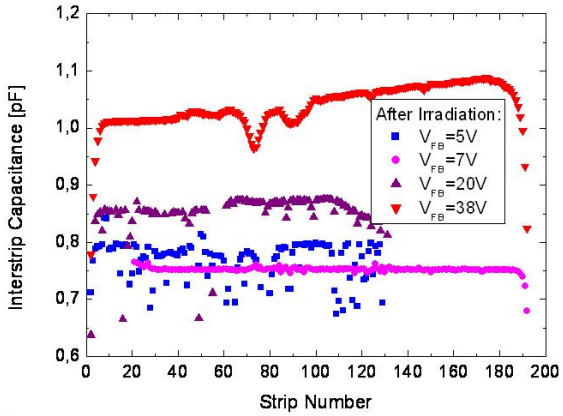

(b)

Figure 3.11: The irradiation of the test structures at fluences equivalent to 10 years of LHC has shown that a high V_{fb}, connected to a bad quality of the interstrip Si oxide, leads to a large increase in the interstrip capacitance. This effect is clearly shown in the pictures where the interstrip capacitance is shown before (a) and after (b) irradiation.

to a small parameter variation in the production line. The problems encountered in STM sensor production are shown in Fig. 3.12 in which the flatband voltage and the interstrip resistance of the sensors are shown as a function of the test structure delivery date.

The following wafer bulk resistivity ranges are requested to assure a depletion voltage below 400 V for all sensors after 10 years of operation at LHC: 1.25 $<$

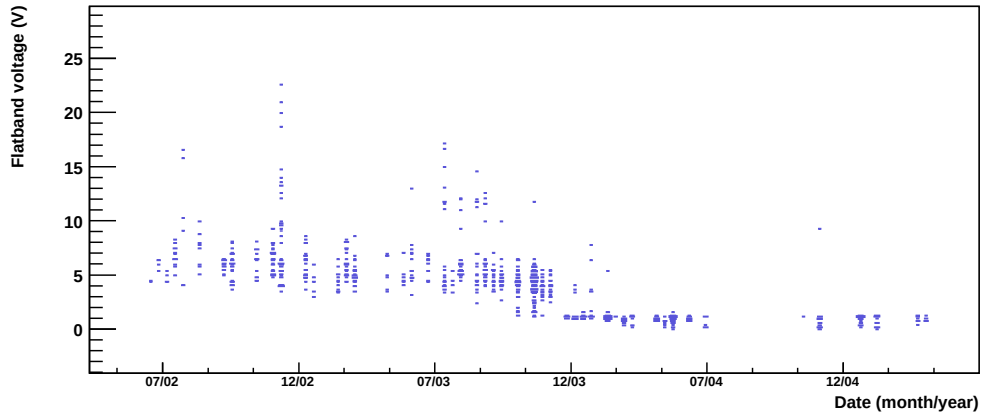

(a)

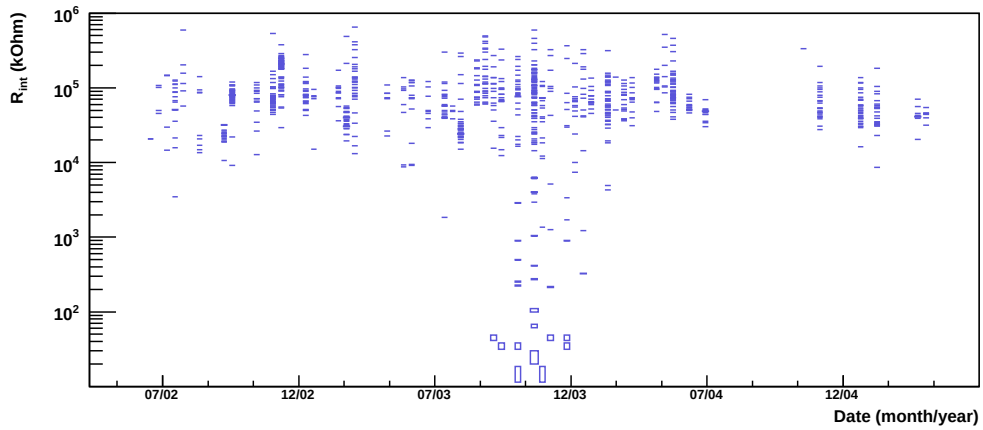

(b)

Figure 3.12: Summary of the problems encountered in the STM sensors production. (a) Flatband voltage as a function of the delivery date of the test structure, the increase of the value of V_{fb}, above the 10 V limit, is clear for the structures delivered at the end of 2002. (b) Interstrip resistance as a function of the delivery date of the test structure, the structures delivered between October 2003 and February 2004 had too small values of R_{int} (limit 1 GΩ).

$\rho < 3.25$ kΩ cm in the inner Tracker and $4.5 < \rho < 7.5$ kΩ cm in the outer Tracker. After the PQC has verified the failure of some HPK batches to satisfy this resistivity condition the company has agreed to substitute the problematic batches and to sort the wafers according to their resistivity in such a way that those with the lower resistivity will be used for the sensor geometries that are mounted in the inner layers, where the irradiation levels will be harsher. The resistivity as a function of the delivery date of the structures is shown in Fig. 3.13.

Except for the above mentioned problems the monitored parameters show a good stability in time. As an example the mini sensor breakdown voltage is in average very high and almost all the structures (95% in STM, 98% in HPK) survive up to 700 V, the upper limit of the IV measurement.

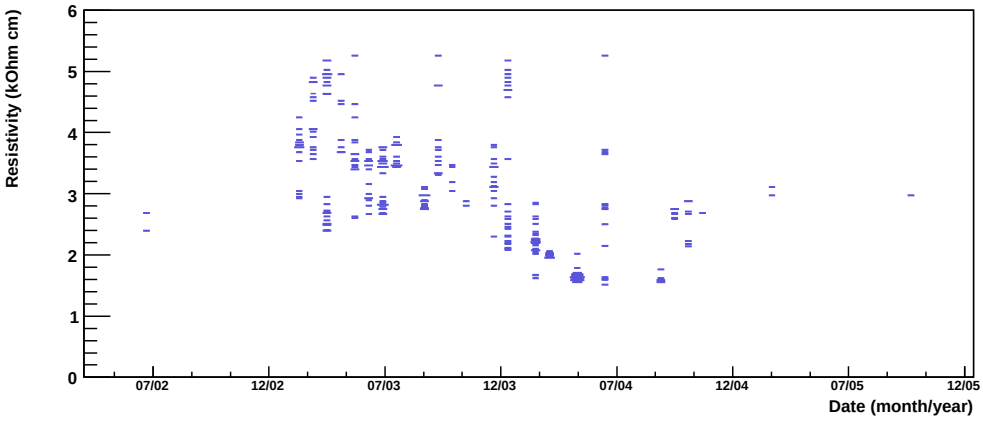

Figure 3.13: HPK thin sensors resistivity as function of the delivery date of the test structures. The picture shows the failure of some batches to satisfy the limits chosen by the CMS Collaboration.

Chapter 4

Simulation and Reconstruction

The software requirements and computing resources needed by LHC experiments exceed by far those of any currently existing high energy physics experiment. Track reconstruction in particular will be a very challenging task due to the high number of tracks foreseen. At high luminosity, an average of 25 minimum bias events are expected per bunch crossing, which will produce more than 1 000 tracks in the tracker and track densities which can be as high as 10 tracks per cm per bunch crossing at a radius of 2 cm.

This complexity led the CMS collaboration to develop software using Object-Oriented programming which ensure the necessary modularity and to implement it using the `C++` [63] programming language. The collaboration has also decided to adopt the same software architecture both for online selection and offline analysis.

This Chapter describes the software used to generate simulated events, to mimic the passage of particles through and their interactions with the CMS detector and the response of the detector elements. Track and muon reconstruction is then described in details, since it is of fundamental importance for the analysis presented in this work.

4.1 CMS software projects

The various CMS Object-Oriented projects and their relations are shown in Fig. 4.1. The CMS reconstruction and analysis software is written in the `C++` programming language and is based on the `COBRA` (Coherent Object-Oriented Base for Simulation Reconstruction and Analysis) [64] software framework, which provides

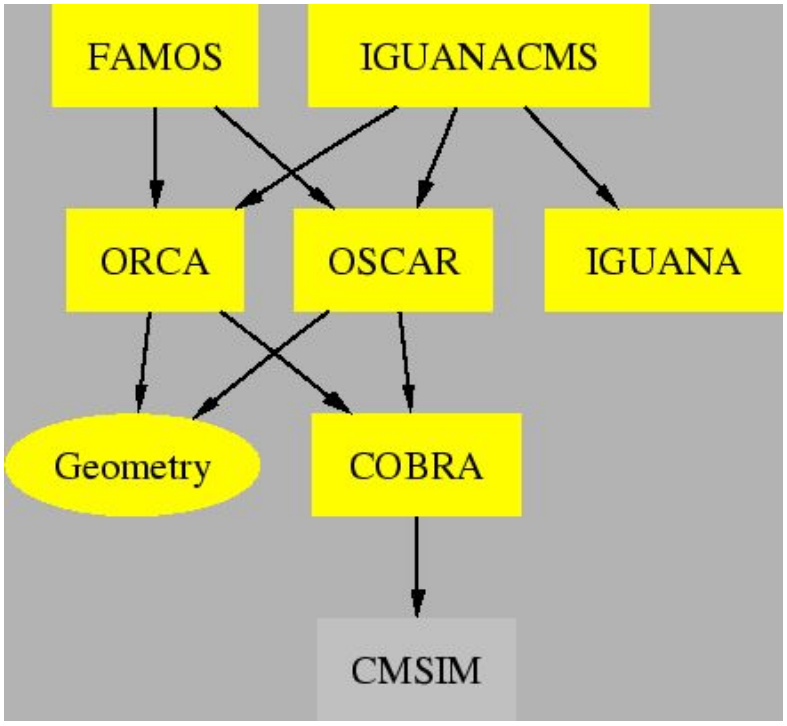

Figure 4.1: Relationship between the various CMS Object-Oriented projects. Arrow direction means "depends on".

basic services and utilities: physics type services (histogrammers, fitters, mathematical algorithms, geometry and physics calculation routines) and computer services (data access, inter-module communication, user interface, etc.).

CMS detector geometry and material composition are simulated with the program `OSCAR` (Object-Oriented Simulation for CMS Analysis and Reconstruction) [65], based on the `GEANT 4` package [66], to mimic the effects of the passage of particles through matter. The description of the CMS geometry is detailed and includes not only active subdetector volumes, but also cables and mechanical support structures and information about the magnetic field.

The CMS program `ORCA` (Object-Oriented Reconstruction for CMS Analysis program) [67] includes the code for reconstruction and analysis but also for simulation of detector response and of Level-1 and High-Level Trigger.

Within the CMS software projects `FAMOS` (Fast Monte Carlo Simulation) [68]

and IGUANA (Interactive Graphics for User Analysis) [69] are also available. The first project is a framework for fast simulation of particle interactions in the CMS detector. The detector response is parametrized so that the output of FAMOS is as close as possible to the output of the full simulation (OSCAR) and full reconstruction (ORCA). Each event is therefore processed in a much smaller time than in the full simulation chain. FAMOS delivers the same physics objects (Calorimeter hits and clusters, Tracker hits and reconstructed tracks, etc...), which then can be used as inputs of the same higher-level analysis algorithms (b-tagging algorithms, electron candidates, jet clustering, etc...).

The latter, IGUANA, is a modular C++ toolkit for interactive visualisation. It covers three domains: graphical user interfaces, interactive detector and event visualisation, and interactive data analysis and presentation.

4.2 Events simulation and reconstruction

The proton-proton interactions at $\sqrt{s} = 14$ TeV/c^2 are generated by standard Monte Carlo generators like PYTHIA [70], CompHep [71] or Alpgen [72]. The events produced are stored in the standard HEPEVT [73] structure in HBOOK [74] ntuples with an average event size of 50 kB.

The collision point is smeared around the CMS reference frame origin according to the composition of three independent gaussian distributions: along the z axis with $\sigma_z = 5.3$ cm and along bending plane (x and y axes) with $\sigma_x = \sigma_y = 15$ μm.

All the final particles produced at generator level are propagated through CMS taking into account multiple scattering, Compton scattering, pair production processes, showering in detector materials and hadronic interactions. The information is stored in the form of *hits*. A simulated hit combines information about energy depositions in the detector, their magnitude, the time at which they occur and their location. The information stored in a hit is detector-dependent and contains all the details needed to simulate the detector response. For tracking detectors (inner Tracker and Muon system) for example the information stored is the entry and exit points of the track, the momentum vector at the entry point, the type of the particle, the energy loss in the sensitive volume, and the time offset with respect to the Trigger interaction time.

In addition to the hits, OSCAR also produces simulated tracks (SimTracks) and vertices. These are not used for detector response simulation or for reconstruc-

tion, but are required for analysis of the reconstruction results. The simulated trajectories covered by the particles are indeed stored to be used in testing of the algorithms as *Monte Carlo truth*. The average size of a simulated event file is 2 MB and the CPU time required to simulate one event ranges from 60 s for a pure minimum bias event to a maximum of 500 s for inclusive 1 TeV di-jet events, if using a 1 GHz Pentium III CPU.

The response of the detector is simulated taking into account the pile-up events of the actual and the contiguous bunch crossings, the number of bunch crossings to be piled up being determined by the subdetector with the slowest response time. Pile-up events from the previous 5 and following 3 bunch crossings are superimposed to the on-time crossing in order to mimic the electronic readout behavior and to take into account the energy pile-up in calorimeters. Pile-up events are randomly added from a minimum bias data base, which contains 200 000 events, separately for low and high luminosity, according to Poisson distributions around the central values calculated in Section 2.1, which are 5 and 25 respectively. The recycling of the same minimum bias events for pile-up is due to the limited available CPU resources used to massively produce them.

After combining a signal event with the selected pile-up events for a particular luminosity, the detector response is simulated taking into account the `SimHits` of all events of a crossing. The time information of each hit is shifted according to the bunch crossing to which the corresponding event belongs. The finite response time and time resolution of the CMS subdetectors defines for each of them a time window of sensitivity, ranging from a few tens of nanoseconds to several hundred nanoseconds. To simulate the full detector response and occupancy, simulated hits in the full time interval of sensitivity need to be taken into account. The final products are the digitized hits (*digis*), which are used as input for the Trigger simulation or the reconstruction programs. The digis are equivalent to the raw data collected by CMS when real data taking will be operational. Digitization is performed independently for low and high luminosity simulations.

4.3 Track reconstruction

Due to the complexity of the CMS Tracker, with its tens of thousands of detector modules, tens of millions of channels, and tens of thousands of hits per bunch crossing, it is not obvious that there is a single optimal track reconstruction algo-

rithm in all circumstances. It is more likely that there should be several specific algorithms, each of them optimized for a specific task within the complex physics at CMS. Therefore a flexible framework for developing and evaluating track reconstruction algorithms is used.

The CMS track reconstruction framework is based on the `KalmanFilter` formalism [75], but not restricted to it. More advanced algorithms, like the `DeterministicAnnealingFilter` [76] or the `MultiTrackFilter` [77] have been successfully implemented as well. In the case of the Kalman filter formalism, the basic operations are propagation of a trajectory state to some surface, and updating of a trajectory state with information from a measurement.

4.3.1 The Kalman filter

The basic object in the implementation of the track reconstruction in `ORCA` is the `RecHit`, which contains the information of the position of the hit and the corresponding errors expressed in different coordinate frames: the measurement frame (a strip, a pixel cell), the local frame (the surface of a detector) and the global CMS frame. The `RecHits` are created from digis and in testing the performance of the reconstruction algorithms it is useful to associate them to the corresponding simulated hits, or `SimHits`. This is done with some hit association criteria, based on information produced during digitization.

The basic object in track reconstruction is the `TrajectoryStateOnSurface`, usually referred to as `TSOS`, which contains the local and global position and direction of the track together with the curvature and the covariance matrix of track parameters. A reconstructed track (`RecTrack`) in the tracker is a sequence of `RecHits` propagated from a surface to another by updating the `TSOS` state with a geometrical extrapolation. The trajectory is fitted to the track model, depending on the shape of the magnetic field, taking into account measurements and errors of the `RecHits` and the stochastic model of material effects (multiple scattering, energy loss). Hence the track fitting requires the knowledge of the detector layout and resolution together with the model describing the trajectory of a particle.

At this level the software is the same for reconstruction of either Monte Carlo tracks or true tracks, because they are reconstructed from `RecHits`, which are digis in case of Monte Carlo events or the raw data when CMS will be turned on. Of course all the operations related to associations of reconstructed with simulated

objects are excepted.

Any RecTrack can be associated with a set of compatible simulated tracks in the tracker (TkSimTracks) by means of a track associator. A TrackAssociatorByHits associates a RecTrack to a TkSimTrack if the number of RecHits associated to the SimHits is greater than a given fraction of the total. Usually this threshold is set to 50%, hence a RecTrack is associated to a TkSimTrack if it shares more than 50% of its RecHits with the simulated track SimHits. This method is useful in studying track reconstruction efficiency and *fake track* rate of the track finding algorithms (fake tracks are reconstructed tracks whose hits are produced by the detector noise and which are not associated to any SimTrack).

The simplest, but probably the more robust, track reconstruction algorithm developed within ORCA is based on the Kalman filter (CombinatorialTrackFinder) a recursive procedure to estimate the states of a dynamic system, a stochastic model evolving in time. It is mathematically equivalent to a global least-squares minimization (LSM). The Kalman filter allows also to incorporate multiple scattering and energy loss during track propagation.

The design and implementation of the Kalman filter in ORCA is modular [78], a ModularKfReconstructor being composed with four C++ classes dealing with different tasks, which interplay with each other. The four objects for track reconstruction in ORCA are

- SeedGenerator generator of seeds, the trajectory starting values;
- TrajectoryBuilder building of the trajectories starting from the seeds;
- TrajectoryCleaner resolution of ambiguities among multiple reconstructed trajectories;
- TrajectorySmoother smoothing of the trajectories, better estimation of the track parameters.

Seed generation

A charged track can be described by five parameters: two positions, the transverse (z_0) and longitudinal (d_0) impact parameter with respect to the interaction point, two directions, the pseudorapidity η and the azimuthal angle ϕ, and finally the transverse momentum p_{T}.

Seed generation provides initial trajectory candidates with an estimation of those five parameters and their errors. Usually seeds consist of pairs of `RecHits` and use a beam spot constraint and a minimal transverse momentum constraint to provide initial trajectory parameters. The beam spot constraint may introduce a bias at this stage, which is removed during the final fit.

A reduced set of data is investigated in order to define those starting values of potential track candidates. The seeds can be extracted by measurements in muon chambers or calorimeters or by pixel hits. They are useful to reduce the parameter space where to look for further hits to add to the trajectory candidate, because they allow a preliminary rough estimate of the track parameters. The choice of the size of the set of data can have dramatic effect on the reconstruction efficiency, fake rate, and CPU time. If the size is too small the track reconstruction efficiency will suffer; if the size is bigger than the physics requirements, additional CPU time will be wasted to reconstruct ghost tracks that will have to be removed with additional track selection criteria. In a similar way, the choice of the minimal transverse momentum has a strong influence on the number of seeds, and even more on the overall CPU time, since it takes longer to reconstruct a soft track than a hard track.

The `CombinatorialSeedGeneratorFromPixel` is used to create seeds from the pixel detector layers. In Fig. 4.2 the principle of seed generation is sketched: all the pairs of hits compatible from being generated by a track originated from the beam spot (a cylinder of 0.1 cm radius and 15 cm long centered in the CMS reference frame origin) and with a minimum p_{T} of 0.9 GeV/c are selected to form the seeds to propagate from inside out through the Tracker layers. Starting from each `RecHit` from the pixel outer layer, the inner `RecHits` compatible with the searched trajectory are linked with the starting one to form a seed.

The pixel layers are therefore essential for fast and accurate track reconstruction. In case of staging of some of them, the innermost double-sided Silicon Strip layers are used. For the baseline Pixel detector (three barrel and two endcap layers on each side), all pairs of layers are used to provide a high degree of redundancy and efficiency.

Trajectory building

In the trajectory builder the seeds are transformed into a set of trajectory candidates. The `CombinatorialTrajectoryBuilder` works in two steps. First the

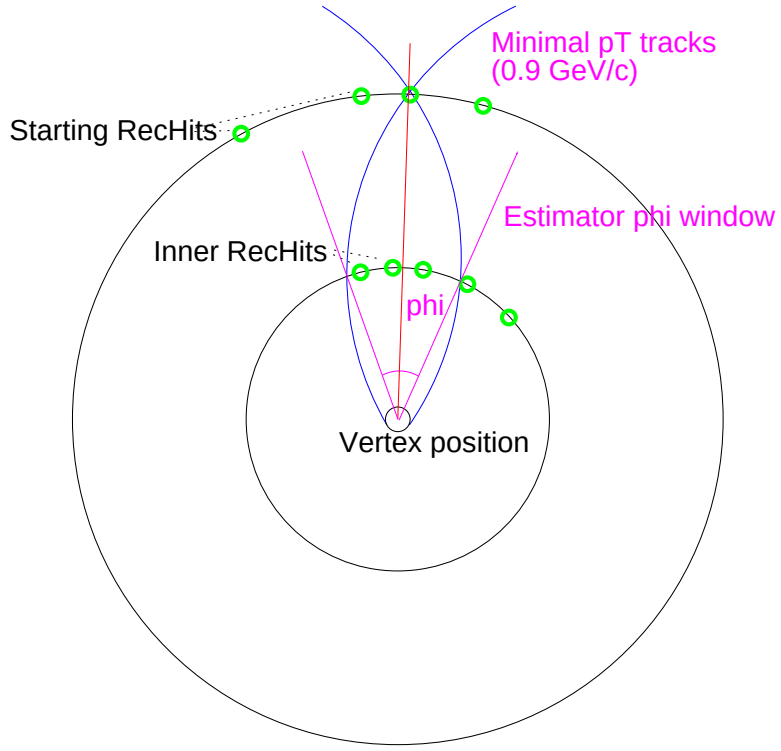

Figure 4.2: Principle of operation of the `CombinatorialSeedGeneratorFromPixel` seed generator.

compatible layers for the propagation of a trajectory candidate are selected (navigation) and then `RecHits` belonging to these layers are consistently added. A combinatorial search of compatible hits is performed. At this stage the trajectory candidates could be more than one per seed.

This part of the track reconstruction is the most expensive in terms of computing power. Even if the search for compatible `RecHits` is optimized for each layer, the combinatorial growth of the number of candidates has to be limited to prevent the `CombinatorialTrajectoryBuilder` from taking an arbitrarily large computing time and memory. In propagating the trajectory candidates from layer to layer it is possible to split a single candidate into two or more candidates if two or more different `RecHits` can be accepted. In this way the number of the trajectories to propagate could grow rapidly for some complex events.

To avoid the explosion of the algorithm, a maximum number of trajectory can-

didates with $p_T > 0.9$ GeV/c is propagated to the following layer starting from the present one (the best N, typically five, candidates in term of χ^2). This procedure goes on until the absence of compatible layers (for instance the Tracker is ended) or compatible hits (typical for fake tracks) occurs. If two consecutive layers with no compatible hits are found, the propagation is immediately stopped. Additional stopping conditions can be inserted, as the maximum number of `RecHits` to be added to each `RecTrack` to perform conditional tracking developed for High-Level Trigger purposes.

Trajectory cleaning

In the combinatorial trajectory building the possibility to reconstruct trajectories sharing a certain number of `RecHits` or the same seed is inherently. The ambiguities of multiple reconstructed trajectories are solved by the trajectory cleaner. The `TrajectoryCleanerBySharedHits` gathers together the mutually exclusive ones from the sample of all the reconstructed trajectories and discards for each set all but the best one, which is defined as the trajectory with the best value of χ^2 normalized to the degrees of freedom. Trajectory cleaning is invoked on all surviving candidates from all seeds, since trajectories from two different seeds can also be mutually exclusive.

Trajectory smoothing

After trajectory building and cleaning, the parameters of each surviving trajectory are fully known at the last measurement (typically at the outer layers of the tracker), but are very poorly determined at the origin. A *backward fit* of the same hits as in the forward fit, but starting from outside, gives optimal knowledge of the parameters at origin, but loses the knowledge at the outer layers. In the Kalman formalism, the procedure of combining the forward and backward fits in a statistically correct way (without double counting) is called *smoothing*. The Kalman filter smoother (`KFFittingSmoother`) performs the statistical combination of the track parameters at every measurement surface along the track, fully including all other measurements, and yields a χ^2 probability of the track which is more reliable than after a forward or a backward fit. At this stage any possible bias introduced by the beam spot constraint of the seed can be removed by repeating the forward fit starting from the first measurement. The track parameters at the

interaction point, at the Calorimeter surface, or at any other surface are computed by extrapolation (propagation) from the nearest measurement on the track.

4.3.2 Regional track reconstruction

A strategy to speed up the reconstruction is the Regional Track reconstruction. The seeds of the muon chambers are used to define a geometrical region in the Tracker, typically a cone, called *region of interest*. The cone axis is given by the momentum direction, while the width of the cone is proportional to the momentum estimation and inversely proportional to the direction error. Inside the region defined by this cone a standard reconstruction is performed. The track propagation time is reduced because a large part of the detector is excluded in the track reconstruction.

4.3.3 Influence of Tracker material on track reconstruction

Track reconstruction is based upon the equations of motion of a charged particle in a magnetic field. In the standard Kalman filter the evolution of the state vector and its covariance matrix is determined. This simple model has to be modified in the presence of matter: deterministic effects are included in the track model, stochastic processes result in additional contributions to the covariance matrix (*process noise* in the terminology of dynamic systems). In order to speed up the reconstruction, the material of the tracker is described in a simplified way

- all material is assumed to be concentrated on thin surfaces and these surfaces coincide with the active elements;
- the material properties of each detector layer are described by two numbers: the thickness in units of radiation length, and the thickness multiplied by the mean ratio of atomic number to atomic mass.

Two kinds of effects are taken into account: energy loss (for electrons due to bremsstrahlung, for all other particles due to ionization), and multiple scattering. Ionization energy loss is described according to the Bethe-Bloch formula without density corrections [79]; the average and variance of the fractional energy loss of electrons due to radiation are computed based on the p.d.f. given by Bethe and

Heitler [80]. The effect of multiple scattering is calculated using the approximation for the gaussian core given by Highland [79].

As explained above, the effects due to the presence of material only enter the propagation stage of the Kalman filter. The track propagation is thus divided into two parts: a purely geometrical extrapolation and an update of track parameters and their covariance matrix at the destination surface. The mean energy loss $\langle dE \rangle$ results in a change of the predicted momentum, while the spread of the energy loss and the deflection due to multiple scattering modify the covariance matrix. Corrections to the path length due to the angle of incidence are also taken into account and applied both in the forward and, reverting the sign of $\langle dE \rangle$, in the backward filter.

The simplified treatment of the material is valid only inside the Tracker volume. Propagation to the Muon system requires detailed knowledge of the passive material. Currently the propagations outside of the Tracker volume are performed with the `GEANE` package [81], which uses the full simulation geometry.

4.3.4 Track reconstruction performance

The track reconstruction efficiency when using the `CombinatorialTrajectoryBuilder` has been estimated for samples of single muons with $p_{\mathrm{T}} = 1$, 10 and 100 GeV/c. A track is deemed to be successfully reconstructed if it shares more than 50% of the hits with a simulated track. Reconstructed tracks are required to have at least eight hits.

The tracking performance is expressed in terms of efficiency and momentum resolution; two efficiencies are then defined. The *algorithmic efficiency* (Fig. 4.3, left plot) is the efficiency of reconstructing correctly tracks which have at least eight hits in the Tracker, of which at least two are in the pixel detector

$$\epsilon_{algo} = \frac{\text{num. reco. tracks with eight hits}}{\text{num. sim. tracks with eight hits}} \,. \tag{4.1}$$

This measures directly the performance of the track reconstruction algorithm and is essentially the efficiency of the trajectory builder, since the seed generator is fully efficient. The *global efficiency* (Fig. 4.3, right plot) is the reconstruction efficiency for all tracks

$$\epsilon_{glo} = \frac{\text{number reconstructed tracks}}{\text{number simulated tracks}} \,. \tag{4.2}$$

In addition to the efficiency of the algorithm, it includes the acceptance, hit efficiency and any other factor influencing reconstruction. It mainly differs from the algorithmic efficiency in the forward region, with the loss of coverage of the disks, especially in the pixel system.

As the algorithmic efficiency shows, the trajectory builder is fully efficient in the full pseudorapidity range, with a drop beyond $|\eta| = 2.4$ due to the lack of coverage of the endcap disks. For the global efficiency, the drop in the region at $\eta \sim 0$ is due to the gaps between the two half barrels of the pixel at $z = 0$. As the gaps for the three layers are aligned, this will cause some tracks not to have the two required pixel hits. At high pseudorapidity, the drop of efficiency is mainly due to the lack of coverage of the two pairs of forward/backward pixel disks.

The resolution on the transverse momentum is shown instead in Fig. 4.4. At high momentum (100 GeV/c), the resolution is around 1-2% up to a pseudorapidity of $|\eta| = 1.75$, for higher values of $|\eta|$ the lever arm of the measurement is reduced resulting in a worse resolution. The degradation around $|\eta| = 1.0$ is due to the gap between the barrel and the endcap disks and the degradation beyond $|\eta| = 1.1$ is due to the lower hit resolution of the last hits of the track measured in the TEC ring 7 with respect to the hit resolution in the TOB layers 5 and 6.

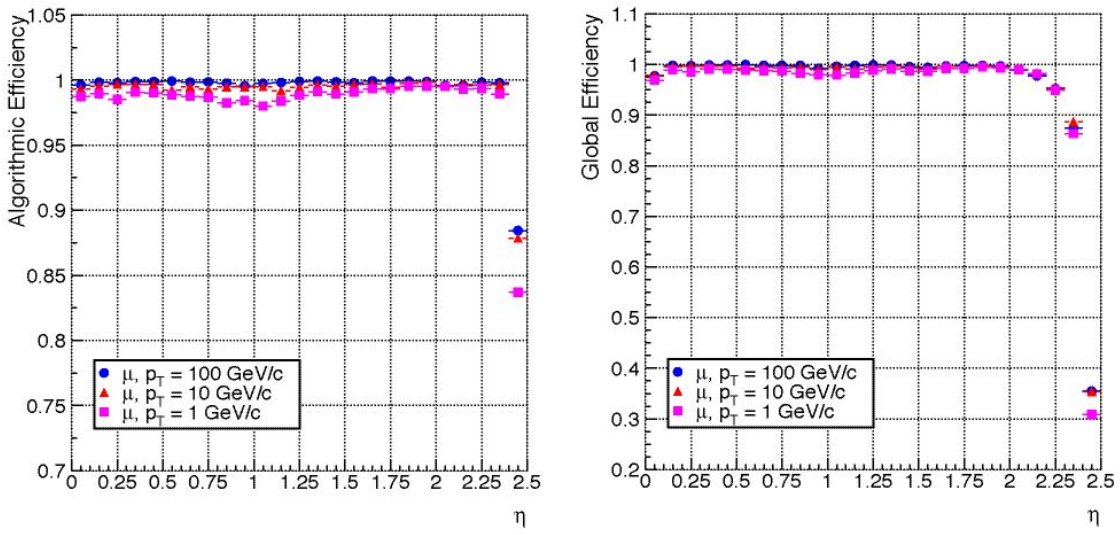

Figure 4.3: Algorithmic (left) and global (right) track reconstruction efficiency for single muons using the Tracker only [40].

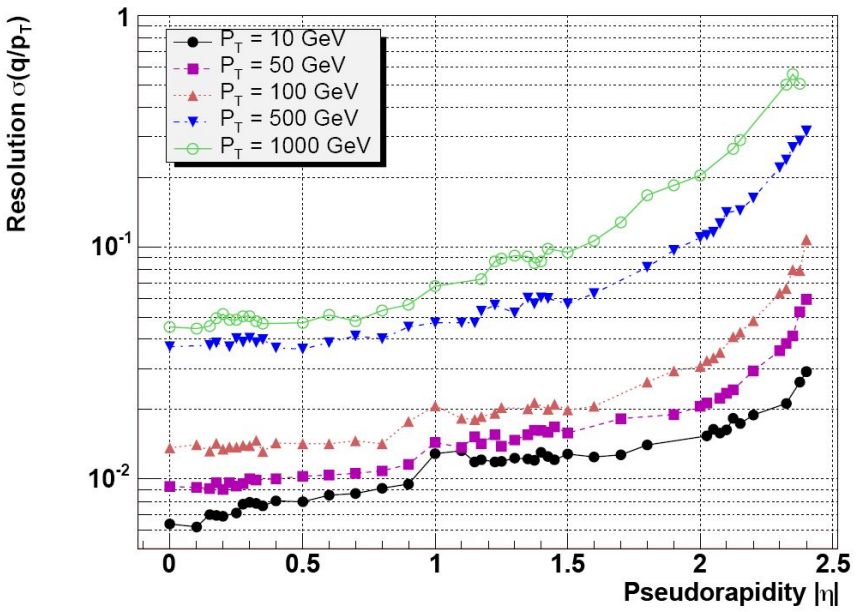

Figure 4.4: Resolution of the p_{T} for single muons with transverse momentum between 10 and 1000 GeV/c using the combined Muon system and Silicon Tracker reconstruction as a function of pseudorapidity [82].

At a transverse momentum of 100 GeV/c, the material in the tracker accounts for between 20 and 30% of the transverse momentum resolution; at lower momenta, the resolution is dominated by multiple scattering and its distribution reflects the amount of material traversed by the track.

4.4 Muon reconstruction

While track reconstruction starts from the inner region, muon reconstruction proceeds outside-in. The low occupancy in the muon chambers allows an easy and fast muon reconstruction for Trigger puproses, but the momentum estimation, given by the muon chambers only, is too rough for analysis and for the fast Trigger decision. Muon tracks have to be reconstructed using the whole detector information and particularly the Tracker data in order to exploit the excellent momentum resolution achievable with the 4 T magnetic field.

The muon reconstruction thus proceeds in two steps: first, muons are fully reconstructed in the muon chambers; next, the muon trajectories are extended into the tracker to further refine the p_{T} measurement. Both steps are performed by the High-Level Trigger and have been called respectively Level-2 and Level-3 reconstruction or Standalone and Global in offline reconstruction.

Isolation criteria can also be applied to the muon candidates to provide additional rejection: at Level-2 using the calorimetric energy sum in a cone around the muon, and at Level-3 using the number of pixel tracks in a region around the projected muon trajectory. This suppresses non-prompt muons from b, c, π, and K decays.

4.4.1 Muon Standalone reconstruction and Level-2 selection

Reconstructed track segments from the muon chambers are used for muon identification and selection at Level-2. The state vectors (track position, momentum and direction) associated with the segments found in the innermost chambers are propagated outwards through the iron yoke using the `GEANE` package, which takes into account the muon energy loss in the material, the effect of the multiple scattering, and the non-constant magnetic field in the muon system.

The estimate of the momentum from the Level-1 Global Muon Trigger is used initially for the track propagation in the magnetic field. The predicted state vector at the next measurement surface is compared with existing measured points and updated accordingly using the Kalman filter technique already described for the Tracker. In the barrel chambers, reconstructed track segments are used as measurements in the Kalman filter procedure; in the endcap chambers, where the magnetic field is inhomogeneous, the individual reconstructed hits belonging to the track segments are used.

The procedure is iterated until the outermost measurement surface of the muon system is reached, when a constrained fit to the track parameters, working from the outside-in, is performed under the assumption that the muon candidate originated from the interaction region (defined by the beam spot size: $\sigma_x = \sigma_y = 15$ μm and $\sigma_z = 5.3$ cm). In both the forward and backward propagations just described, a measurement is not added to the muon trajectory if its contribution to the total χ^2 exceeds 25. The resulting track parameters, propagated inward to the collision

vertex, are used to reject or accept the event for further Level-3 processing [83].

For offline reconstruction a different seed generation algorithm has been developed, which performs local reconstruction in the whole Muon system and uses patterns of segments reconstructed in CSC and/or DT chambers as initial seeds.

Figure 4.5 shows Level-2 constrained fit as expressed by standard deviation of the quantity $1/p_{\mathrm{T}}$.

$$\frac{d(1/p_{\mathrm{T}})}{(1/p_{\mathrm{T}})} = \frac{(1/p_{\mathrm{T}}^{rec} - 1/p_{\mathrm{T}}^{gen})}{(1/p_{\mathrm{T}}^{gen})}\,, \tag{4.3}$$

where p_{T}^{gen} and p_{T}^{rec} are the generated and reconstructed transverse momenta, respectively. Muons from W decays at high luminosity are used as the reference sample. The distributions are broken up into three pseudorapidity intervals: barrel ($|\eta| < 0.8$), overlap ($0.8 < |\eta| < 1.3$) and endcap ($1.3 < |\eta| < 2.1$). In these three regions, the fitted p_{T} resolutions are 10%, 15%, and 16%, respectively.

4.4.2 Global and Level-3 selection

Starting from a Level-2 or Standalone reconstructed muon, respectively in online or offline case, the muon trajectory is extrapolated from the innermost muon station to the outer Tracker surface, taking into account the muon energy loss in the material and the effect of multiple scattering.

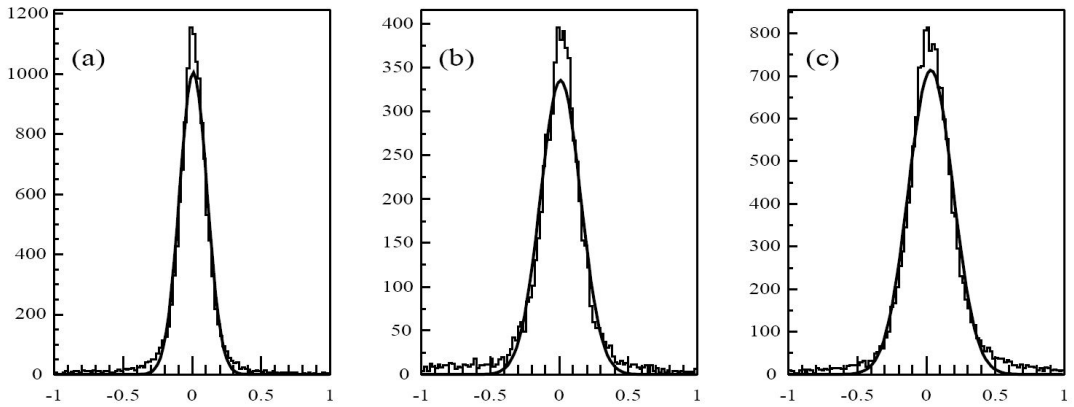

Figure 4.5: Relative error on $1/p_{\mathrm{T}}$ after Level-2 muon reconstruction. The distributions are broken up into three pseudorapidity intervals: barrel ($|\eta| < 0.8$), overlap ($0.8 < |\eta| < 1.3$) and endcap ($1.3 < |\eta| < 2.1$) [40].

As with Level-2/Standalone, the GEANE package is currently used for the propagation through the iron and calorimeters. Silicon layers compatible with the muon trajectory are then determined, and a region of interest within them is defined to perform regional track reconstruction. The determination of the region of interest is based on the track parameters and uncertainties of the extrapolated Level-2/Standalone muon trajectory, obtained with the assumption that the muon originates from the interaction point as described in the previous section. This has a strong impact on the reconstruction efficiency, fake rate, and CPU reconstruction time: well measured muons are reconstructed faster and with higher efficiency than poorly measured ones. Inside the region of interest, initial candidates for the muon trajectory (regional seeds) are built from pairs of reconstructed hits, and starting from these seeds a regional track reconstruction algorithm based on the Kalman filter technique is used to reconstruct tracks inside the selected region of interest. Figure 4.6 shows the relative error on the transverse momentum determined by the Level-3 constrained fit. Muons from W decays at high luminosity are used as the reference sample. The distributions are broken up into three pseudorapidity intervals: barrel ($|\eta| < 0.8$), overlap ($0.8 < |\eta| < 1.3$) and endcap ($1.3 < |\eta| < 2.1$). In these three regions, the fitted p_{T} resolutions are 1.0%, 1.4%, and 1.7%, respectively, thus the improvement over the Standalone muon measurement from Level-2 is substantial.

The efficiency of the Global tracking algorithm is shown in Fig. 4.7 as a function of η for single muons with $p_{\mathrm{T}} > 50$ GeV/c and no pile-up. The muons were generated with four flat distributions in p_{T} up to 1000 GeV/c. The achieved algorithmic efficiency is typically $95 \div 99\%$, except in the regions where the muon traverses cracks in the geometry, less hits are available and the efficieny drops. This effect is visible in the pseudorapidity regions around $|\eta| = 0.25$ and $|\eta| = 0.75$ (the regions between two wheels) and around $|\eta| = 1.2$, where the DT and CSC systems overlap.

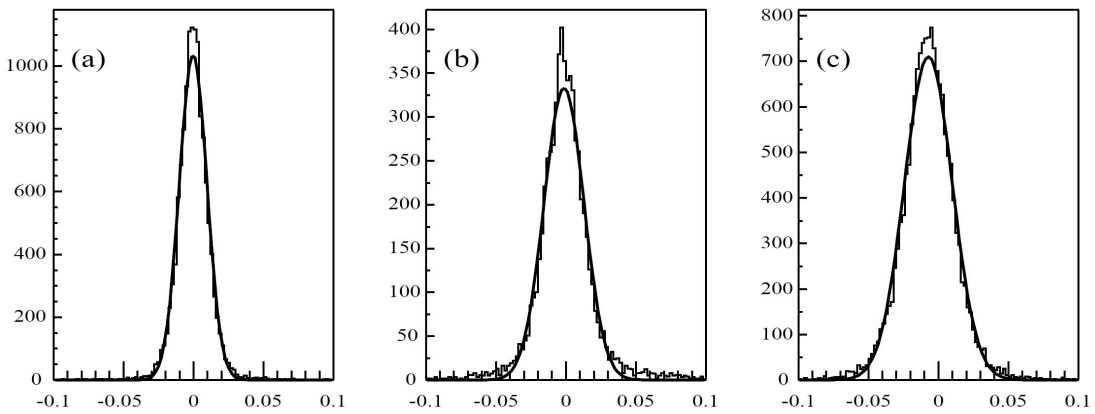

Figure 4.6: Relative error on $1/p_{\mathrm{T}}$ after Level-3 muon reconstruction. The distributions are broken up into three pseudorapidity intervals: barrel ($|\eta| < 0.8$), overlap ($0.8 < |\eta| < 1.3$) and endcap ($1.3 < |\eta| < 2.1$) [40].

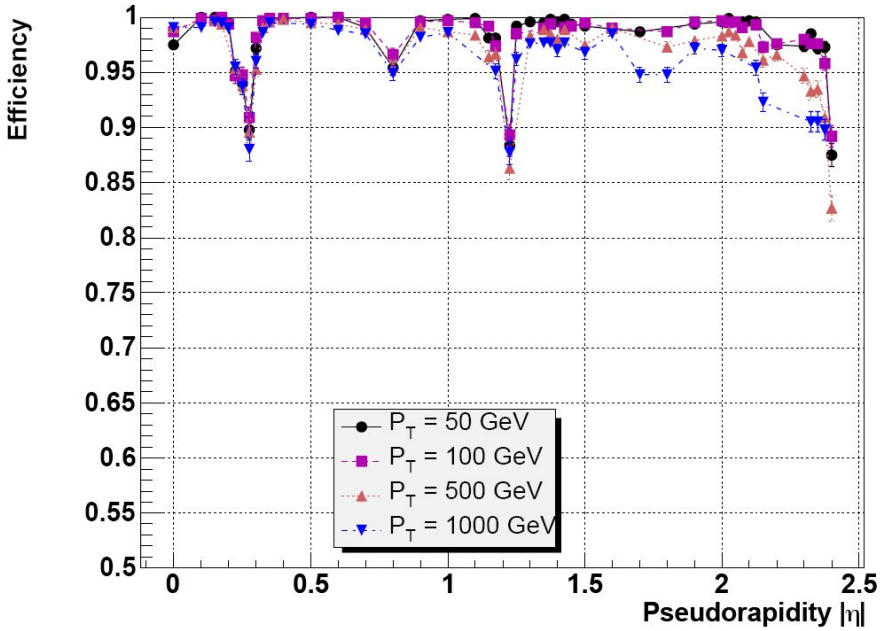

Figure 4.7: Efficiency of the Global tracking algorithm as a function of η for single muons generated with a flat p_{T} distribution over $50 < p_{\mathrm{T}} < 1000$ GeV/c [82].

Chapter 5

Standard Model Higgs Boson Physics at LHC

In this Chapter the production mechanisms, the decay channels of the Higgs boson at LHC and the search strategies for different mass regions are reported.

5.1 Higgs boson production

For all possible Higgs boson masses the dominating Higgs boson production mechanism at the LHC is the gluon fusion process whose Feynman diagram is shown in Fig. 5.1a. The other processes shown in Fig. 5.1 are also of interest because of the special signatures they can provide for the identification of the Higgs boson. In Fig. 5.2 the cross section is shown as a function of the Standard Model Higgs boson mass. At the higher masses a significant part of the cross section is from vector boson fusion.

5.1.1 Gluon fusion: $gg \rightarrow H$

The gluon fusion process for Higgs boson production, shown in Fig. 5.1a, can be calculated from the width of the $H \rightarrow gg$ decay and the gluon structure function. The loop is totally dominated by the top quark because of the strong Higgs boson coupling to the heavy top quark. The cross section for the basic gluon to Higgs boson process is [84]

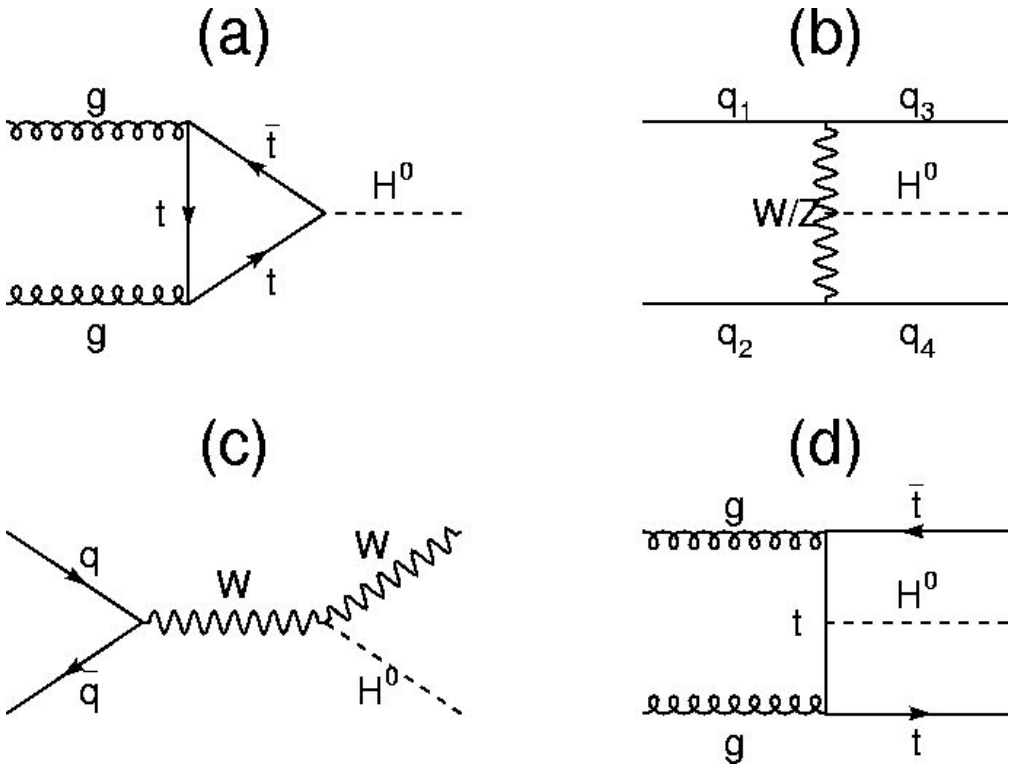

Figure 5.1: The dominant Standard Model Higgs boson production mechanisms in hadronic collisions. (a) Gluon fusion (b) vector boson fusion (c) and (d) associated production.

$$\sigma(\mathrm{gg} \to \mathrm{H}) = \frac{G_\mu \alpha_S^2(\mu_R^2)}{288\sqrt{2}\pi} \left| \frac{3}{4} \sum_q A_{1/2}^H(\tau_Q) \right|^2 , \tag{5.1}$$

where $A_{1/2}^H(\tau_Q)$ with $\tau_Q = \mathrm{M_H^2}/4\mathrm{m_q^2}$ is a form factor [15].

The lowest order cross section has large corrections from higher order QCD diagrams. The increase in cross section from higher order diagrams is conventionally defined as the K-factor

$$K = \frac{\sigma_{HO}}{\sigma_{LO}} , \tag{5.2}$$

where LO (HO) refer to lowest (higher) order results. The K-factor for gluon

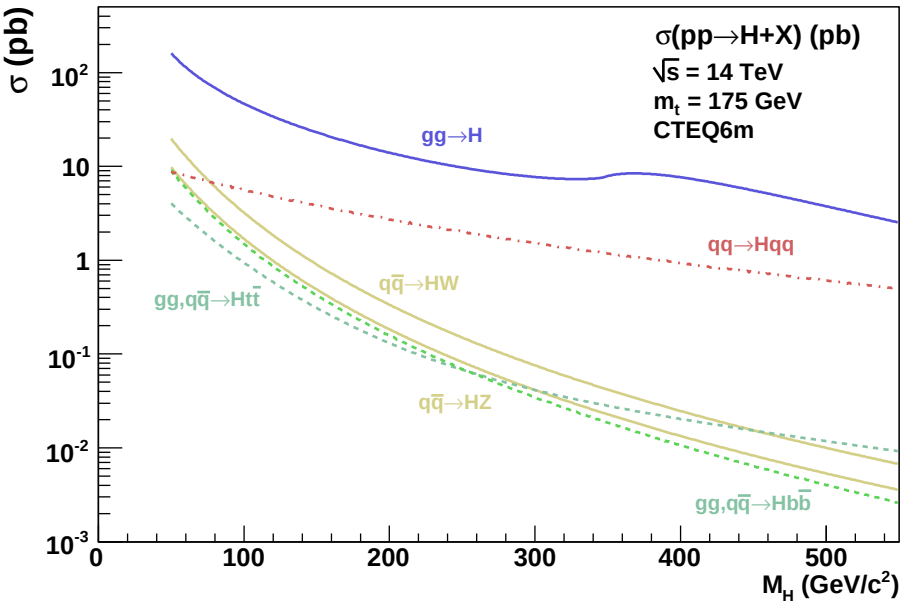

Figure 5.2: Production cross section of the Standard Model Higgs boson as a function of its mass for the main processes. The cross sections are calculated using HIGLU and other programs [86]; they contain higher order corrections and the CTEQ6m [87] p.d.f. has been adopted.

fusion is evaluated in Ref. [85] with a next-to-leading order calculation and K results between 1.5 and 1.8.

The value of the cross section including the K-factor has two main uncertainties. The first is from the gluon structure function which still has large uncertainty in the low x region. The cross section using a large set of todays best available structure functions was calculated in Ref. [88] and the results differ by around 20% which can be taken as the theoretical unertainty from gluon structure function. At the time of data taking for LHC it can be expected to have much better structure functions available with data from HERA [89] and the Tevatron [90].

The second uncertainty in the gluon fusion cross section is from corrections above the next-to-leading order. The cross section changes with the renormalization scale μ as an effect of un-calculated higher order diagrams. By changing μ between $M_H/2$ and $2M_H$ it can be guessed that the remaining uncertainties from

higher order effects are below 15% [91].

The production of the Higgs boson through gluon fusion is sensitive to a fourth generation of quarks. Because the Higgs boson couples in proportion to the fermion mass, a heavier generation of quarks is not suppressed in the process as would be expected for a loop process with a heavier particle in the loop. Including a fourth generation of very heavy quarks will more than double the cross section. This has the consequence that the Higgs boson cross section is sensitive to a fourth generation of quarks even if the quarks are too heavy for a direct discovery at the LHC.

5.1.2 Vector boson fusion: $qq \to qqV^*V^* \to qqH$

The process of Higgs boson production through vector boson fusion shown in Fig. 5.1b is important only for high Higgs boson masses where the coupling to longitudinal polarized vector bosons is strong.

At the high energies where a heavy Higgs particle is created, the vector bosons act essentially as massless particles and can be treated as particles present inside the colliding protons. With this simplification the full process in Fig. 5.1b can be separated into a calculation of the vector boson structure function in the proton and a calculation of Higgs boson production in colliding vector boson beams. The method is called the effective W approximation. The production of a Higgs boson is dominated by the longitudinal polarized state and the small contribution from the transverse polarized state can be ignored.

Following the derivation in Ref. [92] the cross section for production of a Higgs boson in the fusion of two vector bosons can be written as

$$\sigma(q_1 q_2 \to q_1' q_2' H) = \frac{16\pi^2}{\hat{s} M_H} \sum_{V=W,Z} \int_{M_H^2/\hat{s}}^1 \frac{dx}{x} F_V(x) F_V(\frac{M_H^2}{\hat{s}x}) \Gamma_V(H \to VV)\,, \qquad (5.3)$$

where F_V is the structure function for the vector boson V with partial width Γ_V in the longitudinal polarized state and q_1', q_2' denoting the two outgoing quarks.

To get the full cross section for the Higgs boson from vector boson fusion the cross section above has to be convoluted with the structure functions of the incoming quarks. For all possible values of the Higgs boson mass the cross section is below the gluon fusion process, but with the additional signature of the two

outgoing quarks participating in the process the identification could be easier in this production channel.

5.1.3 Associated production

Even if the cross sections for the associated Higgs boson production shown in Fig. 5.1c and 5.1d are low compared to the total Higgs boson cross section, they can be of interest since the final states have some clear signatures.

The associated production with a W vector boson was first mentioned in Ref. [93]. For a Higgs boson mass of 150 GeV/c^2 the production cross section is around 1 pb or 4% of the gluon fusion cross section. With the present structure functions available the uncertainty in the cross section is around 30%.

The other associated production of interest is the $t\bar{t}H$ process. The cross section was first calculated in Ref. [94]. For Higgs boson masses below 200 GeV/c^2 the cross section is about a factor 5 below the cross section for associated production with a W, while for masses above 500 GeV/c^2 it is greater than the WH cross section but is still far below the gluon fusion cross section.

5.2 Higgs boson decay

With the Higgs boson decaying directly into pairs of all massive particles and through loop diagrams even into pairs of massless gluons and photons, the spectrum of Higgs boson signatures is large. After a discovery of a Higgs particle it will be important to detect it in several decay channels to check if the coupling strength is proportional to the fermion mass as the Standard Model predicts.

The total width and the branching ratios are plotted in Fig. 5.3 and Fig. 5.4. They are calculated with the program `HDECAY` [95] which includes the dominant higher order corrections to the decay width.

As shown in Fig. 5.4, the branching ratios change dramatically across the possible range of the Higgs boson mass requiring different strategies for the Higgs particle identification depending on its mass.

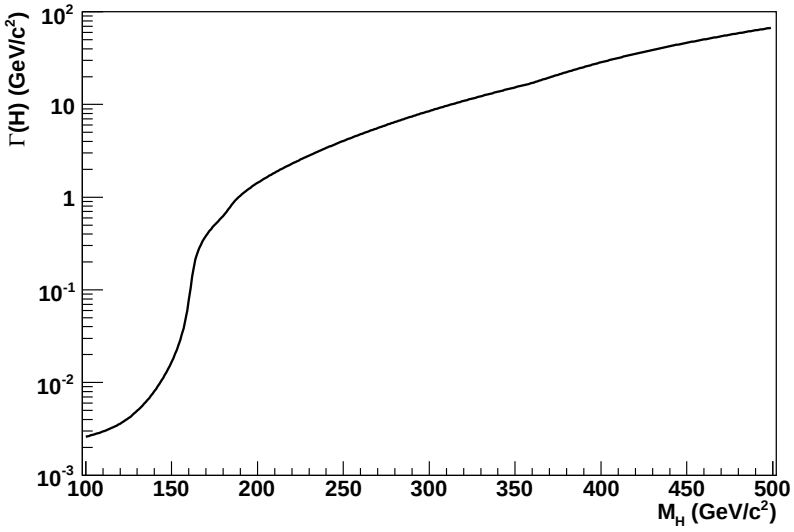

Figure 5.3: The Standard Model Higgs boson total decay width as a function of M_H.

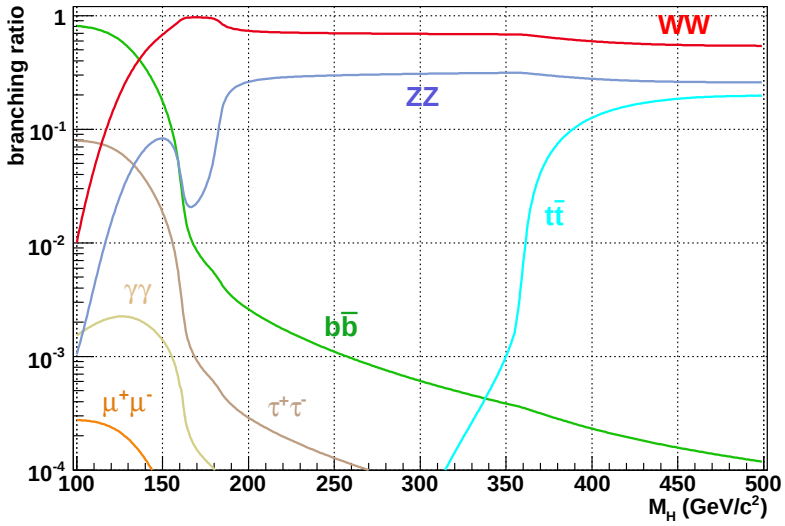

Figure 5.4: The decay branching ratios of the Standard Model Higgs boson into the main channels as a function of its mass.

5.2.1 Fermionic decays

In the Born approximation, the partial width of the Higgs boson decay into fermion pairs, whose diagram is shown in Fig. 5.5, is given by [96]

$$\Gamma_{Born}(\mathrm{H} \to \mathrm{f\bar{f}}) = \frac{G_\mu N_c}{4\sqrt{2}\pi} \mathrm{M_H m_f^2} \beta_f^3 \,, \tag{5.4}$$

with $\beta_f = (1 - 4\mathrm{m_f^2}/\mathrm{M_H^2})^{1/2}$ being the velocity of the fermions in the final state and N_c the colour factor $N_c = 3(1)$ for quarks (leptons). The Higgs particle couples to all fermions proportionally to their mass so the coupling to a pair of top quarks is by far the strongest. If the Higgs boson mass is below twice the top mass the dominant fermionic decay will be to bottom quarks. In the lepton case, only decays into $\tau\tau$ pair and, to a much lesser extent, decays into muons pair are relevant.

In the case of the hadronic decays of the Higgs boson, the QCD corrections turn out to be quite large and therefore must be included. At one loop level the gluon exchange and the emission of a gluon in the final state should be included. The Feynman diagrams for these corrections are shown in Fig. 5.6. In the limit $\mathrm{M_H} >> 2\mathrm{m_f}$, the next-to-leading order decay width is [97]

$$\Gamma(\mathrm{H} \to \mathrm{q\bar{q}}) = \frac{3G_\mu}{4\sqrt{2}\pi} \mathrm{M_H m_q^2} \left[1 + \frac{4\alpha_s}{3\pi} \left(\frac{9}{4} + \frac{3}{2} \log \frac{\mathrm{m_q^2}}{\mathrm{M_H^2}} \right) \right] . \tag{5.5}$$

As can be seen, there is a large logarithmic $\log(\mathrm{m_q}/\mathrm{M_H})$ contribution which, for light quarks, might render the partial decay width very small. These large logarithms, however, can be absorbed in the redefinition of the quark masses: by using the running quark mass in the $\overline{MS}$ scheme at the scale of the Higgs boson mass, these logarithms are summed to all orders in the strong interaction coupling

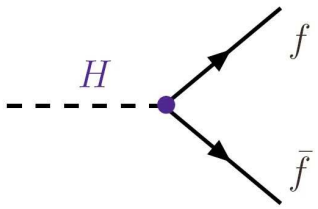

Figure 5.5: Leading order Feynman diagram for the decay process of the Standard Model Higgs boson into a pair of fermions.

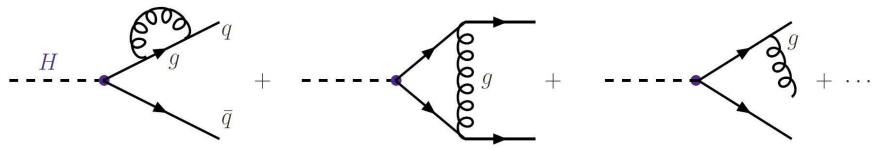

Figure 5.6: Some of the higher order corrections to the decay channel of the Standard Model Higgs boson into two fermions.

constant. The partial Higgs boson decay widths for light quarks can then be written as [97]

$$\Gamma(\mathrm{H} \to \mathrm{q\bar{q}}) = \frac{3G_\mu}{4\sqrt{2}\pi}\mathrm{M_H}\overline{m}_q^2(\mathrm{M_H})\left[1 + \Delta_{\mathrm{q\bar{q}}} + \Delta_{\mathrm{H}}^2\right] , \tag{5.6}$$

with the running quark mass $\overline{m}_q$ and the strong coupling constant defined at the scale $\mathrm{M_H}$.

Since the values of the running b and c quark masses at the scale $\mu \approx \mathrm{M_H} = 100\ \mathrm{GeV/c^2}$ are typically, respectively, a factor 1.5 and a factor 2 smaller than the pole masses, the partial decay widths are suppressed by large factors compared to the case where the pole masses are used.

For Higgs bosons decaying into top quarks, the QCD corrections do not lead to large logarithms since $\mathrm{m_t}$ is comparable to $\mathrm{M_H}$. These corrections however can be sizable, in particular near the threshold $\mathrm{M_H} \approx 2\mathrm{m_t}$.

5.2.2 Vector boson decay

Above the WW and ZZ kinematical thresholds, the Higgs boson decays mainly into pairs of massive gauge bosons, the corresponding diagrams being that in Fig. 5.7. The decay widths are directly proportional to the HVV couplings. The widths are given by [98]

$$\Gamma(\mathrm{H} \to \mathrm{VV}) = \frac{G_\mu \mathrm{M_H^3}}{16\sqrt{2}\pi}\delta_{\mathrm{V}}(\sqrt{1-4x})(1 - 4x + 12x^2) , \tag{5.7}$$

where $x = \mathrm{M_V^2/M_H^2}$ and $\delta_{\mathrm{W}} = 2$ and $\delta_{\mathrm{Z}} = 1$. For large enough Higgs boson masses, when the phase space factors can be ignored, the decay width into WW bosons is

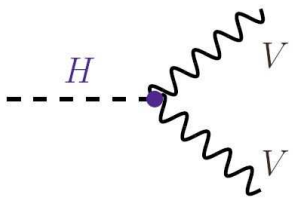

Figure 5.7: Leading order Feynman diagram for the decay process of the Standard Model Higgs boson into two vector bosons.

two times larger than the decay width into ZZ bosons and the branching ratios for the decays are approximately 2/3 and 1/3 for energies below $t\bar{t}$ threshold.

5.2.3 Two photons decay

Since the photon is massless there is no coupling between the Standard Model Higgs boson and the photon. However, the decay is possible through loop processes with either fermions or bosons in the loop. Feynman diagrams for the lowest order processes are shown in Fig. 5.8.

The calculation of the matrix element for the decay is rather difficult and involves dimensional regularization of the infinities arising from the loop. The

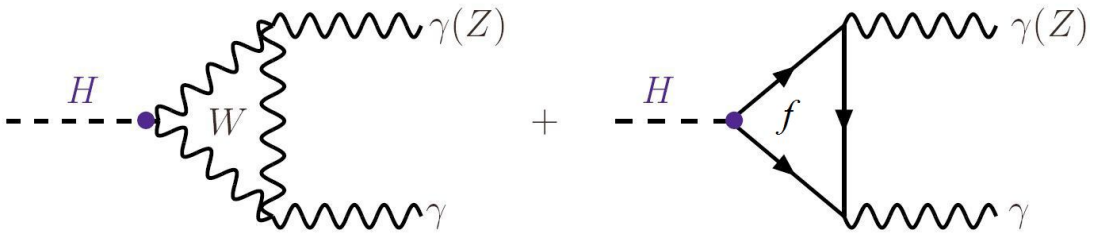

Figure 5.8: Leading order Feynman diagrams for the decay process of the Standard Model Higgs boson into two photons.

final result for the squared matrix element is [99]

$$|M|^2 = \frac{g^2 \mathrm{M_H^4}}{32\pi^2 \mathrm{M_W^2}} \left| \sum_i \alpha N_c e_i^2 F_i \right|^2 , \tag{5.8}$$

with the sum over all scalars, fermions and bosons in the loop with charge e_i and colour factor N_c. The factors F_i depend on the particle in the loop. They disappear for small value of the fermion mass which means that light quarks and leptons are insignificant. The only fermion participating is the top quark. For bosons the loop only contains the charged W.

The width of the $\mathrm{H} \to \gamma\gamma$ decay channel is

$$\Gamma(\mathrm{H} \to \gamma\gamma) = \frac{\alpha^2 g^2 \mathrm{M_H^3}}{1024\pi^3 \mathrm{M_W^2}} \left| \sum_i N_c e_i^2 F_i \right|^2 , \tag{5.9}$$

which always gives a branching ratio below 0.3% due to the much larger width of the $\mathrm{H} \to \mathrm{b\bar{b}}$ decay. The two photon signature is, however, clean and is an important decay channel at the LHC. The radiative corrections to the $\mathrm{H} \to \gamma\gamma$ decay width are relatively simple as they only affect the top quark loop and neither the W loop nor the final state photons. The corrections are below 3% [100] and thus of limited importance.

5.3 Search strategies at LHC

Higgs boson production cross section is greater than 1 pb in the whole mass range (100 GeV/c$^2 \div 1$ TeV/c^2). More than two thousands events are therefore expected in one year of data taking at the nominal low luminosity ($2 \cdot 10^{33}$ cm^{-2} s^{-1}) with an increase of a factor five in the high luminosity regime (10^{34} cm^{-2} s^{-1}).

Fully hadronic events are the most copious final states from Higgs boson decays. These decays can not be easily resolved when merged in QCD background, therefore topologies with leptons or photons are preferred, even if they have smaller branching ratio. Similarly signatures of the associated production, with a leptonically decaying particle, can be searched for.

As decay BR's depend on the Higgs boson mass, search strategies change accordingly.

5.3.1 Low mass region

The region $M_H < 130$ GeV/c^2 is the hardest to be explored. The best way to detect a light Higgs boson would be in the dominant $H \to b\bar{b}$ channel. The large cross section (28 pb for $M_H = 115$ GeV/c^2) is however overwhelmed by the di-jet rate (more than six orders of magnitude higher).

A more favorable situation can be obtained by either looking at associative production ($t\bar{t}H$, WH or ZH) or at one of the rarer decays.

The most promising way of identifying a Higgs boson in the low mass region is to select the decay $H \to \gamma\gamma$. The channel suffers from a branching ratio around 10^{-3}, but the backgrounds are much lower than in the case of the $H \to b\bar{b}$ decay thanks to the clear signature of two isolated photons in the final state. The main backgrounds are from direct photon production and jets faking photons. The expected signal to background ratio is 10^{-2}, which make this channel much more attractive than the $b\bar{b}$ channel.

5.3.2 Intermediate mass region

In the mass region between 130 GeV/c$^2 \leq M_H \leq 2M_Z$ the branching ratio to vector bosons reaches significant levels. The obvious decay channels are $H \to WW^{(*)} \to \ell^+\nu_\ell\ell'^-\bar{\nu}_{\ell'}$ and $H \to ZZ^* \to \ell^+\ell^-\ell'^+\ell'^-$ with only one vector boson on-shell.

The $WW^{(*)}$ decay mode has to be extracted from a background mainly due to non resonant WW production and $t\bar{t} \to W^+W^-b\bar{b}$.

The fully leptonic decay $H \to ZZ^* \to 4\ell$ has the cleanest experimental signature, particularly in the four muon channel. The signal selection is based on the mass constraint which can be made on one of the lepton pairs. The main irreducible background is continuum ZZ production while reducible backgrounds are $t\bar{t}$ and $Zb\bar{b}$.

Looking at Fig. 5.4 a funny shape of the branching ratio to Z bosons can be seen for Higgs boson masses in the interval 130 GeV/c$^2 < M_H < 180$ GeV/c^2 . It is caused by a threshold effect where the decay to two W bosons on the mass shell becomes possible while still at least one of the Z bosons needs to be below the mass shell in the concurrent $H \to ZZ^*$ decay.

5.3.3 High mass region

If the Standard Model Higgs boson has a mass above twice the Z mass the discovery will be easy through the decay channel $H \rightarrow ZZ \rightarrow \ell^+\ell^-\ell^+\ell^-$. This is called the *golden channel* for Higgs boson discovery at LHC. Both lepton pairs will have an on-shell Z mass which makes possible to reduce many types of backgrounds.

The upper mass limit for detecting the Higgs boson in this decay channel is given by the reduced production rate and the increased width of the Higgs boson. As an example fewer than 200 Higgs particles with $M_H = 700$ GeV/c^2 decay in the $H \rightarrow ZZ \rightarrow 4\ell$ channel in a year at high luminosity and the large width of such a heavy Higgs boson makes it very difficult to observe a mass peak.

A selective decay channel like the four lepton channel is thus no longer sufficient for the highest Higgs boson masses. With the decays to vector bosons totally dominating, the only possible detection channels left are with at least one of the vector bosons decaying to neutrinos or jets. The decay channel $H \rightarrow WW \rightarrow \ell\nu_\ell jj$, where j denotes a jet from a quark in the W decay, has a branching ratio just below 30%, yelding a rate some 50 times higher than the four lepton channel from $H \rightarrow ZZ$ decays. The decay channel $H \rightarrow ZZ \rightarrow \ell^+\ell^-\nu_{\ell'}\bar{\nu}_{\ell'}$ which has a six times larger branching ratio than the four lepton channel could also be interesting.

Chapter 6

$H \rightarrow ZZ^{(*)} \rightarrow \mu^+\mu^-\mu^+\mu^-$, Signal and Background

Many decay channels can be exploited in the Higgs boson search, the different strategies depending on the Higgs boson mass range as described in the previous Chapter. The decay channel $H \rightarrow ZZ^{(*)}$, followed by Z decays into lepton pairs, gives however a spectacular signature for Standard Model Higgs boson discovery at LHC in the mass range $130 < M_H < 600$ GeV/c^2.

This decay channel can be divided into three classes depending on the flavor of the four leptons in the final state. In the present work only the Higgs boson decay into four muons, $H \rightarrow ZZ^{(*)} \rightarrow 4\mu$, the so called *golden channel*, is studied. The fully muonic decay of the Higgs boson has in fact the cleanest experimental signature and would allow a very good estimate of the Higgs boson mass thanks to the excellent muon momentum resolution of the CMS detector.

The main background sources of this channel are continuum $ZZ^{(*)} \rightarrow 4\mu$ production, $t\bar{t} \rightarrow 4\mu$ and $Zb\bar{b} \rightarrow 4\mu$. In the second case leptons come from t$\rightarrow$Wb decay followed by W$\rightarrow \mu\nu$ and semileptonic b decay, in the latter case two leptons are from $Z \rightarrow \mu^+\mu^-$ and the other two from b quark decay chains.

In the first part of this Chapter the kinematical characteristics of signal events are reviewed while in the second part the main background sources are described. Attention has been focused on the description of those kinematical variables which mainly allow a selection of the signal events against background.

6.1 Higgs boson signal

It has already been extensively described how the Standard Model Higgs boson cross section is dominated by gluon-gluon fusion (80%) over the mass range 100 GeV/c^2 < M_H < 1 TeV/c^2. At LHC, where $\sqrt{s}$ = 14 TeV/c^2, the cross section for this process is around 45 pb at M_H = 120 GeV/c^2 and decreases monotonically to 5 pb at M_H = 500 GeV/c^2.

The associated production processes, qq→HW, qq→HZ, gg/q$\bar{q}$ → t$\bar{t}$H and gg/q$\bar{q}$ → b$\bar{b}$H have cross sections lower by a factor of 20 at $M_H \approx$ 100 GeV/c^2 and by a factor of 1000 at large masses, $M_H >$ 500 GeV/c^2. The production cross section for the gauge boson fusion, VV→H, is about 10% of the gluon fusion production cross section for $M_H <$ 200 GeV/c^2, and becomes comparable for $M_H \approx$ 1 TeV/c^2.

The QCD corrections for the gg→H process are large, with a K-factor ranging from 1.5 to 1.8 [85]. The QCD corrections are smaller for the gauge boson fusion (K-factor ∼ 1.1) and for the associated production processes qq→HW, qq→HZ (K-factor ∼ 1.3) and gg/qq→ t$\bar{t}$H (K-factor ∼ 1.2) [85].

The numerical values of the Higgs boson cross section can be predicted with `HIGLU 2.1` and other programs which include the next-to-leading order corrections where known so that the uncertainties are quoted of the order of 15%.

Within the CMS Official Production [101], a sample of 10 000 H → ZZ$^{(*)}$ → 4μ simulated events is available for eighteen different Higgs boson masses. Those events were generated with the Monte Carlo generator `PYTHIA 6.2` with the preselection requirements that the four muons should be within the acceptance of the CMS muon chambers: they must have a pseudorapidity smaller than 2.4 and a transverse momentum in excess of 3 GeV/c. Moreover the masses of the generated Z bosons are required to lay between 5 and 150 GeV/c^2.

Events were generated forcing the decays H → ZZ and Z → $\ell^+\ell^-$ and selecting those with at least four muons in the final state. The full simulation of the detector response was performed as described in Chapter 4.

The Higgs boson production cross section for the eighteen simulated samples is reported in Tab. 6.1, where the contributions of the main generation processes are also shown. The numerical results are obtained by using the CTEQ6m [87] parton density function and choosing m_t = 175 GeV/c^2. The branching ratio, the preselection cut acceptance, which contains the probability to have a four muons

final state, and the final cross section are shown in Tab. 6.2 instead.

The $H \rightarrow ZZ^{(*)}$ branching ratios as a function of Higgs boson mass are calculated with the program `HDECAY` which include next-to-leading order corrections, while the values of the other branching ratios are those reported by the Particle Data Group [5]. In the following the main kinematical characteristics of the signal events are described.

6.1.1 Z boson kinematics

One of the most important characteristics of the signal events is the presence of two Z bosons in the intermediate state, which could be either real or off-mass-shell according to the Higgs boson mass. In the mass region $M_H > 2M_Z$ the Higgs boson will decay mainly into two on-shell Z bosons.

The fraction of events with both Z off-mass-shell is decreasing with increasing Higgs boson mass. There are about 20%, 12% and 3% of such events for Higgs boson masses of 130 GeV/c^2, 150 GeV/c^2 and 180 GeV/c^2, respectively. This is illustrated in Fig. 6.1, where the mass distribution of the Z closest to the nominal Z boson mass, for three different Higgs boson masses, is shown. In the following analysis the vector boson closer to the nominal Z mass is referred to as Z boson, and the other one as Z*.

The Z* mass distribution is shown in Fig. 6.2. A M_{Z^*} characteristic upper edge, at the position $M_H - M_Z$ can be noticed, becoming more pronounced as the Higgs boson mass increases.

6.1.2 Muon kinematics

The main characteristic of the studied physics channel is the presence of four relatively isolated and high p_T muons in the final state. These muons properties are used to effectively reduce the backgrounds. As an illustration, in Fig. 6.3 the transverse momentum distributions of the four muons from the Z and Z* decays, sorted by decreasing p_T, for three values of the Higgs boson mass after the preselection cuts are shown. The difference between the distributions for various Higgs boson masses becomes clear on the third muon. From the softest muon distribution, for which the peak at $M_H < 130$ GeV/c^2 is around 10 GeV/c, it can be foreseen that the signal acceptance is very sensitive to the minimum cut chosen. In this mass region, despite the higher cross section, the number of expected signal

Table 6.1: Summary of the production cross section of the Higgs boson signal for the studied masses. The numerical results are obtained by using the CTEQ6m parton density function and choosing $m_t = 175$ GeV/c^2.

M_H (GeV/c^2)	$gg \to H$ (pb)	$VV \to H$ (pb)	WH (pb)	ZH (pb)	$gg, q\bar{q} \to Hq\bar{q}$ (pb)	σ_{TOT} (pb)
115	39.3	4.65	1.98	1.05	0.75	47.64
120	36.5	4.47	1.74	0.92	0.67	44.20
130	31.7	4.14	1.35	0.72	0.53	38.34
140	27.8	3.83	1.06	0.57	0.43	33.59
150	24.6	3.56	0.84	0.45	0.35	29.71
160	21.9	3.32	0.68	0.37	0.29	26.46
170	19.7	3.09	0.55	0.30	0.24	23.79
180	17.8	2.88	0.45	0.25	0.20	21.49
190	16.2	2.71	0.38	0.20	0.17	19.56
200	14.8	2.53	0.31	0.17	0.15	17.86
250	10.2	1.87	0.14	0.08	0.08	12.26
300	8.00	1.42	0.07	0.04	0.05	9.41
350	7.93	1.10	0.04	0.02	0.03	8.53
400	7.88	0.87	0.02	0.01	0.02	8.71
450	5.70	0.70	0.01	0.008	0.02	6.50
500	3.86	0.57	0.01	0.005	0.01	4.53
550	2.58	0.46	0.006	0.003	0.01	3.13
600	1.73	0.39	0.004	0.002	0.01	2.18

Table 6.2: The branching ratio, the preselection cut acceptance ξ and the final cross section for the eighteen studied Higgs boson masses. In the last column the expected number of events after an integrated luminosity of 20 fb^{-1} is also shown.

M_H (GeV/c^2)	BR ($H \to ZZ^{(*)}$)	Preselection acceptance (ξ)	$\sigma_{TOT} \cdot \xi \cdot$ BR (fb)	expected events ($L = 20$ fb^{-1})
115	$0.80 \cdot 10^{-2}$	$5.75 \cdot 10^{-2}$	0.219	4
120	$0.15 \cdot 10^{-1}$	$5.97 \cdot 10^{-2}$	0.396	8
130	$0.39 \cdot 10^{-1}$	$6.25 \cdot 10^{-4}$	0.934	18
140	$0.68 \cdot 10^{-1}$	$6.54 \cdot 10^{-4}$	1.509	30
150	$0.83 \cdot 10^{-1}$	$6.76 \cdot 10^{-4}$	1.667	34
160	$0.43 \cdot 10^{-1}$	$6.90 \cdot 10^{-4}$	0.785	16
170	$0.22 \cdot 10^{-1}$	$6.97 \cdot 10^{-4}$	0.365	7
180	$0.58 \cdot 10^{-1}$	$7.26 \cdot 10^{-4}$	0.904	18
190	0.22	$7.48 \cdot 10^{-4}$	3.220	64
200	0.26	$7.48 \cdot 10^{-4}$	3.473	70
250	0.30	$7.55 \cdot 10^{-4}$	2.777	56
300	0.31	$7.91 \cdot 10^{-4}$	2.310	46
350	0.31	$8.19 \cdot 10^{-4}$	2.166	43
400	0.28	$8.63 \cdot 10^{-4}$	2.105	30
450	0.26	$8.91 \cdot 10^{-4}$	1.506	30
500	0.26	$8.99 \cdot 10^{-4}$	1.060	20
550	0.26	$9.20 \cdot 10^{-4}$	0.749	15
600	0.27	$9.56 \cdot 10^{-4}$	0.563	11

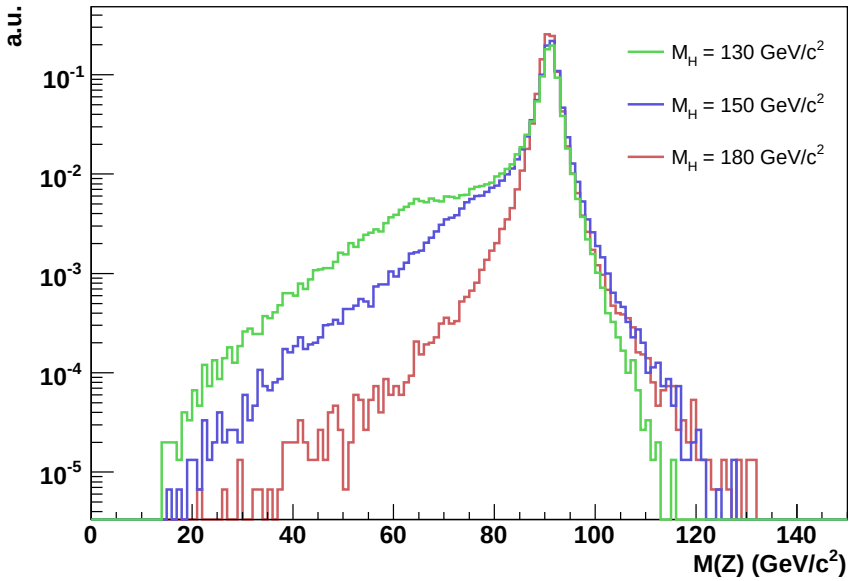

Figure 6.1: The mass distribution of the on-shell Z boson (the Z closer to the nominal Z boson mass) for three different Higgs masses.

events is small due to the low branching ratio and it is very important to maximize the acceptance together with the reconstruction efficiency to optimize the low mass reach.

6.1.3 Internal bremsstrahlung

Another specificity of this channel is the radiation of photons in the Z decays, which is called internal bremsstrahlung (also Final State Radiation photons). Those photons are emitted by muons as shown in Fig. 6.4.

This process is taken into account using the program `PHOTOS` [102], which implements an algorithm for single and double photon emission in these decays. The distribution of the angular distance (ΔR) between the emitted photon and the muon, as well as the photon p_{T} are shown in Fig. 6.5. Most of emitted photons have low energy ($E_T < 1$ GeV/c^2) but the fraction of events with highly energetic photons increase with the Higgs boson mass; for example it is respectively 18% and

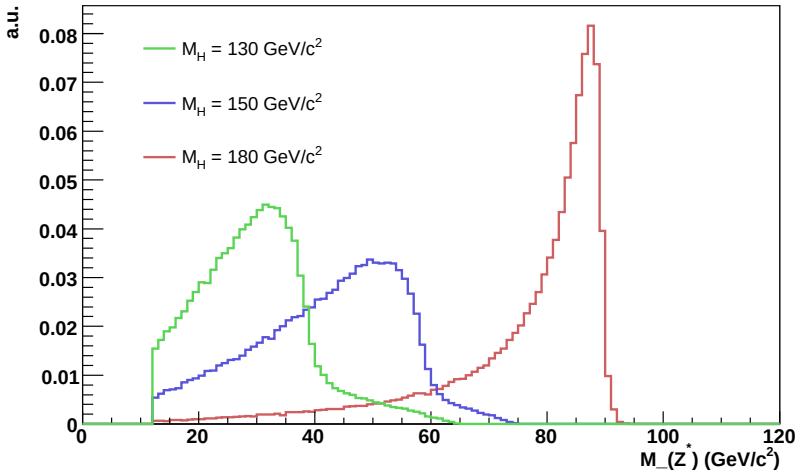

Figure 6.2: The mass distribution of the off-shell Z^* boson for three different Higgs masses.

37% with $M_H = 130$ GeV/c^2 and $M_H = 500$ GeV/c^2. The mean angular distance between the photon and the muon ($< \Delta R_{\mu\gamma} >$) decreases instead monotonically from 0.57 when $M_H = 130$ GeV/c^2 to 0.27 at $M_H = 500$ GeV/c^2. However, an important fraction of the photons are clearly separated from the muons with a non-negligible p_T [103]. These photons can be important in improving the Higgs boson mass resolution expecially at low mass.

6.2 Background

The background of the $H \rightarrow ZZ^{(*)} \rightarrow 4\mu$ channel is composed by all processes with four muons in the final state. There are two basic classes of such processes, called *reducible* and *irreducible* backgrounds. The reducible backgrounds have very pronounced kinematical and topological differences with respect to the signal, both in the final states as well as in the two and four muon combinations. Therefore, by appropriate kinematical and topological cuts, these backgrounds can be effectively suppressed. The main reducible background processes are $t\bar{t} \rightarrow W^-W^+b\bar{b} \rightarrow 4\mu$ and $Zb\bar{b} \rightarrow 4\mu$.

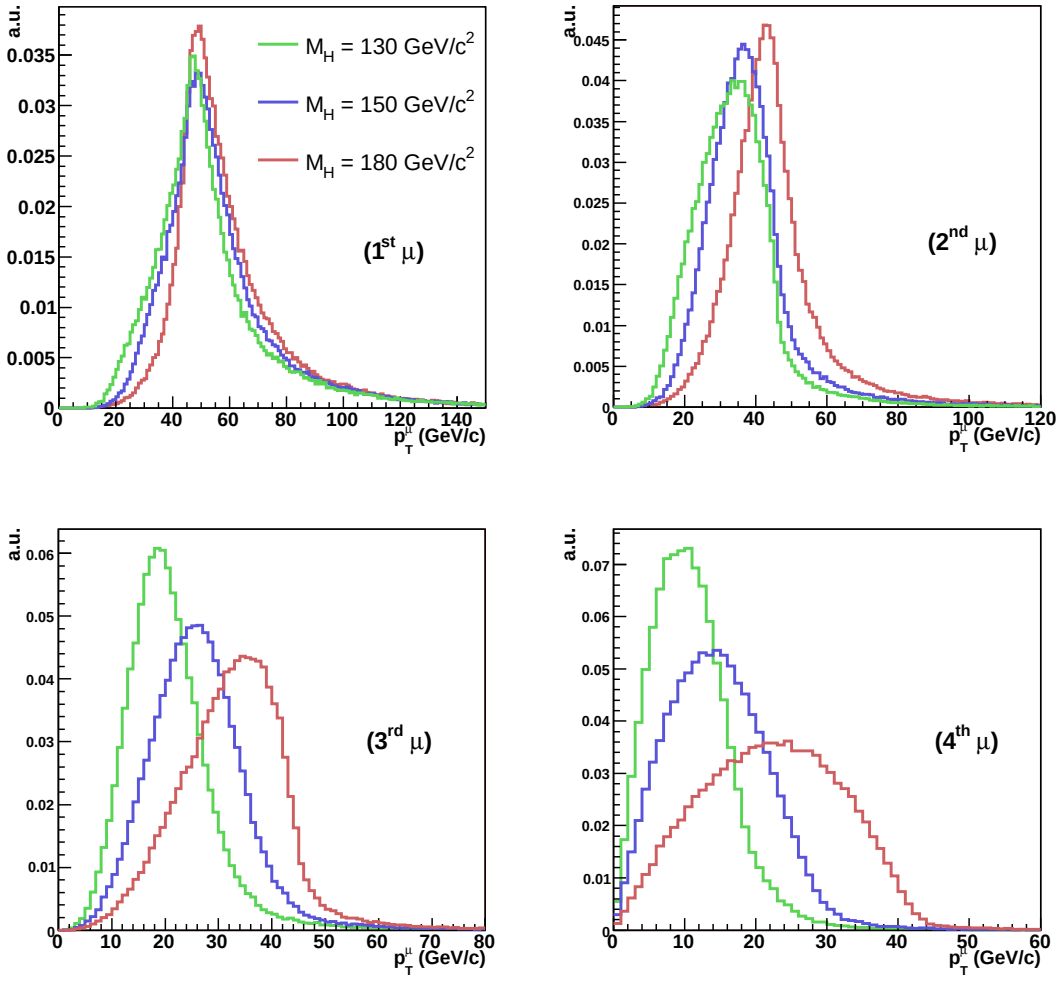

Figure 6.3: The p_{T} distributions of the four muons in signal events for three different Higgs boson masses. In each event muons are sorted according to p_{T} value.

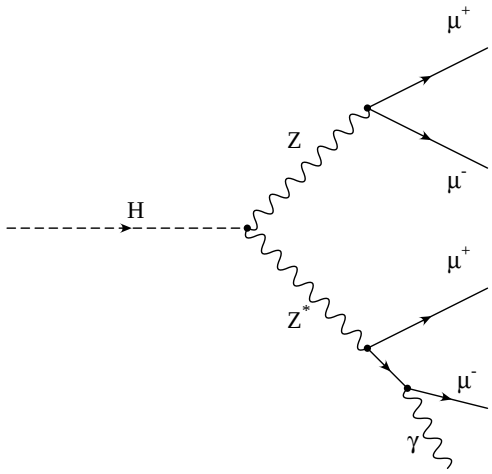

Figure 6.4: Feynman diagram showing the internal bremmstrahlung process.

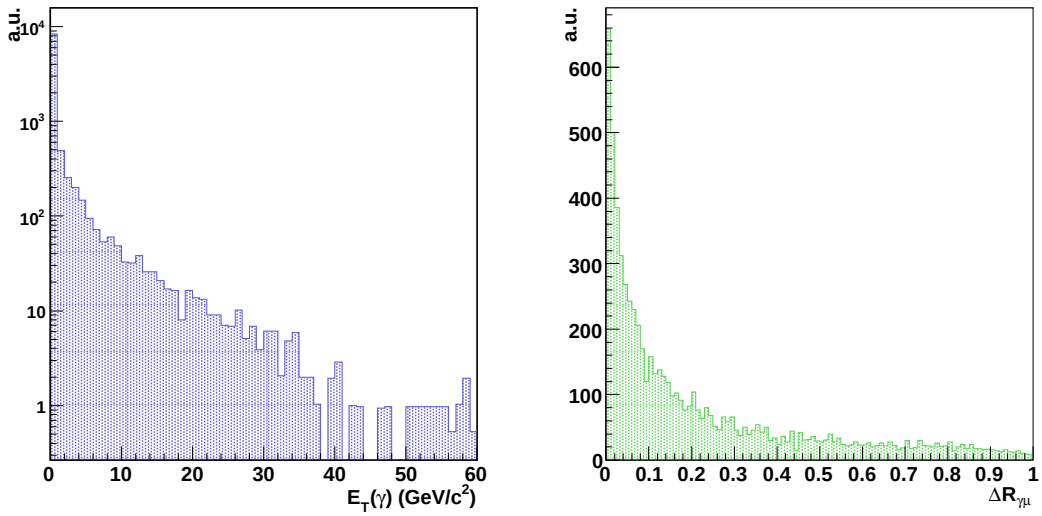

Figure 6.5: Transverse energy distribution of the final state radiation photons (left) and angular separation between the photon and the muon (right) in signal events for $M_H = 150$ GeV/c^2.

The only irreducible background is $ZZ^{(*)}/\gamma^* \rightarrow 4\mu$, with very similar final and intermediate state kinematics when compared to the signal events. Nevertheless, adjusting properly the kinematical cuts and using some additional cuts, like the four-muons transverse momentum, this background can also be suppressed to some extent.

6.2.1 $ZZ^{(*)}/\gamma^*$ background

At LHC two are the main processes which contribute to Z boson pairs production: $q\bar{q} \rightarrow ZZ^{(*)}$ and $gg \rightarrow ZZ^{(*)}$. The leading order diagrams for such processes are shown in Fig. 6.6.

The $q\bar{q} \rightarrow ZZ^{(*)}$ cross section has been evaluated with the Monte Carlo generator `MCFM` [104], which performs the calculation in next-to-leading order in α_S. The expected cross section has been calculated using CTEQ6m as parton distribution function set and the factorization and renormalization scales μ are set equal to the average of the produced vector boson masses. The cross section results to be

$$\sigma_{LO}(ZZ) = 10.7 \text{ pb}\,, \qquad \sigma_{NLO}(ZZ) = 15.3 \text{ pb}\,. \tag{6.1}$$

The uncertainty due to the parton density function is around 6%.

Although being a loop process of higher order in α_S, $gg \rightarrow ZZ^{(*)}$ is important since the gluon-gluon luminosity is much higher than the quark-antiquark luminosity for small x at hadron colliders. At the leading order, its contribution has been calculated for the case of two real Z production [105]. The $gg \rightarrow ZZ$ cross section

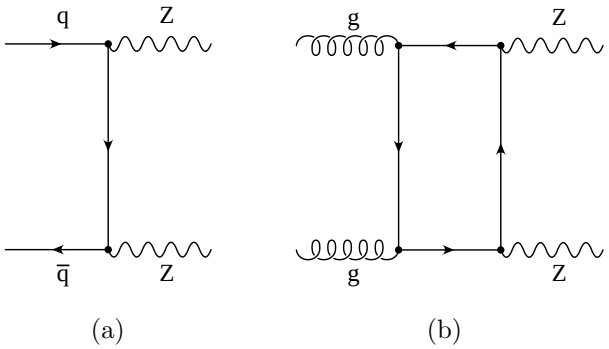

Figure 6.6: Leading order Feynman diagrams of the main production mechanisms of a ZZ pair at LHC.

was estimated to be 20% of $q\bar{q} \rightarrow ZZ$ while next-to-leading order corrections to this process are still unknown. To summarize, the $ZZ^{(*)}$ production cross section used in this study is

$$\sigma(pp \rightarrow ZZ^{(*)}) = 15.3 + 0.20 \cdot 10.7 = 17.4 \text{ pb}\,. \tag{6.2}$$

A sample of 10 000 $ZZ^{(*)}$ simulated events is available within the CMS Official Production. The events were generated with `PYTHIA 6.2` and with the same preselection cuts ($|\eta_\mu| < 2.4$, $p_T^\mu > 3.0$ GeV/c and $5 < M_Z < 150$ GeV/c^2) as the Higgs boson sample. In those events the Z bosons are allowed to decay only into a pair of leptons then only the events with four muons in the final state are selected. The acceptance to these generation cuts is 3.42%. The sample contains 52.7% of events with two on-mass-shell Z bosons, 35.9% with only one Z while 11.4% have both Z bosons off-mass-shell.

It is important to note that the $ZZ^{(*)}$ sample does not contain $gg \rightarrow ZZ^{(*)}$ events, in fact this production mechanism has not been yet implemented in the Monte Carlo generator `PYTHIA`.

As an illustration of the `PYTHIA` generated Zs kinematics, in Fig. 6.7 the invariant mass distributions of the Z and Z* bosons are shown. The $p_T(ZZ^{(*)})$ and the invariant mass m(ZZ*) distributions are shown in Fig. 6.8. A detailed study of the $p_T(ZZ^{(*)})$ distribution is presented in the last Section of this Chapter.

The p_T distributions of the four muons from the Z decays are shown in Fig. 6.9, sorted in decreasing order of p_T. The softest muon distribution shows an almost exponential fall off, giving a potentially high rejection power by increasing the threshold.

6.2.2 $t\bar{t}$ background

The top quark decays almost exclusively into W bosons and b quarks. In the decay chain of a $t\bar{t}$ pair there are several sources which lead to final states with muons. They can come directly from the W decay, in the leptonic decay of a τ coming from the W, from the semileptonic decay of mesons produced in the fragmentation of a b quark or of its decay products. Anyhow at least two out of the four muons belong to a hadronic jet and they are not isolated. The most probable scenario is given by two muons produced directly from the W decays and the other two produced in the b semileptonic decay. This typical decay chain is schematically shown in Fig. 6.10.

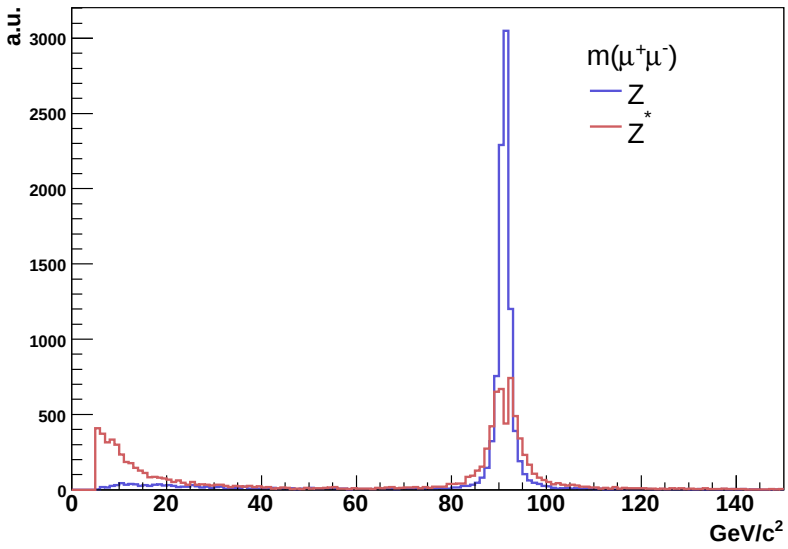

Figure 6.7: The Z and $Z^{(*)}$ boson mass distribution as produced by PYTHIA.

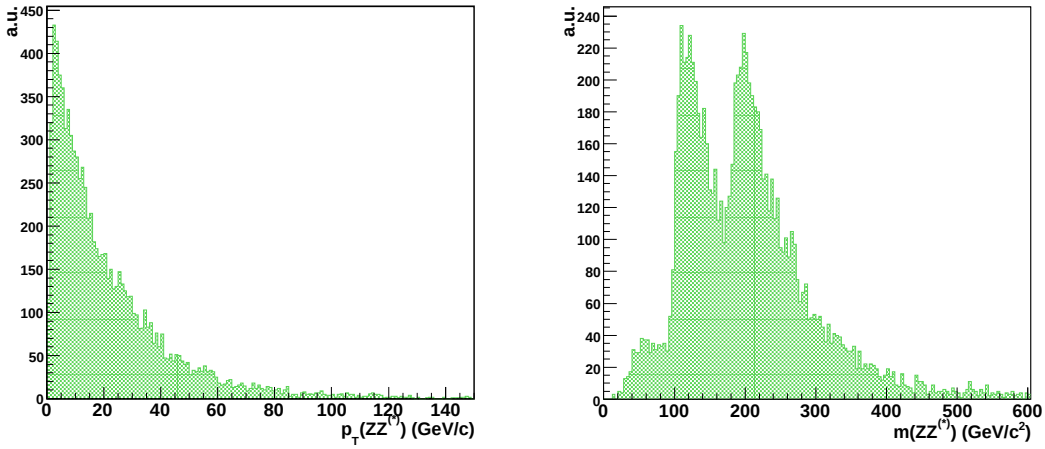

Figure 6.8: Transverese momentum (left) and invariant mass distribution (right) of the $ZZ^{(*)}$ system.

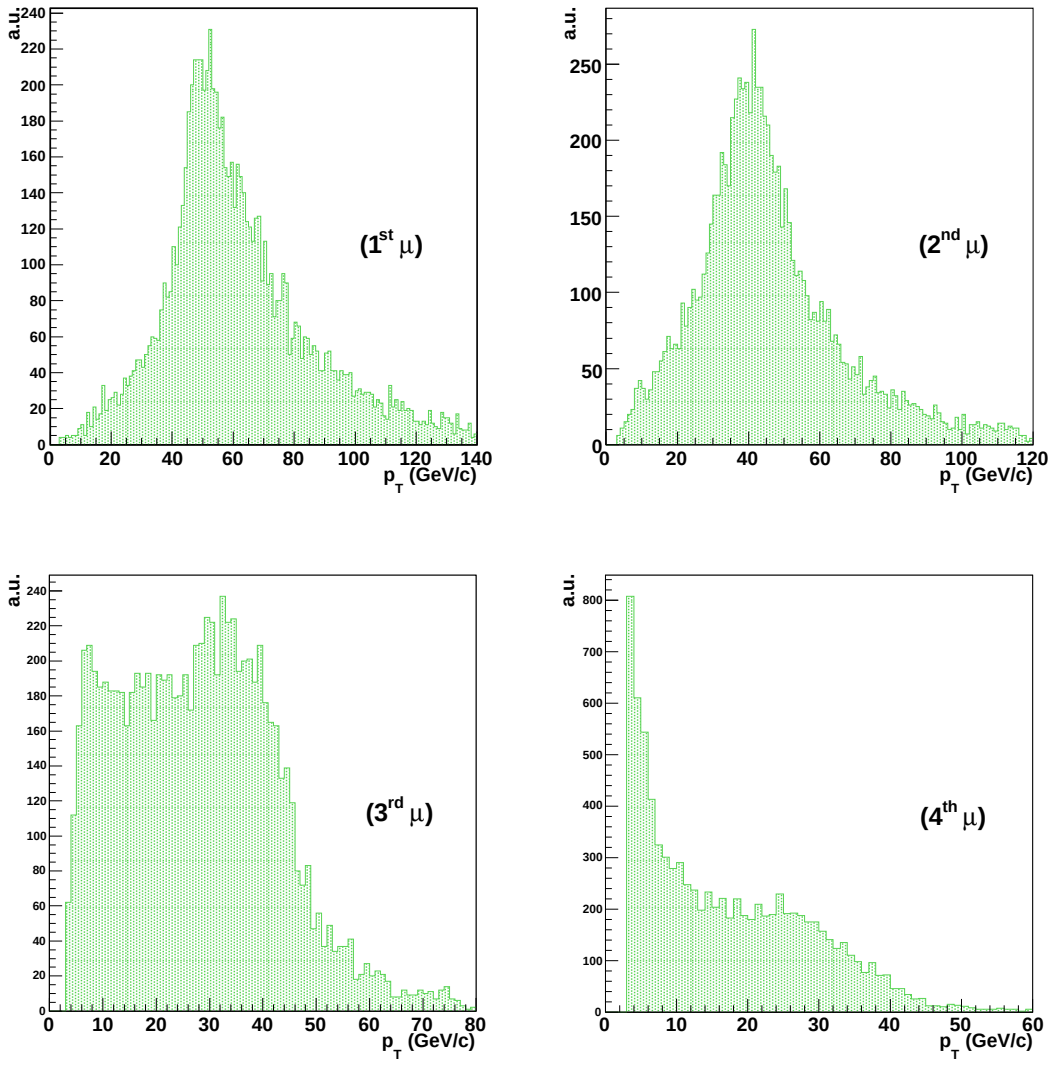

Figure 6.9: The p_{T} distributions of the four muons in $ZZ^{(*)}$ events. In each event muons are sorted according to p_{T} value.

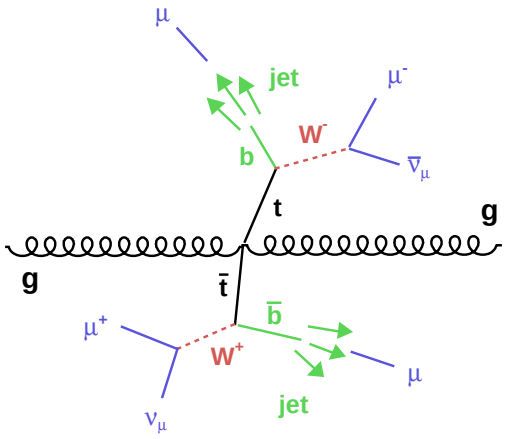

Figure 6.10: Typical decay chain of a $t\bar{t}$ pair. Two muons come from the W bosons decays, the other two come from the b-jet hadronization.

At hadron colliders, like LHC, the most important contributions to the $t\bar{t}$ production cross section are gluon fusion and $q\bar{q}$ annihilation. Some leading order Feynman diagrams are shown in Fig. 6.11.

The $t\bar{t}$ cross section has been calculated to be [106, 107]

$$\sigma(t\bar{t}) = 840 \pm 5\%_{\text{scale}} \pm 3\%_{\text{PDF}} \text{ pb}\,. \tag{6.3}$$

In the calculation the mass of the top quark has been set to 175 GeV/c^2 and the

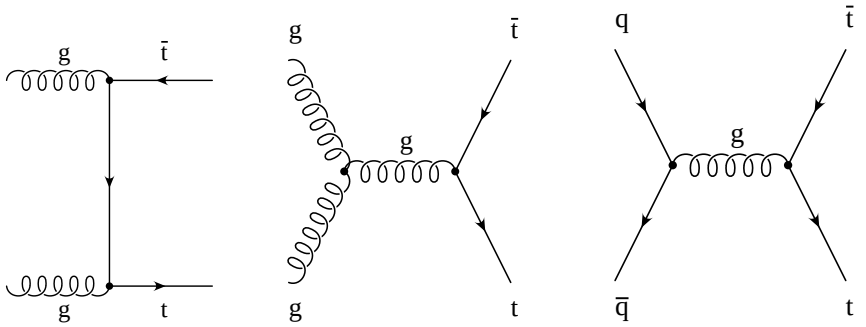

Figure 6.11: Leading order Feynman diagrams which contribute to the $t\bar{t}$ production at LHC.

MRST [108] parton density function has been used. The full next-to-leading order corrections are included, while no complete or consistent result beyond NLO is available at the moment.

The total $t\bar{t}$ production cross section is given in Fig. 6.12 as a function of the top mass, in the lower inset the scale uncertainty of the theoretical predictions is shown. The dashed lines refer to the NLO scale dependence, which is of the order of 5%. The dotted lines refer to the inclusion of the NLL corrections, according to the results of Ref. [109].

The PDF dependence is shown on the right hand side of Fig. 6.12. The current uncertainty is at the level of 3%. Notice that the largest deviations from the default set occur for sets using different input values of $\alpha_S(M_Z)$. The difference between the reference sets of the two groups (MRST and CTEQ5m) is at the level of few percent.

Combining in quadrature the scale and PDF dependence of the total $t\bar{t}$ cross section, the overall theoretical systematic uncertainty is 4%.

A sample of 90 000 $t\bar{t}$ fully simulated events is available within the CMS Official Production. The events were generated with `PYTHIA 6.2` and with the same preselection cuts ($|\eta_\mu| < 2.4$, $p_T^\mu > 3.0$ GeV/c and $5 < m(\mu^+\mu^-) < 150$ GeV/c^2) as the Higgs boson sample. The W bosons are forced to decay into leptons while b

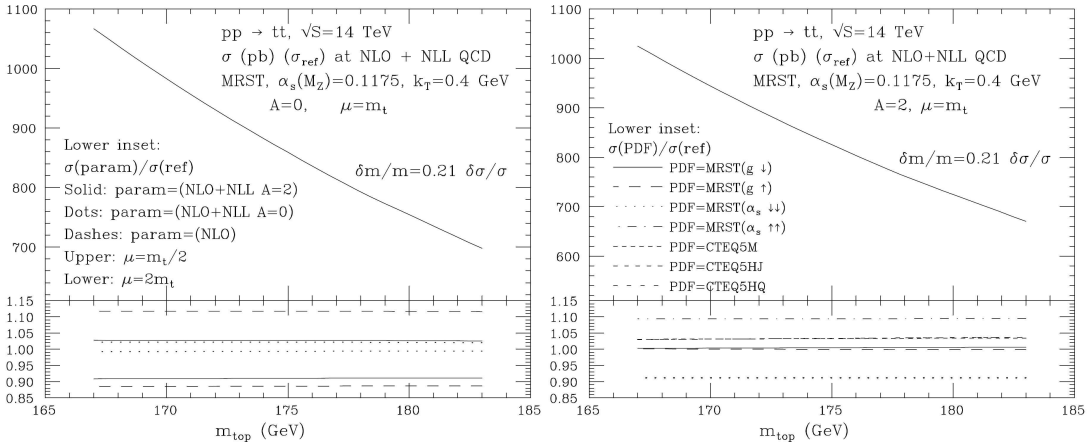

Figure 6.12: $t\bar{t}$ production rates. Left: scale dependence at fixed order (NLO, dashed lines in the lower inset) and at NLO+NLL (solid lines). Right: PDF dependece [106].

quarks are left free to decay, but eventually only events with four muons in the final state are selected. The generation of those events is very CPU time consuming being the acceptance of the preselection cuts only 0.45%.

In Fig. 6.13 the p_T of the four muons is reported. The soft spectra of the third and forth muons explain the low acceptance of the generation cut and show the high rejection power of a p_T cut.

Some of the interesting two-muons and four-muons distributions are shown in Fig. 6.14 and 6.15. The first muon pair is chosen as the one with the invariant mass closest to the nominal Z mass. From the two muons invariant mass distribution the power of a Z mass cut is evident (requesting one $\mu^+\mu^-$ pair to have an invariant mass compatible with the Z mass). Moreover, it is interesting to note a low mass peak in the second two-muons invariant mass distribution which is due to leptons originating from the same cascade. This peak will be effectively suppressed by a lower Z^* mass cut.

6.2.3 Z plus jets background

The third important source of background are 4 muons coming from Zjj production and decay. In most of the cases, two muons come from the Z decay while the other two originate from cascade decays of mesons produced in the quark hadronization. The presence of a real Z boson makes this background insensitive to a Z mass cut (in the case $M_H < 2M_Z$), unlike to the $t\bar{t}$ background. This background is also characterized by the presence of two non-isolated muons, coming from the b-meson cascade decays.

Particularly important is the case in which the Z boson is produced in association with two b quarks which is described in this Section. In the next Chapter a detailed study of the Zjj (with j = u, d, s, c) contribution to the $H \to ZZ^{(*)} \to 4\mu$ background is presented.

At leading order, there are two processes for the production of this background at hadron colliders: $gg \to Zb\bar{b}$ and $q\bar{q} \to Zb\bar{b}$. Some of their leading order Feynman diagrams are shown in Fig. 6.16. The total cross section has been calculated using the `CompHep` Monte Carlo generator [71] at the leading order, and a value of about 650 pb was found.

The Monte Carlo generator `PYTHIA` produces such final states starting from $q\bar{q} \to Zg$ and $gq \to Zq$, then it generates additional b quarks with the parton

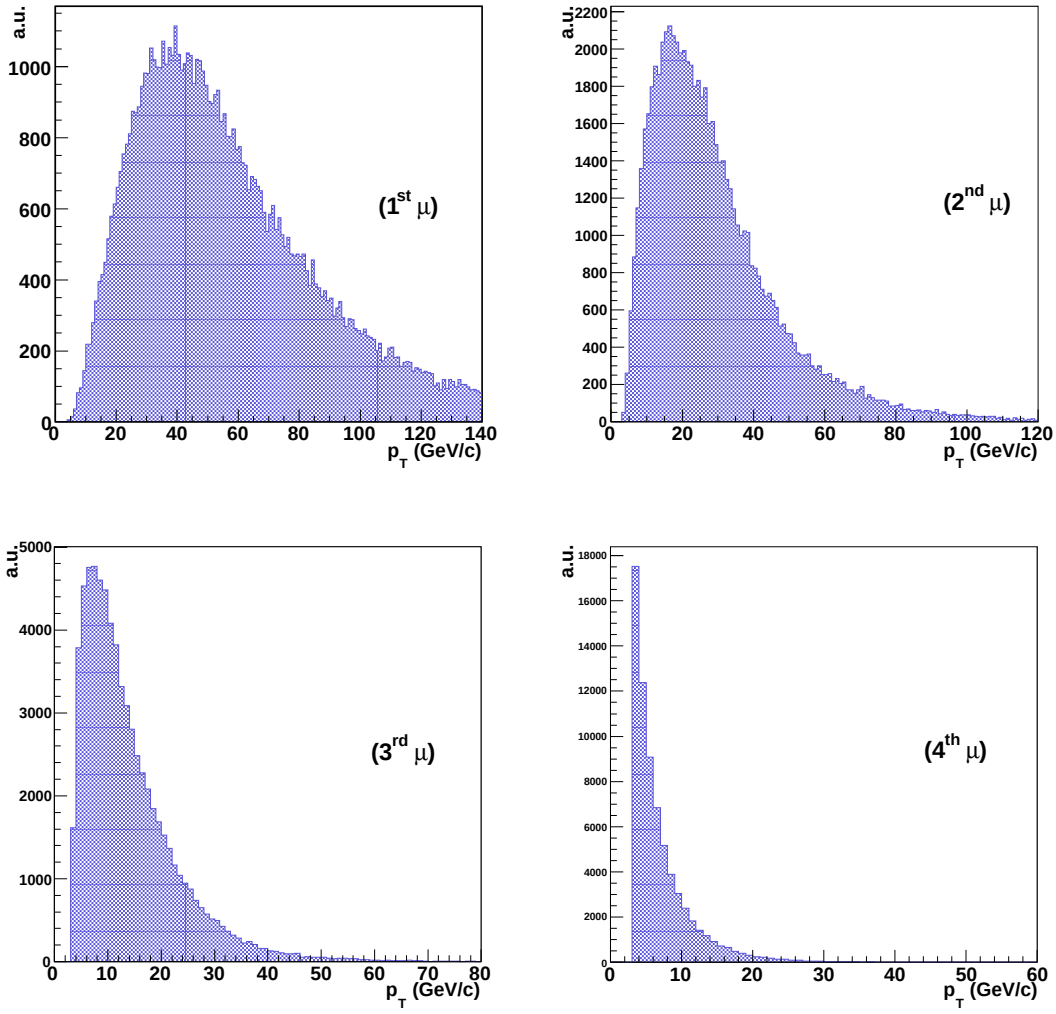

Figure 6.13: p_{T} distribution of the four muons in $\mathrm{t\bar{t}}$ events. The muons are sorted by decreasing p_{T}.

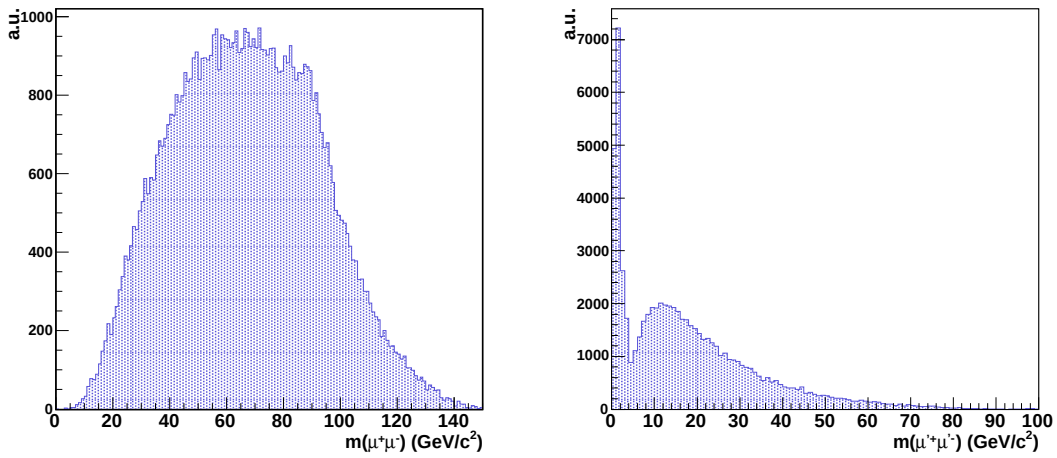

Figure 6.14: Invariant mass distributions of the two $\mu^+\mu^-$ pairs in $t\bar{t}$ background. The first muon pair (left) is chosen as the one with the invariant mass closest to the nominal Z mass.

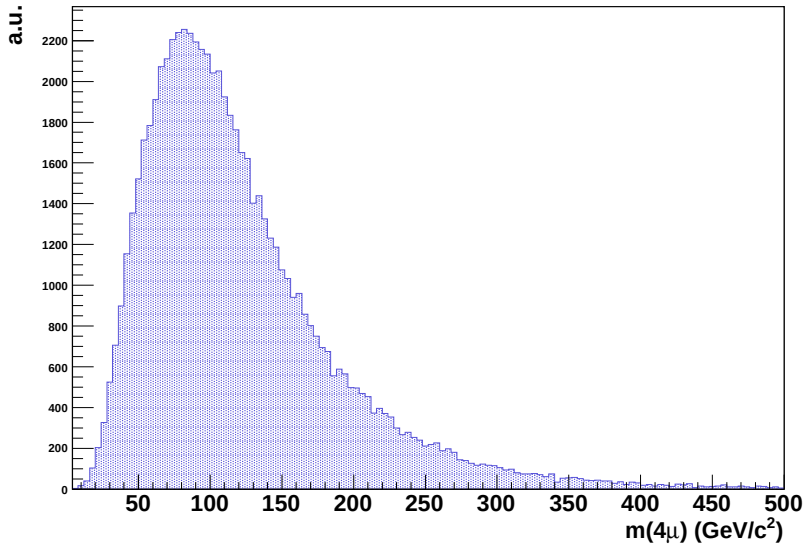

Figure 6.15: Invariant mass distribution of the four muons coming from $t\bar{t}$ events.

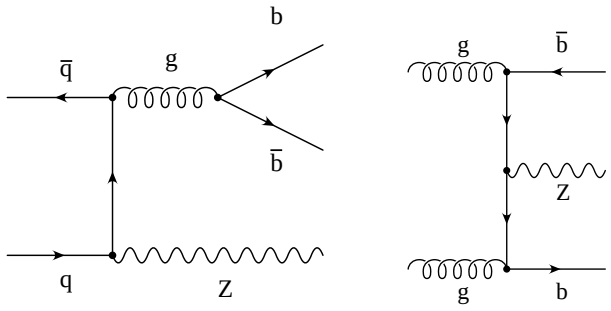

Figure 6.16: Some leading order Feynman diagrams which contribute to the $Zb\bar{b}$ production at LHC.

showering. This approach significantly underestimates the final rates after selection cuts, since the quarks generated by the parton shower evolution have a softer spectrum than those generated using exact matrix elements [110]. Then for the events generation, the `CompHEP` Monte Carlo generator has been used [71]. In `CompHEP`, the matrix elements of the $Zb\bar{b}$ are calculated exactly at leading order. As an example the p_T and η distributions of the b quarks generated by `PYTHIA` and `CompHEP` are shown in Fig. 6.17. The softer p_T spectrum of the b quark produced by `PYTHIA` is evident.

The partonic events generated by `CompHEP` are then passed through `PYTHIA` for the hadronization and the initial and final state parton showers generation. The generation of internal photons in the Z decay is done using `PHOTOS`, as in the case of the signal and of the other backgrounds. The Z boson is forced to decay in a couple of leptons while b quarks are left free to decay in order not to bias the sample. Furthermore, to obtain a sufficiently large statistical sample, the same preselection cut as above has been imposed demanding $|\eta_\mu| < 2.4$, $p_T^\mu > 3.0$ GeV/c and $5 < M_Z < 150$ GeV/c^2. The acceptance to these preselection cuts is 0.1%.

The invariant mass distributions of the two muons coming from Z and Z* are shown in Fig. 6.18. The interesting property of the invariant mass distribution is a large near zero mass peak of the smaller two-muons combination mass (muons coming from the same cascade), which will allow a considerable reduction of this background by an appropriate threshold. In Fig. 6.19 the four muons mass distribution is shown. It clearly has a similar shape as for the $t\bar{t}$ background.

The transverse momentum distribution of the four muons, sorted in decreasing order, is given in Fig. 6.20. In comparison with the signal and the other back-

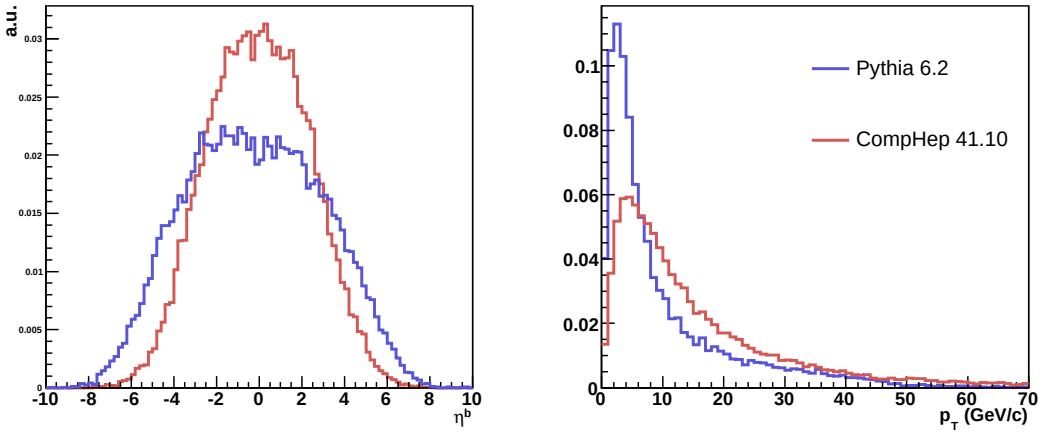

Figure 6.17: Comparison of the η (left) and p_T (right) distributions of the b quarks in Z$b\bar{b}$ events generated by PYTHIA and CompHEP.

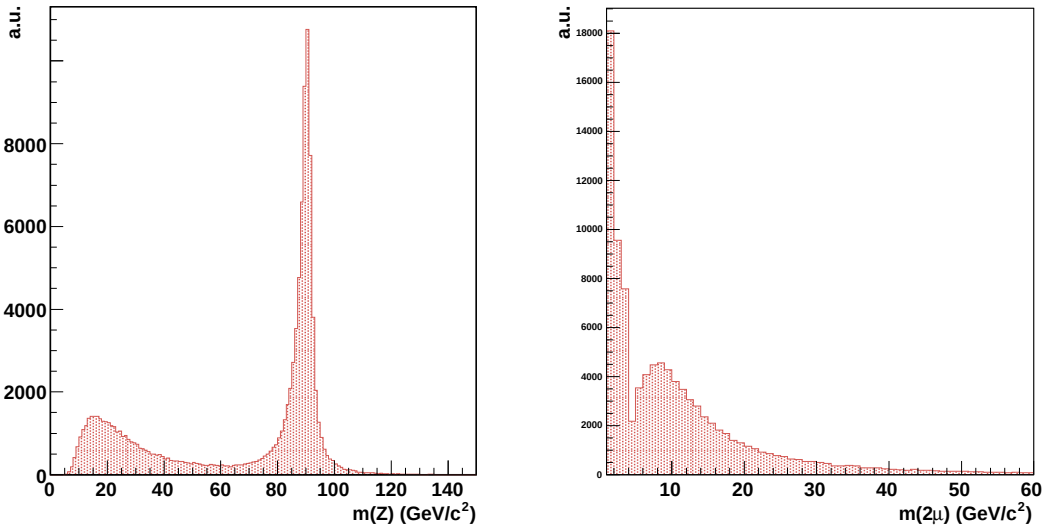

Figure 6.18: Invariant mass distribution of the the two $\mu^+\mu^-$ pairs in Z$b\bar{b}$ events.

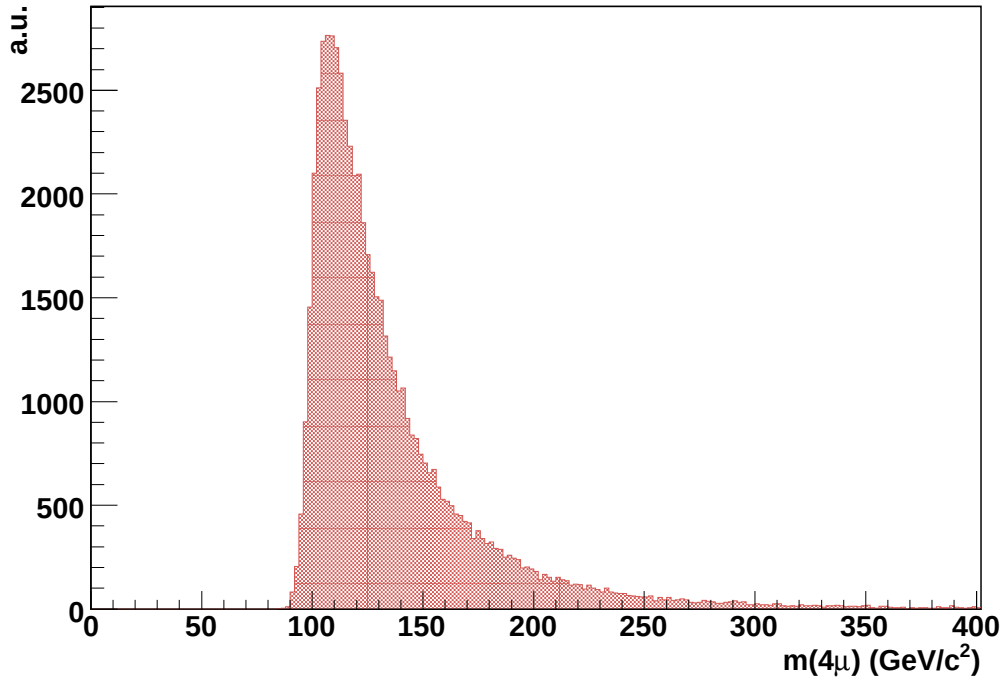

Figure 6.19: Invariant mass distribution of the four muons coming from the $Zb\bar{b}$ events.

grounds, a softer distribution of the two lightest muons can be noticed, making this background particularly sensitive to this kinematical cut.

6.2.4 Background summary

A summary of the cross section, preselection cut acceptance and expected number of events for an integrated luminosity of 20 fb^{-1} of the backgrounds described above is reported in Tab. 6.3.

6.3 Higher order predictions

In recent years much effort has been devoted to refining the theoretical predictions for the various Higgs production channels and the corresponding backgrounds,

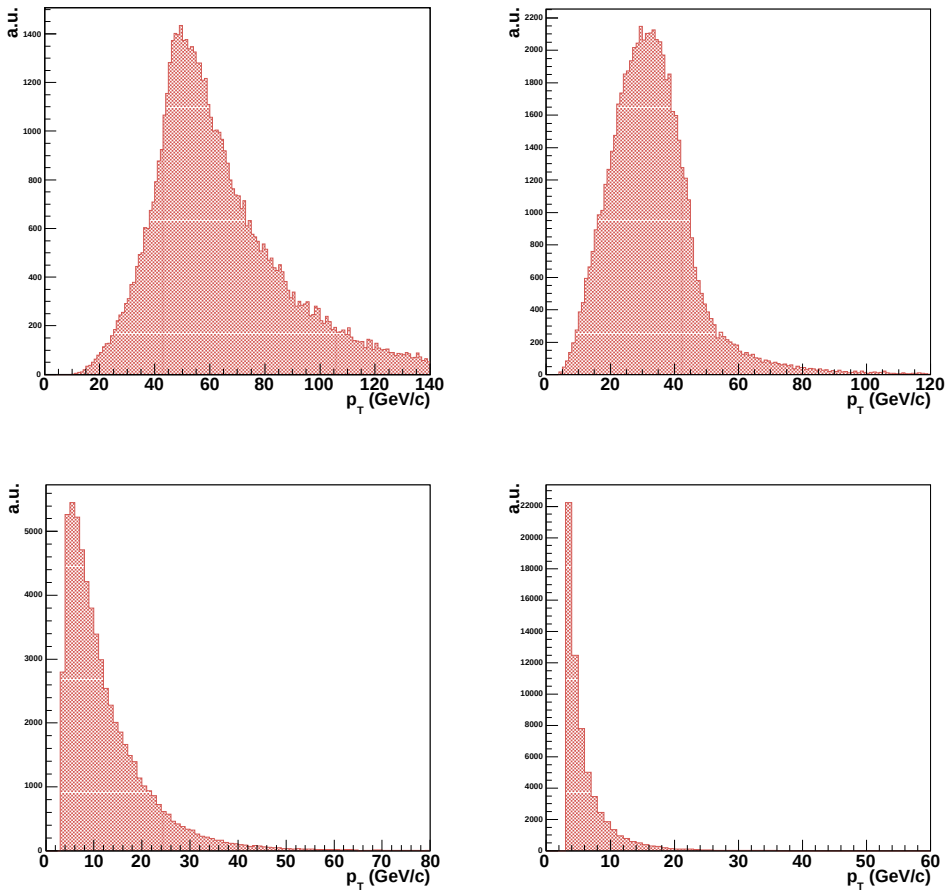

Figure 6.20: p_{T} distribution of the four muons in Zb$\bar{\mathrm{b}}$ events. The muons are sorted by decreasing p_{T}.

which are now known to next-to-leading order accuracy (NLO) in most of the cases. For the main Standard Model Higgs boson production channel, gluon-gluon fusion, even next-to-next-to-leading order (NNLO) QCD corrections to the total rate have been computed [111]. Nonetheless, predictions for less inclusive observables are definitely required to perform realistic studies. In particular, an accurate knowledge of the transverse momentum distribution of the Higgs boson can be important to enhance the statistical significance of the signal over the background in $\mathrm{H} \rightarrow \mathrm{ZZ} \rightarrow 4\mu$ channel. In this section the most recent prediction

Table 6.3: Cross section, preselection cut acceptance (ξ) and expected number of events after an integrated luminosity of 20 fb^{-1} for the main background sources.

Background	σ (pb)	BR $\cdot\ \xi$	BR $\cdot\ \xi \cdot \sigma$ (fb)	Events ($L = 20$ fb^{-1})
$ZZ^{(*)}$	17.4	$4.3 \cdot 10^{-4}$	7.48	150
$t\bar{t}$	840	$2.0 \cdot 10^{-4}$	168.0	3360
$Zb\bar{b}$	650	$1.8 \cdot 10^{-4}$	120.7	2414

available on the SM Higgs production channel is reviewed.

6.3.1 Parton shower Monte Carlo

The Monte Carlo (MC) generators usually used to simulate events, like `PYTHIA` or `HERWIG` [112], are referred to as Parton Shower Monte Carlo (PSMC).

The way events are generated can be divided into three steps: first the leading order cross section calculation is performed, then the shower mechanism lets partons emit as many gluons and quarks as possible, last final state partons are hadronized.

This procedure, shown in Fig. 6.21, has some advantages: for example the analytic computations are easy to calculate and the mechanism is very flexible. However there are some drawbacks: the high p_T and multijet configurations are not properly described and the total rate is computed to leading order accuracy only. The problems stem from the fact that PSMCs predict correctly only collinear emissions but underestimate the high p_T spectrum.

A series of next-to-leading order Monte Carlo generators have been developed in order to obtain better prediction but usually they do not perform the showering step thus they are not useful in the event simulation. However recently a new MC generator, `MC@NLO`, has been developed. It is a NLO Monte Carlo which is interfaced to the `HERWIG` Parton Shower to yield useful events. Unlike the standard PSMCs, the partonic hard subprocesses are computed by including the full NLO

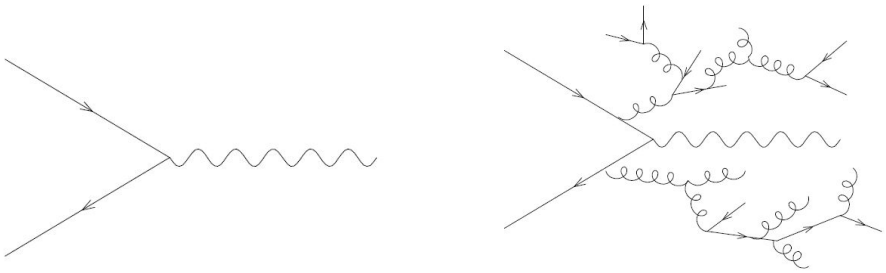

(a) (b)

Figure 6.21: Events generation is carried out by Parton Shower Monte Carlo into three steps: initially the leading order cross section calculation is performed (a), then the shower mechanism let partons emit as many gluons and quarks as possible (b). After these two steps final state partons are hadronized.

QCD corrections, as shown in Fig. 6.22. This has non trivial implications on the dynamics of most of the processes relevant to LHC physics. The hardest p_{T} emission is computed exactly and it provides the only way to sensibly compute the K-factors event by event and to use this information in detector simulation, which is impossible with analytic NLO parton level calculations.

Just as an example in Fig. 6.23 the comparision between the p_{T} distribution of the Standard Model Higgs boson generated by `PYTHIA` and `MC@NLO` is shown. As can be seen the NLO spectrum is harder than the LO one, as expected.

The same distributions calculated for the ZZ background are reported in

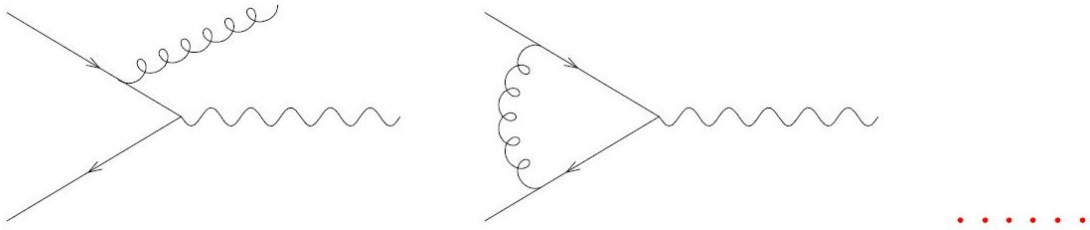

Figure 6.22: In NLO Parton Shower Monte Carlo, like `MC@NLO`, the partonic hard subprocesses are computed by including the full NLO QCD corrections.

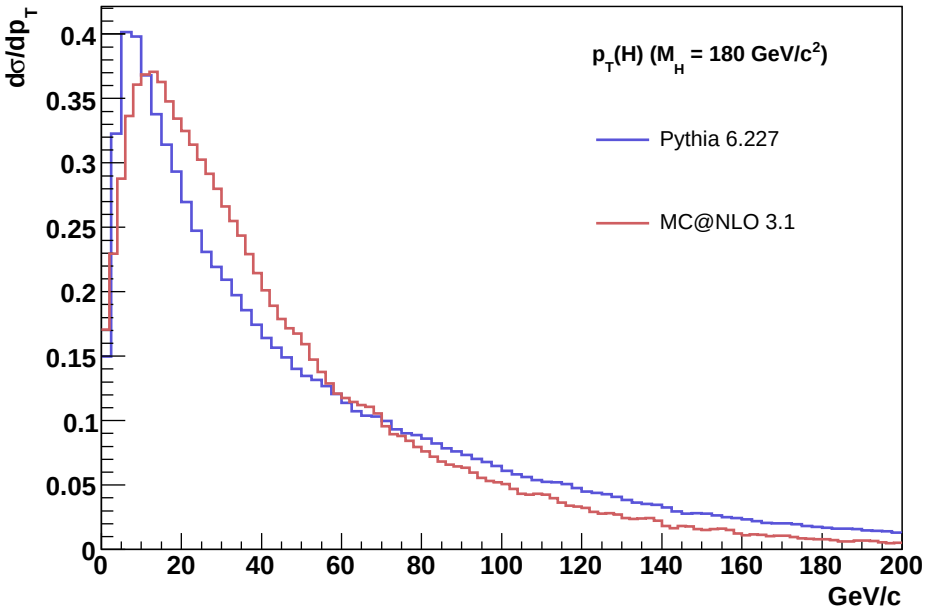

Figure 6.23: p_T distributions of the Higgs boson in the case $M_H = 180$ GeV/c^2 predicted by PYTHIA (LO) and MC@NLO (NLO), both distributions are normalized to the same cross section.

Fig. 6.24, which show a different behavior. In ZZ production PYTHIA underestimates the number of events at high p_T [113]. This is to be expected, since this transverse momentum region is dominated by the higher order processes with one or more associated hard jets in the final state, which are not properly modeled in PYTHIA.

A practical application of the results discussed in this Section is presented in the next Chapter in the context of the Higgs boson search in the $H \rightarrow ZZ \rightarrow 4\mu$ channel. As an approximate way to include higher order effects in the analysis, the corrected spectra presented above have been used to reweight signal events generated with the Monte Carlo PYTHIA.

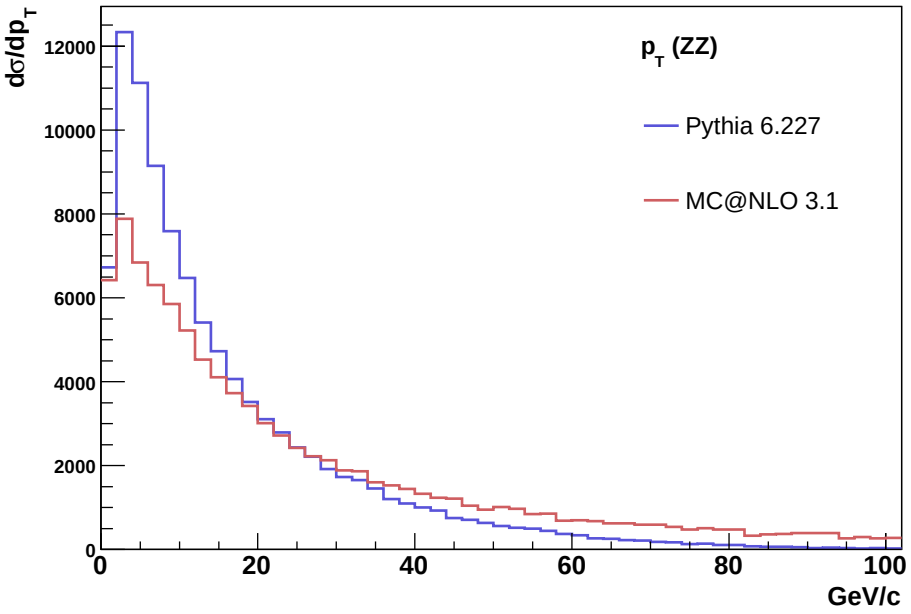

Figure 6.24: The p_{T} distribution of the ZZ system predicted by LO Monte Carlo PYTHIA and NLO Monte Carlo MC@NLO, both distributions are normalized to the same cross section.

6.3.2 Next leading logarithmic predictions

When the transverse momentum p_{T} of the Higgs boson is of the order of its mass ($\mathrm{M_H}$), the perturbative series is controlled by a small expansion parameter, $\alpha_S(\mathrm{M_H^2})$, and the fixed order prediction is reliable. The leading order [114] calculation shows that the large-$\mathrm{m_t}$ approximation ($\mathrm{m_t}$ being the mass of the top quark) works well as long as both $\mathrm{M_H}$ and $p_{\mathrm{T}}(\mathrm{H})$ are smaller than $\mathrm{m_t}$. In the framework of this approximation, the NLO QCD corrections have been computed [115].

The small p_{T} region ($p_{\mathrm{T}} << \mathrm{M_H}$) is the most important, because it is here that the bulk of events is expected. In this region the convergence of the fixed order expansion is spoiled, since the coefficients of the perturbative series in $\alpha_S(\mathrm{M_H^2})$ are enhanced by powers of large logarithmic terms, $\log^m(\mathrm{M_H^2}/p_{\mathrm{T}}^2)$.

To obtain reliable perturbative predictions, these terms have to be systematically resummed to all orders in α_S [116]. The fixed order and resummed approaches

then have to be consistently matched at intermediate values of p_T, so as to avoid double counting. In the case of the Higgs boson, the resummation has been explicitly worked out up to next-to-next-to-leading logarithmic (NNLL) level [117].

The NNLL+NLO distributions has been calculated in the mass range $180 < M_H < 300$ GeV/c^2 using the MRST set of parton density functions. The effect of the resummation starts to be relevant below $p_T < 100$ GeV/c and it increases the LO result by about 40% at $p_T = 30$ GeV/c. In Fig. 6.25 the full NNLL+NLO result is compared with the LO and NLO ones for the Higgs boson with a mass of 180 GeV/c^2. The `MC@NLO` predictions are in good agreement with the NNLL analytical calculation.

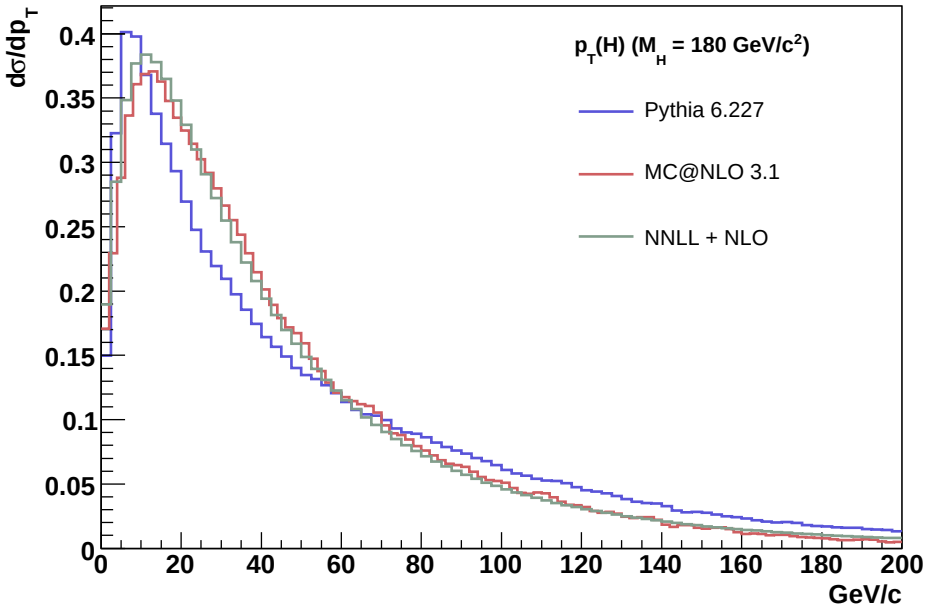

Figure 6.25: The full NNLL+NLO result is compared with the LO and NLO ones for the Higgs boson with a mass of 180 GeV/c^2. The three distributions are normalized to the same cross section.

Chapter 7

$H \rightarrow ZZ^{(*)} \rightarrow \mu^+\mu^-\mu^+\mu^-$, Event Selection

To extract the $H \rightarrow ZZ^{(*)} \rightarrow 4\mu$ signal from the most important sources of background, selection criteria, based on the kinematical characteristics described in the previous Chapter, can be used.

Selection cuts were designed to maximize the expected signal statistical significance with an integrated luminosity of 20 fb^{-1}, one year of LHC operation at the designed low luminosity. To account for the presence of one or two on-shell Z bosons in the final state, two different mass regions were considered: below and above the ZZ threshold.

In this Chapter the selection criteria applied both below and above the ZZ threshold are described in details. Then the discovery potential of the Higgs boson in the mass range $115 < M_H < 600$ GeV/c^2 with the $H \rightarrow ZZ^{(*)} \rightarrow 4\mu$ channel is reported.

7.1 Detector response simulation and reconstruction

All the generated events, as described in previous Chapter, were processed with `OSCAR_3_6_5` to simulate the detector response and then digitized with `ORCA_8_7_1`, adding minimum bias pile-up events of the Monte Carlo Official Production. Low luminosity conditions are simulated by superimposing on average 3.4 events with

low transfered momentum to the interesting one.

All the samples have been preselected by requiring $|\eta_\mu| < 2.4$, a p_{T}^{μ} in excess of 3.0 GeV/c and the invariant mass of the muon-antimuon pairs to lay between 5 and 150 GeV/c^2. The invariant mass distributions of the four muons coming from Higgs boson decay (three different masses) and from the background after the preselection cuts only are shown in Fig. 7.1. The contributions of the three main background sources are also shown.

The reconstruction of the four muons in the events was performed using `ORCA_8_7_3` and in particular the `GlobalMuonReconstructor` offline algorithm which gets muon trajectories at the innermost muon station and propagates them to the outer Tracker surface and then to the interaction point [40].

In signal events the reconstruction efficiency (ϵ_{reco}), expressed as the ratio between number of events with four reconstructed muons and the total number of simulated events, is about 65% for $\mathrm{M_H} = 115$ GeV/c^2 and increases with the Higgs

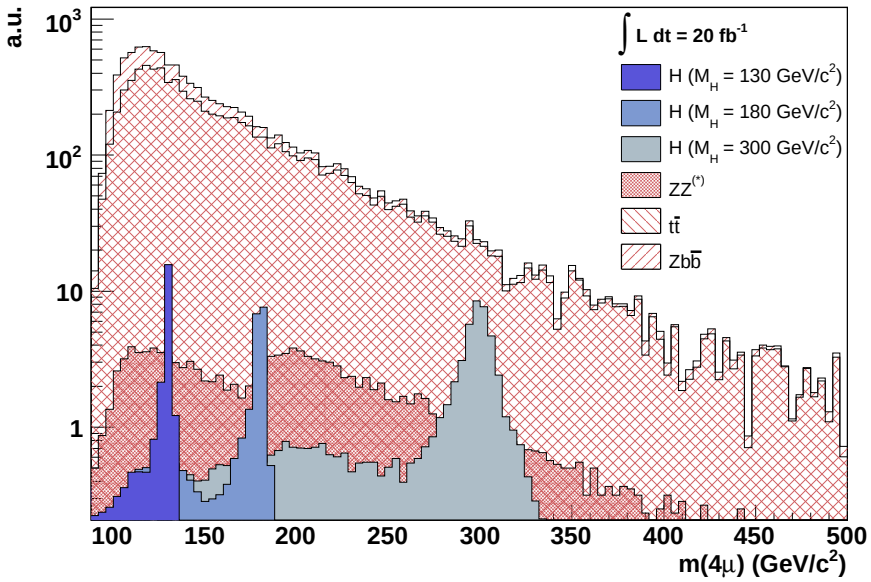

Figure 7.1: The invariant mass distributions of the four muons coming from Higgs boson decay and from the three main sources of background after the preselection cuts described in the text.

boson mass up to $\sim 90\%$ for $M_H > 300$ GeV/c^2. For $ZZ^{(*)}$ the efficiency is 70% while in $t\bar{t}$ and $Zb\bar{b}$ it is lower, $\sim 48\%$ and $\sim 34\%$ respectivley. Muons coming from b jets have indeed a softer p_T spectrum and are reconstructed less efficiently.

7.1.1 Online event selection

The online selection of $H \rightarrow ZZ^{(*)} \rightarrow \mu^+\mu^-\mu^+\mu^-$ events relies on the single-muon and di-muon triggers. In the present study the full online selection has not been applied to the simulated events, in particular, thresholds on muon p_T and η acceptance of the Trigger have not been applied.

In the low luminosity running period, the Level-1 Trigger accepts muons in the barrel region only, e.g. $|\eta| < 2.1$. The transverse momentum threshold for single-muon selection is 14 GeV/c, while the threshold for di-muon events is 3 GeV/c. In the High-Level Trigger, p_T thresholds of 19 GeV/c for single muons and of 7 GeV/c for di-muons events are chosen.

It has been already stressed that the studied channel is characterized by a final state with four high p_T muons. Therefore the probability to have one or two muons out of the four within the Trigger thresholds is expected to be very high.

In order to correctly estimate the Trigger efficiency, a signal sample has been processed. The reconstruction of the muons has been performed through the simulation of the CMS Trigger system using the `L3MuonReconstructor` algorithm. As expected the Trigger efficiency is very high, greater than 99%.

To summarize, the inefficiency of the online selection for the channel under study is expected to be below 1% and therefore it has been neglected in this study.

7.2 Offline event selection

In this Section the event selection criteria used in the present analysis are described. The cut thresholds vary according to the Higgs boson mass. In order to perform a mass dependent threshold optimization a `ROOT` [118] macro, based on the minimization package `MINUIT` [119], has been developed.

7.2.1 Selection above ZZ threshold

Di-muon mass and transverse momenta

For each event all possible combinations of two muon-antimuon pairs are considered. The reconstructed Z mass distribution obtained in signal events with $M_H = 200$ GeV/c^2 is shown in Fig. 7.2.

Both di-muon pairs must have an invariant mass compatible with the Z hypothesis, for example for $M_H = 200$ GeV/c^2 it must be within 10 GeV/c^2 from the nominal Z mass, $M_Z = 91.2$ GeV/c^2. The $t\bar{t}$ and $Zb\bar{b}$ backgrounds are suppressed, leaving ZZ events as the only relevant background.

The distributions of the four muon transverse momenta in signal events with $M_H = 200$ GeV/c^2, in $Zb\bar{b}$ and in $t\bar{t}$ events are shown in Fig. 7.3, sorted according to the p_T. The corresponding distributions in ZZ are similar to those of the signal and a significant rejection against this background can not be achieved using these variables. Cuts at 20 GeV/c and 15 GeV/c are applied to the most energetic two

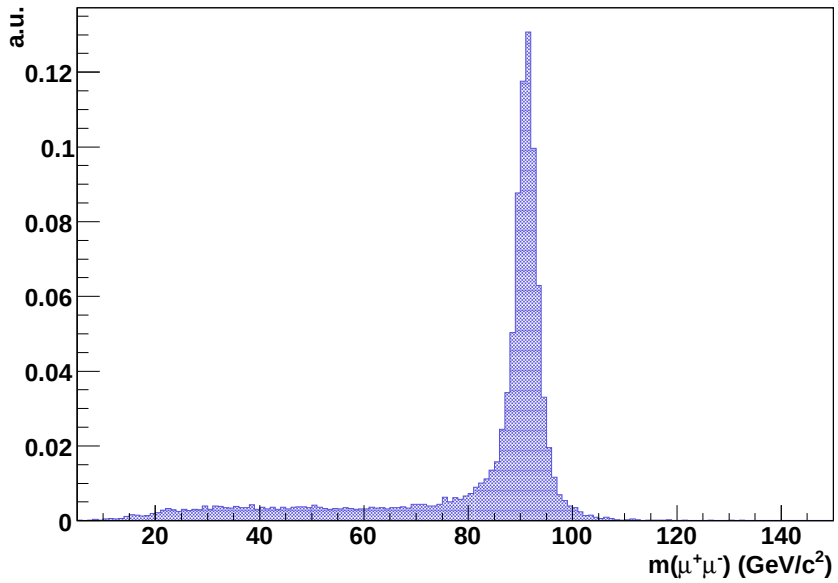

Figure 7.2: Reconstructed Z mass distribution in signal events with $M_H = 200$ GeV/c^2.

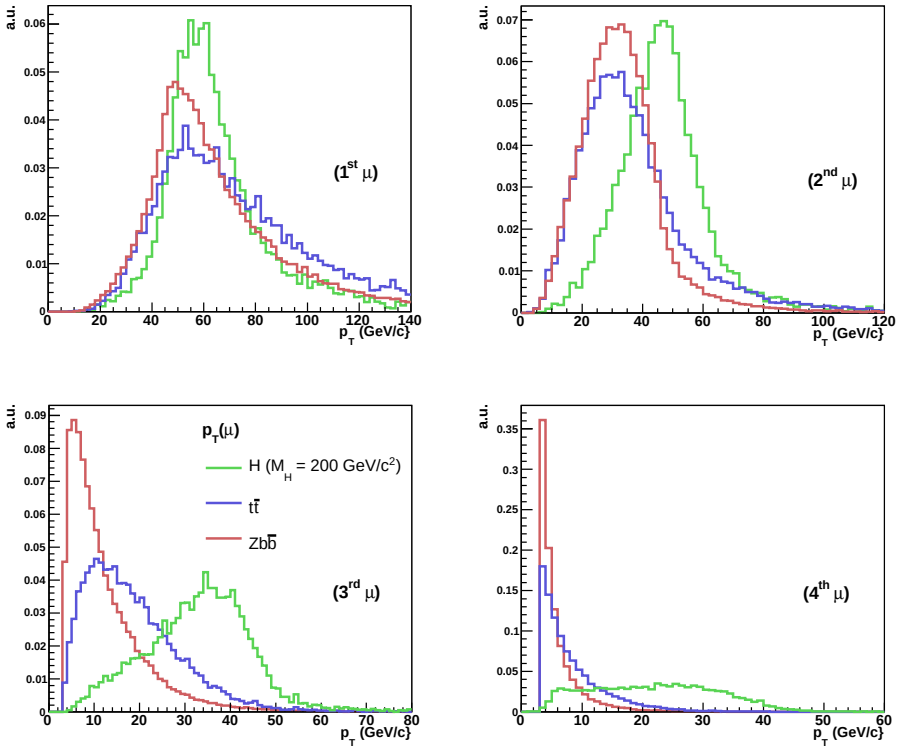

Figure 7.3: p_T distributions of the muons, before any other cut, in signal events with $M_H = 200$ GeV/c^2, $t\bar{t}$ and $Zb\bar{b}$ events. In each event the four muons are sorted according to the p_T value.

muons, with a signal efficiency of more than 98%. Cuts with variable thresholds are then applied to the other two muons. Due to the soft p_T spectrum of the softest muon in $t\bar{t}$ and $Zb\bar{b}$ events further reduction of those backgrounds can be easily achieved. The related efficiencies are: more than 98% for Higgs boson signal and ZZ, 55% and 35% for $t\bar{t}$ and $Zb\bar{b}$ respectively.

Transverse momentum of the four muons cut

The gluon fusion contribution is about 80% of the signal cross section. This is a $2 \rightarrow 1$ process and the produced Higgs boson has a small p_T, of the order of the gluon transverse momentum inside the proton. Higgs bosons with higher p_T are produced by higher order processes, where the Higgs boson is generated with one

or more partons in the final state.

Even for the ZZ background the transverse momentum of the four muon system with respect to the incident protons is generated by higher order processes, but the predominance of the quark-antiquark annihilation as production mechanism gives it a softer transverse momentum distribution than that of the signal.

The p_T distribution of the four muons system in signal events with M_H = 200 GeV/c^2 and 300 GeV/c^2 and in ZZ background events is shown in Fig. 7.4.

In order to reduce the ZZ background against the signal a p_T cut on the four muon system is applied with a variable threshold between 10 and 18 GeV/c according to the Higgs mass, with an efficiency greater than 80% for the signal and of about 50% for the ZZ.

A summary of the reconstruction efficiency, cut thresholds and selection efficiencies in the case M_H = 200 GeV/c^2 is given in Table 7.1. The efficiencies for the other Higgs boson masses are shown in Appendix A.

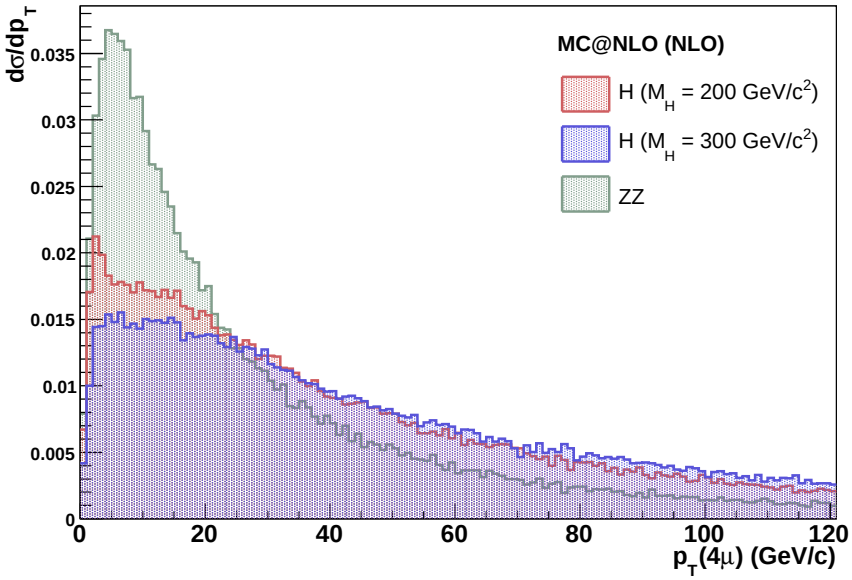

Figure 7.4: Higgs boson candidate p_T distribution in signal (M_H = 200 and 300 GeV/c^2) and ZZ$^{(*)}$ background events. The distributions are normalized to the same cross section.

Table 7.1: Efficiencies after applying the cuts described in the text for $M_H = 200$ GeV/c^2.

	ϵ_{reco}	Z **mass cut** (8 GeV/c^2)	p_T^{μ} **cut** (20, 15, 15, 10 GeV/c)	$p_T^{4\mu}$ **cut** (10 GeV/c)
H (200 GeV/c^2)	82.9%	46.9%	45.1%	38.7%
ZZ	71.5%	28.1%	27.0%	15.2%
$Zb\bar{b}$	34.0%	0.14%	0.08%	0.07%
$t\bar{t}$	48.2%	0.07%	0.05%	0.05%

7.2.2 Selection below the ZZ threshold

Isolation

Signal events have four *isolated* muons in the final state and the same holds for $ZZ^{(*)}$ background events. In $t\bar{t}$ and $Zb\bar{b}$ events instead the two muons coming from b-quark decays are *not isolated*. An isolation cut therefore yields substantial rejection for these two backgrounds.

Two different algorithms, belonging to the standard `MuonIsolation` ORCA package [120] have been used: Tracker and Calorimeter isolation.

The base algorithm is sketched in Fig. 7.5. Both Tracker and Calorimeter isolation exploit the sum of a discriminant variable, p_T and E_T respectively, of all the reconstructed charged particles between a cone with a variable width $\Delta R = \sqrt{\Delta\eta^2 + \Delta\phi^2}$ and a veto cone ($\Delta R = 0.005$) both around the muon direction. The veto region is needed in order to exclude the muon itself in the calculation. Muons are considered isolated if the summed p_T (E_T) is lower than a fixed threshold p_T^{max} (E_T^{max}).

The Tracker isolation cut efficiencies on signal and background as a function of $p_T^{\max}$ for a cone size $\Delta R = 0.25$ are shown in Fig. 7.6. With the threshold $p_T^{\max} = 4.0$ GeV/c, the efficiency is about 10% for $t\bar{t}$ and 30% for $Zb\bar{b}$, while signal (both $M_H = 130$, 160 GeV/c^2) and $ZZ^{(*)}$ have an efficiency greater than 85%. The $Zb\bar{b}$ efficiency is three times greater than that for $t\bar{t}$ events because the b jets

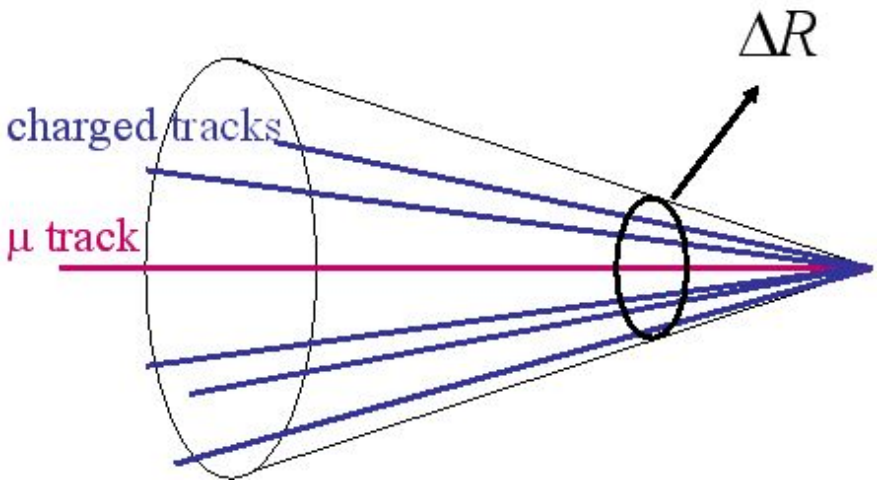

Figure 7.5: Schematic view of the `MuonIsolation` algorithm.

in $Zb\bar{b}$ events are less energetic and muons coming from them tend to be more isolated.

The cone sizes chosen in the analysis are $\Delta R = 0.25$ in Tracker and $\Delta R = 0.45$ in Calorimeter. The thresholds vary from 3 to 4.5 GeV/c in the Tracker isolation and from 10 to 20 GeV/c^2 in the Calorimeter isolation.

Di-muon mass and transverse momenta

For each event, all possible combinations of opposite signed muon pairs are built. At least one combination is required to have one and only one muon pair with an invariant mass compatible with a Z hypothesis, $M_Z = 91.2$ GeV/c^2. For example for $M_H = 130$ GeV/c^2 it must be within 15 GeV/c^2. The reconstructed Z mass distribution is shown in Fig. 7.7.

The signal efficiency is about 75% for $M_H = 130$ GeV/c^2 and $M_H = 150$ GeV/c^2 and 40% in ZZ^* background. This cut alone rejects more than 70% of $t\bar{t}$ events and $Zb\bar{b}$ background.

Cuts at 15 GeV/c and 12 GeV/c are applied to the p_T of the most energetic two muons. Variable cuts depending on M_H are then applied to the other two muons, for example for $M_H = 130$ GeV/c^2 the thresholds are 12 GeV/c and 8 GeV/c. The overall efficiencies for this set of p_T cuts are near 72% for signal at 130 GeV/c^2, 65% for $ZZ^{(*)}$, 20% for $Zb\bar{b}$ and 50% for $t\bar{t}$.

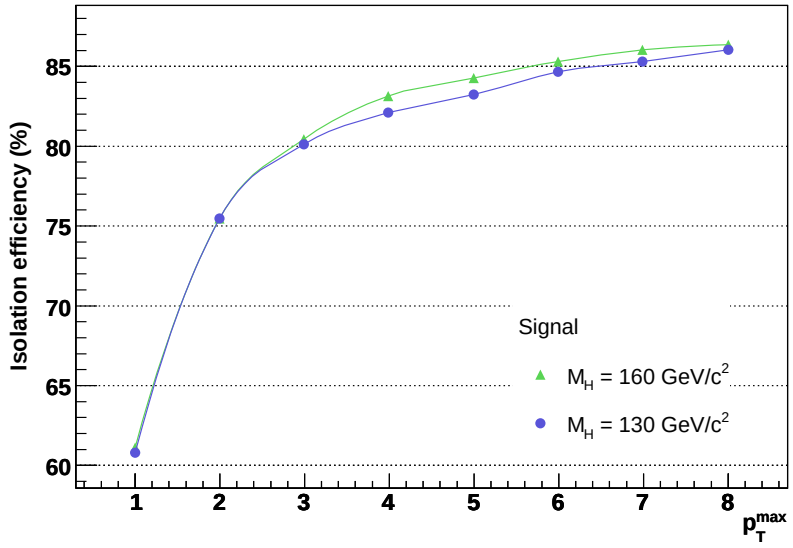

(a)

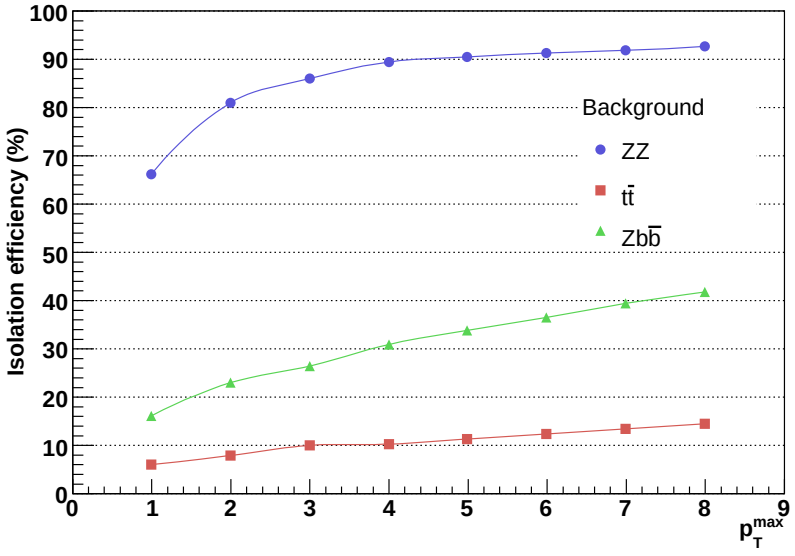

(b)

Figure 7.6: Tracker isolation cut acceptances as a function of the threshold p_{T}^{max} ($\Delta R = 0.25$) for signal (a) and background (b).

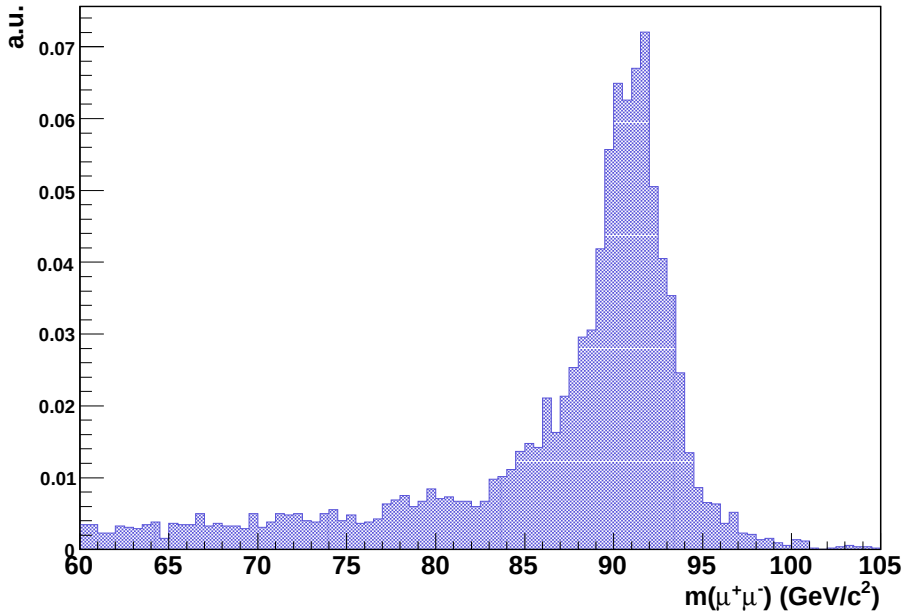

Figure 7.7: Reconstructed Z mass distribution in signal events with $M_H = 130$ GeV/c^2.

A summary of the reconstruction efficiency, cut thresholds and selection efficiencies in the case $M_H = 130$ GeV/c^2 is given in Table 7.2. The efficiencies for the other Higgs boson masses are shown in Appendix B.

7.3 Additional cuts

Isolation cuts allow to highly suppress the $t\bar{t}$ and $Zb\bar{b}$ backgrounds below the signal level and finally the $ZZ^{(*)}$ background remains as the most important contribution. Besides the cuts used up to now in the analysis, there are some additional cuts which could help to further suppress these backgrounds.

Those additional cuts however reduce the number of signal events without a substantial rejection of the $ZZ^{(*)}$ background. Therefore they have not been applied in the present analysis, preferring a greater signal selection instead.

Table 7.2: Efficiencies after applying the cuts described in the text for $M_H = 130$ GeV/c^2.

	ϵ_{reco}	Z **mass cut** (15 GeV/c^2)	p_T^μ **cut** (15, 12, 12, 8 GeV/c)	**isolation cut** (3, 15 GeV/c)
H (130 GeV/c^2)	75.4%	55.0%	39.9%	34.9%
ZZ	71.5%	29.3%	19.4%	17.0%
$Zb\bar{b}$	34.0%	10.8%	2.57%	0.15%
$t\bar{t}$	48.2%	8.48%	3.97%	0.06%

7.3.1 Decay angle cut

To further reduce the $ZZ^{(*)}$ background, the scalar nature of the Higgs boson can be exploited by cutting on the Higgs boson decay angle θ_D, i.e. the angle between the reconstructed Z and H direction in the H rest frame. The $\cos\theta_D$ distribution in signal and background events is shown in Fig. 7.8. The $Zb\bar{b}$ background peaks at $\cos\theta_D = 1$ because the Z boson has a large momentum compared to the muon pair from b quarks. About 85% of the signal is kept by the requirement that $\cos\theta_D$ be greater than 0.7, while the efficiency is 70% for ZZ and $t\bar{t}$ and about 55% for $Zb\bar{b}$.

7.3.2 Muon transverse impact parameter cut

It is possible to further reduce $Zb\bar{b}$ and $t\bar{t}$ backgrounds, where two muons come from secondary vertices, by applying a cut on the transverse impact parameter of the muons with respect to the beam line. As an example, requiring all four muons to have a transverse impact parameter within 200 μm rejects 36% of the $Zb\bar{b}$ and 44% of the $t\bar{t}$, while 98% of the Higgs signal at 130 GeV/c^2 is kept.

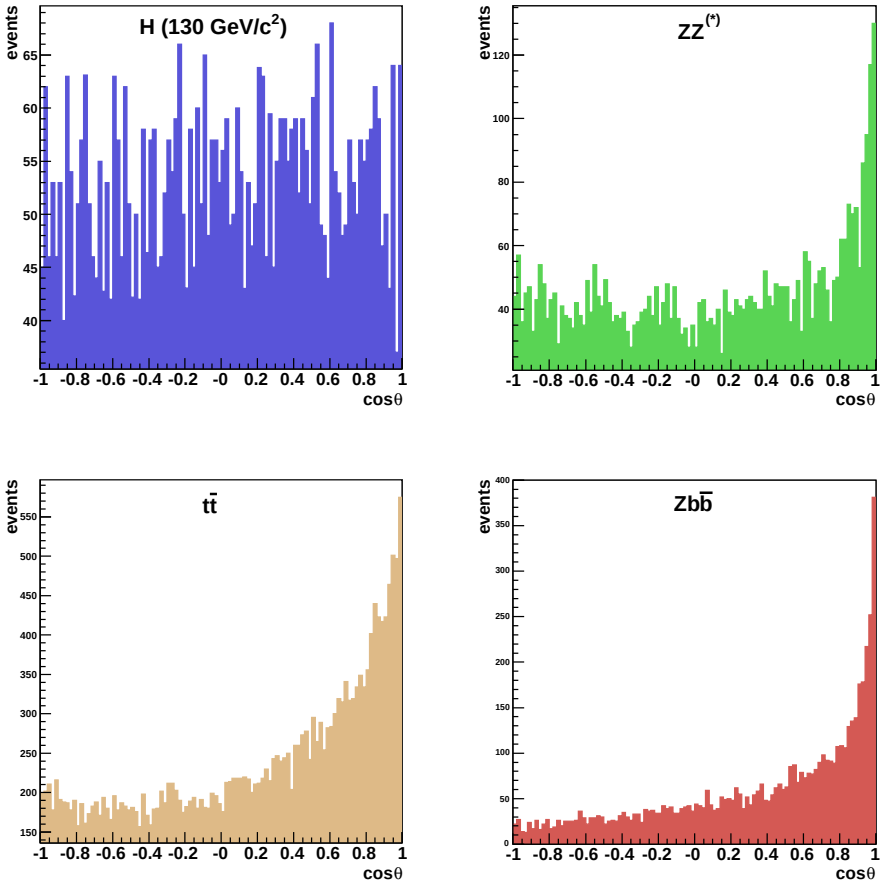

Figure 7.8: Distribution of $\cos\theta_{\mathrm{D}}$ in signal and background events.

7.4 Additional background sources

In this Section additional background sources are reviewed and their influence on the results of the present analysis is studied in detail.

7.4.1 Zjj background

The total cross section foreseen by `PYTHIA` for the production of a Z boson in association with two c or light quarks is about 40 times greater than the Zb$\bar{\mathrm{b}}$ one

$$\sigma_{LO}(\mathrm{Zjj}) = 30\ 425\ \mathrm{pb}\,. \tag{7.1}$$

Though the probability to find four muons in the final state is much lower the contribution of this background may not be negligible. To estimate it a fully simulated sample of about one million of events available within the Official Production has been used. The production of the sample has been carried out using the PYTHIA Monte Carlo generator. The only preselection required in this sample is the Z boson forced to decay in a pair of leptons.

The fraction of Zjj events with a four muon final state with $p_T > 3.0$ GeV/c and $|\eta| < 2.4$ in this sample is $\sim 2 \cdot 10^{-5}$. The p_T spectrum of the muons coming from jet hadronization is shown in Fig. 7.9. The muons are very soft and only a small fraction (0.2%) has a $p_T > 3.0$ GeV/c, the minimum p_T needed to reach the muon chambers. Therefore the number of Zjj expected events for an integrated luminosity of 20 fb^{-1} is 1 460, about half of the expected Zb$\bar{b}$ events, see Tab. 6.3.

The same set of cuts described above has been applied to the Zjj sample. Both below and above ZZ threshold no Zjj event passes the selection.

The limited available statistic does not allow to set an upper limit to the final

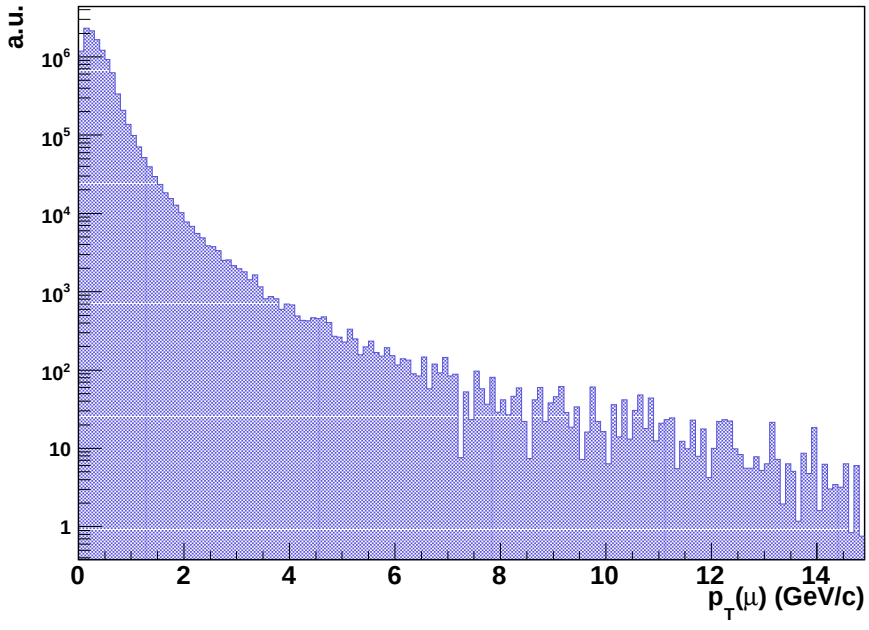

Figure 7.9: p_T distribution of the muons coming from c or light jets in Zjj events.

cross section of the events surviving the selection. In a conservative approach however, the Zjj selection efficiency can be assumed to be the same of the $Zb\bar{b}$ events. According to the expectation of the number of events, the selected Zjj events should be about half of the $Zb\bar{b}$ events which in turn are greatly reduced by the selection cuts as can be seen in Tab. 7.3; thus Zjj background can be regarded as negligible.

7.4.2 Background from multiple collisions

Events with muons from different collisions in the same bunch crossing may become a significant source of background due to the much higher rates compared to genuine 4μ processes. The extra muon might also occur in the same collision, but from a double parton scattering process.

Sources of 3μ backgrounds result from processes which could also give a four muon background like $t\bar{t}$, $Zb\bar{b}$ and $ZZ^{(*)}$. There can also be other processes like $Wb\bar{b}$ and ZW. All of the backgrounds are characterized by the occurrence of a heavy gauge boson. This heavy particle is needed in order to mimic kinematic distributions similar to the signal. The total cross sections for these three muons backgrounds has been estimated to be 21 pb [121].

The expected rate of single muons was studied with `PYTHIA`; in minimum bias events, the probability of occurrence of such muons is determined to be $6.12 \cdot 10^{-4}$, after preselection cuts of $p_{\mathrm{T}} > 3$ GeV/c, $|\eta| < 2.4$. Misidentified muons and the effect of non prompt muons must be studied with the full detector simulation.

For this purpose, the large minimum bias sample of 200 000 fully simulated events was analysed. The probability for the occurrence of reconstructed muons satisfying the preselection criteria $p_{\mathrm{T}} > 3$ GeV/c and $|\eta| < 2.4$ was thus determined to be $(3.6 \pm 0.4) \cdot 10^{-4}$. Overall, the probability of an extra single, reconstructed muon within the preselection cuts was determined to be approximately 10^{-3} per collision. To get the cross section of an event consisting of a three muon process plus one extra muon, $\sigma_{3\mu+\mu}$, the three muon cross section, $\sigma_{3\mu}$, is multiplied by the probability for such an extra muon to occur in any of the collisions of the event,

$$\sigma_{3\mu+\mu} = \sigma_{3\mu} \cdot P(\mu) \cdot N_{pu} \,. \tag{7.2}$$

Here, $P(\mu)$ is the probability to find one reconstructed muon in a minimum bias event, and N_{pu} is the number of underlying events. Thus at low luminosity (when $n_{pu} = 3.4$) the resulting cross section is estimated to be about 21 fb.

In order to estimate the contribution of single muons in combination with three muon processes to the background after all cuts, the muons found in a sample of fully simulated three muon events must be combined with reconstructed, single muons from the minimum bias sample. A detailed study of the dominant three muon background, $Zb\bar{b}$, is described below [121]. Dedicated data samples of the $Zb\bar{b} \rightarrow 3\mu$ background and of minimum bias events with a muon in each event were produced and processed through the full simulation.

The efficiency to reconstruct all three muons of the $Zb\bar{b}$ background was found to be 47%. The reconstruction efficiency of single muons from minimum bias is 35%, which is rather low due to the typically very low value of p_T of such muons as described in Chapter 2. All cuts described above, for a Higgs mass of 130 GeV/c^2, are applied to the combined events. Furthermore the invariant mass of the four muons is required to lie in the range $110 \div 145$ GeV/c^2. The final rejection factor is 10^{-4}.

An additional muon in the same collision could arise either from a misidentified muon in the beam remnant, or from double parton scattering. The cross section of double parton scattering is estimated to be [122]

$$\sigma_{doubleparton} = \frac{\sigma_{3\mu} \cdot \sigma_{1\mu}}{\sigma_{eff}}\,, \tag{7.3}$$

where $\sigma_{1\mu}$ is the one muon cross section of the minimum bias, and σ_{eff} is estimated to range between $(10 \div 30)$ mb, which is not far from the minimum bias cross section.

The total four muon cross section of 21 fb approximates well the case of double parton scattering. The cross section after all cuts for three muon background plus an extra muon from a double parton scattering is estimated to be only 0.002 fb. In case of three muons plus a minimum bias muon a vertex cut could further reduce this background with a rejection factor of 0.003.

In summary this background is totally negligible compared to the other background sources.

7.5 Discovery potential

The invariant mass distributions of the Higgs boson were fitted with a double Gaussian function in order to take into account the radiative tails. The σ_H was

then calculated as the weighted mean of the two sigmas of the Gaussian distributions. The resolution on the Higgs boson mass, σ_H, is about 2.4 GeV/c^2 for $M_H = 200$ GeV/c^2. At 300 GeV/c^2 and 500 GeV/c^2, σ_H is completely dominated by the natural width and amounts to respectively 9 GeV/c^2 and 36 GeV/c^2. The reconstructed mass peak at $M_H = 500$ GeV/c^2 is shifted by about 10 GeV/c^2 due to internal bremsstrahlung and to the showering of high energy muons which worsen track reconstruction. Those effects are clearly shown in Fig. 7.10.

For Higgs boson masses below the ZZ threshold the resolution on the Higgs boson mass is completely dominated by the muon momentum resolution, the natural width of the Higgs boson is in fact less than 0.2 GeV/c^2 for $M_H < 160$ GeV/c^2. The reconstructed Higgs boson mass distributions in the two cases are shown in Fig. 7.11. The measured resolution is about 1.1 and 1.4 GeV/c^2 for $M_H = 130$ GeV/c^2 and 160 GeV/c^2 respectively.

In a real experiment a discovery is claimed when the probability for the background to reproduce the observed events is less than $2.85 \cdot 10^{-7}$, corresponding to a deviation by more than 5σ on the positive tail of a Gaussian distribution. In a planned experiment, however, an expected significance of five means that this experiment has 50% probability of discovery, in case the signal hypothesis is correct. In order to estimate the expected significance, events were counted in a window of variable width (depending on M_H) around the reconstructed Higgs boson mass and compared to the number of background events alone. Some examples of signal efficiencies for the mass cut are: about 87% for $M_H = 130$ GeV/c^2, about 85% for

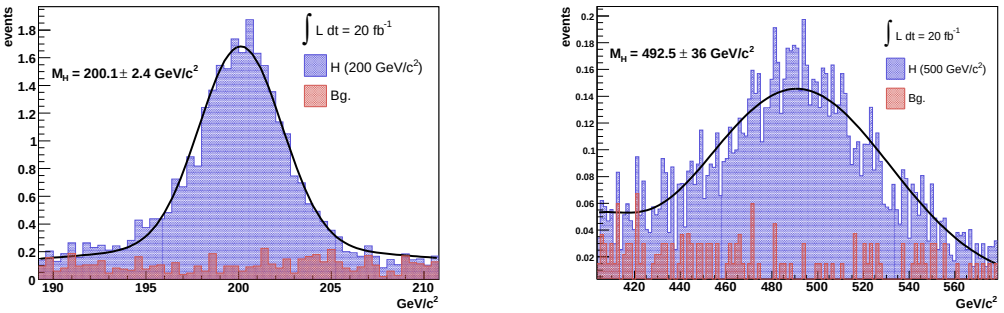

(a) (b)

Figure 7.10: Reconstructed Higgs boson mass in signal at $M_H = 200$ GeV/c^2 on the left and at $M_H = 500$ GeV/c^2 on the right.

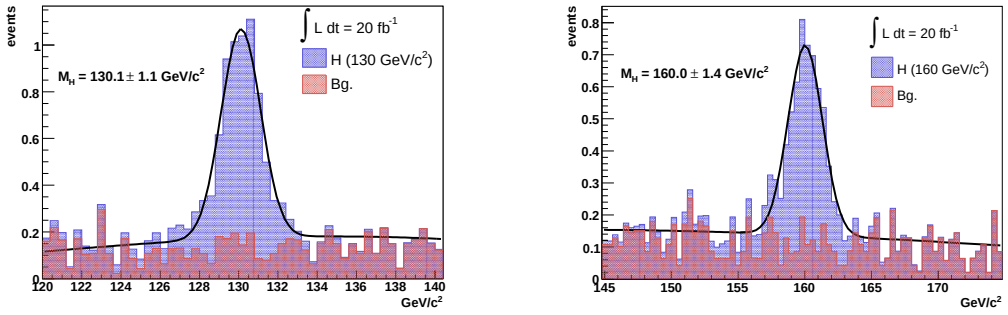

(a) (b)

Figure 7.11: Reconstructed Higgs boson mass for $M_H = 130$ GeV/c^2 on the left and for $M_H = 160$ GeV/c^2 on the right.

$M_H = 200$ GeV/c^2 and 86% for $M_H = 600$ GeV/c^2. The final cross sections for signal and background events after all selection cuts are shown in Table 7.3.

In the limit of large number of background events, the significance is given by $S_1 = N_s/\sqrt{N_b}$. Since in the present case the number of events is of the order of 10, the Gaussian approximation cannot be used, and the Poisson probability distribution

$$f(n;\lambda) = \frac{\lambda^n}{n!}\exp(-\lambda)$$

must be considered. The significance was therefore estimated using the likelihood ratio [123], i.e.

$$Q = \frac{\mathcal{L}_{S+B}}{\mathcal{L}_B} = \left(1 + \frac{N_s}{N_b}\right)^{N_s+N_b} \exp(-N_s)\,,$$

where N_s and N_b are respectively the number of signal and background events in the chosen mass window, $\mathcal{L}_B = f(N_s + N_b; N_b)$ and $\mathcal{L}_{S+B} = f(N_s + N_b; N_s + N_b)$. The significance was defined as $S_L = \sqrt{2\ln Q}$ and it was found that $S_L = 5$ actually corresponds to 50% probability of discovery with the given expected signal and background events. The probability of discovery is given by [124]

$$P = \sum_{n=n_0+1}^{\infty} f(n; N_b + N_s)\,,$$

where n_0 is the maximum number of events compatible with the background only

Table 7.3: Final cross section for signal and background events after all the described cuts. The statistical error is also shown.

	σ_s (fb)	σ_b (fb)		
M_H(GeV/c^2)	-	$ZZ^{(*)}$	$Zb\bar{b}$	$t\bar{t}$
115	0.050 ± 0.003	0.008 ± 0.003	0.024 ± 0.005	0.003 ± 0.002
120	0.108 ± 0.004	0.046 ± 0.007	0.039 ± 0.006	0.022 ± 0.006
130	0.295 ± 0.005	0.052 ± 0.007	0.012 ± 0.004	0.007 ± 0.004
140	0.451 ± 0.008	0.038 ± 0.006	0.008 ± 0.003	0.005 ± 0.003
150	0.557 ± 0.009	0.055 ± 0.007	0.005 ± 0.002	0.003 ± 0.002
160	0.270 ± 0.004	0.083 ± 0.009	0.017 ± 0.004	0.007 ± 0.004
170	0.077 ± 0.001	0.044 ± 0.007	0.002 ± 0.001	0.007 ± 0.004
180	0.151 ± 0.003	0.081 ± 0.009	0.014 ± 0.004	0.020 ± 0.006
190	1.041 ± 0.015	0.092 ± 0.008	0.004 ± 0.002	0.015 ± 0.005
200	1.083 ± 0.016	0.082 ± 0.007	0.009 ± 0.003	0.009 ± 0.004
250	0.919 ± 0.013	0.086 ± 0.008	0.016 ± 0.004	0.020 ± 0.006
300	0.540 ± 0.009	0.035 ± 0.005	0.001 ± 0.001	0.002 ± 0.002
350	0.752 ± 0.010	0.086 ± 0.008	0.003 ± 0.002	0.002 ± 0.002
400	0.710 ± 0.010	0.045 ± 0.005	0.005 ± 0.002	0.003 ± 0.002
450	0.506 ± 0.007	0.032 ± 0.005	0.006 ± 0.003	0.002 ± 0.002
500	0.421 ± 0.005	0.055 ± 0.006	0.004 ± 0.002	0.003 ± 0.002
550	0.289 ± 0.004	0.052 ± 0.006	0.001 ± 0.001	0.001 ± 0.001
600	0.214 ± 0.003	0.043 ± 0.005	0.002 ± 0.001	0.003 ± 0.003

hypothesis at 5σ, i.e.

$$\sum_{n=n_0+1}^{\infty} f(n; N_b) \leq 2.85 \cdot 10^{-7} .$$

An alternative significance estimator has been suggested recently. In this method [123], likelihood fits to the mass distribution are performed with the signal plus background and the background only hypotheses, and the significance is defined as $S_{L2} = \sqrt{2 \ln (\mathcal{L}_{\mathrm{S+B}}/\mathcal{L}_{\mathrm{B}})}$. In those fits only the number of background and signal events are left free, while the parameters for the shapes are fixed to the results obtained separately on background and signal events. As an example the fits performed for $\mathrm{M_H} = 300$ GeV/c^2 are shown in Fig. 7.12.

In Table 7.4 the expected number of signal and background events for an integrated luminosity of 20 fb^{-1} are shown together with the discovery probability and the different significance estimates.

Compared to S_L, the significance S_{L2} is slightly lower because the number of background events is not constrained to the expectations, but is left free to

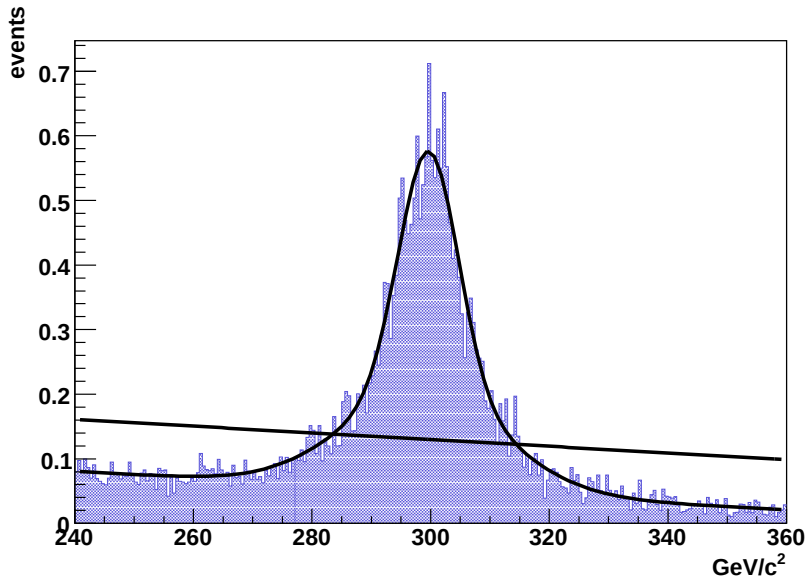

Figure 7.12: Results used to estimate S_{L2} for $\mathrm{M_H} = 300$ GeV/c^2. Fits to signal plus background distribution either with the background shape only and with both background and signal shape are shown.

Table 7.4: Number of expected signal and background events with 20 fb^{-1} integrated luminosity, together with 5σ discovery probability and significance estimates. The significance S_L with background set to its upper limit is given between parenthesis. The statistical uncertainty is also shown.

M_H(GeV/c^2)	N_s	N_b	5σ **prob.** (%)	S_L	S_{L2}
115	1.00 ± 0.06	0.60 ± 0.20	0.02	1.18 (0.9)	1.14
120	2.2 ± 0.8	1.42 ± 0.30	0.04	1.54 (1.43)	1.70
130	5.9 ± 0.1	1.42 ± 0.30	6.9	3.5 (3.3)	3.2
140	9.0 ± 0.2	1.02 ± 0.24	54.5	5.3 (4.9)	4.7
150	11.2 ± 0.2	1.26 ± 0.22	69.9	5.9 (5.7)	5.2
160	5.4 ± 0.08	2.0 ± 0.3	3.9	2.9 (2.8)	2.6
170	1.54 ± 0.02	1.06 ± 0.24	0.04	1.26 (1.16)	1.05
180	3.2 ± 0.1	2.2 ± 0.3	0.1	1.81 (1.73)	1.22
190	20.8 ± 0.3	1.94 ± 0.22	98.9	8.5 (8.1)	7.5
200	21.7 ± 0.3	2.0 ± 0.3	99.3	8.7 (8.3)	7.7
250	18.4 ± 0.3	2.8 ± 0.3	89.7	7.0 (6.8)	5.6
300	10.8 ± 0.2	0.76 ± 0.16	81.4	6.4 (6.2)	5.0
350	15.1 ± 0.2	1.80 ± 0.24	86.0	6.7 (6.6)	5.5
400	14.2 ± 0.2	1.06 ± 0.18	93.8	7.3 (7.0)	5.9
450	10.1 ± 0.1	0.8 ± 0.2	75.9	6.1 (5.7)	4.2
500	8.4 ± 0.10	1.22 ± 0.20	36.9	4.8 (4.6)	3.4
550	5.8 ± 0.1	1.08 ± 0.16	15.7	3.7 (3.5)	3.0
600	4.3 ± 0.1	0.96 ± 0.16	4.2	3.1 (2.9)	2.6

partially accommodate for the signal excess, thus reducing the likelihood ratio.

The expected significance calculated with both estimators after an integrated luminosity of 20 fb^{-1} is shown in Fig. 7.13 (left). On the right-hand side of this figure a comparison between the results obtained by a fast simulation study performed by the ATLAS Collaboration in the channel $H \rightarrow ZZ^{(*)} \rightarrow 4\ell$ [125] and the present study is reported. To compare the results the efficiencies in the four electron and in the mixed e-μ channel are assumed equal to the four muon channel.

Whatever method is used to estimate the significance, with an integrated luminosity of 20 fb^{-1} a good discovery probability is found for an Higgs boson mass from 200 to 500 GeV/c^2 and from 130 to 150 GeV/c^2. In fact only few months of data taking at the nominal low luminosity should be needed for a discovery in this mass range. For a Higgs boson mass below 130 or above 500 GeV/c^2, and in the region $160 \div 180$ GeV/c^2, different channels will have to be combined to discover it in the first year of data taking. In Fig. 7.14 the luminosity required for a five sigma expected significance is reported as a function of the Higgs boson mass.

7.6 Higher order corrections

Generally speaking, the number of events for a given integrated luminosity and a particular process, as computed at NLO, is given by

$$N/\mathcal{L} = \sigma_{NLO} = K_I \sigma_{LO}\,, \tag{7.4}$$

where K_I is called the inclusive K-factor, which is thus defined as the ratio of the inclusive (total) NLO and LO cross sections. At LO, the produced particle (system) has no transverse momentum, while in (N)NLO additional partons lead to a non-vanishing p_{T} spectrum.

Most experimental simulations are based on LO cross sections, supplemented with parton showering through the standard MC programs. Thanks to additional (mostly soft) jets, an approximate p_{T} spectrum of the particular final state is generated. However, this spectrum is at best an approximation, since only soft and collinear radiation from the primary parton subprocess can be generated correctly (QCD radiation at large transverse momenta is strongly suppressed and can be accounted for either with matrix-element corrections [126] or by matching the full NLO calculation to the parton shower [127]).

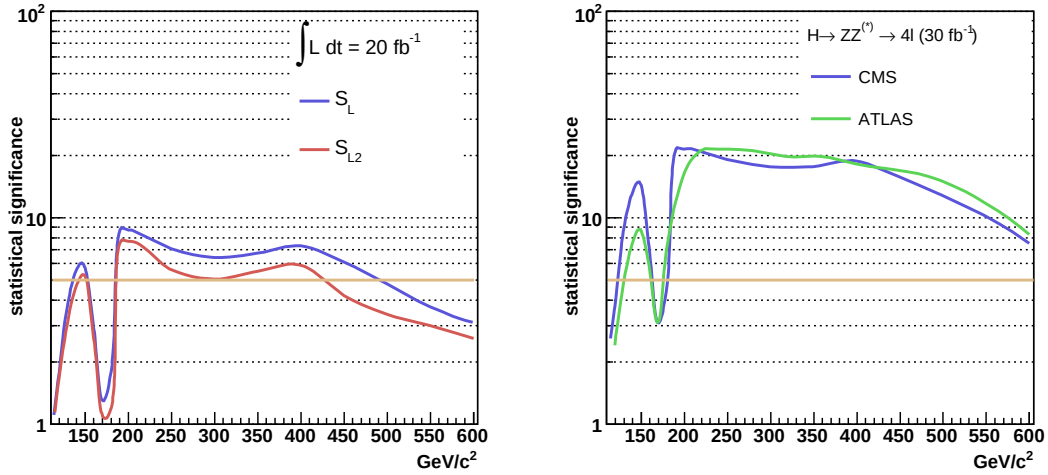

Figure 7.13: Expected statistical significance after an integrated luminosity of 20 fb^{-1} (left). A comparison between the results obtained by the present work and by a fast simulation study performed by the ATLAS Collaboration (right).

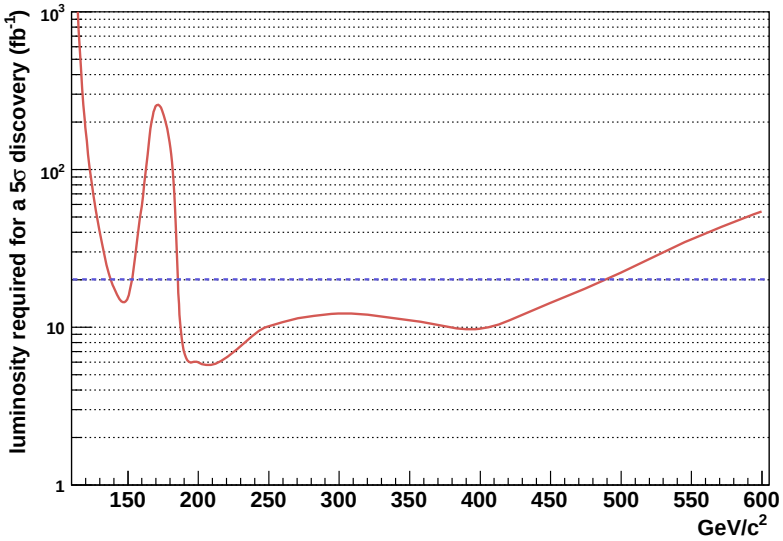

Figure 7.14: Luminosity required for a five sigma expected significance as a function of the Higgs boson mass.

On the other hand, if the (N)NLO calculation has been performed differentially as a function of a kinematical variable β, the above equation can then be rewritten as [128]

$$N/\mathcal{L} = \int \frac{d\sigma_{NLO}}{d\beta} d\beta = \int K(\beta) \frac{d\sigma_{MC-LO}}{d\beta} d\beta \,, \tag{7.5}$$

where the integral goes over the complete possible range of β, and the β-dependent K-factor is defined as

$$K(\beta) = \left(\frac{d\sigma_{NLO}(\beta)}{d\beta} \right) / \left(\frac{d\sigma_{MC-LO}(\beta)}{d\beta} \right) . \tag{7.6}$$

In order to study the effects of selection cuts that depend on β every simulated event can be corrected (reweighted) according to the differential K-factor defined in Eq. 7.6.

7.6.1 Results

As described in the previous Section the discovery potential of the Higgs boson with mass greater than $2M_Z$ is strongly related to the rejection efficiency of the p_T cut on the Higgs boson candidate. To better determine this efficiency the technique described before has been applied in order to correct the simulated events for signal and ZZ background according to the next-to-leading order prediction of the Monte Carlo generator `MC@NLO`.

In Fig. 7.15 the p_T distributions of the Higgs boson with M_H = 200 and 300 GeV/c^2 and of the ZZ system are shown. As already described in the previous Chapter, the NLO Higgs p_T spectrum is harder, for example leading order ZZ spectrum has to be corrected for the underestimation of the events in the high p_T region.

In order to include the higher order prediction in a more complete way the kinematical variables of the four final state muons generated by `MC@NLO` and `PYTHIA` have been compared, as shown in Fig. 7.16. The preselection acceptance increases by 2.5% in ZZ events due to the more central distribution of the muons, while the di-muon mass distributions of both Higgs and ZZ background are nearly identical as shown in Fig. 7.16b. Finally the p_T distributions of the generated muons are softer in the next-to-leading order case as the Higgs boson mass increases. The distributions for a Higgs boson with a mass of 300 and 500 GeV/c^2 is shown in Fig. 7.16c. This effect is clearer for the fourth (softest) muon leading to a worsening

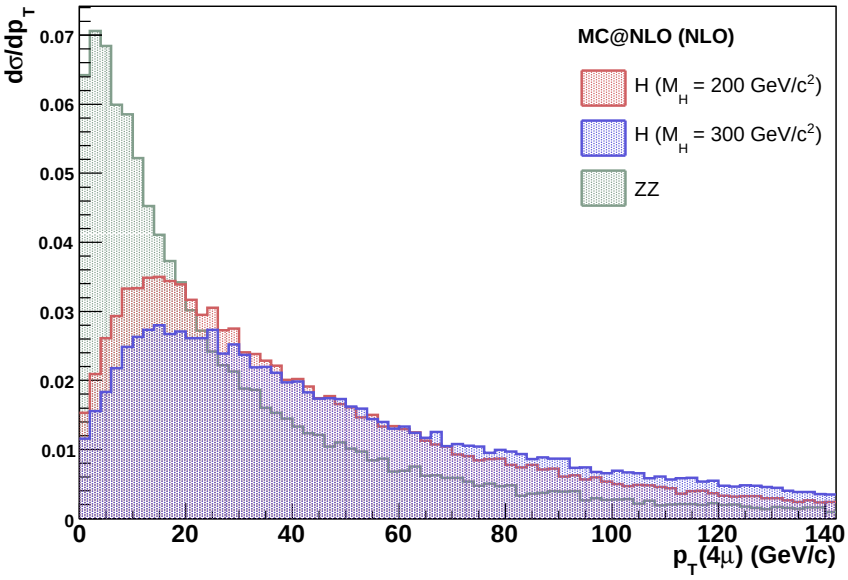

Figure 7.15: Higgs boson candidate p_{T} distribution in signal ($\mathrm{M_H}$ = 200 and 300 GeV/c^2) and $\mathrm{ZZ}^{(*)}$ background events.

of the efficiency of the p_{T} cut which is of a few percent for $\mathrm{M_H} = 300$ GeV/c^2 but 10% for $\mathrm{M_H} = 500$ GeV/c^2.

In Tab. 7.5 the efficiencies related to the selection cuts described in LO analysis are compared to those obtained at NLO for $\mathrm{M_H} = 200$, 300 and 500 GeV/c^2. As expected greater changes are in the p_{T} of Higgs candidate cut thresholds.

If the next-to-leading order predictions are taken into account with the same cut thresholds used in the LO analysis the significance decreases respectively from 8.7 to 8.3 and from 6.4 to 5.9 for $\mathrm{M_H} = 200$ and 300 GeV/c^2. For greater Higgs boson masses the results are worsened by the softer p_{T}^{μ} spectrum generated by `MC@NLO`, for $\mathrm{M_H} = 500$ GeV/c^2 it drops down from 4.8 to 3.5.

A further optimization of the cuts tends to decrease p_{T} thresholds in order to increase the number of selected signal events. The resulting significances are 8.6, 6.2 and 4.7 for $\mathrm{M_H} = 200, 300$ and 500 GeV/c^2 respectively.

In conclusion when the higher order predictions are included in the calculation of the selection cut efficiencies through the reweighting procedure the discovery potential is slightly reduced, especially at high Higgs masses.

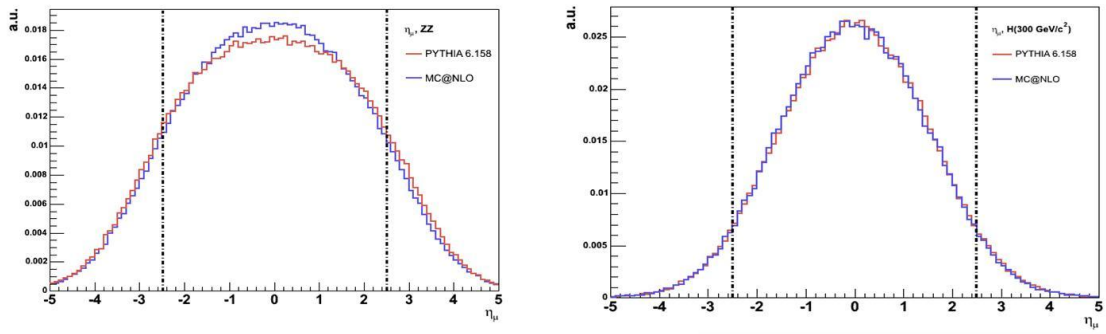

(a)

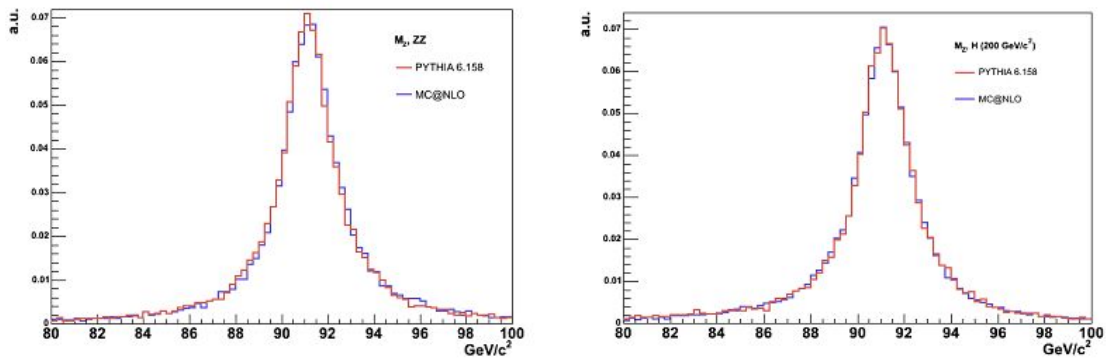

(b)

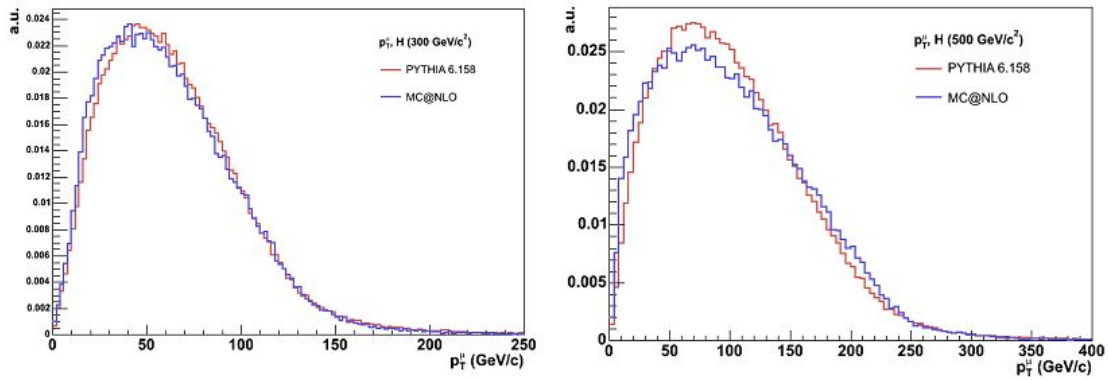

(c)

Figure 7.16: Comparison between the PYTHIA and MC@NLO prediction for η_μ (a) di-muon mass (b) and p_{T}^{μ} (c).

Table 7.5: Selection efficiencies obtained after reweighting of the events for $M_H = 200, 300$ and 500 GeV/c^2. In parenthesis the leading order efficiencies.

	Z mass cut	p_T^{μ} **cut**	$p_T^{4\mu}$ **cut**
H (200 GeV/c^2)	46.9% (46.9%)	44.4% (45.1%)	38.5% (38.7%)
ZZ	28.8% (28.1%)	27.5% (27.0%)	24.1% (15.2%)
H (300 GeV/c^2)	46.6% (46.6%)	40.3% (41.6%)	36.8% (37.4%)
ZZ	32.5% (31.9%)	28.6% (27.9%)	24.6% (15.9%)
H (500 GeV/c^2)	57.5% (57.5%)	47.9% (53.3%)	45.1% (50.1%)
ZZ	37.9% (37.1%)	32.7% (32.1%)	24.6% (18.8%)

Chapter 8

Z Boson Production in Association with Two b Quark

The discovery of new physics at hadron colliders often relies on a detailed understanding of Standard Model background processes. Prominent among these is the production of weak bosons (W, Z) in association with jets which contains a b quark.

In the search for an intermediate mass Higgs boson with the $H \rightarrow ZZ^{(*)} \rightarrow 4\mu$ channel, one of the possible backgrounds is the production and decay of a Z boson in association with two b quarks which with a probability of few percent yield a stiff lepton with sufficient isolation to mimic a lepton from an off-shell Z decay. The cross section is related to the b-quark parton density function therefore it is not precisely known. Moreover $Zb\bar{b}$ events are background to many other interesting physics channels at LHC, for example the SM channel $pp \rightarrow HZ$ with $H \rightarrow b\bar{b}$ or the MSSM channel $pp \rightarrow b\bar{b}H$.

A detailed understanding of $Zb\bar{b}$ events is therefore of crucial interest and a precise estimation of the production cross section is useful for b quark parton density function evaluation [129].

In the first part of this Chapter the jet finding algorithm and some technique to identify b-quark jets are reviewed. Then a technique to measure the $Zb\bar{b}$ cross section is presented and the obtained results are reported.

8.1 Jet reconstruction

8.1.1 Jet finding algorithm

The Calorimeter data are organized into towers. The towers are treated as massless particles with energy equal to the scalar sum of the energies of the components of the tower, and using the center of the tower and the nominal interaction point to define the jet direction.

Jet finding is done using a simple `Iterative Cone Algorithm`. In this algorithm, a list of towers is made, and a *protojet* is formed using the tower with the highest E_{T} (*seed tower*). The direction of the protojet is calculated from the transverse-energy-weighted angles of the towers in a cone of fixed width around the seed tower direction in η-ϕ space and the transverse energy of the protojet is calculated using the direction of the seed tower and the sum of the energies of the towers in the cone. The direction of this protojet is used to seed a new protojet iteratively. The procedure is repeated until the energy of the protojet changes by less than 1% between iterations and the direction of the protojet changes in $\Delta\eta^2 + \Delta\phi^2$ by less than 0.01, or until 100 iterations are reached.

When a stable protojet is found, the towers used to form the jet are removed from the list of detected objects, and the procedure is repeated until no objects are left or until the tower with the highest E_{T} is below a seed threshold, which is a parameter of the algorithm. The simple cone algorithm has therefore two parameters, namely the size of the cone and the minimum jet E_{T}.

8.1.2 Jet energy scale correction

The CMS Calorimeter system is optimized for the precision measurement of electrons and photons, and has a non-linear response to pions. Since the energy of a typical pion in a jet is roughly proportional to $1/\sin(\theta)$, where θ is the polar angle of the pion, the response of the Calorimeter to jets of a given transverse energy varies with η. In addition, since only those channels that are above a threshold are read out, a random cone on the Calorimeter could have a positive energy due to noise alone. At high luminosity, there will be an additional offset due to energy from particles from pile-up interactions.

Corrections for these effects are introduced both at Level-1 and in the HLT. At the start of the experiment, the corrections will be derived from Monte Carlo

data by comparing the energies of jets found using the generator-level particles of the hard interaction to jets reconstructed in the Calorimeter. As soon as sufficient data is collected, new corrections will be derived from single photon plus jet data and Z boson plus jet data.

In the following analysis jet energies are calibrated using the γ+jet algorithm. In this algorithm the total transverse momentum in the initial state of this scattering process is assumed negligible, then the direct photon produced in γ+jet events has a transverse momentum that is equal and opposite to the recoiling jet. The high resolution ($\sim 1\%$) of the Electromagnetic Calorimeter provides an accurate measurement of the photons and through the direct kinematical relationship is the basis of the jet calibration procedure [130].

8.2 B tagging

The identification of b-quark decays allows the selection of processes in which b quarks are produced in heavy particle decays. The identification of hadron jets originating from b quarks relies on the properties of B decays. B hadrons have a lifetime $\tau_B \sim 1.56$ ps, which corresponds to a $c\tau_B \sim 468$ μm, and produce on average five charged particles per decay.

The lifetime information can be exploited in different ways. The first class of methods relies on tracks with a large impact parameter. As shown in Fig. 8.1, tracks from B decays have a large impact parameter because they originate from a displaced vertex, while the impact parameter of tracks coming from the primary vertex is compatible with the tracking resolution.

A complementary approach is based on the reconstruction of the decay vertex associated with a B hadron. The reconstruction of this vertex would be the clearest evidence of such a decay. This method is however limited by the secondary vertex reconstruction efficiency.

Both methods rely on a powerful microvertex detector. Their power is limited both by inefficiency in track and vertex reconstruction and by the experimental resolution of tracks parameters. The mistagging rate for these algorithms is due to secondary interactions and decays of long-lived particles. Secondary interactions with the Tracker material can provide secondary vertices and thus tracks with a large impact parameter. Long-lived particles, such as K^0_S, Λ^0 and especially charm, can provide real decay vertices and therefore constitute a physical

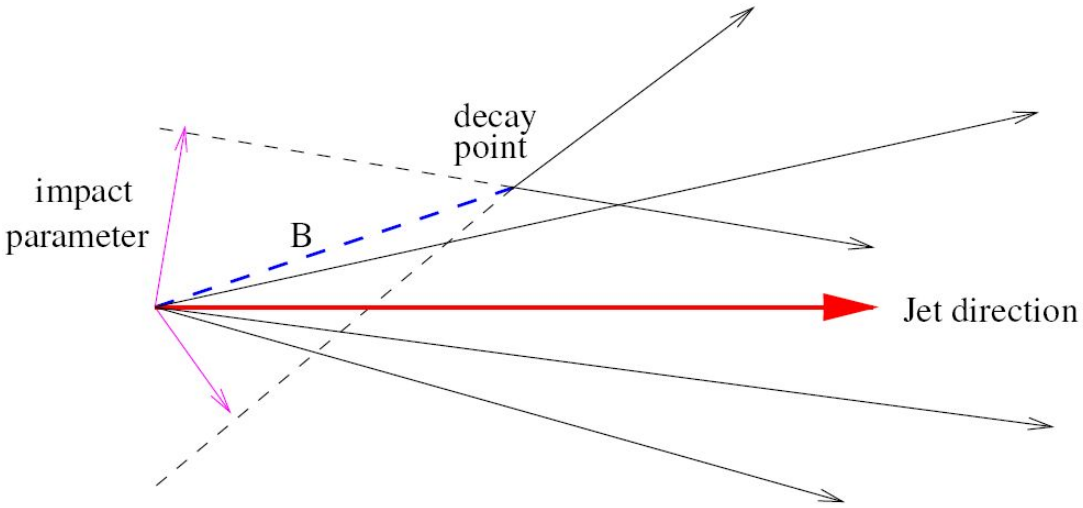

Figure 8.1: Representation (not on scale) of a hadron jet from a b quark.

irreducible background.

A completely different approach for b tagging relies on low p_{T} leptons produced in the decays b→clν and c→(d, s)lν. This method has a lower efficiency, since it is limited only to the leptonic decays (BR(b→ μ) $\sim$ 20%), but can be useful in analysis where the charge information carried by the lepton helps in determining the flavour of the B meson.

The best performance however is obtained by combining results from the different methods since a greater amount of information about B decays would be used.

The b-tagging performance is studied in terms of the b-tagging efficiency (ϵ_b) and mistagging rate (ϵ_j). Both variables are related to the single jet: the b-tagging efficiency is the fraction of jets tagged as b, while the mistagging rate is the fraction of non b-jets tagged as b in the samples with light quark and c$\bar{\mathrm{c}}$ pairs.

In the following two b-tagging algorithms used in the analysis are briefly described.

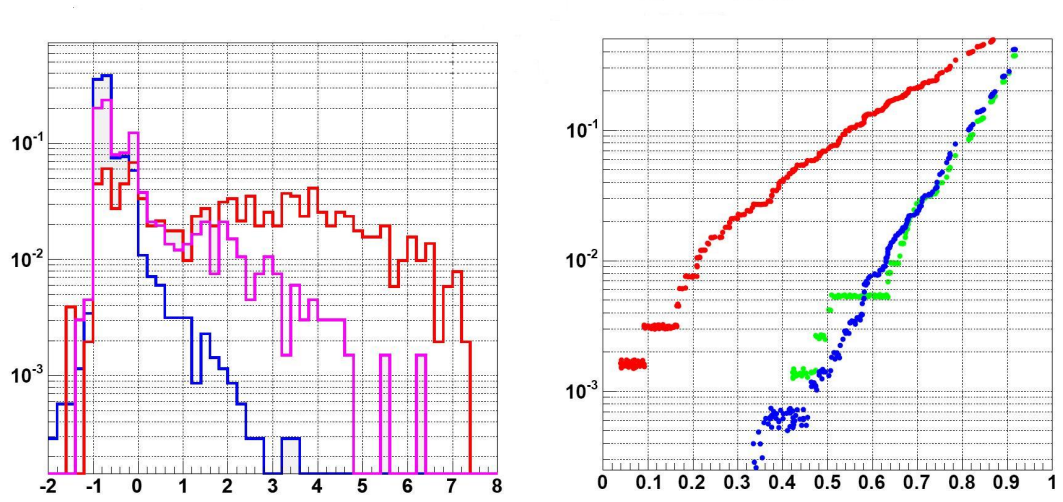

Figure 8.2: Left: the spectrum of the discriminator for b (red), c (violet) and udsg (blu) jets; right: misidentification efficiency versus b-efficiency for c, gluon and uds jets. All plots are for jets in the barrel region of the detector ($|\eta| < 1.4$).

8.2.1 Combined b tagging

The `CombinedBTag` algorithm [131] is based on the use of multiple variables which are combined in a single discriminating variable. Three jet categories are defined:

- the algorithm finds a secondary vertex candidate for the weak b-hadron decay;
- if no secondary vertex is found a so-called Pseudo Vertex is built from tracks which are not compatible with the primary event vertex if a certain number of such tracks is available;
- none of the conditions mentioned above is fulfilled.

Depending on the category, a different set of variables is used to build the final discriminator. It is important to note, that the category itself is already a strong discriminator. Figure 8.2 shows a typical spectrum for the discriminator (left) and the resulting misidentification efficiency versus b-tagging efficiency (right). The working point has to be chosen by putting a proper cut on the discriminator

8.2.2 Soft lepton tag

The soft lepton b-tagging algorithm is based on the relatively high b quark decay branching ratio to electrons and muons, about 20% for each lepton family. The key point is the identification of leptons among the tracks associated to each jet; to increase the purity of the selection additional cuts are performed on the parameters of the leptons relative to the jet.

Once the leptons have been identified in the event, jet b-tagging purity is increased feeding some of the lepton parameters through a neural network and cutting on the networks output depending on the desired trade off between efficiency and purity. The lepton parameters currently used are:

- lepton transverse momentum relative to the lepton-excluded jet axis;
- significance of the three-dimensional lepton impact parameter;
- pseudo angular distance in the η-ϕ plane between the lepton and the lepton-excluded jet axis;
- lepton momentum to jet energy ratio.

8.3 $Zb\bar{b}$ cross section measurement

8.3.1 Simulation and reconstruction

The main processes involved in the measurement are $Zb\bar{b}$ as signal, Zjj (with $Z \to \ell^+\ell^-$ and j=u, d, s, c) and $t\bar{t} \to W^+W^-\bar{b}$ (with $W \to \ell\nu$) as backgrounds.

The signal sample was generated using the `CompHep` Monte Carlo generator. The partonic final state was passed through `PYTHIA` for the hadronization and the initial and final state parton showers generation. The $t\bar{t}$ sample was generated using `PYTHIA` while the Zjj sample was available in the Official Monte Carlo Production. In every sample both the Z and W bosons were forced to decay in leptons while no other kinematical preselection was applied.

It is important to note that Zjj sample already contains events in which the Z boson is produced in association with two b jets, i.e. signal events. The production processes through which `PYTHIA` generates those events are already implemented in `CompHep`, as shown in Fig. 8.3, so in order to avoid *double counting* problems those events have been not considered in the analysis.

All the events were processed with the CMS fast simulation program, `FAMOS_1_2_0`.

8.3.2 Event selection

Events are selected requiring two opposite signed isolated leptons with $p_{\mathrm{T}}^{lepton} > 10$ GeV/c and an invariant mass ($\mathrm{m}_{\ell\ell}$) compatible with the Z boson mass

$$|\mathrm{M_Z} - \mathrm{m}_{\ell\ell}| < 10 \text{ GeV/c}^2 \tag{8.1}$$

plus two jets with $p_{\mathrm{T}}^{jets} > 10$ GeV/c, $|\eta^{jet}| < 2.5$ and at least two associated charged tracks. The low threshold for the p_{T} of the jet is justified by the very soft momentum spectrum of b-quark jets in signal events. The selection efficiencies are reported in Tab. 8.1. The $\mathrm{t\bar{t}}$ events are greatly suppressed due to the almost flat invariant mass distribution of the Z candidate. The invariant mass distribution of the lepton pairs for 20 fb^{-1} is shown in Fig. 8.4.

A b-tag identification is then performed using a logical combination of both `CombinedBTag` and `SoftLeptonTag` algorithms, which have been described in the previous Section. The discriminant thresholds have not yet been optimized. The related b-tagging and mistagging efficiencies are reported in Tab. 8.2.

In Fig. 8.5 the flavor, associated through the Monte Carlo truth, of the mistagged jets is reported. The association algorithm tries to find the highest p_{T} parton compatible with the jet direction inside the cone defined by the reconstructed jet itself. As can be seen many mistagged jets are associated by the algorithm to gluons. In those events probably a pair of b quarks is generated from a hard gluon,

Figure 8.3: The same production process which produces $\mathrm{Zb\bar{b}}$ in `PYTHIA` (left) and `CompHep` (right). In the first case the other b is produced by the showering while in second the $\mathrm{b\bar{b}}$ acts as a spectator.

Table 8.1: Lepton selection efficiency (ϵ_{lepton}) and jet selection efficiency (ϵ_{jet}) for the three studied samples.

channel	ϵ_{lepton}	ϵ_{jet}
$Zb\bar{b}$	86.7%	75.1%
Zjj	61.9%	52.9%
$t\bar{t}$	6.1%	6.1%

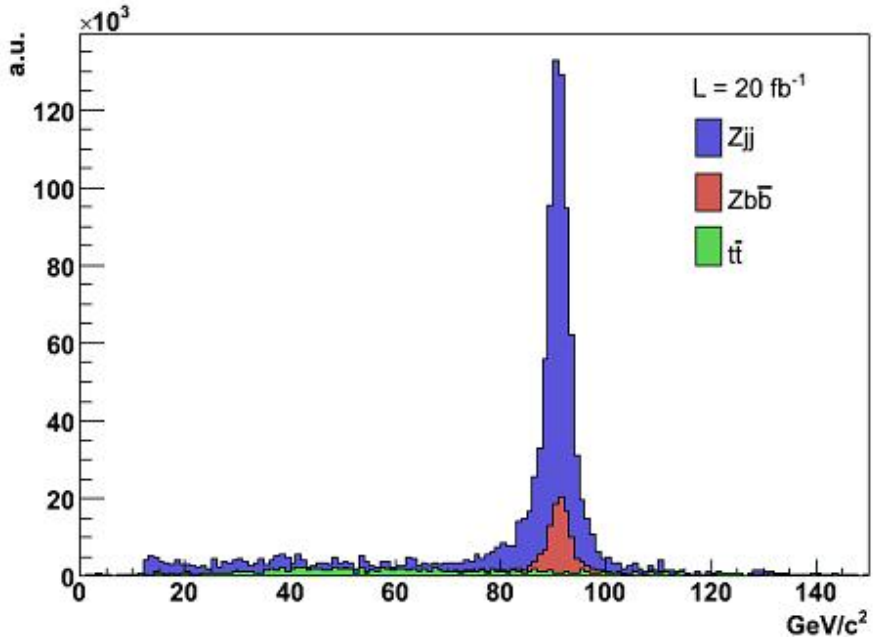

Figure 8.4: Invariant mass distribution of the lepton pairs from both signal and background after an integrated luminosity of 20 fb^{-1}.

but either one of the two b's carries a large fraction of the gluon momentum or both b's were reconstructed as a single jet.

8.3.3 Cross section measurement

If the b-jet identification has been carried out, the whole sample can be divided into three classes according the number of b jets found in each event. If η_{bb} and η_{bj} are respectively the fractions of events with two and one jet tagged as b, the following system can be written

$$\begin{cases} \eta_{bb} = f\epsilon_b^2 + f f_{bj}\epsilon_b\epsilon_j + [1 - f(1 + f_{bj})]\,\epsilon_j^2 \\ \\ \eta_{bj} = 2f\epsilon_b(1-\epsilon_b) + f f_{bj}[\epsilon_b(1-\epsilon_j) + \epsilon_j(1-\epsilon_b)] + \\ \qquad\qquad +2[1 - f(1 + f_{bj})]\epsilon_j(1-\epsilon_j) \end{cases} \tag{8.2}$$

where ϵ_b is the b-tagging efficiency, ϵ_j the mistagging efficiency and

$$f = \frac{N_{bb}}{N_{TOT}}\,, \qquad f_{bj} = \frac{N_{bj}}{N_{bb}}\,, \tag{8.3}$$

i.e. f is the true fraction of events with two b jets and f_{bj} the true ratio between events with one b jet and events with two b jets. If the b-tagging efficiency and the fraction f_{bj} are known, the system can be solved for the mistagging efficiency and the fraction f which gives the real number of event with two b jets.

The estimates of ϵ_b and f_{bj} have been obtained from the Monte Carlo and are 47% and 0.75 respectively. In a real measurements of the Zb$\bar{\text{b}}$ cross section however those values have to be estimated indipendently. A recent theoretical calculation has evaluated the fraction of Zjj with only one b jet [132].

The numbers η_{bb} and η_{bj} can be determined from the invariant mass distribution of the two leptons in events with one or two b-tagged jets. In Fig. 8.6 the invariant mass distributions of the leptons in those events are shown together with the fitting function and the chosen mass window.

The fitting function ($\mathcal{F}$) is a Pearson like function [133]

$$\mathcal{F} = k\left[\frac{1}{(1+x^2)^m}\right] e^{\arctan(x)} \tag{8.4}$$

Table 8.2: The b-tagging (ϵ_b) and mistagging (ϵ_j) efficiency of both used algorithms for the three studied samples.

channel	CombinedBtag		Soft lepton tag	
	ϵ_b	ϵ_j	ϵ_b	ϵ_j
$Zb\bar{b}$	30.7%	1.0%	10.8%	1.0%
Zjj	-	$< 1.0\%$	-	4.5%
$t\bar{t}$	54.6%	1.1%	16.4%	4.1%

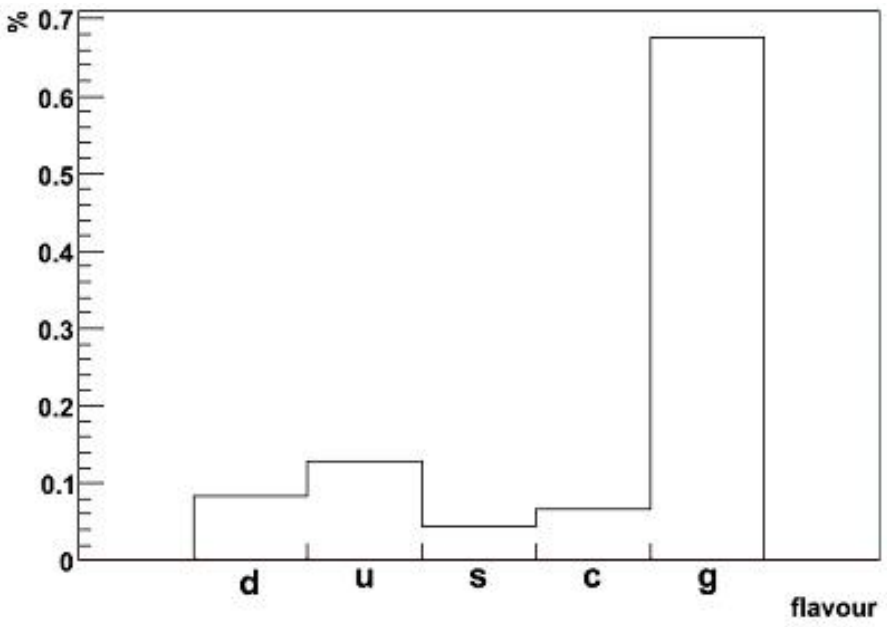

Figure 8.5: Flavor of the mistagged jets.

plus a Landau to reproduce the invariant mass distribution of the leptons coming from $t\bar{t}$ events. The Pearson function is essentially an asymmetric version of Student's t distribution. In particular, for small values of the parameter m, the tails are much longer than those of a Gaussian. For $m = 1$ the Pearson distribution become an asymmetric version of the Breit-Wiegner.

The fitted values of η_{bb} and η_{bj} are: $\eta_{bb} = 2.63 \cdot 10^{-2} \pm 0.12$ and $\eta_{bj} = 0.17 \pm 0.02$. An upper limit on the uncertainty of η_{bb} and η_{bj} has been estimated as the statistical error on the selected sample normalized to the integrated luminosity corresponding to the sample with the lowest number of events. The available statistic is limited by the Zjj sample which corresponds to a luminosity of about 0.5 fb^{-1}. No effects due to the choice of the fitting function are included yet.

8.3.4 Results

The numerical system resolution is obtained with an iterative process (Newton-Raphson method [134]). The starting point is a linear approximation of the system

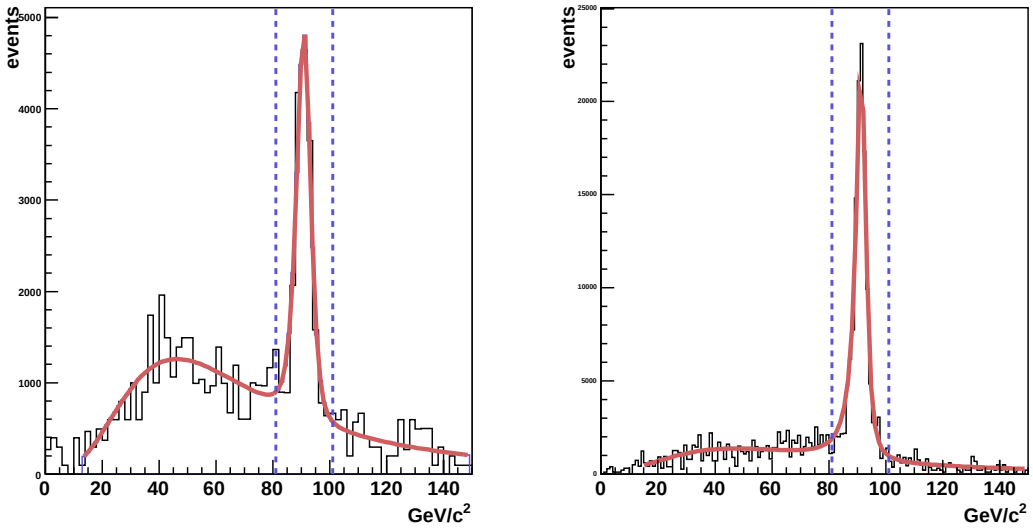

Figure 8.6: Fits to the invariant mass distributions of the lepton pair in events with two (left) and one (right) b-tagged jets).

to solve

$$\mathbf{F}(\mathbf{x}+\delta\mathbf{x}) = \mathbf{F}(\mathbf{x}) + \mathbf{J}\cdot\delta\mathbf{x} + O(\delta\mathbf{x^2})\,, \tag{8.5}$$

where $J_{ij} = \partial F_i/\partial x_i$ is the Jacobian of the system. The resulting set of linear equation gives the corrections to the solution that move each function to zero simultaneously

$$\mathbf{J}\cdot\delta\mathbf{x} = -\mathbf{F}\,. \tag{8.6}$$

The solution of the linearized system is added to the starting guess vector ($\mathbf{x}_{old}$)

$$\mathbf{x}_{new} = \mathbf{x}_{old} + \delta\mathbf{x}\,. \tag{8.7}$$

The process is iterated to convergence.

The results obtained for f and ϵ_j are reported in Tab. 8.3. The poor agreement of these results with the Monte Carlo expectation depends on the approximate parametrization used in the system. Some correlation has to be taken into account for a better description of the events.

In Monte Carlo events it is found that events with two leading b jets have higher b-tagging efficiency ($\sim$ 12% greater). Applying a correction factor for it the aggreement with Monte Carlo truth is clearly improved. The new results are also shown in Tab. 8.3. Other correlation with smaller contribution to the final result however has to be included with a refinement of the parametrization.

Once the value of f, hence of N_{bb}, is known, $Zb\bar{b}$ events remain to be selected against $t\bar{t}$. The fraction $N(t\bar{t})/N(Zb\bar{b})$ can be extracted from the invariant mass

Table 8.3: Results obtained from the numerical solution of the system and, as a comparison, the MC expectation. The results are reported in both cases with or without correlation.

	Numerical results (without corr.)	Numerical results (with corr.)	MC truth
f	10%	13.9%	16.5%
ϵ_j	5.5%	3.9%	3.4%

distribution of the two reconstructed leptons. The shape of the distribution of the combinatorial of the leptons coming from the leptonic decay of the two W bosons in $t\bar{t}$ events is obtained by a fit to the invariant mass distribution of the totally uncorrelated e-μ pairs. The results are shown in Fig. 8.7. The fraction $N(t\bar{t})/N(Zb\bar{b})$ is found to be 6.6% in good agreement with the value of 6.2% obtained from the MC truth.

In order to estimate the error associated with the measured quantities ϵ_j and f, the statistical errors of η_{bj} and η_{bb} have been combined with the uncertainties assumed on the knowledge of the two parameters ϵ_b and f_{bj}. To roughly calculate the final uncertainties they are taken with a 10% errors. In Tab. 8.4 the relevant quantities are shown together with the final determination of f and ϵ_j.

The main contribution to the uncertainties of f is given by the errors on the determination of the b-tagging efficiency. A detailed study of the systematic uncertainties involved in the procedure (Monte Carlo choice, fitting functions,...) will have to be done. The very high expected cross section of the processes involved in the measurements makes the statistical uncertainties negligible after an integrated luminosity of few hundreds of pb^{-1} has been collected.

In conclusion the method presented in this Chapter should allow to cross-check Monte Carlo predictions for the $Zb\bar{b}$ events with a 20% uncertainty after few weeks of LHC data taking.

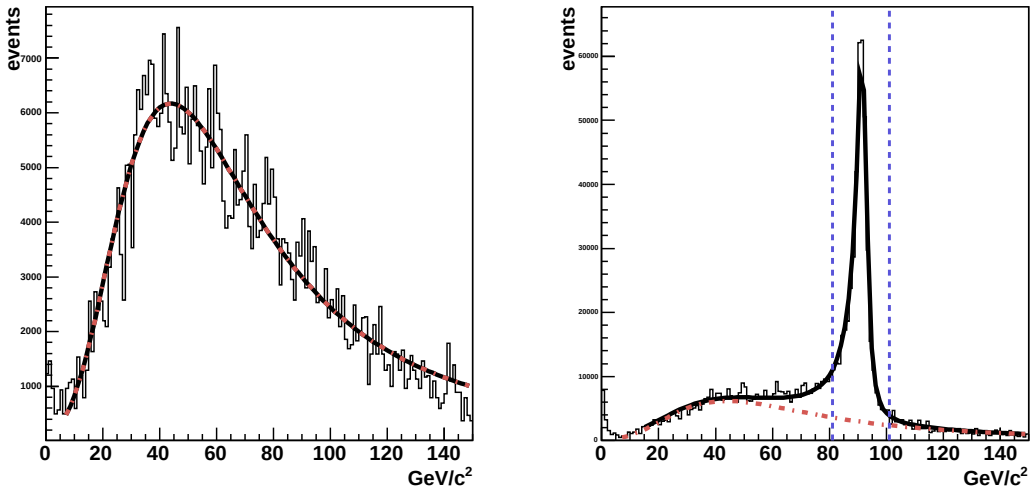

Figure 8.7: Fits to the invariant mass distributions of the e-μ pairs (left) and to the $e^+e^-/\mu^+\mu^-$ pairs in $Zb\bar{b}$ and $t\bar{t}$ events (right).

Table 8.4: Parameters of the system with their errors and final results.

Parameter	Value
η_{bb}	$(2.63 \pm 0.12) \cdot 10^{-2}$
η_{bj}	0.17 ± 0.02
f_{bj}	0.76 ± 0.08
ϵ_b	0.47 ± 0.05
η_j	3.9 ± 2.6
f	13.9 ± 4.0

Conclusions

Although all experimental data agree with extraordinary precision with Standard Model expectations, the Higgs boson has not yet been observed. The mass range of the search extends from the direct limit of 115 GeV/c^2 to 1 TeV/c^2, even though a fit to experimental data indicates a Higgs boson mass in the range ($110 \div 200$ GeV/c^2).

In the mass range from about 120 to 500 GeV/c^2 one of the main Higgs search channels is $H \rightarrow ZZ^{(*)} \rightarrow \ell^+\ell^-\ell^+\ell^-$, where the leptons could be muons or electrons. The present work consists in the study of the CMS potential for the Higgs search in the four muon final state.

The signal cross section and branching ratios have been estimated with the programs implementing the most recent theoretical calculations, including QCD next-to-leading order corrections. The final state particles have been generated using the Monte Carlo programs `PYTHIA` and `CompHep` and full detector response has been simulated.

The main background processes $t\bar{t} \rightarrow W^-W^+b\bar{b} \rightarrow 4\mu$, $Zb\bar{b} \rightarrow 4\mu$ and $ZZ^{(*)} \rightarrow 4\mu$ have been analyzed with a full simulation of detector response. Other sources of background like Zjj (with j=c,u,d,s) or the background coming form multiple collisions have also been studied and found to be negligible.

To account for the presence of one or two on-shell Z bosons in the final state, two different sets of selection cuts were considered in two different mass regions: below and above the ZZ threshold. In addition a mass dependent thresholds optimization has been performed in both regions.

The effects of the next-to-leading order predictions obtained with the Monte Carlo generator `MC@NLO` on cut efficiencies have been studied in detail including the corrections through a reweighting procedure. The corresponding K-factors have been calculated with a comparison of the corresponding NLO and LO distributions. Analytical computations including NNLL terms have also been considered and found to be in good agreement with the predictions of `MC@NLO`. Similar results for the irreducible ZZ background are not yet available.

With the set of cuts presented in this work a high statistical significance, hence a good discovery probability, is expected after an integrated luminosity of 20 fb^{-1}. Few months of data taking at the nominal low luminosity should be enough for the discovery of a Higgs boson with a mass between 200 and 500 GeV/c^2 or between

130 and 150 GeV/c^2. The combination of different channels is needed instead to discover a Higgs boson with a mass below 130 or above 500 GeV/c^2 in the first year of data taking.

As this work was going on, it was found that a detailed understanding of $Zb\bar{b}$ events is of crucial interest, not only in the search for an intermediate-mass Higgs boson, but in many other interesting physics channels like $pp \rightarrow HZ$ with $H \rightarrow b\bar{b}$ or the MSSM channel $pp \rightarrow b\bar{b}H$. Furthermore a precise estimation of the production cross section is useful for b-quark parton density function evaluation.

Therefore a technique to measure the $Zb\bar{b}$ cross section has been studied. It relies on the selection of events with two opposite signed leptons and two jets. After b-jets identification and a Z mass cut on the lepton pairs the whole sample can be divided into three classes according to the number of b jets found in each event. The real number of events with two b jets can then be extracted as a function of b-tagging and mistagging efficiencies and the ratio between events with one b jet and events with two b jets.

The preliminary results of this study show that the cross section measurements can be performed after few hundreds of pb^{-1} of data taking with an error of 20%, mainly due to the uncertainty on the b-tag efficiency estimation, the statystical uncertainty being already negligible. A detailed study of the systematic uncertainties involved in the procedure will have however to be done.

Appendix A

Summary of efficiencies for $M_H > 2M_Z$

In this Appendix a complete list of the selection efficiencies obtained for Higgs boson masses above ZZ threshold is reported.

Table A.1: Efficiencies after applying the cuts described in the text for $M_H = 190$ GeV/c^2.

	ϵ_{reco}	**Z mass cut** (8 GeV/c^2)	p_T^{μ} **cut** ($20, 15, 15, 10$ GeV/c)	$p_T^{4\mu}$ **cut** (10 GeV/c)
H (190 GeV/c^2)	82%	46.2%	44.3%	38.0%
ZZ	71.5%	28.1%	27.0%	15.2%
Zb$\bar{\text{b}}$	34.0%	0.14%	0.08%	0.07%
t$\bar{\text{t}}$	48.2%	0.07%	0.05%	0.05%

Table A.2: Efficiencies after applying the cuts described in the text for $M_H = 250$ GeV/c^2.

	ϵ_{reco}	Z **mass cut** (12 GeV/c^2)	p_T^μ **cut** (20, 15, 15, 10 GeV/c)	$p_T^{4\mu}$ **cut** (10 GeV/c)
H (250 GeV/c^2)	84.9%	51.9%	50.0%	44.5%
ZZ	71.5%	31.9%	30.5%	17.6%
Zb$\bar{b}$	34.0%	0.29%	0.16%	0.16%
t$\bar{t}$	48.2%	0.16%	0.12%	0.11%

Table A.3: Efficiencies after applying the cuts described in the text for $M_H = 300$ GeV/c^2.

	ϵ_{reco}	Z **mass cut** (12 GeV/c^2)	p_T^μ **cut** (20, 15, 15, 15 GeV/c)	$p_T^{4\mu}$ **cut** (10 GeV/c)
H (300 GeV/c^2)	77.0%	46.6%	41.6%	37.4%
ZZ	71.5%	31.9%	27.9%	15.9%
Zb$\bar{b}$	34.0%	0.29%	0.11%	0.11%
t$\bar{t}$	48.2%	0.16%	0.08%	0.08%

Table A.4: Efficiencies after applying the cuts described in the text for $M_H = 350$ GeV/c^2.

	ϵ_{reco}	**Z mass cut** (12 GeV/c^2)	p_T^μ **cut** (20, 15, 15, 10 GeV/c)	$p_T^{4\mu}$ **cut** (13 GeV/c)
H (350 GeV/c^2)	87.0%	51.6%	47.1%	42.9%
ZZ	71.5%	31.9%	27.9%	15.9%
Zb$\bar{\text{b}}$	34.0%	0.29%	0.11%	0.10%
t$\bar{\text{t}}$	48.2%	0.16%	0.08%	0.08%

Table A.5: Efficiencies after applying the cuts described in the text for $M_H = 400$ GeV/c^2.

	ϵ_{reco}	**Z mass cut** (20 GeV/c^2)	p_T^μ **cut** (20, 15, 15, 15 GeV/c)	$p_T^{4\mu}$ **cut** (16 GeV/c)
H (400 GeV/c^2)	86.7%	57.4%	52.7%	44.5%
ZZ	71.5%	36.3%	31.4%	12.6%
Zb$\bar{\text{b}}$	34.0%	0.72%	0.24%	0.23%
t$\bar{\text{t}}$	48.2%	0.52%	0.24%	0.22%

Table A.6: Efficiencies after applying the cuts described in the text for $M_H = 450$ GeV/c^2.

	ϵ_{reco}	Z **mass cut** (20 GeV/c^2)	p_T^μ **cut** (20, 15, 15, 15 GeV/c)	$p_T^{4\mu}$ **cut** (18 GeV/c)
H (M_H= 450 GeV/c^2)	87.2%	57.3%	52.9%	44.5%
ZZ	71.5%	36.3%	31.4%	11.2%
Zb$\bar{b}$	34.0%	0.72%	0.24%	0.22%
t$\bar{t}$	48.2%	0.52%	0.24%	0.22%

Table A.7: Efficiencies after applying the cuts described in the text for $M_H = 500$ GeV/c^2.

	ϵ_{reco}	Z **mass cut** (22 GeV/c^2)	p_T^μ **cut** (20, 15, 15, 15 GeV/c)	$p_T^{4\mu}$ **cut** (10 GeV/c)
H (500 GeV/c^2)	86.6%	57.5%	53.3%	50.1%
ZZ	71.5%	37.1%	32.1%	18.8%
Zb$\bar{b}$	34.0%	0.85%	0.27%	0.26%
t$\bar{t}$	48.2%	0.67%	0.31%	0.30%

Table A.8: Efficiencies after applying the cuts described in the text for $M_H = 550$ GeV/c^2.

	ϵ_{reco}	**Z mass cut** (22 GeV/c^2)	p_T^μ **cut** (20, 15, 15, 15 GeV/c)	$p_T^{4\mu}$ **cut** (13 GeV/c)
H (550 GeV/c^2)	86.9%	56.2%	52.7%	48.5%
ZZ	71.5%	37.1%	32.1%	15.5%
Zb$\bar{\text{b}}$	34.0%	0.85%	0.27%	0.26%
t$\bar{\text{t}}$	48.2%	0.67%	0.31%	0.30%

Table A.9: Efficiencies after applying the cuts described in the text for $M_H = 600$ GeV/c^2.

	ϵ_{reco}	**Z mass cut** (22 GeV/c^2)	p_T^μ **cut** (20, 15, 15, 15 GeV/c)	$p_T^{4\mu}$ **cut** (16 GeV/c)
H (600 GeV/c^2)	86.3%	56.0%	52.7%	47.4%
ZZ	71.5%	37.1%	32.1%	12.9%
Zb$\bar{\text{b}}$	34.0%	0.85%	0.27%	0.26%
t$\bar{\text{t}}$	48.2%	0.67%	0.31%	0.28%

Appendix B

Summary of efficiencies for $M_H < 2M_Z$

In this Appendix a complete list of the selection efficiencies obtained for Higgs boson masses below ZZ threshold is reported.

Table B.1: Efficiencies after applying the cuts described in the text for $M_H = 115$ GeV/c^2.

	ϵ_{reco}	Z **mass cut** (30 GeV/c^2)	p_T^μ **cut** (20, 15, 10, 6 GeV/c)	**isolation cut** (3.5, 10 GeV/c)
H (115 GeV/c^2)	67.9%	51%	39.6%	34.2%
ZZ	71.5%	36.6%	29.8%	26.4%
$Zb\bar{b}$	34.0%	12.5%	5.4%	0.47%
$t\bar{t}$	48.2%	18.4%	12.2%	0.23%

Table B.2: Efficiencies after applying the cuts described in the text for $M_H = 120$ GeV/c^2.

	ϵ_{reco}	Z **mass cut** (30 GeV/c^2)	p_T^μ **cut** ($20, 15, 10, 6$ GeV/c)	**isolation cut** ($3.5, 10$ GeV/c)
H (120 GeV/c^2)	70.5%	56.9%	46%	39.8%
ZZ	71.5%	36.6%	29.8%	26.4%
Zb$\bar{\text{b}}$	34.0%	12.5%	5.4%	0.47%
t$\bar{\text{t}}$	48.2%	18.4%	12.2%	0.22%

Table B.3: Efficiencies after applying the cuts described in the text for $M_H = 140$ GeV/c^2.

	ϵ_{reco}	Z **mass cut** (10 GeV/c^2)	p_T^μ **cut** ($20, 15, 12, 8$ GeV/c)	**isolation cut** ($4, 15$ GeV/c)
H (140 GeV/c^2)	77.9%	54.1%	43.6%	39.0%
ZZ	71.5%	26.2%	17.0%	15.2%
Zb$\bar{\text{b}}$	34.0%	9.7%	2.27%	0.19%
t$\bar{\text{t}}$	48.2%	5.56%	2.60%	0.05%

Table B.4: Efficiencies after applying the cuts described in the text for $M_H = 150$ GeV/c^2.

	ϵ_{reco}	Z **mass cut** (15 GeV/c^2)	p_T^μ **cut** (20, 15, 12, 10 GeV/c)	**isolation cut** (3.5, 10 GeV/c)
H (150 GeV/c^2)	80.7%	62.2%	47.9%	42.1%
ZZ	71.5%	29.3%	16.6%	14.7%
Zb$\bar{\text{b}}$	34.0%	10.8%	1.67%	0.08%
t$\bar{\text{t}}$	71.5%	8.48%	2.90%	0.03%

Table B.5: Efficiencies after applying the cuts described in the text for $M_H = 160$ GeV/c^2.

	ϵ_{reco}	Z **mass cut** (15 GeV/c^2)	p_T^μ **cut** (20, 15, 12, 8 GeV/c)	**isolation cut** (3.5, 10 GeV/c)
H (160 GeV/c^2)	83.3%	53.3%	45.5%	39.8%
ZZ	71.5%	29.3%	19.4%	17.1%
Zb$\bar{\text{b}}$	34.0%	10.8%	2.57%	0.17%
t$\bar{\text{t}}$	48.2%	8.5%	3.97%	0.05%

Table B.6: Efficiencies after applying the cuts described in the text for $M_H = 170$ GeV/c^2.

	ϵ_{reco}	Z **mass cut** (30 GeV/c^2)	p_T^μ **cut** ($20, 15, 12, 10$ GeV/c)	**isolation cut** ($4, 15$ GeV/c)
H (170 GeV/c^2)	83.0%	54.4%	41.3%	36.9%
ZZ	71.5%	36.6%	22.2%	19.9%
Zb$\bar{\text{b}}$	34.0%	12.5%	2.02%	0.11%
t$\bar{\text{t}}$	48.2%	18.4%	6.08%	0.09%

Table B.7: Efficiencies after applying the cuts described in the text for $M_H = 180$ GeV/c^2.

	ϵ_{reco}	Z **mass cut** (30 GeV/c^2)	p_T^μ **cut** ($20, 15, 10, 6$ GeV/c)	**isolation cut** ($4, 15$ GeV/c)
H (180 GeV/c^2)	83.5%	43.8%	39.6%	34.2%
ZZ	71.5%	36.6%	29.8%	26.8%
Zb$\bar{\text{b}}$	34.0%	12.5%	5.40%	0.58%
t$\bar{\text{t}}$	48.2%	18.4%	12.2%	0.29%

Bibliography

[1] F. Halzen and A. Martin, *Quarks and leptons: an introductory course in modern Particle Physics* (Wiley, New York USA, 1984).

[2] E. Fermi, "*Trends to a theory of Beta radiation.*", *Nuovo Cimento* **11**, (1952) 1.

[3] M. Goldhaber, L. Grodzins and A. W. Sunyar, "Helicity of Neutrinos", *Phys. Rev.* **109**, (1958) 1015.

[4] J. S. Schwinger, "Quantum Electrodynamics. A covariant formulation", *Phys. Rev.* **74**, (1948) 1439.

[5] Particle Data Group, "Review of Particle Physics", *Phys. Rev.* **D66** 010001.

[6] N. Cabibbo, "Unitarity Symmetry and Leptonic Decays", *Phys. Rev. Lett.* **10**, (1963) 531.

[7] S. L. Glashow, "Partial Symmetries of Weak Interactions", *Phys. Rev.* **22**, (1961) 579.

[8] S. Weinberg, "A Model of Leptons", *Phys. Rev. Lett.* **19**, (1967) 1264.

[9] A. Salam, *Elementary Particle Theory* (Almquist and Wiksells, N. Svartholm, Stockholm, 1968).

[10] R. K. Ellis, W. J. Stirling and B. R. Webber, *QCD and Collider Physics* (Cambridge University Press, N. Svartholm, Stockholm, 1996).

[11] P. W. Higgs, "Broken Symmetries, Massless Particles and Gauge Fields", *Phys. Lett.* **12**, (1964) 132.

[12] Lep Injector Study Group, "LEP Design Report Vol. 1: The LEP Injector Chain", CERN-LEP-TH-83-29, CERN-PS-DL-83-81, CERN-SPS-83-26, LAL-RT-83-09 (1983).

[13] Lep Injector Study Group, "LEP Design Report Vol. 2: The LEP Main Ring", CERN-LEP/8-01 (1984).

[14] Lep Injector Study Group, "LEP Design Report Vol. 3: LEP2", CERN-AC-96-01-LEP2 (1996).

[15] A. Djouadi, "The Anatomy of Electroweak Symmetry Breaking", LPT-Orsay 05-17 (2005), `hep-ph/05031724`.

[16] J. F. Gunion, H. E. Haber, G. Kane and S. Dawson, *The Higgs Hunters Guide* (Addison Wesley, Menlo Park, 1990).

[17] K. Riesselmann, "Limitations of a Standard Model Higgs Boson", DESY 97-222 (1997), `hep-ph/9711456`.

[18] T. Hambye and K. Riesselmann, "Matching conditions and Higgs mass upper bounds revisited", *Phys. Rev.* **D55**, (1997) 7255.

[19] The ALEPH Collaboration, "The ALEPH Detector (Apparatus for LEp PHysics) Technical Report", CERN-LEPC-83-2, LEPC-p-1, Geneva, CERN (1983).

[20] The DELPHI Collaboration, "DELPHI: The DELPHI Detector (Detector with Lepton Photon and Hadron Identification) Technical Proposal", CERN-LEPC-83-3, DELPHI-83-66, LEP-P-2, Geneva, CERN (1983).

[21] The L3 Collaboration, "L3 Technical Proposal", CERN-LEPC-83-5, LEPC-P-4, Geneva, CERN (1983).

[22] The OPAL Collaboration, "OPAL: The OPAL Detector (an Omni Purpouse Apparatus for Lep) Technical Proposal", CERN-LEPC-83-4, LEPC-P-3, Geneva, CERN (1983).

[23] The SLD Collaboration, "The SLD Design Report", SLAC-Report-273 (1984).

[24] The CDF Collaboration, "The CDF Detector: An Overview", *Nucl. Instrum. Meth.* **A272**, (1988) 487.

[25] The D0 Collaboration, "The D0 Detector", *Nucl. Instrum. Meth.* **A338**, (1994) 185.

[26] The LEP Collaborations and ALEPH and DELPHI and L3 and OPAL and the LEP Electroweak Working Group, "A combination of preliminary Elecroweak measurements and constraints on the Standard Model", LEPEWWG/2005-01, hep-ex/0511027 (2005).

[27] The LHC Study Group, "The Large Hadron Collider Conceptual Design Report", CERN/AC 95-05 (1995).

[28] The ATLAS Collaboration, "ATLAS: A Toroidal LHC ApparatuS Technical Proposal", CERN/LHCC 94-18, LHCC/P1 (1994).

[29] The CMS Collaboration, "The Compact Muon Solenoid Technical Proposal", CERN/LHCC 94-38, LHCC/P1 (1994).

[30] The ALICE Collaboration, "A Large Ion Collider Experiment Technical Proposal Design", CERN/LHCC 95-71, LHCC/P3 (1995).

[31] The LHCb Collaboration, "A Large Hadron Collider Beauty Experiment for Precision Measurements of CP-Violation and Rare Decays LHCb Technical Proposal", CERN/LHCC 98-04, LHCC/P4 (1998).

[32] The ATLAS Collaboration, "ATLAS Detector and Physics Performance - Technical Design Report Vol. I", ATLAS TDR 14, CERN/LHCC 99-14 (1999).

[33] Particle Data Group, *Review of Particle Physics*, page 300 (Phys. Rev., 2002).

[34] The LHC Study Group, "The Large Hadron Collider Conceptual Design Report", CERN/AC 95-05 (1995).

[35] J. Velasco, J. Perez-Peraza, A. Gallegos-Cruz, M. Alvarez-Madrigal, A. Faus-Golfe and A. Sanchez-Hertz, "Parametrization of Proton-Proton Total Cross Sections from 10 GeV to 100 TeV", IFIC 99-28, `hep-ph/0011167`.

[36] The CMS Collaboration, "CMS: The Tracker Project Technical Design Report", CERN/LHCC 98-06, CMS TDR 5 (1998).

[37] The CMS Collaboration, "The Compact Muon Solenoid Letter of Intent", CERN/LHCC 92-3, LHCC/I1 (1992).

[38] The CMS Collaboration, CMS Design Team, "CMS: The Magnet Project Technical Design Report", CERN/LHCC 97-10, CMS TDR 1 (1997).

[39] "Florence integration group", `http://hep.fi.infn.it/CMS/Florence_integration/index.html`.

[40] The CMS Collaboration, "CMS: The Trigger and Data Acquisition Project, Volume II: Data Acquisition and High-Level Trigger Technical Design Report", CERN/LHCC 02-26, CMS TDR 6.2 (2002).

[41] The CMS Collaboration, "The CMS Electromagnetic Calorimeter Technical Design Report", CERN/LHCC 97-33, CMS TDR 4 (1997).

[42] G. Dissertori, "Electromagnetic Calorimetry and e/γ performance in CMS", 2003 LHC Symposium (CMS NOTE-CR-2003/024, Fermilab, 2003).

[43] D. Green, P. Hidas, K. Maeshima, R. Vidal, W. Wu and S. Kunori, ""Dijet Mass Resolution With or Without the Endcap Ecal at CMS", CMS NOTE-IN 2002/062.

[44] The CMS Collaboration, "CMS: The Hadron Calorimeter Project Technical Design Report", CERN/LHCC 97-31, CMS TDR 2 (1997).

[45] S. Banerjee, "Performance of Hadron Calorimeter with and without HO", CMS Note 1999/063.

[46] The CMS Collaboration, "CMS: The Muon Project Technical Design Report", CERN/LHCC 97-31, CMS TDR 2 (1997).

[47] The CMS Collaboration, "CMS: The Trigger and Data Acquisition Project, Volume I: The Level-1 Triggger Technical Design Report", CERN/LHCC 2000-038, CMS TDR 6.1 (2000).

[48] "Pentium III", `http://www.intel.com/design/pentiumiii`.

[49] L. L. Jones, M. J. French, Q. Morrissey, A. Neviani, M. Raymond, G. Hall, P. Moreira and G. Cervelli, "The APV25 Deep Submicron Readout Chip for CMS Detector", CERN/LHCC 99-09 (1999).

[50] S. Gadomski, G. Hall, T. Hogh, P. Jalocha, E. Nygard and P. Weilhammer, "The Deconvolution Method of Fast Pulse Shaping at Hadron Colliders", *Nucl. Instrum. Meth.* **A320**, (1992) 217.

[51] R. Wunstorf, T. Rohe and A. Rolf, "Simulation of Irradiation-Induced Surface Effects in Silicon Detectors", *Nucl. Instrum. Meth.* **A338**, (1997) 308.

[52] B. C. MacEvoy, G. Hall and K. Gill, "Defect Evolution in Irradiated Silicon Detector Material", *Nucl. Instrum. Meth.* **A374**, (1996) 12.

[53] H. Feick, E. Fretwurst, G. Lindstroem and M. Moll, "Long Term Damage Studies Using Silicon Detectors Fabricated from Different Starting Materials and Irradiated with Neutrons, Protons and Pions", *Nucl. Instrum. Meth.* **A377**, (1996) 217.

[54] J. A. J. Matthews, P. Berduis, M. Frautschi, J. Schuler, H. Sadrozinski, K. O'Shaughnessy, L. Spiegel, A. Palounek, H. Ziock, N. Bacchetta, D. Bisello and A. Giraldo, "Bulk Radiation Damage in Silicon Detectors and Implications for LHC Experiments", *Nucl. Instrum. Meth.* **A381**, (1996) 338.

[55] R. Wunstorf, *Systematische Untersuchungen zur Strahlenresistenz von Silizium-Detektoren f ur die Verewendung in Hochenergiephysik-Experimenten*, Ph.D. thesis, University of Hamburg (1992).

[56] S. Braibant, N. Demaria, L. Feld, A. Frey, A. Furtjes, W. Glessing, R. Harmastrom, A. Homma, M. Mannelli, C. Mariotti, P. Mattig, E. Migliore, S. Piperov, Runolfsoon, B. Schmitt and B. Surrow, "Investigation of Design Parameters and Choice of Substrate Resistivity and Crystal Orientation for the CMS Silicon Microstrip Detector", CMS NOTE 2000/011.

[57] J. Agram, "The Silicon Sensors for the Compact Muon Solenoid Tracker - Design and Qualification Procedure", Accepted by *Nucl. Instr. Meth.* A.

[58] "ST Microelectronics", `http://www.st.com`.

[59] "Hamamatsu Photonics KK", http://www.hamamatsu.com.

[60] "National Instruments, Labview - Graphical Development Environment for Data Acquisition, Analysis and Presentation", http://ww.ni.com/labview.

[61] "Tracker Database, CMS Tracker Construction Database System", http://cmsdoc.cern.ch/cmstrkdb/.

[62] C. Becker, "Gate-controlled diodes for characterization of the Si-SiO_2 interface with respect to surface effects of silicon detectors", *Nucl. Instrum. Meth.* **A444**, (2000) 605.

[63] B. Stroustrup, *The C++ Programming language (third edition)* (Addison Wesley, 1997), ISBN 0-201-88954-4.

[64] V. Innocente, L. Silvestris and D. Stickland, "CMS Software Architecture - Software Framework, Services and Persistency in High-Level Trigger, Reconstruction and analysis", *Comput. Phys. Commun.* **140**, (2001) 31, http://cobra.web.cern.ch/cobra.

[65] "OSCAR, Object oriented Simulation for CMS Analysis and Reconstruction", http://cmsdoc.cern.ch/oscar/.

[66] S. Agostinelli, "GEANT 4: a simulation toolkit", *Nucl. Instrum. Meth.* **A506**, (2003) 250.

[67] The CMS Software and Computing Group, "Object Oriented Reconstruction for CMS Analysis", http://cmsdoc.cern.ch/orca/orca.html.

[68] "FAMOS, Fast Monte Carlo Simulation", http://cmsdoc.cern.ch-/famos/.

[69] "IGUANA, Interactive Graphics for User Analysis", http://iguana.web.-cern.ch/iguana/.

[70] T. Sjostrand, P. Eden, C. Friberg, L. Lonnblad, G. Miu, S. Mrenna and E. Norbin, *The Complete PYTHIA 6.206 manual*, lu tp 01-21 edition (2002), hep-ph/0108264.

[71] A. Pukhova, E. Boos, M. Dubinin, V. Edneral, V. Ilyin, D. Kovalenko, A. Kryukov, V. Savrin, S. Shichanin and A. Semenov, *CompHEP - a package for evaluation of Feynman diagrams and integration over multi-particle phase space*, preprint inp msu 98-41/542 edition (1999), `hep-ph/9908288`.

[72] M. L. Mangano, M. Moretti, F. Piccinini, R. Pittau and A. Polosa, *ALPGEN, a generator for hard multiparton processes in hadronic collision*, jhep 0307:001lu tp 01-21 edition (2003), `hep-ph/020293`.

[73] T. Sjostrand, "Z physics at LEP 1", CERN 89-08.

[74] Software Application group, *HBOOK - Statistical Analysis and Histogramming*, CERN Program Library Long Writeup Y250 edition.

[75] R. Fruehwirt, "Application of Kalman Filter to Track and Vertex Fitting", *Nucl. Instrum. Meth.* **A262**, (1997) 444.

[76] R. Fruehwirt, T. Todorov and M. Winkler, "A Comparative Study of the Deterministic Annealing Filter at CMS", .

[77] R. Fruehwirt, T. Todorov and M. Winkler, "MultiTrack Fitting Methods in ORCA", CMS NOTE-IN 2003/042.

[78] T. Todorov, "An Object Framework for Track Reconstruction and its Implementation for the CMS Tracker", (International Conference on Computing in High Energy and Nuclear Physics, CHEP 2000, Padova (Italy), 2000).

[79] K. Hagiwara, "Review of Particle Physics", *Phys. Rev.* **D66** 010001, (2002) 242.

[80] H. A. Bethe and W. Heitler, "On the Stopping of fast particles and on the creation of positive electrons", *Proc. Roy. Soc. Lond.* **A146** 83.

[81] V. Innocente, M. Maire and E. Nagy, "GEANE", CERN program library long writeup W5013-E.

[82] I. Belotelov and N. Neumeister, "Performance of the CMS Offline Muon Reconstruction Software", CMS NOTE-AN 2005/010.

[83] G. Bruno, "Local reconstruction in muon detector", CMS NOTE 2002/039.

[84] H. Georgi, S. Glashow, M. Machacek and D. Nanopulous, "Higgs Bosons from Two Gluon Annhilation in Proton Proton Collision", *Phys. Rev. Lett.* **40**, (1978) 692.

[85] R. Rainwater, M. Spira and D. Zeppenfeld, "Higgs boson production at Hadron Collider", `hep-ph/0203187`.

[86] M. Spira, "HIGLU: A Program for the Calculation of the Total Higgs Production Cross Section at Hadron Colliders via Gluon Fusion Including QCD Corrections", DESY T-95-05 (1995), `hep-ph/9510347`.

[87] J. Pumplin, D. R. Stump, J. Huston, H. L. Lai, P. Nadolsky and W. K. Tung, "New generation of parton distributions with uncertainties from global QCD analysis", *JHEP* **0207:012**, (The CTEQ Collaboration).

[88] M. Kramer, E. Laenen and M. Spira, "Soft gluon radiation in Higgs boson production at the LHC", *Nucl. Phys.* **B511**, (1998) 523, `hep-ph/9611272`.

[89] "HERA, Hadron-Electron Ring Accelerator at DESY", `http://-www-hera-b.desy.de/general/info/`.

[90] "Fermilab Tevatron", `http://adcon.fnal.gov/userb/www/tevatron/`.

[91] V. Ravindran, J. Smith and W. L. van Neerven, "NNLO corrections to the total cross section for Higgs boson production in hadron hadron collisions", *Nucl. Phys.* **B665**, (2003) 325, hep-ph/0302135.

[92] G. L. Kane, W. W. Repko and W. B. Rolnick, "The Effective $W^{\pm}$, Z Approximation for High-Energy Collisions", *Phys. Lett.* **B148**, (1984) 367.

[93] E. Eicthen, J. Hinchliffe, K. Lane and C. Quigg, "Super Collider Physics", *Rev. Mod. Phys.* **56**, (1984) 579.

[94] Z. Kunszt, "Associated Production of Heavy Higgs Boson with Top Quarks", *Nucl. Phys.* **B247**, (1984) 339.

[95] A. Djouadi, J. Kalinowski and M. Spira, "HDECAY: a Program for Higgs Boson Decays in the Standard Model and its Supersymmetric Extension", DESY 97-079 (1997), `hep-ph/9704448`.

[96] J. Ellis, M. K. Gaillard and D. V. Nanopoulos, "A Phenomenological Profile of the Higgs Boson", *Nucl. Phys.* **B106**, (1976) 292.

[97] M. Drees and K. Hikasa, "Heavy Quark Thresholda in Higgs Physics", *Phys. Rev.* **D41**, (1990) 1547.

[98] L. Resnick, M. K. Sundaresan and P. J. S. Watson, "Is There a Light Scalar Boson ?", *Phys. Rev.* **D8**, (1973) 172.

[99] A. I. Vaĭnshteĭn, M. B. Voloshin, V. I. Zakharov and M. A. Shifman, "Low-Energy Theorems for Higgs Boson Couplings to Photons", *Sov. J. Nucl. Phys.* **30**, (1979) 711.

[100] J. Fleischer and O. V. Tarasov, "Calculation of Feynman diagrams from their small momentum expansion", *Z. Phys.* **C64**, (1994) 401, `hep-ph/9403230`.

[101] "Official Production", `http://cmsdoc.cern.ch/cms/production/www/-html/general/index.html`.

[102] E. Barberio and Z. Was, "PHOTOS, A Universal Monte Carlo for QED Radiative Corrections", CERN-TH 7033/93.

[103] B. Mangano, *Studi sulla misura della massa dell'Higgs del Modello Standard nel canale di decadimento* $\mathrm{H} \to \mathrm{ZZ}^{(*)} \to 4\mu$ *con CMS a LHC*, Degree's thesis, Universita' di Pisa (2003).

[104] "MCFM - Monte Carlo for FeMtobarn Processes", `http://mcfm.fnal-.gov/`.

[105] W. N. Glower and J. J. van der Bij, "Boson Pair Production Via Gluon Fusion", *Nucl. Phys.* **B321**, (1989) 561.

[106] G. Altarelli and M. L. Mangano, *Proceedings of the Workshop on Standard Model Physics at LHC*, page 428 (CERN 2000-004, 2000), `hep-ph/0003033`.

[107] F. Maltoni, "Theoretical Issues and Aims at the Tevatron and LHC", (HCP2005, 2005).

[108] A. D. Martin, R. G. Roberts, W. J. Stirling and R. S. Thorne, "Uncertainties of predictions from parton distributions. I: Experimental errors.", *Eur. Phys. J.* **C28**, (2003) 455, (The MRST Collaboration), `hep-ph/0211080`.

[109] R. Bonciani, S. Catani, M. L. Mangano and P. Nason, "NLL resummation of the heavy-quark hadroproduction cross section", *Nucl. Phys.* **B529**, (1998) 424, hep-ph/9801375.

[110] T. Sjostrand, P. Eden, C. Friberg, L. Lonnblad, G. Miu, S. Mrenna and E. Norbin, *The Complete PYTHIA 6.206 manual*, page 140 (2002), hep-ph/0108264.

[111] C. Anastasiou and K. Melnikov, "Higgs Boson Production at Hadron Collider in NNLO QCD", *Nucl. Phys.* **B646**, (202) 220.

[112] G. Corcella, I. G. Knowles, G. Marchesini, S. Moretti, K. Odagiri, P. Richardson, M. H. Seymour and B. R. Webber, "HERWIG 6.5", *JHEP 0101:010* hep-ph/0210213.

[113] S. Kunszt, *Proceedings of the Workshop on Standard Model Physics at the LHC*, page 163 (CERN 2000-004, 2000).

[114] S. Dawson, "Radiative corrections to Higgs boson production", *Nucl. Phys.* **B359**, (1991) 283.

[115] G. Bozzi, S. Catani, D. de Florian and M. Grazzini, "The q(T) spectrum of the Higgs boson at the LHC in QCD perturbation theory", *Phys. Lett.* **B564**, (2003) 65, hep-ph/0302104.

[116] C. Balazs and C. P. Yuan, "Higgs boson production at the LHC with soft gluon effects", *Phys. Lett.* **B478**, (2000) 192.

[117] D. de Florian and M. Grazzini, "The structure of large logarithmic corrections at small transverse momentum in hadronic collisions", *Nucl. Phys.* **B616**, (2001) 247.

[118] The ROOT team, "ROOT: an Object-Oriented Data Analysis Framework", *Linux Journal* .

[119] F. James and M. Roos, "MINUIT a System for Function Minimization and Analysis of the Parameter Errors and Correlations", *Comput. Phys. Commun.* pages 343–367, cERN-DD-75-20.

[120] N. Amapane, M. Fierro and M. Konecki, "High-Level Trigger Algorithms For Muon Isolation", CMS NOTE 2002/040.

[121] V. Bartsch, J. Weng and G. Quast, "Observability of Higgs boson decays to four muons in the mass range from 115 to 140 GeV", CMS NOTE-IN 2003/07.

[122] A. D. Fabbro, "Double parton scattering processes in pp collisions and the scale factors", `hep-ph/0111416`.

[123] V. Bartsh and G. Quast, "Expected Signal Observability at Future Experiments", CMS NOTE-IN 2003/039.

[124] S. I. Bityokov and N. V. Krasnikov, "Signal Significance in the Presence of Systematic and Statistical Uncertainties", *Nucl. Instrum. Meth.* **A502**, (2003) 795.

[125] The ATLAS Collaboration, "ATLAS: Detector and Physics Performance Technical Design Report (Vol. II)", CERN/LHCC/99-15 (1999).

[126] M. H. Seymour, "Matrix-Element Corrections to Parton Shower Algorithms", *Comput. Phys. Commun.* **90** 95, `hep-ph/9410414`.

[127] S. Frixione and B. R. Webber, "Next-to-leading Order Calculations with Parton Showers", *JHEP* **0206** 029.

[128] G. Davatz, G. Dissertori, M. Dittmar, M. Grazzini and F. Pauss, "Effective K-factors for gg$\rightarrow$ H $\rightarrow$WW$\rightarrow$ $\ell\nu\ell\nu$ at the LHC", ETHZ-IPP PR-04-01, CERN-PH-TH/2004-035 (2004), `hep-ph/0402218`.

[129] J. Campbell, R. Ellis, F. Maltoni and S. Willenbrock, "Associated Production of a Z boson and a Single Heavy Quark Jet", *Phys. Rev.* **D69** 074021, `hep-ph/0312024`.

[130] V. Konoplianikov, A. Ulyanov and O. Kodolova, "Jet Calibration using γ+jet Events in the CMS detector", CMS NOTE-AN 2005/04.

[131] G. Segneri and F. Palla, "Lifetime based b-tagging with CMS", CMS NOTE 2004/046.

[132] J. Campbell, R. K. Ellis, F. Maltoni and S. Willenbrock, "Production of a Z Boson and Two Jets with One Heavy-quark Tag", CERN-PH-TH/2005-064.

[133] J. Heinrich, "A Guide to the Pearson Type IV distribution", CDF/MEMO/STATISTICS/PUBLIC/6820.

[134] W. H. Press, B. P. Flannery, S. A. Teukolsky and W. T. Vetterling, *Numerical recipes: The Art of Scientific Computing* (Cambridge University Press, 2002).

Acknowledgements

Nessun lavoro é il risultato dello sforzo di un singolo e questa Tesi non fa certamente eccezione.

Insieme a tutti coloro che hanno direttamente lavorato con me, in particolare Vitaliano e tutti gli amici della stanza 183, voglio ringraziare anche tutti quelli che mi hanno accompagnato e spronato fino a questo importante traguardo.

Grazie a babbo e mamma, a David, a Rebecca e a Franci che hanno sempre saputo consigliarmi, permettendomi però di scegliere sempre in assoluta libertà.

Per concludere credo sia doveroso un ringraziamento anche a quei pochi dischi che hanno sostenuto senza problemi un backup di questo lavoro.